AD-A064 198 UTAH STATE UNIV LOGAN ELECTRO-DYNAMICS LAB F/G 20/6
INCREASING THE THROUGHPUT OF HADAMARD SPECTROMETERS BY THE USE --ETC(U)
SEP 78 R W ESPLIN, G A VANASSE, D J BAKER F19628-77-C-0203
UNCLASSIFIED EDL-SRL-78-2 AFGL-TR-78-0232 NL

1 OF 4
AD A064198



BLANK PAGE

DDC FILE COPY AD A064198

(18) (19) AFGL-TR-78-0232

(12) SC

LEVEL II

(6) INCREASING THE THROUGHPUT OF HADAMARD SPECTROMETERS BY THE USE OF CURVED SLOTS

(10) Roy W./Esplin,
George A./Vanasse,
Doran J./Baker
Ronald J./Huppi

Electro-Dynamics Laboratories (SRL)
Utah State University
Logan, Utah 84322

(12) 318 p.

(11) 22 Sept[redacted]78

(15) F19628-77-C-0203

(14) EDL-SRL-78-2,
Scientific [redacted]-1

(16) 2310, 8603

(17) G1, 01

DDC RECEIVED FEB 6 1979 A

Approved for public release; distribution unlimited

This research was sponsored by the Air Force Systems Command under Project 2310 (8603), Task 2310G1 (860301), Work Unit 2310G101 (86030101) entitled: Infrared and Optical Techniques

AIR FORCE GEOPHYSICS LABORATORY
AIR FORCE SYSTEMS COMMAND
UNITED STATES AIR FORCE
HANSCOM AFB, MASSACHUSETTS 01731

123 870

79 02 05 020

Qualified requestors may obtain additional copies from the Defense Documentation Center. All others should apply to the National Technical Information Service.

UNCLASSIFIED

SECURITY CLASSIFICATION OF THIS PAGE (When Data Entered)

REPORT DOCUMENTATION PAGE		READ INSTRUCTIONS BEFORE COMPLETING FORM
1. REPORT NUMBER AFGL-TR-78-0232	2. GOVT ACCESSION NO.	3. RECIPIENT'S CATALOG NUMBER EDL-SRL-78-2
4. TITLE (and Subtitle) INCREASING THE THROUGHPUT OF HADAMARD SPECTROMETERS BY THE USE OF CURVED SLOTS		5. TYPE OF REPORT & PERIOD COVERED Scientific Report No. 1 6. PERFORMING ORG. REPORT NUMBER
7. AUTHOR(s) Roy W. Esplin, George A. Vanasse, Doran J. Baker, and Ronald J. Huppi		8. CONTRACT OR GRANT NUMBER(s) F19628-77-C-0203
9. PERFORMING ORGANIZATION NAME AND ADDRESS Electro-Dynamics Laboratories Utah State University Logan, Utah 84322		10. PROGRAM ELEMENT, PROJECT, TASK AREA & WORK UNIT NUMBERS 2310G101 (8630101) 61102F
11. CONTROLLING OFFICE NAME AND ADDRESS Air Force Geophysics Laboratory Hanscom AFB, Massachusetts 01731 Monitor/ Dean F. Kimball, OPR		12. REPORT DATE 22 September 1978 13. NUMBER OF PAGES 327
14. MONITORING AGENCY NAME & ADDRESS (if different from Controlling Office)		15. SECURITY CLASS. (of this report) UNCLASSIFIED 15a. DECLASSIFICATION/DOWNGRADING SCHEDULE

16. DISTRIBUTION STATEMENT (of this Report)

Approved for public release, distribution unlimited.

17. DISTRIBUTION STATEMENT (of the abstract entered in Block 20, if different from Report)

18. SUPPLEMENTARY NOTES

This research was sponsored by the Air Force Systems Command under Project 2310 (8603), task 2310G1 (860301), Work Unit 2310G101 (86030101).

19. KEY WORDS (Continue on reverse side if necessary and identify by block number)

Hadamard, spectrometer, multiplexing, optical aberrations, encoding.

20. ABSTRACT (Continue on reverse side if necessary and identify by block number)

NEXT PAGE

DD FORM 1 JAN 73 1473 EDITION OF 1 NOV 65 IS OBSOLETE

UNCLASSIFIED

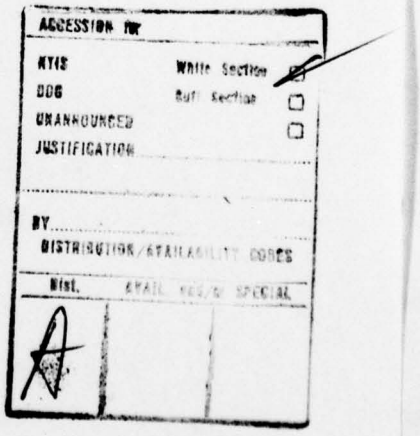
SECURITY CLASSIFICATION OF THIS PAGE (When Data Entered)

This report proves that the optical throughput of Hadamard spectrometers can be significantly increased by using curved rather than straight slots. The slot curvature for a representative Hadamard spectrometer is optimized. For this Hadamard spectrometer the throughput is increased by a factor of ten by using optimally curved slots instead of straight slots. Analytic and ray-tracing methods are used to optimize the slot curvature. Experimental measurements with both straight and optimally curved slots are given for comparison. Ammonia absorption spectra taken in the 9 to 13-μm wavelength interval using 20-mm tall curved slots are given.

micrometers

ACKNOWLEDGEMENTS

The technical assistance of Randy B. Shipley in constructing and operating the Hadamard spectrometer is gratefully acknowledged. Thanks go to A.T. Stair, Jr. and Randall Murphy for their support.



79 02 05 020

TABLE OF CONTENTS

Page

ACKNOWLEDGEMENTS 3

LIST OF FIGURES 8

LIST OF TABLES 14

INTRODUCTION 17

OBJECTIVES 21

Principal Objective 21
Secondary Objectives 21

BACKGROUND AND REVIEW OF LITERATURE 23

THEORY OF ABERRATION NEUTRALIZATION THROUGH THE USE OF CURVED SLOTS 39

Description of the Representative Hadamard Spectrometer 40

Analytic Expressions for the Optical Aberrations of the Representative Hadamard Spectrometer 47

Conversion of path-length variation expressions into transverse aberration expressions 49
Spherical aberration 52
Coma 54
Astigmatism 57
The spot size 58
Field curvature 59
Spectrum line curvature 68
Accuracy 71

A Ray-Tracing Analysis of the Imaging Fidelity of the Representative Hadamard Spectrometer 72

Cartesian coordinates of the representative Hadamard spectrometer 73
Ray-tracing computer programs 79

PRECEDING PAGE NOT FILMED
BLANK

Page

Optimization of the focal plane location 84
Spot diagrams 87
Spectrum line curvature 90
Selection of the slot width 91

Theoretical Performance of the Representative Hadamard Spectrometer when Equipped with Straight Slots 93

Theoretical Performance of the Representative Hadamard Spectrometer when Equipped with Curved Slots 102

Optimization of slot curvature 104
Theoretical performance with the slot curvature optimized 117

EXPERIMENTAL VERIFICATION 129

Experimental Prototype Hadamard Spectrometer . . . 129

Masks 129
Entrance slits 129
Detectors 131
The signal-to-noise ratio 133
Data reduction 133

Experimental Comparison between the Performance of Curved and Straight Slots 134

Measurement procedure 134
Direct-mode measurements 140
Transform-mode measurements 154

Measurement of a Representative Infrared Spectrum . 157

Measurement procedure 157
The measured ammonia spectrum 163

CONCLUSIONS 171

LITERATURE CITED 173

APPENDIXES 179

Page

Appendix A. Hadamard Spectroscopy 181

Hadamard encoding masks 181
Singly-encoded Hadamard spectrometers 185
Doubly-encoded Hadamard spectrometers 191

Appendix B. Relationship Between Total-Mean-Square Error and Signal-to-Noise Ratio Descriptions of Hadamard Spectrometers. 207

Appendix C. Generation of Hadamard Mask Patterns. . 211

Appendix D. Multiplication by the Inverse of the *S* Matrix Using the Fast Hadamard Transform 225

Step 1 of the algorithm 229
Step 2 of the algorithm 231
Step 3 of the algorithm 240
Evaluation of the algorithm 243
Computer programs to implement the algorithm . . 247

Appendix E. A General Ray-Tracing Procedure 251

Transformation to the local coordinate system. . 252
Computation of the coordinates of the point of intersection of the ray with the optical surface 256
Computation of the direction cosines of the ray after its direction is altered by the optical surface 263
Transformation to the reference coordinate system 270
Summary 271

Appendix F. Derivation of Expression for Meridional Focal Length of a Spherical Mirror . . 273

Appendix G. Derivation of an Expression for the Grating Rotation Angle of a Czerny-Turner Spectrograph 277

Appendix H. Computer Program Listings 281

General purpose ray-tracing subroutines 281
Programs representative of those used in the ray-tracing analysis of the Czerny-Turner optical system 290
Basic programs to recover the spectrum from the measurements of a Hadamard spectrometer 302

DISTRIBUTION LIST 308

LIST OF FIGURES

Figure		Page
1.	The spectrum of the 0.5461-μm mercury emission line measured with the spectrometer constructed for this investigation operated (a) as a monochromator and (b) as a singly-encoded Hadamard spectrometer. The observation time was the same for both plots	19
2.	The optical system of the Czerny-Turner spectrograph	41
3.	The optical system of the Model 305-HS Hadamard spectrometer of Minuteman Laboratories, Inc.	43
4.	The optical system used for the theoretical analysis	44
5.	Geometry defining parameters to compute the focal surface of a Czerny-Turner optical system	60
6.	Geometry for central ray	62
7.	Relationship between the best-fit focal line described by Equation (44) and the coordinate system used in the ray-tracing analysis	65
8.	The analytically computed focal surface	67
9a.	Geometry for principal rays at the grating	70
9b.	Mecator projection of the unit sphere; (dimensions are angular)	70
10.	Definition of several points used in the ray-tracing analysis	74
11.	Geometrical drawing from which expressions for the Cartesian coordinates of the optical components were derived. The lines marked with the two vertical bars are parallel	75
12a.	The cones of rays surrounding the principal ray	81
12b.	Ray intersections with a plane perpendicular to the principal plane looking in the direction of the principal ray	81

Figure Page

13. Cross sections of the ray-trace and the actual collimated beams. Dimensions are in millimeters 83

14. On-axis spot diagrams with the focal plane inclined at an angle of 8.25° to the X-axis for wavelengths (a) 10.5 μm, (b) 11 μm, (c) 11.5 μm, (d) 11.75 μm, (e) 12 μm, (f) 12.25 μm, and (g) 12.5 μm. All dimensions are in microns with each spot diagram having its own scale 88

15. Astigmatism and image curvature combine to broaden the image of a straight entrance slit 94

16. Spot diagrams at a wavelength of 11.5 μm at object heights of (a) 9 mm (b) 29 mm 96

17. Image curvature limitation for straight entrance slit and straight mask slots if no astigmatism were present 98

18. Neutralization of spectrum line curvature by aligning straight slots with the spectral images . 99

19. Geometry used to derive an expression for the image width 101

20. A curved slot 105

21. The horizontal distance from the mask slot center line to the principal ray versus the mask slot radius for an entrance slit radius of 91.110 mm and an object height of 15 mm . . . 107

22. The required mask slot width to collect 85 percent of the spot diagram versus the mask slot radius for an entrance slit radius of 91.110 mm and an object height of 15 mm 108

23. The required mask slot width to collect 85 percent of the spot diagram versus the mask slot radius for an entrance slit radius of 91.110 mm and an object height of 25 mm 109

24. The horizontal distance from the mask slot center line to the principal ray versus the common radius value of the entrance slit and the mask slots for an object height of 15 mm . . 112

Figure Page

25. The required mask slot width to collect 85 percent of the spot diagram versus the common radius value of the entrance slit and the mask slots for an object height of 15 mm 113

26. Center line of entrance slit plotted on the coordinate system used for ray tracing when (a) the center line passes through the origin and (b) when the center line crosses the Y axis at a height of 19.05 mm 116

27. The horizontal distance from the mask slot center line to the principal ray. The parameter Y_s is the height of a point object located in the entrance slit 119

28. The required mask slot width to collect 85 percent of the spot diagram. The parameter Y_s is the height of a point object located in the entrance slit 120

29. The maximum object height for which there is no significant deterioration in the resolution of the representative Hadamard spectrometer 124

30. The slot width required for the grating angles tabulated in Table 11 128

31. The curved slot Hadamard mask 130

32. The relative response of the HgCdTe detector and order-sorting filter combination 132

33. The instrumental profile at spectral element number 500 with an entrance slit length of 20 mm 144

34. The width of the instrumental profile, normalized to 197 μm, at 50 percent of the peak value. The symbol ℓ represents the entrance slit length 143

35. The width of the instrumental profile, normalized to 197 μm, at 50 percent of the peak value for spectral element number 50 . . . 145

36. The resolution of two equal intensity lines spaced 1.5 slot widths apart 147

Figure Page

37. Direct-mode measurements of the sodium doublet with the stronger line at spectral element number 303 with the following conditions: (a) curved slots, ℓ = 20 mm, (b) straight slots, ℓ = 2 mm, (c) straight slots, ℓ = 5 mm, (d) straight slots, ℓ = 10 mm, (e) straight slots, ℓ = 15 mm, (f) straight slots, ℓ = 20 mm. The symbol ℓ is the entrance slit length. 149

38. Direct mode measurements of the sodium doublet with an entrance slit length of 20 mm with the stronger line located in the following spectral element numbers: (a) 56, (b) 143, (c) 255, (d) 303, (e) 383, (f) 496. 151

39. The normalized ratio of the dip height to the maximum spectrum height for the sodium doublet. 153

40. The spectrum of the 18th order of the mercury 0.5461-μm line measured by operating the prototype Hadamard spectrometer in the transform mode 155

41. Transform-mode measurements of the sodium doublet made with straight slots and entrance slit lengths of (a) 20 mm and (b) 15 mm 158

42. Transform-mode measurements of the sodium doublet made with straight slots and entrance slit lengths of (a) 10 mm and (b) 5 mm 159

43. Transform-mode measurements of the sodium doublet with curved slots and a 20-mm long entrance slit. 160

44. Equipment configuration used to measure absorption spectrum of ammonia 162

45. The absorption spectrum of ammonia at a pressure of one atmosphere and a temperature of 25 degrees Celsius measured over the 8.8 to 10.7-μm wavelength interval using the prototype spectrometer in the transform mode with an observation time of 20 seconds. 164

Figure Page

46. The absorption spectrum of ammonia at a pressure of one atmosphere and a temperature of 25 degrees Celsius measured over the 10.6 to 12.3-μm wavelength interval using the prototype spectrometer in the transform mode with an observation time of 20 seconds 165

47. Results of coadding nine measurements of the 8.8 to 10.7-μm wavelength interval of the ammonia absorption spectrum 166

48. Results of coadding nine measurements of the 10.6 to 12.3-μm wavelength interval of the ammonia absorption spectrum 167

A-1. Relationship between Hadamard matrices and Hadamard encoding masks 183

A-2. Basic types of singly-encoded Hadamard spectrometers 186

A-3. *Sloane's* [1970] matrix $\{b_{ij}\}$ for $N = 7$ 200

C-1. (a) A general n-stage shift register circuit to generate *PN* sequence with period $N = 2^n-1$ where the values of (a_i) are determined by a n-th order primitive polynomial. (b) A three-stage shift register circuit based on the primitive polynomial $f(x) = x^3 + x + 1$ which generates the PN sequence 1110010 218

D-1. FHT signal flow graphs. (a), (b), and (c) correspond, respectively, to Equations (D-17), (D-21), and (D-25) 237

D-2. The signal flow graph for the FHT algorithm of *Nelson* and *Fredman* [1972] with $N = 7$ 238

E-1. The reference coordinate system $(\overline{X},\overline{Y},\overline{Z})$ and the local coordinate system (X,Y,Z) of the optical surface. The point P is a point on the ray. . . 253

E-2. Transformation of the coordinate system $(\overline{X},\overline{Y},\overline{Z})$ into the local coordinate system (X,Y,Z) after translating $\overline{O}$ to O. (a) The angular rotation α transforms $(\overline{X},\overline{Y},\overline{Z})$ into (X',Y',Z'). (b) The angular rotation β transforms (X',Y',Z') into (X'',Y'',Z''). (c) The angular rotation γ transforms $X',Y',Z')$ into (X,Y,Z) 255

Figure Page

E-3. Specification of the rulings of a conventional grating by means of the intersection of a family of parallel planes with the grating surface 267

F-1. The meridional focal length of a spherical mirror 275

G-1. The optical path, in the region of the grating, of a ray that passes through the center of the focal plane in a Czerny-Turner spectrograph 278

LIST OF TABLES

Table		Page
1.	Values of the optical parameters of the Minuteman Model 305-HS Hadamard spectrometer optimized for a central wavelength of 11.5 μm	45
2.	Values of selected angles when k equals unity and λ equals 11.5 μm	49
3.	Coordinates of points defined in Figure 10	77
4.	Values of several angles defined in Figure 11	78
5.	Dimensions of on-axis spot diagrams at selected focal plane angles. The spot widths were scaled from plots and have a tolerance of ± 5 μm. The spot lengths were taken from computer listings and have tolerances of ± 0.5 μm	85
6.	Dimensions of spot diagrams for focal planes translated small distances from the meridional focal length. Positive and negative translations signify, respectively, translations away from and toward the spherical mirror 2. Tolerances are ± 5 μm for spot width and ± 0.5 μm for spot length	86
7.	The lateral translation due to spectrum line curvature for several object heights, Y_s, at a 11.5-μm wavelength	91
8.	Required slot width required to fit N spectral elements within a field stop 100-mm wide	93
9.	Image widths and parameters from which these widths were computed for the representative Hadamard spectrometer when equipped with straight slots and the wavelength is 11.5 μm	102
10.	The spectral interval over which there is no degradation in resolution for a slot width of 197 μm	122
11.	The grating angles and wavelengths used to compute the data plotted in Figure 30	127

Table Page

12. Wavelengths of absorption lines identified in Figures 45, 46, 47, and 48. These wavelength values were computed by converting the wavenumber values given by the *International Union of Pure and Applied Chemistry* [1961] to wavelength values 168

A-1. A signal-to-noise ratio comparison between singly-encoded Hadamard spectrometers with codes based on H, G, and S matrices and a monochromator 190

A-2. Comparison between Sloane's doubly-encoded $2N$-1 measurement scheme and a monochromator for N = 7. (Both instruments measure $2N$-1 = 13 spectral elements.) 201

B-1. The signal-to-noise advantage for several Hadamard spectrometer encoding schemes derived from total-mean-square error expressions in the literature 210

C-1. An example primitive polynomial (modulo 2) for each degree from 2 to 15 [*Watson*, 1962] . . 215

C-2. A $2N$-1 mask pattern for N equal to 511. Codes of 1 and 0 represent transparent and opaque slots, respectively. 220

D-1. The permutation π_1 for the singly-encoded Hadamard spectrometer example described by Equation (D-2) 230

D-2. The permutation π_2 for the singly-encoded Hadamard spectrometer described by Equation (D-2) 242

D-3. The required number of computer storage locations and operations for three algorithms which implement multiplication by S^{-1}. 246

D-4. A numerical comparison of the computer operations required for the fast algorithm and the exploited algorithm 248

INTRODUCTION

Three basic procedures are used to maximize the capability of spectrometers to measure small amounts of optical energy. The first is to use the most sensitive detector possible. The second procedure is to maximize the energy collecting capability of the spectrometer, the optical throughput. The third is to maximize the measurement time. One method of increasing the measurement time is to employ multiplexing, a technique that allows energy of many elements of the spectrum to be simultaneously collected onto a single detector. In multiplexing, the optical energy is encoded so that the energy in each spectral element can be found by decoding the detector signal. The energy in each spectral element is utilized for a larger percentage of the time with a multiplex spectrometer than it is by a spectrometer that measures each spectral element sequentially in time. If the dominant source of noise is either the detector or the signal-processing electronics, multiplexing improves the capability of a spectrometer to measure small amounts of optical energy.

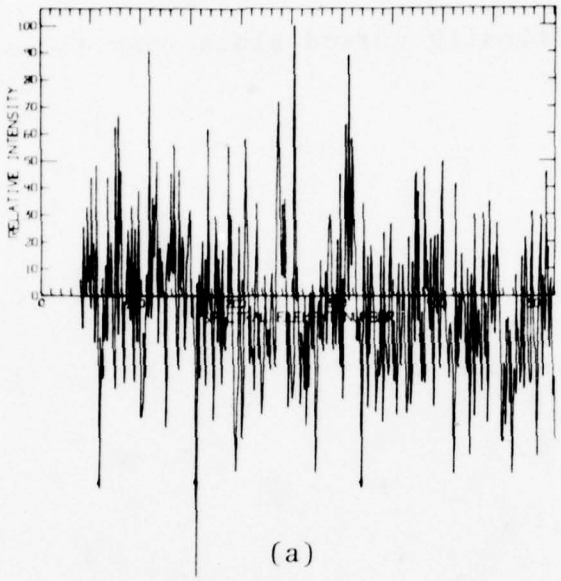
If either the entrance slit or exit slit of a conventional monochromator is replaced with an encoding mask based on a Hadamard matrix, a multiplex spectrometer results.

PRECEDING PAGE NOT FILMED
BLANK

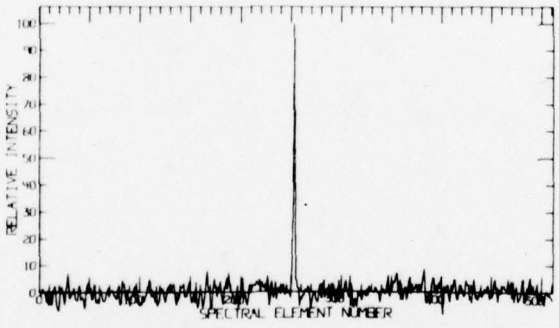
This multiplex spectrometer is referred to as a singly-encoded Hadamard spectrometer. If both the entrance and exit slits of a conventional monochromator are replaced with encoding masks based on Hadamard matrices, a multiplex spectrometer with an optical throughput greater than the monochromator results. This spectrometer is referred to as a doubly-encoded spectrometer. The theory of both singly and doubly-encoded Hadamard spectrometers is given in Appendixes A, B, C, and D.

The practical significance of the multiplex advantage of a singly-encoded Hadamard spectrometer is illustrated in Figure 1. The plots in this figure were made using the singly-encoded Hadamard spectrometer constructed for this investigation. Plot (a) was made by operating the spectrometer as a monochromator, and plot (b) was made by operating the spectrometer as a singly-encoded Hadamard spectrometer. Both these plots are measurements of the 0.5461-μm mercury emission line, where the same observation time was used for both plots.

The effects of optical aberrations on the operation of Hadamard spectrometers has been almost ignored in the literature. The purpose of this Hadamard investigation is to prove that the effects of optical aberrations can be significantly reduced by properly curving the slots in the Hadamard mask. It is proven by using both theoretical and experimental methods that the usable slot length of a



(a)



(b)

Figure 1. The spectrum of the 0.5461-μm mercury emission line measured with the spectrometer constructed for this investigation operated (a) as a monochromator and (b) as a singly-encoded Hadamard spectrometer. The observation time was the same for both plots.

representative Hadamard spectrometer is a factor of ten larger for optimally curved slots than for straight slots.

OBJECTIVES

Principal Objective

The principal objective of this Hadamard spectrometer investigation is to prove, by using both theoretical and experimental methods, that the optical throughput of a Hadamard spectrometer can be made significantly larger with curved slots, all of which have the same curvature, than with straight slots.

Secondary Objectives

The secondary objectives of this investigation are the following:

(1) Provide engineering guidelines for the optimization of the slot curvature of Hadamard spectrometers.

(2) Derive transverse-aberration expressions for the Czerny-Turner optical system.

(3) Demonstrate the practicality of using the Hadamard spectrometer to make spectral measurements.

BACKGROUND AND REVIEW OF LITERATURE

The basic principles of Hadamard spectroscopy are described in Appendixes A and B. In these appendixes, it is shown how the capability of dispersive spectrometers to measure low-energy spectra can be increased by encoding the optical energy passing through them according to codes based on Hadamard matrices. The use of encoding masks to improve the measurement capability of dispersive spectrometers to measure low-energy spectra was first demonstrated by *Golay* [1949]. He proposed a method of encoding the energy passing through N entrance slits and N exit slits using sinusoidal modulation.

Golay compared his method with the encoding method that was being developed at that time by *Fellgett* [1951], who used an interferometer to sinusoidally encode the optical radiation. Fellgett pointed out that for the infrared spectral region his interferometric measurement method had a signal-to-noise ratio advantage over spectrometers that measure the spectral elements sequentially in time. This advantage is often referred to as the multiplex advantage [*Vanasse* and *Sakai*, 1967]. Golay argued that his sinusoidal-modulation encoding method would give a

PRECEDING PAGE NOT FILMED
BLANK

dispersive spectrometer the multiplex advantage as well as increase its optical throughput.

However, Golay did not find it practical to construct a spectrometer to implement his sinusoidal-modulation encoding technique. Instead, he demonstrated a binary-modulation encoding technique that increased the optical throughput but did not have the multiplex advantage. Golay implemented his binary-modulation encoding method by replacing the entrance and exit slits with revolving encoding masks.

Although Golay did not mention it, his binary encoding functions are related to Hadamard matrices, and perhaps Hadamard spectroscopy should be considered to date back to the work of Golay. His method of forming higher order codes by iterating the pattern

$$\begin{matrix} 0 & 0 \\ 0 & 1 \end{matrix}$$

is basically the Kronecker-product method [*Harmuth*, 1972] of forming higher order Hadamard matrices from the basic

$$\begin{bmatrix} 1 & 1 \\ 1 & -1 \end{bmatrix}$$

Hadamard matrix.

Golay [1951] also showed that if the proper pseudo-random encoding masks and two detectors are used, the throughput can be increased without requiring encoding

mask motion. He referred to spectrometers using this technique as static multislit spectrometers. The basic principle of static multislit spectrometers can be summarized in the following manner. At the desired wavelength the path to one detector is relatively unobstructed while the path to the other detector is completely obstructed. For the undesired wavelengths the paths to both detectors are equally obstructed. Thus, the difference between the signals from the two detectors is a measure of the desired wavelength. The spectrum is scanned by rotating the dispersive element.

About a decade after Golay proposed the static multislit spectrometer, *Girard* [1960, 1963] introduced his grill spectrometer, which also depended on encoding to increase the throughput of a dispersive spectrometer. From today's perspective it is apparent that Girard's grill spectrometer is just another implementation of the basic principle of Golay's static multislit spectrometer using a different encoding pattern. Originally Girard's encoding masks were one-dimensional Fresnel zone plates, but he subsequently used two-dimensional hyperbolic zone plates. *Despain* and *Vanasse* [1972] have pointed out the close similarity between Girard's hyperbolic zone plates and a two-dimensional pattern of sal functions. Sal functions are the Walsh functions of odd symmetry [*Harmuth*, 1972]. The letter *s* is used in the acronym to indicate that there is a similarity between sal functions and the sine function, while *al*

indicates that sal functions are a subset of Walsh functions. Since Hadamard matrices can be formed from Walsh functions [*Harmuth*, 1972], there is a close similarity between Hadamard spectrometers and grill spectrometers using hyperbolic zone plates.

The grill spectrometer can also be thought of as a spectrometer that forms a convolution-type transform of the spectrum along the plane of the exit mask [*Mertz*, 1965]. The exit mask is simply an electro-mechanical means of recovering one spectral component. Information about all spectral components is present in the exit mask plane; and if the spatial energy distribution in this plane were recorded for subsequent inversion, the multiplex advantage could be realized. However, this procedure has never been implemented.

Mertz [1965] showed that it is possible to use encoding techniques to both increase the throughput of a dispersive spectrometer and to give it the multiplex advantage when he introduced his Mock interferometer. The Mock interferometer is a dispersive spectrometer with the entrance and exit slits replaced with rotating Ronchi rulings. If the two masks are rotated together at a speed proportional to the sine of the rotation angle, each wavelength is modulated at a different frequency. The spectrum is recovered by mathematical inversion.

The first specific mention of Hadamard matrices in connection with encoding an optical spectrum seems to have

been made by *Ibbett, Aspinall* and *Grainger* [1968]. They suggested using N encoding masks based on an $(N+1) \times (N+1)$ Hadamard matrix to encode N spectral elements. Their code was derived from a Hadamard matrix by replacing 1's with 0's and -1's with 1's and then deleting the first row and column. Each row of the resulting matrix corresponded to an encoding mask with a 0 representing an opaque area and a 1 a transmitting area. They pointed out both the mechanical advantage of a multiplex technique that uses a dispersive spectrometer instead of an interferometer and the mathematical advantage of a data inversion process requiring only additions and subtractions that can be implemented in real time. The major limitation of the method is the requirement for N masks to encode N spectral elements.

At approximately the same time that Ibbett, Aspinall, and Grainger reported their work, *Gottlieb* [1968] suggested a multiplexing scheme for detector-noise-limited television systems. Gottlieb's method used codes based on pseudo-noise sequences [*Baumert*, 1964], often referred to as *PN* sequences or pseudo-random binary sequences. The major advantage of Gottlieb's method over the method of Ibbett, Aspinall, and Grainger is that only one mask with $2N-1$ slots is required to encode N elements. However, as shown in Appendix C, *PN* sequences are trivially related to Hadamard matrices. Gottlieb formed code words from the *PN* sequence by replacing +1's with 1's and -1's with 0's, where 1's and 0's represent transparent and opaque mask

areas, respectively. He showed that his multiplexing method yields a gain of approximately $\sqrt{N/8}$ over an unmultiplexed system. He also showed that the same results are obtained regardless of whether the mask is moved in a stepped or continuous fashion.

A few months after Ibbett, Aspinall and Grainger published their encoding method, *Decker* and *Harwit* [1968] published a similar encoding scheme for dispersive spectrometers. However, Decker and Harwit did not specifically use a Hadamard code. Instead they proposed that the N spectral elements be considered as N unknowns that could be recovered from N independent equations. The N independent equations would be determined from N measurements taken with N encoding masks.

The following year *Sloane et al.* [1969] published a comparison of the noise in the recovered spectrum for three codes based on Hadamard matrices. They identified the matrices representing these codes as H^T, G^T, and S^T. These three codes are discussed extensively in Appendixes A and B, where these matrices are identified as the H, G, and S matrices. Sloane et al. pointed out the conditions under which the matrices G^T and S^T can be made cyclic. They pointed out that cyclic codes are particularly advantageous, since they can be implemented with a single mask containing $2N$-1 slots instead of requiring N masks each with N slots for a total of N^2 slots. They emphasized the reduced instrument fabrication cost that should result from using

cyclic codes. The introduction of cyclic codes was an important advancement, since these codes make it possible to multiplex a large number of spectral elements with a simple and compact Hadamard spectrometer.

Sloane et al. compared the effectiveness of these three codes by computing the total-mean-square error in the recovered spectrum. The definition of total-mean-square error is given in Appendix B. The total-mean-square error is a measure of the error in the entire spectrum. This is a different method of expressing the error or noise than that used in Appendix A, where the noise associated with an individual spectral element is computed. However, the computations of Appendix A are reconciled with those of Sloane et al. in Appendix B. Thus, in both Appendixes A and B the multiplex advantage for the codes identified by the H^T, G^T, and S^T matrices are shown to be $\sqrt{N}$, $\sqrt{N/2}$, and $\sqrt{N}/2$, respectively. The S^T-matrix code has a multiplex gain that is a factor of two greater than the $\sqrt{N/8}$ gain of the Gottlieb code. Gottlieb's code is formed from the G^T matrix by replacing +1's with 1's and -1's with 0's.

Sloane et al. suggested that the codes G^T and H^T could be implemented with masks consisting of reflecting and transmitting segments. Since infrared detectors usually require chopped radiation, the chopper could chop between transmitted and reflected radiation. They also suggested using a stationary slit together with a cyclic mask to implement the H^T code. However, apparently no one has yet

constructed a Hadamard spectrometer with a reflecting and transmitting mask. All Hadamard spectrometers constructed to this date have implemented the S^T code, which requires masks consisting of transparent and opaque areas.

Nelson and *Fredman* [1970] have summarized the basic theory of Hadamard spectrometers that use a single encoding mask. Appendixes C and D and the section on singly-encoded Hadamard spectrometers in Appendix A are amplifications of their paper.

The first cyclic singly-encoded Hadamard spectrometer appears to have been a 19-slot unit constructed by *Decker* [1970]. *Decker* [1970] also reported construction of a 255-slot singly-encoded Hadamard spectrometer. Using this 255-slot Hadamard spectrometer, he later [*Decker*, 1971] reported experimental verification of the multiplex advantage.

Graauw and *Veltman* [1970] constructed a solar-eclipse spectrometer that multiplexed 255 spectral elements using an encoding pattern based on a pseudo-random binary sequence. As stated previously, pseudo-random sequences are trivially related to Hadamard matrices. Since the spectrometer was used in the visible spectral region with photomultiplier tubes, it did not have the multiplex advantage. Multiplexing was used only because it made possible increased temporal resolution (40 msec). The temporal resolution was achieved by locating 255 masks on a rapidly rotating cylinder.

As shown herein, the optical system must be carefully selected so that the length of the slots can be maximized. It appears that the first Hadamard spectrometer with a usable slot length long enough to provide a practical measurement advantage over an optimized monochromator was constructed by *Hansen* and *Strong* [1972]. Their high resolution (0.1 cm^{-1}) infrared Hadamard spectrometer encoded 127 spectral elements using 12 mm long slots. In order to attain this slot length, they used an on-axis configuration using an echelle grating, an infrared achromatic lens, and an image slicer.

Ware [1973] showed that if the spectrum varies during the time that the required N Hadamard encoded measurements are taken, serious errors in the recovered spectrum result. He showed that these errors result because the rows of the S^T matrix are not orthogonal. He also proved that for the H^T matrix code the recovered spectrum is the mean value of the changing spectrum.

Harwit et al. [1970] proposed replacing both the entrance and exit slits with Hadamard encoding masks in order to increase the throughput. They called such spectrometers doubly multiplexed dispersive spectrometers, but these spectrometers are better described as doubly-encoded dispersive spectrometers. The theory of doubly-encoded spectrometers is given in Appendixes A and B. They showed that if N entrance and N exit slots are used, that N spectra, one for each entrance slot, can be recovered

from N^2 measurements. They also pointed out that there are only $2N$-1 spectral elements and that the signal-to-noise ratio can be improved by adding all the estimates of each spectral element. As shown in Appendix B, calculations show that if this is done, a doubly-encoded Hadamard spectrometer has a signal-to-noise ratio gain proportional to N over a conventional monochromator. Harwit et al. also pointed out that the $2N$-1 spectral elements can be recovered from $2N$-1 measurements; however, they were unable to give a simple rule for specifying the particular $2N$-1 measurements to take.

Sloane [1970] used a computer to search for sets of $2N$-1 measurements that yield $2N$-1 independent equations in the $2N$-1 unknown spectral elements. In general, there are many possible sets for each N, and the noise properties of each set must be independently calculated. Sloane published sets of measurements for N = 3, 7, 11, and 15; however, the value of any encoding technique depends on the noise in the recovered spectrum. As shown in Appendix A, Sloane's set of measurements for N = 7 yields an average signal-to-noise ratio gain over a conventional monochromator of 1.2, compared with 1.8 for a singly-encoded Hadamard. It is shown in Appendix A that the noise for 4 of the 13 spectral elements is actually worse for the doubly-encoded Hadamard than for the monochromator. *Phillips* and *Harwit* [1970] recovered a spectrum with a laboratory prototype using Sloane's set of $2N$-1 measurements for N = 7. The author has also used a

computer to search for linearly independent sets of $2N-1$ equations, but he has not found a set that yields a signal-to-noise ratio significantly better than a singly-encoded Hadamard spectrometer.

Laboratory spectra taken with a doubly-encoded Hadamard spectrometer with 19 entrance slots and 19 exit slots have been reported by *Phillips* and *Harwit* [1971]. They recovered spectra of each of the 19 entrance slots and then summed these 19 spectra. This same spectrometer was later used by *Phillips* and *Briotta* [1974] to take spectra of the atmospheres of the Earth and of Jupiter. However, measurements of the atmosphere of Jupiter were taken with only three entrance slots, and those of the Earth's atmosphere were taken with a single entrance slit.

The doubly-encoded Hadamard spectrometer provides a spectrum for each individual entrance slit. The information in these spectra may also be displayed as one-dimensional images in each of the spectral element wavelengths. In order to provide two-dimensional spectral images, *Harwit* [1971] proposed folding the one-dimensional entrance mask into a two-dimensional cyclic Hadamard mask. Since the resulting instrument provides images at the wavelengths of each of the spectral elements, he called this instrument a spectrometric imager. Two-dimensional masks based on cyclic Hadamard matrices had been proposed earlier [*Gottlieb*, 1968], but *Harwit* [1971] showed that it is possible to encode mp spatial elements with an entrance mask

containing only $(2m-1)(2p-1)$ elements if $mp+1$ is a multiple of 4, $p = m+2$, and both p and m are prime numbers. Gottlieb's method required an entrance mask containing $m(mp+p-1)$ elements. Harwit also pointed out that his spectrometric imager can be described using mathematics identical in form to the mathematics used to describe the doubly-encoded Hadamard spectrometer. The spectrometric imager can also display the spectrum for each point on the object imaged on the entrance mask. Later, *Harwit* [1973] described a spectrometric imager prototype with 63 two-dimensional spatial elements and 15 spectral elements.

There has been much controversy about the relative merits of Hadamard and Fourier spectrometers [*Hirschfeld* and *Wyntjes*, 1973, 1974; *Decker* 1974]. Throughout this controversy it has been assumed that the doubly-encoded Hadamard has an encoding gain over a monochromator proportional to the number of entrance slots. Although a method of doubly-encoding a Hadamard spectrometer so that it has this gain may exist, the best encoding methods proposed to this date provide a gain proportional to the square root of the number of entrance slots. The encoding gain for doubly-encoded Hadamard spectrometers is discussed in Appendixes A and B.

Wyatt and *Esplin* [1974] have pointed out that for some detectors the signal-to-noise ratio of doubly-encoded Hadamard spectrometers is less than it is for singly-encoded Hadamard spectrometers.

Harwit et al. [1974] introduced two methods for doubly encoding Hadamard spectrometers that require only N measurements to recover N spectral elements. However, these are not optimal codes since, as shown in Appendix B, they improve the performance of the doubly-encoded Hadamard over a singly-encoded Hadamard case by a factor of $\sqrt{M}/2$ instead of $M/2$, where M is the number of entrance slots. As shown by Equation (A-32) in Appendix A, this is the same improvement given by the method requiring MN measurements and summing all the estimates of each wavelength. However, since these two encoding schemes of Harwit et al. require only as many measurements as there are spectral elements, the problems pointed out by Wyatt and Esplin do not apply, since a monochromator must also make the same number of measurements.

Tai et al. [1975a] introduced a real-time algorithm to recover the spectra for each entrance slot of a doubly-encoded Hadamard. They used the same instrument used by *Harwit et al.* [1974]. For 15 entrance and 255 exit slots their algorithm took 13 minutes on a minicomputer to complete a run.

Tai et al. [1975b] presented an analysis of the spectral errors resulting when the transparent areas of the mask are either all too wide or all too narrow. In both cases they have shown that a single line is recovered as a line plus four small blips. They considered this to be an impulse response and showed that the response to an arbitrary spectrum could be computed using it.

Hadamard spectroscopy has been summarized and compared with other multiplex techniques by *Vanasse* [1972]. *Decker* [1977] has written a summary of Hadamard spectroscopy.

Three publications that mention using curved slots with Hadamard spectrometer were found. *Esplin, Shipley* and *Huppi* [1975] have reported infrared spectra taken using curved slots with the Hadamard spectrometer that is analyzed in greater depth herein. *Swift et al.* [1976] constructed an imaging Hadamard spectrometer that used curved slots. *Decker* [1977] described the spectrometer constructed by Swift et al.

For both prism and grating instruments the images of an array of straight slots are curved. Golay considered this when he constructed his spectrometers. For example, in introducing the dynamic multislit spectrometer [*Golay*, 1949], he indicated that he had to shorten the effective slit height from the 13 mm used for a single slit to 8 mm for his 64-slit arrangement because he said there was no correction made for slit curvature. In fabricating the static multislit spectrometer, *Golay* [1951] had his mask slots painstakingly shaped to correct for slit curvature.

Randall and *Firestone* [1938] showed that in a grating spectrograph with a straight entrance slot the lateral displacement of an image point from a straight line (slit curvature) is proportional to the square of the distance above or below the optical axis. A few years later *Minkowski* [1942], apparently unaware of the work of Randall

and Firestone, gave an analytical derivation of this relationship. *James* and *Sternberg* [1969] have also given a derivation for slit curvature.

Fastie [1952a, 1952b, 1953] reintroduced Ebert's monochromator and showed that with this configuration the effects of slit curvature could be completely neutralized by using curved entrance and exit slits with radii equal to the distance from the slit to the optical center line. In addition, he showed that this arrangement partially neutralizes the effects of astigmatism, since the astigmatic line images of a point are formed tangent to the exit slit. *Rupert* [1952], a contemporary of Fastie at John Hopkins University, published a paper giving expressions to compute the curvatures required for the entrance and exit slits of grating monochromators.

In a doubly-encoded spectrometer the imaging of an extended source must be considered. *Laws* [1962] derived an expression giving the distortion of an extended monochromatic image. He showed that lateral aberrational displacement is proportional to the square of the distance between the object point and the optical axis. *Girard* [1963] corrected for distortion in his grill spectrometer (a doubly-encoded spectrometer) by using a photograph of the entrance grill as imaged by the spectrometer as his exit mask. *Tinsley* [1966] neutralized the effects of astigmatism and distortion in his grill spectrometer by using an Ebert configuration with a circularly-symmetric grill pattern.

Mertz [1965] used an ingenious method to correct line curvature and varying lateral magnification in his Mock interferometer (a doubly-encoded spectrometer). His technique is similar to a field compensation technique commonly used with Michelson interferometers [*Bouchereine* and *Connes*, 1963]. He used a prism in front of the grating in his Littrow system so that the vertical image as seen through the prism is normal to the Littrow axis.

THEORY OF ABERRATION NEUTRALIZATION THROUGH THE USE OF CURVED SLOTS

As can be seen from the description of Hadamard spectrometer theory given in Appendix A, a Hadamard spectrometer will function properly only if the spectral images of each entrance slot are approximately the same size and shape as the exit slots. The size and shape of the spectral images of an entrance slot depend on the size and shape of the entrance slot and on the imaging properties of the spectrometer optics. Ideal Hadamard spectrometer optics would form spectral images with the same shape as the entrance slot. The spectral images formed by ideal spectrometer optics need not be the same size as the entrance slot; that is, ideal spectrometer optics can introduce magnification. Magnification can be neutralized by making the entrance and exit slots differ in size by the magnification factor. Practical Hadamard spectrometer optics will not form spectral images which are exact scaled replicas of the entrance slot; the spectral images will be degraded by optical aberrations. These aberrations increase as the encoded areas at the entrance and exit masks increase. Thus, the size that these encoded areas can be

is limited by optical aberrations. The theoretical computations reported herein prove that this aberration limitation can be partially neutralized by using curved rather than straight slots.

The degree to which the aberration limitations can be neutralized through the use of curved slots was investigated by analyzing a representative Hadamard spectrometer design. A singly-encoded Hadamard spectrometer design that uses the optical system of the Czerny-Turner spectrograph was selected as the representative Hadamard spectrometer design. The optical system of the Czerny-Turner spectrograph is shown schematically in Figure 2. The disperse-encode-dedisperse type of singly-encoded spectrometer, which is defined in Appendix A, was selected for analysis. This analysis was conducted using both analytic and numerical ray-tracing procedures. The results of this analysis showed that the use of curved rather than straight slots significantly reduces the aberration limitation.

Description of the Representative Hadamard Spectrometer

The Hadamard spectrometer model 305-HS of Minuteman Laboratories, Inc., optimized for a central wavelength of 11.5 μm, was selected as the representative Hadamard spectrometer. The theoretical performance of this spectrometer when equipped with straight slots and also when equipped with curved slots was computed. The optical

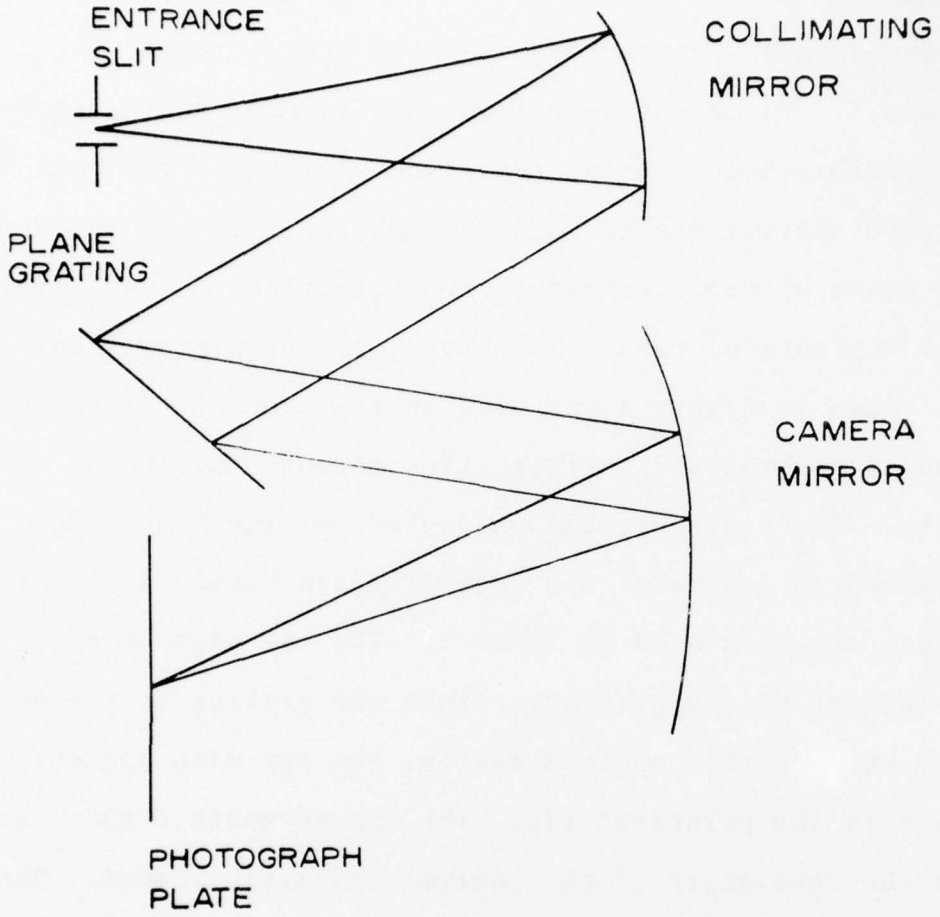


Figure 2. The optical system of the Czerny-Turner spectrograph.

system of this spectrometer which is a modification of a Czerny-Turner spectrograph is shown schematically in Figure 3. As can be seen from this figure, dedispersion is accomplished by using two plane mirrors to redirect the encoded optical energy back through the spectrometer optics. The plane mirrors contribute no aberrations; they simply fold the optical path. Therefore, the simpler optical system shown in Figure 4 was used in the theoretical investigation of aberration neutralization through the use of curved slots. The basic optical parameters of the Minuteman Hadamard spectrometer are identified in Figure 4, and their values are tabulated in Table 1. The ray segment B strikes the center of the grating. Since the grating is the aperture stop of this optical system, the ray with segments A and B is the principal ray. The ray segments C and D are for the wavelength of the central spectral element. The point P is at the center of the field stop. The lengths of ray segments A and D equal the meridional focal lengths of the spherical mirrors 1 and 2, respectively. The values of A and D tabulated in Table 1 were computed using Equation (F-6) in Appendix F. The reference line identified in Figure 4 is the direction of the grating normal which causes the zero-order-diffraction ray to strike the point P. Since for the zero-order-diffraction ray the grating acts like a mirror, the angle θ_1 must equal θ_2. The angles α and β in Figure 4 are the angles of incidence and

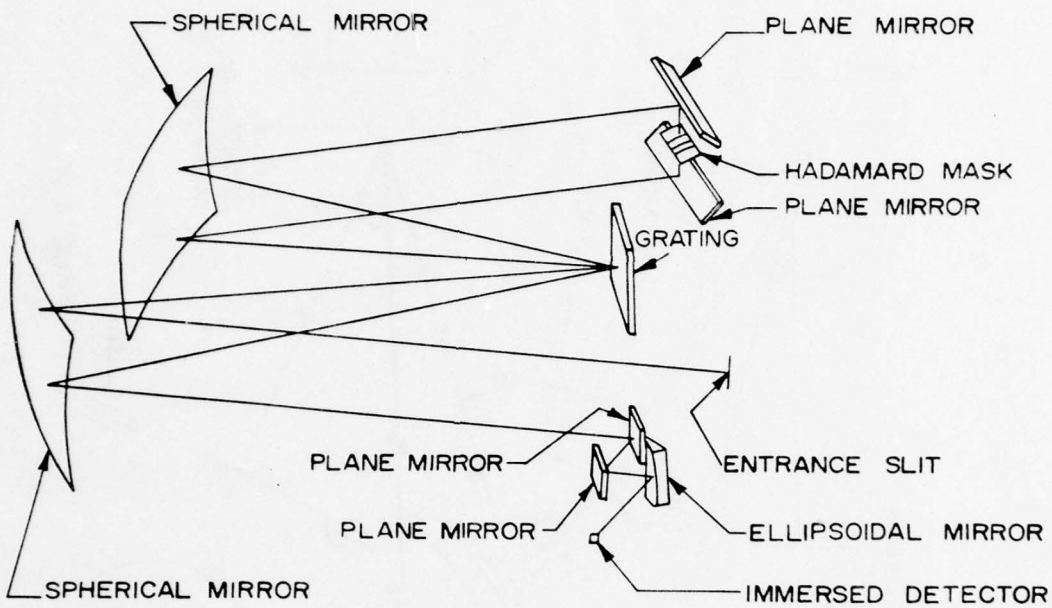


Figure 3. The optical system of the Model 305-HS Hadamard spectrometer of Minuteman Laboratories, Inc.

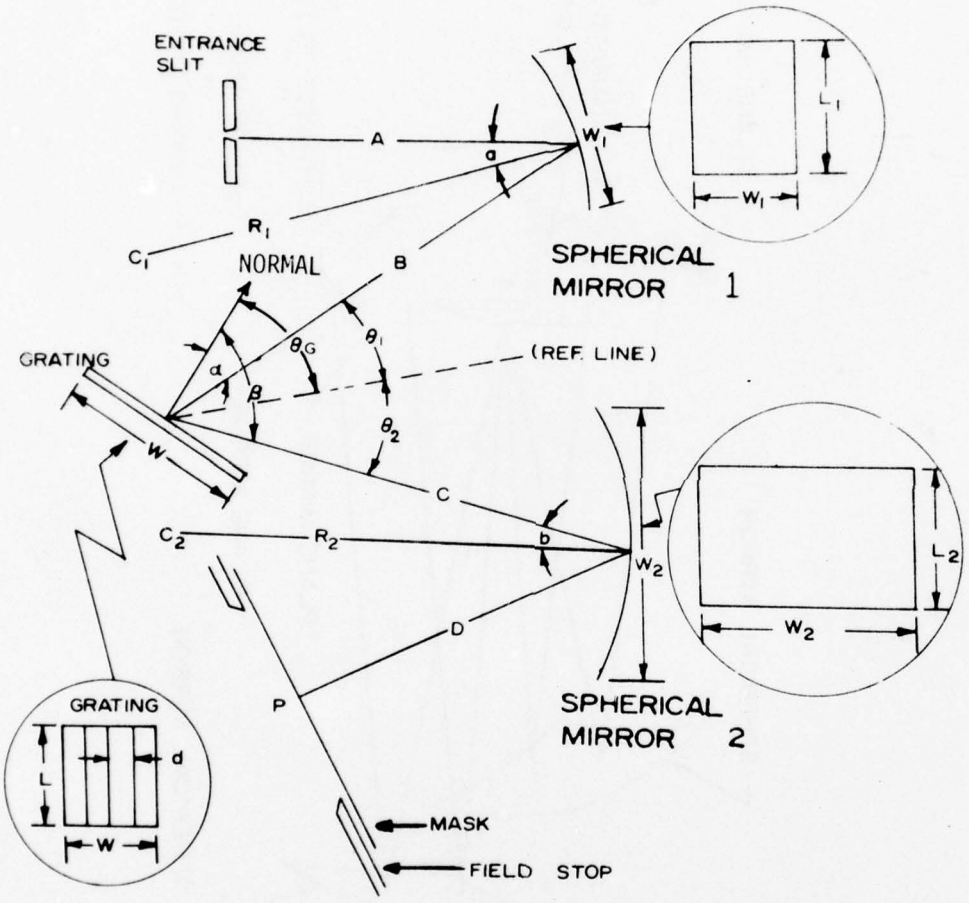


Figure 4. The optical system used for the theoretical analysis.

Table 1. Values of the optical parameters of the Minuteman Model 305-HS Hadamard spectrometer optimized for a central wavelength of 11.5 μm.

Parameter	Description	Value
A	Meridional focal length of spherical mirror 1	497.107 mm
B	Ray segment from spherical mirror 1 to grating	412.750 mm
C	Ray segment from grating to spherical mirror 2	365.252 mm
D	Meridional focal length of spherical mirror 2	454.652 mm
R_1	Radius of spherical mirror 1	1000.0 mm
R_2	Radius of spherical mirror 2	925.0 mm
W	Width of grating	64.0 mm
L	Length of grating	64.0 mm
W_1	Width of spherical mirror 1	61.976 mm
L_1	Length of spherical mirror 1	120.650 mm
W_2	Width of spherical mirror 2	146.050 mm
L_2	Length of spherical mirror 2	120.650 mm
$1/d$	The reciprocal of the spacing between grating rulings	90 rulings/mm
a	Off-axis angle of spherical mirror 1	6.17 degrees
b	Off-axis angle of spherical mirror 2	10.57 degrees
θ_1	Angle between ray segment B and the reference line	10.50 degrees
θ_2	Angle between ray segment C and the reference line	10.50 degrees

diffraction at the diffraction grating. Since θ_1 equals θ_2, it follows from Figure 4 that

$$\beta = \alpha + 2\theta_1 \quad . \tag{1}$$

The angle θ_G is referred to as the grating rotation angle. From Figure 4,

$$\theta_G = \alpha + \theta_1 \quad . \tag{2}$$

It is proven in Appendix G that radiation of wavelength λ will be directed to point P when

$$\sin \theta_G = \frac{k\lambda}{2d \cos\theta_1} \quad , \tag{3}$$

where k is the diffraction order and d is the distance between the grating rulings. This equation can be used to compute the required grating rotation to place a particular wavelength in the central spectral element. When λ is expressed in microns and θ_1 and d have the values given in Table 1, Equation (3) reduces to

$$\sin \theta_G = 4.5766 \times 10^{-2} \, k\lambda \quad . \tag{4}$$

The values of θ_G, α, and β computed from Equations (4), (2), and (1), respectively, for k equal to unity and λ equal to 11.5 μm are tabulated in Table 2.

Table 2. Values of selected angles when k equals unity and λ equals 11.5 μm.

Angle	Description	Degrees
θ_G	Grating rotation angle	31.757
α	Angle of incidence	21.257
β	Angle of diffraction	42.257

Analytic Expressions for the Optical Aberrations of the Representative Hadamard Spectrometer

Since the representative Hadamard spectrometer uses a Czerny-Turner configuration, the aberration expressions given in this section can be used for any Hadamard spectrometer using the Czerny-Turner configuration. Two basic types of aberration expressions are given. The first type describes the image of a point object. Aberrations of this type are spherical aberration, coma, astigmatism, and field curvature. The second type describes the difference between the shape of the entrance slit and its image. This second type of aberration is commonly referred to as distortion when describing optical systems. However, when describing dispersive spectrometers, this aberration is often called spectrum line curvature.

It has been common practice to express the aberrations of grating spectrometers in terms of optical-path-length variations, since *Beutler* [1945] derived optical-path-length expressions for the aberrations of the concave grating. If the variation in the optical path length is on the order of the wavelength of the optical radiation, this method of describing the optical aberrations is very useful. For example, if the path length variation is less than $\lambda/4$, where λ is the wavelength, the aberration is insignificant relative to the effects of diffraction. This is the well known Rayleigh criteria [*Born* and *Wolf*, 1965] for diffraction-limited imaging. If the variation in the optical path length is significantly larger than $\lambda/4$, the image of a point is essentially determined by the aberrations. The effect of an aberration on the width and length of the image of a point is best described by expressing the aberration as a transverse aberration [*Welford*, 1974]. Transverse-aberration descriptions are more useful than path-length-variation descriptions for analyzing Hadamard spectrometers because the degree to which the image is formed within one slot width can be directly ascertained from the transverse aberration description. Transverse-aberration expressions for the spherical aberration, coma, and astigmatism of the Czerny-Turner configuration were derived by converting the path-length-variation expressions of *Lindblom* [1972] into transverse-aberration expressions.

Conversion of path-length variation expressions into transverse aberration expressions

The path-length function used to derive path-length-variation expressions is an analytic expression for the optical path length between an object point and its image. This function is also known as the point characteristic function [*Born* and *Wolf*, 1965]. This functions is analogous to a potential function because the optical aberrations can be ascertained by differentiating this function. The point characteristic function is closely related to the wavefront aberration. As shown by *Welford* [1962],

$$W = NR - F \quad , \tag{5}$$

where W is the wavefront aberration, F is the point characteristic function, N is the index of refraction, and R is the radius of the reference sphere. The commonly used value for R is the distance from the image point to the exit pupil [*Welford*, 1962]. As can be seen from examining the ray paths in Figure 2, the exit pupil of the Czerny-Turner configuration is located at the camera mirror. This mirror is identified as spherical mirror 2 in Figure 4. Thus, for the Czerny-Turner spectrograph, R is the meridional focal length of spherical mirror 2. Therefore, it follows from Equation (F-6) in Appendix F that

$$R = \frac{R_2 \cos b}{2} \tag{6}$$

for the Czerny-Turner optical system. As shown by *Welford* [1962], the transverse aberrations are given by

$$\xi = \frac{R}{n} \frac{\partial W}{\partial x} \tag{7}$$

and

$$\eta = \frac{R}{n} \frac{\partial W}{\partial y} \quad , \tag{8}$$

where the xy-coordinate system is located in the exit pupil and ξ and η are parallel to the x and y axes, respectively. It follows from Equations (5), (6), (7) and (8) that the transverse aberrations of the Czerny-Turner optical system are given by

$$\xi = \frac{R_2 \cos b}{2} \frac{\partial F}{\partial x} \tag{9}$$

and

$$\eta = \frac{R_2 \cos b}{2} \frac{\partial F}{\partial y} \quad . \tag{10}$$

The variation in the length of the optical path with changes in the x coordinate is given by

$$\Delta F_x = \int_0^x \frac{\partial F}{\partial x} \, dx \quad . \tag{11}$$

The corresponding path-length variation in the y dimension is given by

$$\Delta F_y = \int_0^y \frac{\partial F}{\partial y}\, dy \quad . \tag{12}$$

Expressions for $\partial F/\partial x$ and $\partial F/\partial y$ can be found by differentiating expressions for ΔF_x and ΔF_y with respect to x and y, respectively. Then the expressions for the transverse aberrations can be ascertained by substituting these expressions for $\partial F/\partial x$ and $\partial F/\partial y$ into Equations (9) and (10), respectively.

Lindblom [1972] has given expressions for the total-path-length variation. These expressions are equivalent to the results obtained if the integrations in Equations (11) and (12) are performed with the variable upper limits replaced with the maximum values of x and y, respectively. The maximum values of x and y are

$$x = \frac{W \cos\beta}{2} \tag{13}$$

and

$$y = \frac{L}{2} \quad , \tag{14}$$

where W and L are the dimensions of the grating as identified in Figure 4 and β is the diffraction angle. Thus, the total-path-length variation expressions given by *Lindblom* [1972] are equivalent to results of the integrations

$$\Delta F_{\frac{W\cos\beta}{2}} = \int_0^{\frac{W\cos\beta}{2}} \frac{\partial F}{\partial x}\, dx \qquad (15)$$

and

$$\Delta F_L = \int_0^L \frac{\partial F}{\partial y}\, dy \quad . \qquad (16)$$

Thus, Lindblom's total-path-length variation expressions can be converted to ΔF_x and ΔF_y expressions by replacing W and L in his expressions with $2x/\cos\beta$ and $2y$, respectively. Transverse aberration expressions can then be found using the procedure described in the previous paragraph. Transverse aberration expressions for spherical aberration, coma, and astigmatism were derived from Lindblom's expressions using this procedure.

Spherical aberration

For rays in the plane of Figure 4, *Lindblom's* [1972] expression for the total-path-length variation due to spherical aberration reduces to

$$\Delta F_{\text{sph.ab.}} = \frac{W^4}{64}\left\{\left(\frac{\cos^4\alpha}{R_1^3\cos^5\alpha}\right)(10\sin^2\alpha - 1) + \left(\frac{\cos^4\beta}{R_2^3\cos^5 b}\right)(10\sin^2 b - 1)\right\} . \qquad (17)$$

As explained in the previous paragraphs, this expression can be converted to a path-length-variation expression by

replacing W with $2x/\cos\beta$. This replacement yields

$$\Delta F_{\text{sph.ab.}} = \frac{x^4}{4\cos^4\beta}\left\{\left(\frac{\cos^4\alpha}{R_1^3\cos^5 a}\right)(10\sin^2 a - 1) + \left(\frac{\cos^4\beta}{R_2^3\cos^5 b}\right)(10\sin^2 b - 1)\right\} \quad . \tag{18}$$

Differentiating Equation (18) with respect to x gives an expression for $\partial F/\partial x$. If this expression for $\partial F/\partial x$ is then substituted into Equation (9), the transverse aberration is given by

$$\xi = \frac{x^3 R_2\cos b}{2\cos^4\beta}\left\{\left(\frac{\cos^4\alpha}{R_1^3\cos^5 a}\right)(10\sin^2 a - 1) + \left(\frac{\cos^4\beta}{R_2^3\cos^5 b}\right)(10\sin^2 b - 1)\right\} \quad . \tag{19}$$

As can be seen from Equation (19), the transverse aberration of the ray increases as the third power of the x coordinate in the exit pupil. An expression for the maximum value of x is given in Equation (13). Substituting this expression in Equation (19) gives the following expression for the transverse aberration of the Czerny-Turner configuration due to spherical aberration:

$$\xi_{\text{sph.ab.}} = \frac{W^3 R_2 \cos b}{16 \cos\beta} \left\{ \left(\frac{\cos^4 \alpha}{R_1^3 \cos^5 a} \right) (10 \sin^2 a - 1) + \left(\frac{\cos^4 \beta}{R_2^3 \cos^5 b} \right) (10 \sin^2 b - 1) \right\} \quad . \tag{20}$$

The value of $\xi_{\text{sph.ab.}}$ computed from Equation (20) using the parameter values tabulated in Tables 1 and 2 is 19 μm.

The effect of exit-pupil size on the amount of spherical aberration can be seen from Equations (18) and (19). The path-length variation caused by spherical aberration increases as the fourth power of the exit-pupil size. The transverse aberration caused by spherical aberration increases as the third power of the exit-pupil size. Since the path-length variation due to spherical aberration is an even function of x, the broadening of the image of a point caused by spherical aberration is symmetrical. Thus, if the only aberration were spherical aberration, the width of the image of a point would be $2\xi_{\text{sph.ab.}}$.

Coma

For rays in the plane of Figure 4, *Lindblom's* [1972] expression for the total-path-length variation due to coma reduces to

$$\Delta F_{\text{coma}} = \frac{W^3}{8} \left\{ \left(\frac{\cos\alpha}{\cos a} \right)^3 \left(\frac{\sin a}{R_1^2} \right) - \left(\frac{\cos\beta}{\cos b} \right)^3 \left(\frac{\sin b}{R_2^2} \right) \right\} \quad . \tag{21}$$

Replacing W with $2x/\cos\beta$ yields

$$\Delta F_{\text{coma}} = \frac{x^3}{\cos^3\beta}\left\{\left(\frac{\cos\alpha}{\cos a}\right)^3\left(\frac{\sin a}{R_1^2}\right) - \left(\frac{\cos\beta}{\cos b}\right)^3\left(\frac{\sin b}{R_2^2}\right)\right\}. \qquad (22)$$

Differentiating Equation (22) with respect to x gives an expression for $\partial F/\partial x$. Substituting this expression in Equation (9) yields

$$\xi = \frac{3x^2 R_2 \cos b}{2\cos^3\beta}\left\{\left(\frac{\cos\alpha}{\cos a}\right)^3\left(\frac{\sin a}{R_1^2}\right) - \left(\frac{\cos\beta}{\cos b}\right)^3\left(\frac{\sin b}{R_2^2}\right)\right\} \qquad (23)$$

for the transverse aberration of a ray due to coma. As can be seen from Equation (23), the maximum aberration results for the ray with the maximum x coordinate. Therefore, it follows from Equations (13) and (23) that the transverse aberration due to coma is given by

$$\xi_{\text{coma}} = \frac{3W^2 R_2 \cos b}{8\cos\beta}\left\{\left(\frac{\cos\alpha}{\cos a}\right)^3\left(\frac{\sin a}{R_1^2}\right) - \left(\frac{\cos\beta}{\cos b}\right)^3\left(\frac{\sin b}{R_2^2}\right)\right\}. \qquad (24)$$

It can be shown that this equation is equivalent to the equation for transverse coma derived by *Reader* [1969]. For the parameter values given in Tables 1 and 2, the values of ξ_{coma} given by Equation (24) is 6 μm.

By the proper choice of the spectrometer-parameter values, Equation (24) can be made equal to zero. If these parameter values are selected such that

$$\frac{\sin a}{\sin b} = \left(\frac{\cos\beta\ \cos a}{\cos\alpha\ \cos b}\right)^3 \left(\frac{R_1}{R_2}\right)^2 \quad , \tag{25}$$

the value of ξ_{coma}, given by Equation (24), is zero. Equation (25) is the coma-free condition derived by *Shafer, Megill,* and *Droppleman* [1964] and verified by *Reader* [1969]. If Equations (1) and (25) are solved simultaneously using the parameter values for θ_1, R_1, R_2, a, and b tabulated in Table 1, the requires values of α and β to make the coma zero are 22.48 and 43.78 degrees, respectively. For these values of α and β and the value of $1/d$ tabulated in Table 1, the grating equation [*Born* and *Wolf*, 1965],

$$\sin\alpha + \sin\beta = k\lambda/d \quad , \tag{26}$$

requires that $k\lambda$ equals 11.89 μm. Thus, the coma of the representative Hadamard spectrometer is zero when the grating is rotated such that the value of $k\lambda$ of the central spectral element is 11.89 μm.

The effect of exit-pupil size on the amount of coma can be seen from Equations (22) and (23). The path-length variation due to coma increases with the third power of the exit-pupil size; transverse aberration due to coma increases as the second power of the exit-pupil size. The broadening of the image of a point due to coma is asymmetrical because the path-length variation is an odd function of x. Because of this asymmetry, the contribution of coma to

the width of the image of a point is approximately equal to ξ_{coma}.

Astigmatism

Lindblom's [1972] expression for the total-path-length variation due to astigmatism is

$$\Delta F_{ast.} = \left(\frac{L}{2}\right)^2 \left\{\frac{\sin^2 a}{R_1 \cos a} + \frac{\sin^2 b}{R_2 \cos b}\right\} . \qquad (27)$$

This expression can be converted to a path-length-variation expression by replacing $L/2$ with y. This replacement yields

$$\Delta F_{ast.} = y^2 \left\{\frac{\sin^2 a}{R_1 \cos a} + \frac{\sin^2 b}{R_2 \cos b}\right\} . \qquad (28)$$

Differentiating Equation (28) with respect to y gives an expression for $\partial F/\partial y$. Substituting this expression in Equation (10) yields

$$\eta = y R^2 \cos b \left\{\frac{\sin^2 a}{R_1 \cos a} + \frac{\sin^2 b}{R_2 \cos b}\right\} \qquad (29)$$

for the transverse aberration of a ray due to astigmatism. As can be seen from Equation (29), the transverse aberration caused by astigmatism increases linearly with y. Since by Equation (14) the maximum value of y is $L/2$, the transverse aberration due to astigmatism results if the variable y in Equation (29) is replaced with $L/2$. Thus,

the transverse aberration due to astigmatism of the Czerny-Turner configuration is given by

$$\eta_{ast.} = \frac{R_2 L \cos b}{2} \left\{ \frac{\sin^2 a}{R_1 \cos a} + \frac{\sin^2 b}{R_2 \cos b} \right\} \quad . \qquad (30)$$

If the parameter values tabulated in Table 1 are substituted in Equation (30), the value of $\eta_{ast.}$ is 1.414 mm.

The effect of exit-pupil size on the amount of astigmatism can be seen from Equations (28) and (29). The path-length variation caused by astigmatism increases as the square of the exit-pupil size. The transverse aberration caused by astigmatism increases linearly with y. Since the path-length variation due to astigmatism is an even function of y, the lengthening of the image of a point due to astigmatism is symmetrical. Thus, the contribution of astigmatism to the length of the image of a point is $2\eta_{ast.}$

The spot size

The size of the image of a point predicted by aberration theory can be computed simply from the transverse aberration expressions for spherical aberration, coma, and astigmatism. The width of the image of a point predicted by aberration theory is

$$i_W = 2\xi_{sph.ab.} + |\xi_{coma}| \quad . \qquad (31)$$

The length of this image predicted by aberration theory is

$$i_L = 2(\eta_{ast.} + \xi_{sph.ab.}) \quad . \qquad (32)$$

If the values of $\xi_{sph.ab.}$, ξ_{coma}, and $\eta_{ast.}$, computed in the previous paragraphs for the parameter values tabulated in Tables 1 and 2, are substituted in Equations (31) and (32), the values for i_W and i_L are 44 μm and 2.828 mm, respectively. The length of the predicted image of a point is 64 times as it is wide because of the large amount of astigmatism.

Field curvature

Mielenz [1964c] derived equations for the coordinates of the focal surface of an Ebert spectrograph. However, as shown by *Reader* [1969], his expressions can be adapted to a Czerny-Turner spectrograph. Figure 5 defines the parameters used to apply the equations of Mielenz to obtain the focal curve in the meridional plane of a Czerny-Turner optical system. The center of curvature for spherical mirror 2 is at C_2. The focal curve in the meridional plane is given by

$$z'' = -\frac{R_2}{4}\left[1 - 3\left(\frac{m}{R_2}\right)^2\right]\gamma^2 + \frac{R_2}{48}\left[1 - 30\left(\frac{m}{R_2}\right)^2 + 48\left(\frac{m}{R_2}\right)^3 - 27\left(\frac{m}{R_2}\right)^4\right]\gamma^4 \tag{33}$$

and

$$x'' = -\frac{R_2}{2}\gamma + \frac{R_2}{12}\left[1 - 9\left(\frac{m}{R_2}\right)^2 + 12\left(\frac{m}{R_2}\right)^3\right]\gamma^3 \quad , \tag{34}$$

where terms of order higher than γ^4 are neglected. When m

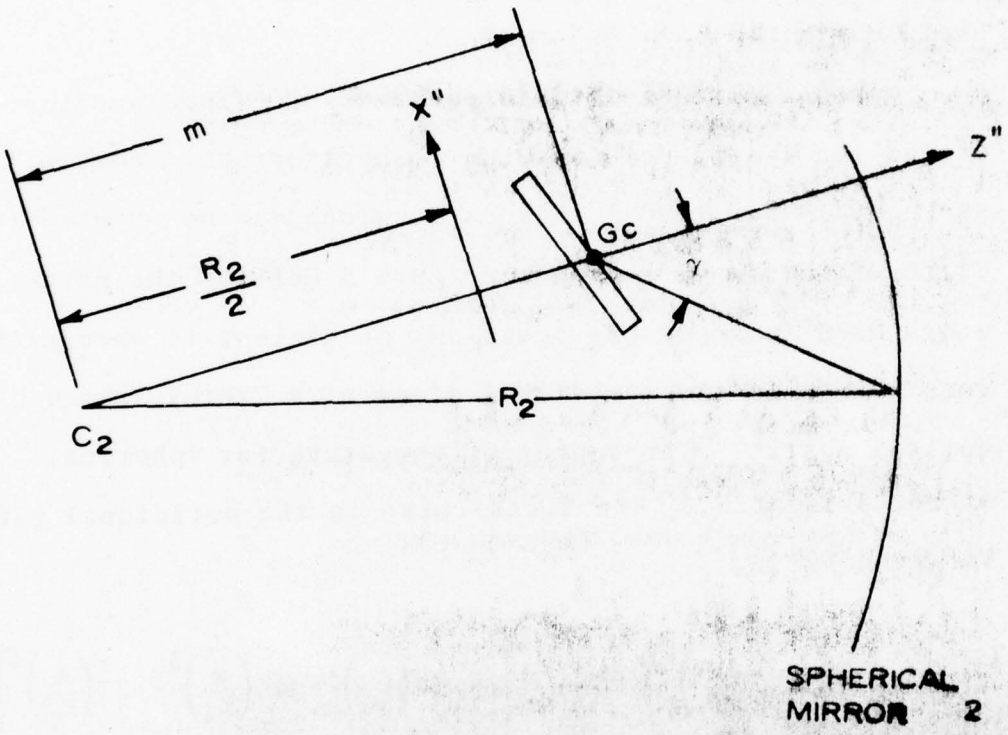


Figure 5. Geometry defining parameters to compute the focal surface of a Czerny-Turner optical system.

equals $R_2/\sqrt{3}$, the γ^2 term in Equation (33) is zero. This is commonly known as the flat-field grating position.

The value of m for the representative Hadamard spectrometer can be determined from Figure 6. The line from G to M_{2V} is a segment of the central ray, which, if continued, would strike the mask at point P in Figure 4. The value of γ for this central ray is designated γ_P. Applying the law of cosines to the trinagle in Figure 6 yields

$$m = (R_2^2 + C^2 - 2R_2 C \cos b)^{1/2} \quad . \tag{35}$$

For the values of R_2, C, and b tabulated in Table 1, the value of m found from Equation (35) is 569.9 mm. Substituting this value of m and the value of R_2 given in Table 1 into Equations (33) and (34) yields

$$z'' = 32.09\gamma^2 - 53.82\gamma^4 \tag{36}$$

and

$$x'' = -462.5\gamma + 30.07\gamma^3 \quad . \tag{37}$$

The optimum orientation of the mask was also computed using a ray-tracing analysis. In order to facilitate the comparison between this orientation and the orientation computed from Equations (36) and (37), the values of x'' and z'' computed from these equations were transformed to the XZ-coordinate system used in the ray-tracing analysis. The relative orientation of the XZ and the $x''z''$-coordinate

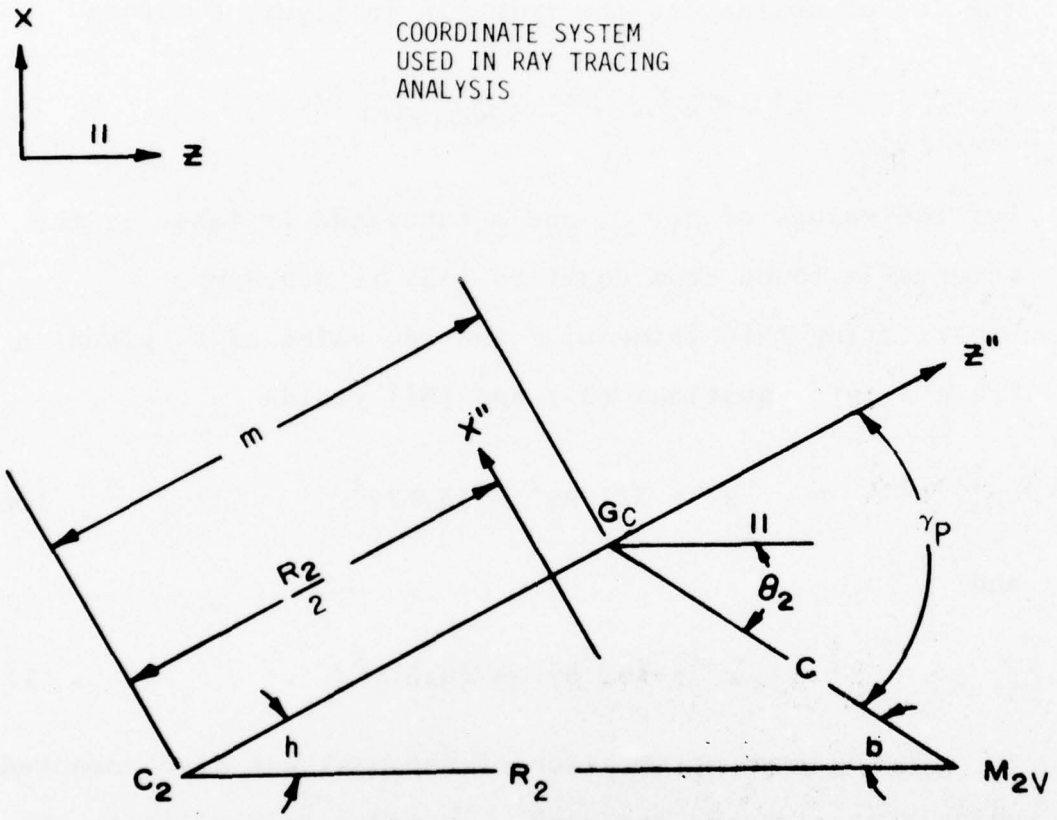


Figure 6. Geometry for central ray.

systems is shown in Figure 6. The required transformation equations are

$$z = z'' \cos(\gamma_P - \theta_2) - x'' \sin(\gamma_P - \theta_2) + Z_{G_C} - (m - \frac{R_2}{2}) \cos(\gamma_P - \theta_2) \tag{38}$$

and

$$x = z'' \sin(\gamma_P - \theta_2) + x'' \cos(\gamma_P - \theta_2) + X_{G_C} - (m - \frac{R_2}{2}) \sin(\gamma_P - \theta_2) \quad , \tag{39}$$

where X_{G_C} and Z_{G_C} are the coordinates of the point G in the XZ-coordinate system. The values of X_{G_C} and Z_{G_C} for the representative Hadamard spectrometer are -91.110 and 91.015 mm, respectively.

In order to use Equations (38) and (39), γ_P must be computed. Since the exterior angle of a triangle must equal the sum of the opposite interior angles,

$$\gamma_P = h + b \quad . \tag{40}$$

By the law of sines

$$h = \sin^{-1}\left[\frac{C}{m} \sin b\right] \quad . \tag{41}$$

Substituting the values for C and b tabulated in Table 1 and the value for m computed above, 569.9 mm, in Equation (41) yields 6.75 degrees for the value of h. Thus, by Equation (40) the value of γ_P for the representative

Hadamard spectrometer is 17.32 degrees. Consequently, the Equations (38) and (39) reduce to

$$Z = z'' \cos 6.82 - x'' \sin 6.82 - 15.625 \text{ mm} \qquad (42)$$

and

$$X = z'' \sin 6.82 + x'' \cos 6.82 - 103.864 \text{ mm} \quad . \qquad (43)$$

The coordinates of 26 points on the focal surface were computed by letting γ vary from 0.18 to 0.43 radians in steps of 0.01 radian. The equation for the best-fit straight line through these coordinate pairs, using the method of least squares, is

$$X = -6.807Z - 219.098 \text{ mm} \quad . \qquad (44)$$

The coefficient of determination of this line is 0.99998, which indicates that the fit is very good. It follows from Equation (44) that the angle between the best-fit line and the X axis is 8.357 degrees as illustrated in Figure 7.

In order to compute the focal shift caused by using a straight rather than a curved mask, it is useful to transform to a coordinate system that has an axis along the best-fit line. The ZX-coordinate system can be transformed to the $Z'X'$-coordinate system shown in Figure 7 by the equations

$$Z' = Z \cos 8.357 + (X + 219.098) \sin 8.357 \qquad (45)$$

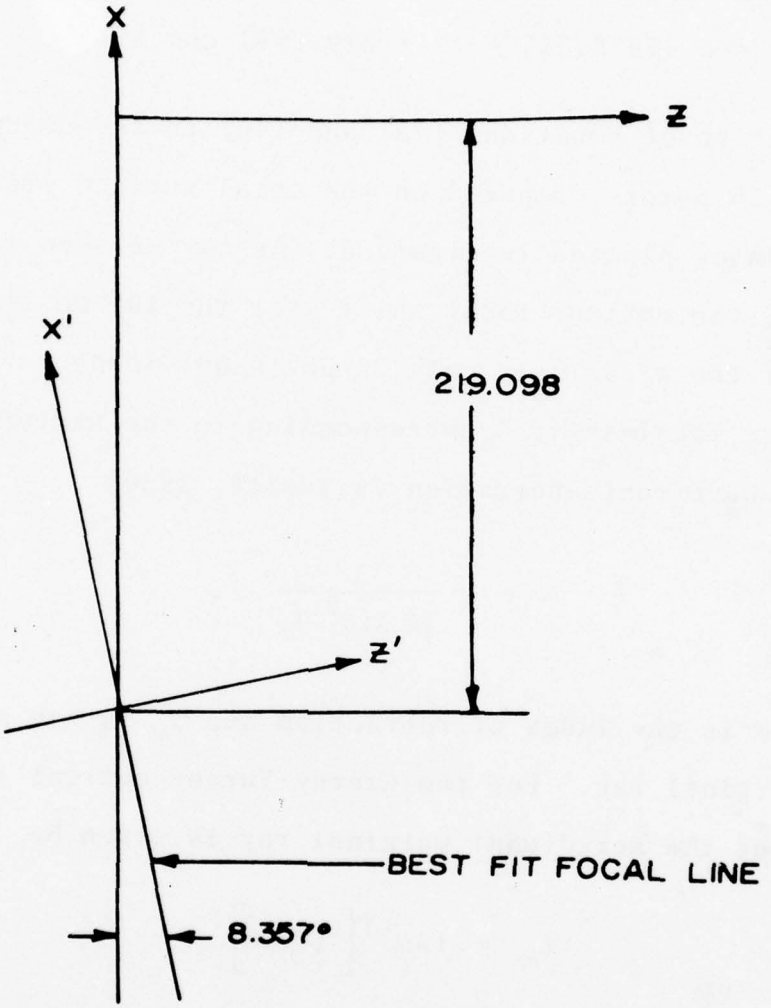


Figure 7. Relationship between the best-fit focal line described by Equation (44) and the coordinate system used in the ray-tracing analysis.

and

$$X' = -Z \sin 8.357 + (X + 219.098) \cos 8.357 \quad . \qquad (46)$$

Application of Equations (45) and (46) to the coordinates of the 26 points computed on the focal surface yields the coordinates plotted in Figure 8. As can be seen from this figure, the maximum focal shift over the 109 mm long section of the X' axis is only 38 μm (0.001 inch).

The focal shift δ corresponding to the Rayleigh limit of $\lambda/4$ wavefront aberration is [*Smith*, 1966]

$$\delta = \pm \frac{\lambda}{2N \sin^2 U_m} \quad , \qquad (47)$$

where N is the index of refraction and U_m is the angle of the marginal ray. For the Czerny-Turner optical system the angle of the meridional marginal ray is given by

$$U_m = \tan^{-1}\left[\frac{W \cos \beta}{2D}\right] \quad , \qquad (48)$$

where W, D, and β are the parameters identified in Figure 4. It follows from Equations (47) and (48) that for the representative Hadamard spectrometer the focal shift of

$$\delta = \pm 185\lambda \qquad (49)$$

produces a wavefront aberration of $\lambda/4$. For λ equal to 11.5 μm, Equation (49) indicates that a focal shift of ± 2 mm produces no significant deterioration in the image.

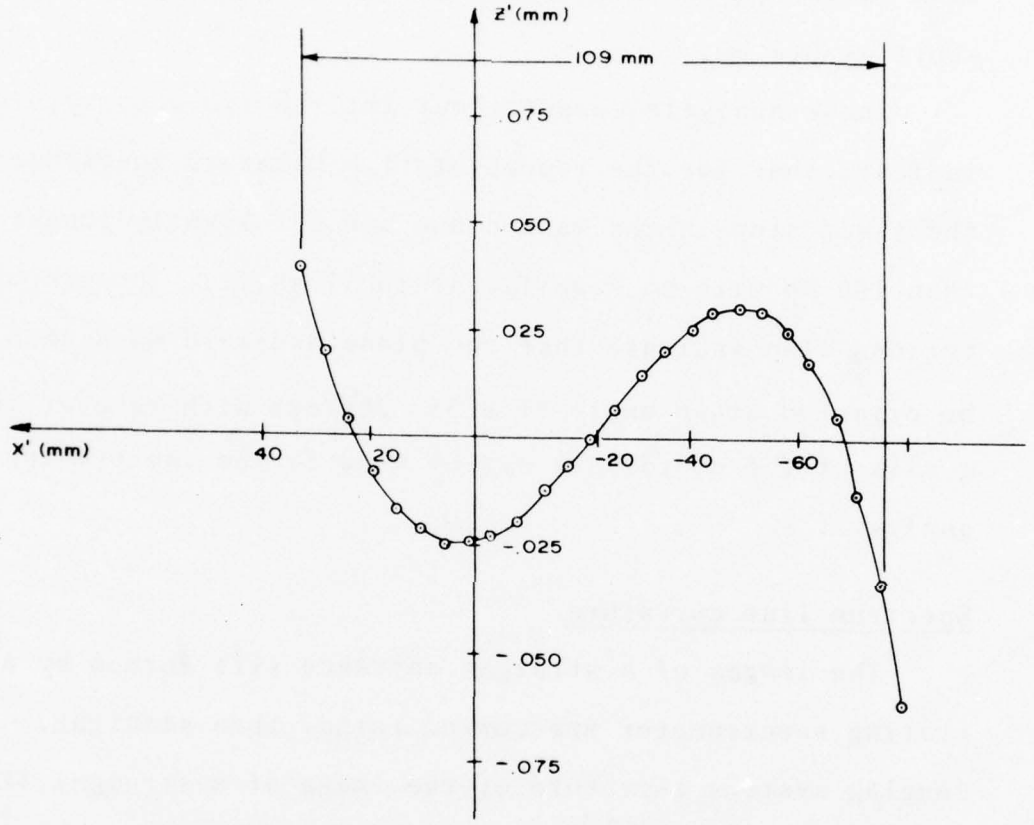


Figure 8. The analytically computed focal surface.

Thus, the maximum focal shift of 38 μm caused by using a straight rather than a curved mask produces no measurable errors for λ equal to 11.5 μm. In fact, the 38-μm variation satisfies the Rayleigh criteria for wavelengths as short as 0.2 μm.

These analytic computations for the field curvature indicate that for the representative Hadamard spectrometer, the field stop in the mask plane can be slightly longer than 100 mm with no significant focal shift. These computations also indicate that the plane Hadamard mask should be oriented at an angle of 8.357 degrees with respect to the X axis of the coordinate system used in the ray-tracing analysis.

Spectrum line curvature

The images of a straight entrance slit formed by a grating spectrometer are curved rather than straight. In imaging systems, curvature of the image of a straight line is called distortion, but in grating spectrometers it is usually called spectrum line curvature. *Mielenz* [1964a, 1964b, 1964c] has derived general equations which could theoretically be used to compute the shape of the spectral images of an entrance slot formed by a Czerny-Turner optical system. He has applied his equations to the Ebert spectrometer and confirmed the optimum slit radius for an Ebert spectrometer given by *Fastie* [1952a, 1952b, 1953].

Kudo [1960] has shown that the optimal slit shape for the Czerny-Turner spectrometer is elliptical.

Spectrum line curvature is not predicted by the common form of the grating equation, which is given in Equation (26). The general grating equation [*James* and *Sternberg*, 1969] must be used when investigating the spectrum line curvature of a plane-grating spectrometer. *James* and *Sternberg* [1969] have shown that the curvature introduced by the plane grating is

$$\Delta\beta = \frac{k\lambda\theta^2}{2d\cos\beta} \quad , \tag{50}$$

where θ and $\Delta\beta$ are the angles identified in Figure 9. An expression for the spectral line curvature of the Czerny-Turner spectrometer was derived using Equation (50). A principal ray from a point in the entrance slit a distance Y_s above the plane of Figure 4 will strike spherical mirror 1, approximately a distance Y_s above this plane. Thus,

$$\theta = \frac{Y_s}{B} \quad , \tag{51}$$

where B is defined in Figure 4. The lateral translation of the principal ray at the focal plane is approximately equal to its lateral translation at spherical mirror 2. Consequently, the curvature expressed as a lateral translation in the focal plane is given by

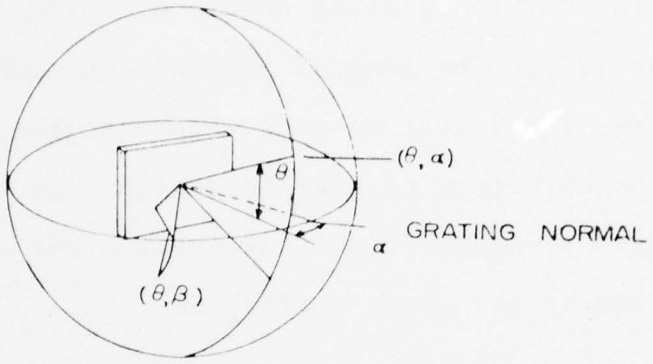


Figure 9a. Geometry for principal rays at the grating.

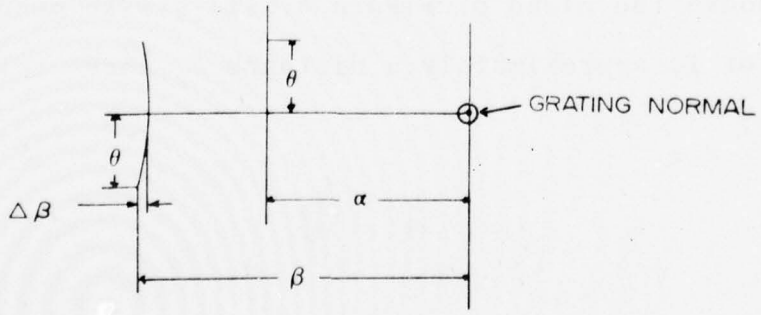


Figure 9b. Mercator projection of the unit sphere; (dimensions are angular).

$$\Delta X' = \Delta\beta\, C \quad , \tag{52}$$

where C is defined in Figure 4. It follows from Equations (50), (51), and (52) that the slit curvature introduced in the image of a straight entrance slit by the Czerny-Turner optical system is given by

$$\Delta X' = \frac{C\, k\lambda\, Y_s^2}{2dB^2 \cos\beta} \quad . \tag{53}$$

Equation (49) indicates that the spectrum line curvature increases as the square of the distance above the optical axis. For the parameter values given in Table 1 and $k\lambda$ equal to 11.5 μm, Equation (53) reduces to

$$\Delta X' = 1.19 \times 10^{-3}\, Y_s^2 \text{mm} \quad , \tag{54}$$

when Y_s is in millimeters. The quadratic dependency of spectral line curvature on the distance above the optical axis severely limits the usable length of straight slots. For example, if Y_s is 29 mm, then by Equation (54) the lateral shift $\Delta X'$ is 1 mm.

Accuracy

The accuracy of the analytic expressions which have been derived in the preceding pages for the aberrations of the Czerny-Turner optical system was evaluated by comparing analytic results with ray-tracing results. This comparison indicated that these analytic expressions give

a reasonably accurate description of the imaging properties of the Czerny-Turner optical system.

A Ray-Tracing Analysis of the Imaging Fidelity of the Representative Hadamard Spectrometer

The imaging fidelity of the representative Hadamard spectrometer was ascertained by using ray tracing to compute spot diagrams [*Cox*, 1964] and the intersection points of principal rays with the mask plane. Ray tracing can be used to ascertain the geometrical imaging properties of an optical system. Since diffraction is not described by geometrical optics, tracing rays through an optical system containing a diffraction grating requires some explanation. An examination of the derivation of the grating equation from diffraction theory [*Born* and *Wolf*, 1965] reveals that the grating equation describes the direction of propagation of the maxima only. Some optical energy is diffracted into angles other than those of the maxima. However, for most applications the general grating equation [*James* and *Sternberg*, 1969] satisfactorily describes the operation of the diffraction grating. The grating equation is a geometrical description that can be implemented using ray tracing.

Ray-tracing computer programs were developed to analyze the imaging fidelity of the representative Hadamard spectrometer. Subroutines were developed for each of the

basic ray-tracing operations. These subroutines can be used to analyze any optical system.

Cartesian coordinates of the representative Hadamard spectrometer

The ray-tracing analysis of the representative Hadamard spectrometer was conducted using the XYZ-coordinate system shown in Figure 10. The origin is located at the center of the entrance slit, the Z axis is parallel with the reference line, the X axis is directed toward the top of Figure 10, and the Y axis is out of the plane of this figure. The points M_{1T}, M_{1V}, M_{1B}, G_T, G_C, G_B, M_{2T}, M_{2V}, M_{2B}, and P are defined in this figure.

Expressions for the points M_{1V}, G_C, M_{2V}, and P in terms of the parameters given in Table 1 were derived from the geometrical drawing in Figure 11. The XYZ coordinates of the vertex of spherical mirror 1, the point M_{1V}, are given by

$$X_{M_{1V}} = - A \sin \gamma_1 \quad , \tag{55}$$

$$Y_{M_{1V}} = 0 \quad , \tag{56}$$

$$Z_{M_{1V}} = A \cos \gamma_1 \quad , \tag{57}$$

where

$$\gamma_1 = 2a - \theta_1 \quad . \tag{58}$$

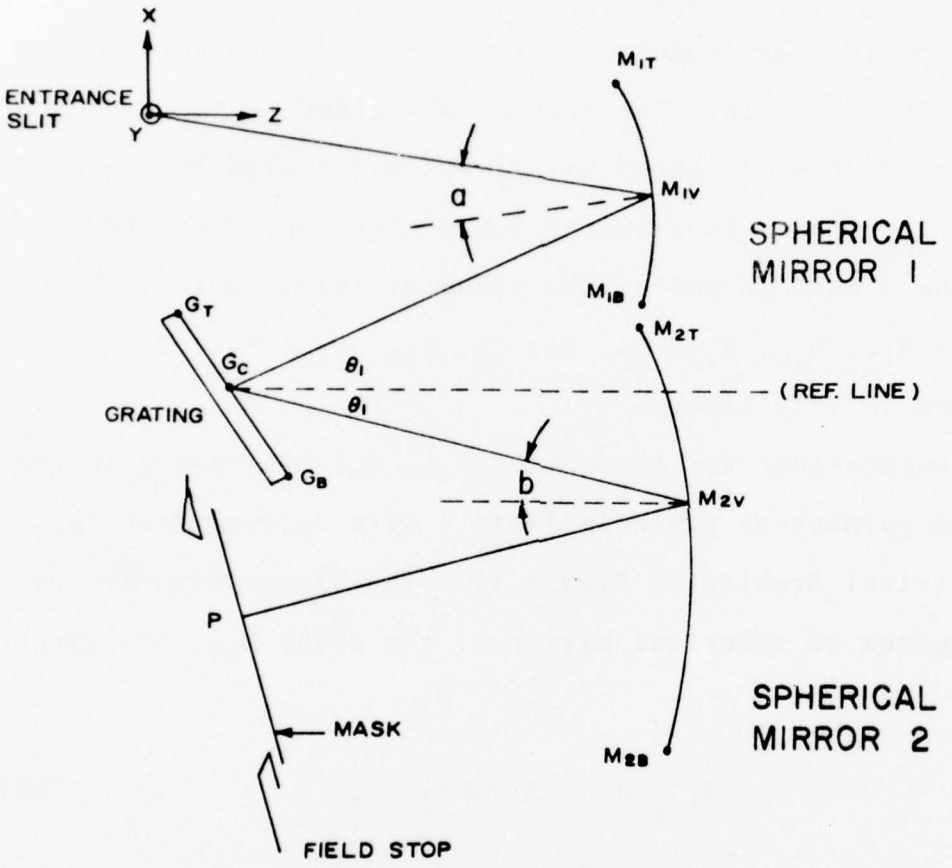


Figure 10. Definition of several points used in the ray-tracing analysis.

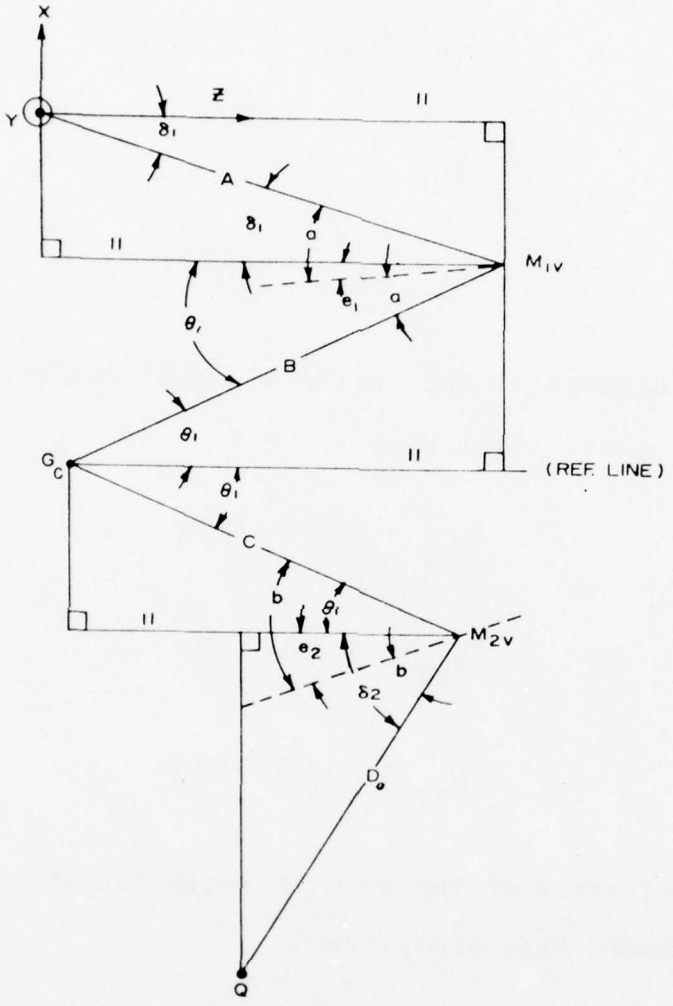


Figure 11. Geometrical drawing from which expressions for the Cartesian coordinates of the optical components were derived. The lines marked with the two vertical bars are parallel.

The coordinates of the grating center, the point G, are given by

$$X_{G_C} = X_{M_{1V}} - B \sin \theta_1 \quad , \tag{59}$$

$$Y_{G_C} = 0 \quad , \tag{60}$$

$$Z_{G_C} = Z_{M_{1V}} - B \cos \theta_1 \quad . \tag{61}$$

The coordinates of the vertex of spherical mirror 2, the point M_{2V}, are given by

$$X_{M_{2V}} = X_{G_C} - C \sin \theta_1 \quad , \tag{62}$$

$$Y_{M_{2V}} = 0 \quad , \tag{63}$$

$$Z_{M_{2V}} = Z_{G_C} + C \sin \theta_1 \quad . \tag{64}$$

The coordinates of the point P where the central ray strikes the Hadamard mask are given by

$$X_P = X_{M_{2V}} - D \sin \gamma_2 \quad , \tag{65}$$

$$Y_P = 0 \quad , \tag{66}$$

$$Z_P = Z_{M_{2V}} - D \cos \gamma_2 \quad , \tag{67}$$

where

$$\gamma_2 = 2b - \theta_1 \quad . \tag{68}$$

The coordinates of the points M_{1V}, G_C, M_{2V}, and P computed by substituting the required parameter values from Table 1 into Equations (55) through (68) are tabulated in Table 3. The coordinates of the points M_{1T}, M_{1B}, G_T, G_B, M_{2T}, and M_{2B} are also tabulated in Table 3.

Table 3. Coordinates of points defined in Figure 10.

Point	description	Coordinates (mm) X	Y	Z
M_{1T}	Top of spherical mirror 1	14.971	0	494.033
M_{1V}	Vertex of spherical mirror 1	-15.892	0	496.853
M_{1B}	Bottom of spherical mirror 1	-46.828	0	498.716
G_T	Top of grating (when θ_G = 31.757 degrees)	-63.901	0	74.173
G_C	Center of grating	-91.110	0	91.015
G_B	Bottom of grating (when θ_G = 31.757 degrees)	-118.319	0	107.857
M_{2T}	Top of spherical mirror 2	-84.651	0	447.175
M_{2V}	Vertex of spherical mirror 2	-157.672	0	450.151
M_{2B}	Bottom of spherical mirror 2	-230.700	0	447.353
P	Center of focal plane	-241.618	0	3.316

The angles e_1 and e_2 defined in Figure 11 are Euler angles used in the ray-tracing computer programs for coordinate transformations. It follows from Figure 11 that these Euler angles for spherical mirrors 1 and 2 are given by

$$e_1 = \theta_1 - a \tag{69}$$

and

$$e_2 = b - \theta_1 \quad . \tag{70}$$

The values of e_1 and e_2, as well as γ_1 and γ_2, for the representative Hadamard spectrometer are tabulated in Table 4.

Table 4. Values of several angles defined in Figure 11.

Angle	Description	Value (degrees)
e_1	Euler angle of spherical mirror 1	4.334
e_2	Euler angle of spherical mirror 2	.07
γ_1	Angle between Z axis and the principal ray from the entrance slit	1.832
γ_2	Angle between Z axis and the principal ray to point P	10.640

Ray-tracing computer programs

The ray-tracing computer programs developed to analyze the imaging properties of the representative Hadamard spectrometer used the ray-tracing procedure of *Spencer* and *Murty* [1962], which is described in Appendix E. Subroutines to implement the basic ray-tracing operations were developed and used in several mainline programs. These subroutines, TRNS1, TRNS2, TRNS3, TRNS4, RMAT, ITSP, ITPL, RFL and DFR, are listed in Appendix H. These subroutines together with subroutine RFR, which describes refraction, form a basic set of general-purpose subroutines that can be used to analyze optical systems with spherical and planar surfaces. Optical systems with other surfaces can be analyzed by using the procedures described in Appendix E to develop subroutines to compute the intersection of a ray with these surfaces. The subroutine DFR describes the change in direction of a ray at a diffraction grating predicted by the general grating equation [*James* and *Sternberg*, 1969]. Therefore, spectrum line curvature is predicted by this subroutine.

These general-purpose subroutines describe a ray in terms of the coordinates of a point on the ray and the direction cosines of the ray. The computations are algebraic instead of trigonometric, and the accuracy can be set by specifying the iteration difference at which the Newton-Raphson iteration is to terminate. The computer programs were run on a Digital Equipment Corporation PDP-8/E computer

using Fortran II, which provides seven significant digits for arithmetic computations. The accuracy of the ray-trace results were ascertained by ray-tracing the same Czerny-Turner optical system on both a Univac 1108 computer and the PDP-8/E computer. The Univac 1108 provides nine significant digits. The maximum difference between the ray intersections in the focal plane computed with these two machines was 0.1 μm. Consequently, the ray trace data reported herein are accurate to 0.1 μm.

Since the PDP-8/E computer used was configured with only 12 thousand words of memory, several of the mainline programs had to be written in segments. The computations were accomplished by loading each program segment into the computer in turn in a process known as chaining. This memory-size limitation made the mainline programs long and of limited value to other researchers using different computers. Consequently, only a few of the mainline programs used are listed in Appendix H.

Spot diagrams were computed using a mainline program consisting of six segments, CT1, CT2, CT3, CT4, CT5 and CT6, which are listed in Appendix H. This program traces 41 rays from the object point in the entrance slit to the mask plane. These 41 rays are chosen in the manner used by *Megill* and *Droppleman* [1962] and illustrated in Figure 12. The radii of the circles in this figure are related by the recursion relation

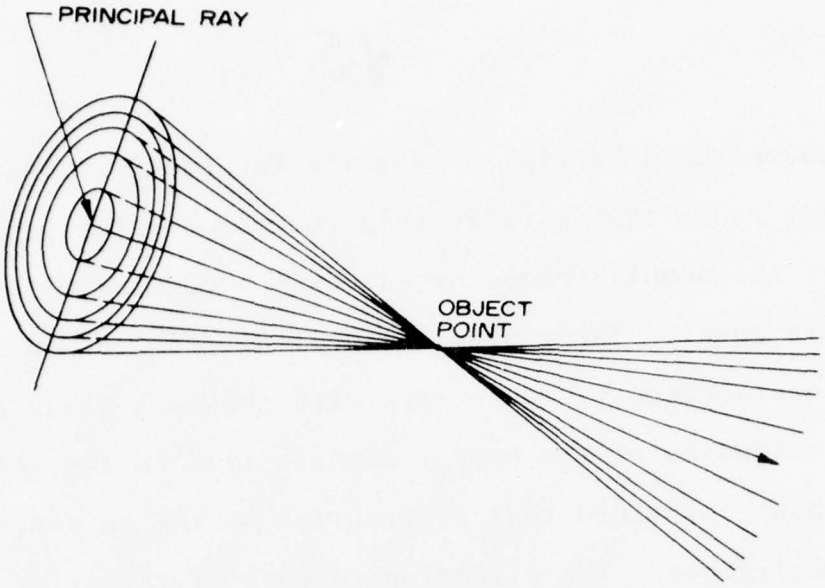


Figure 12a. The cones of rays surrounding the principal ray.

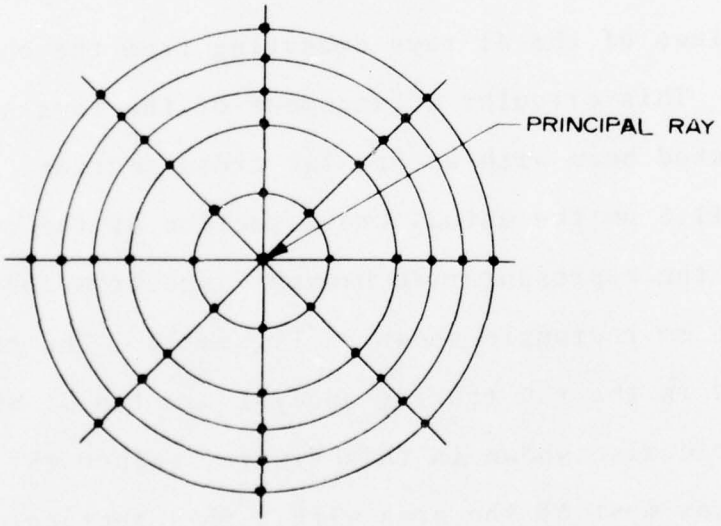


Figure 12b. Ray intersections with a plane perpendicular to the principal plane looking in the direction of the principal ray.

$$\rho_k = \sqrt{\frac{k}{k+1}}\,\rho_{k+1} \quad , \tag{71}$$

where the subscript k is unity for the innermost circle. For radii that satisfy this recursion relation, the areas of the annuli formed by successive circles with these radii are equal. Therefore, the spot diagram formed by the intersection of these rays with the mask plane gives an indication of the energy distribution in the image of a point, provided that diffraction by the entrance pupil is negligible. The direction cosines of the principal ray, the ray through the grating center, are found by subroutine CRAY. After the direction cosines of the principal ray are found, the subroutine DCOS is used to compute the direction cosines of the 41 rays emanating from the object point.

This circular arrangement of the rays simulates a collimated beam with a circular cross section. For $k\lambda$ equal to 11.5 μm the actual cross section of the collimated beam for the representative Hadamard spectrometer is the 64 by 59.6-mm rectangle shown in Figure 13. The cross section used in the ray-tracing analysis is the 71-mm diameter circle also shown in this figure. Since this circle encloses most of the area within this rectangle, the ray-tracing analysis gives a reasonable approximation of the imaging fidelity of the representative Hadamard spectrometer.

In order to compare the results of the ray-tracing analysis with the results of the aberration expressions,

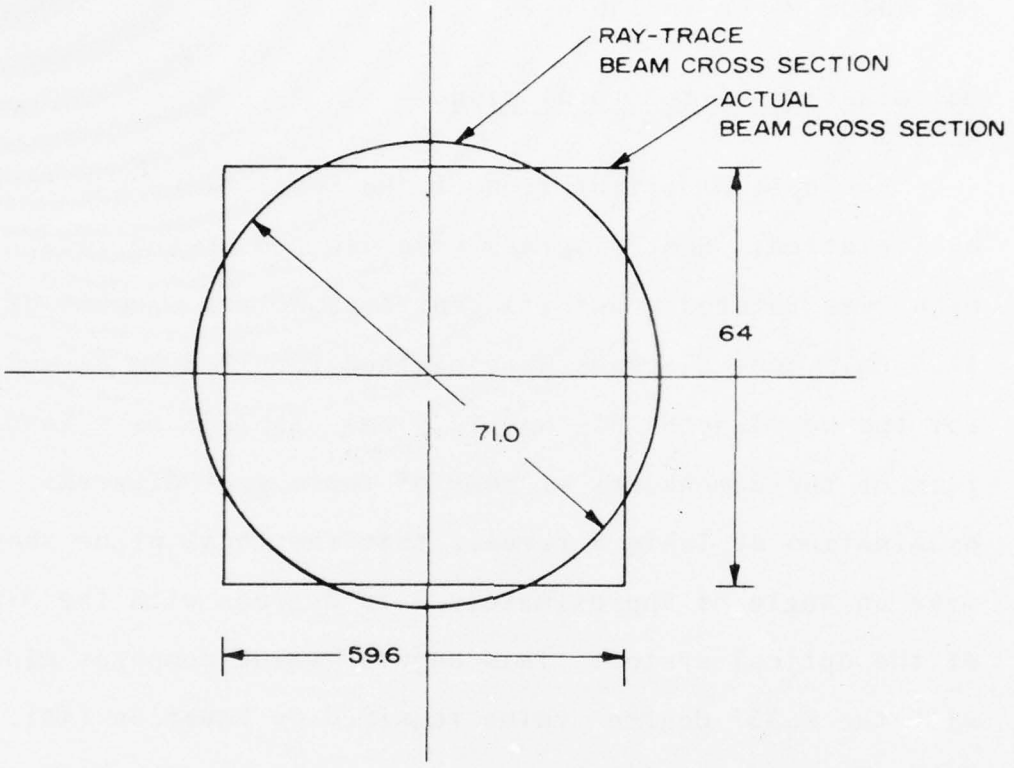


Figure 13. Cross sections of the ray-trace and the actual collimated beams. Dimensions are in millimeters.

the values of W and L used in the aberration expressions must be 76.2 and 71.0 mm, respectively. The 76.2 mm value was computed by dividing 71.0 mm by the cosα, where α had the value given in Table 2.

Optimization of the focal plane location

The optimum orientation of the focal plane was found by iteration. Spot diagrams were plotted as the focal plane was rotated about its central spectral element of 11.5 μm. Spot diagrams were plotted for 11.5 μm as well as for the wavelength 10.5 and 12.5 μm. Table 5 is a tabulation of the dimensions of some of these spot diagrams. An examination of Table 5 reveals that the focal plane should make an angle of approximately 8.25 degrees with the X-axis of the optical system. This angular value compares closely with the 8.357-degree value required by Equation (44). In fact, for a focal plane 100-mm long, the angular difference between 8.357 and 8.25 degrees corresponds to a focal shift of only 95 μm at the ends of the focal plane. The focal plane was oriented at 8.25 degrees for all subsequent ray tracing.

Depth of focus

The depth of focus was checked by computing spot diagrams for focal planes located closer and further than the meridional focal length given by Equation (F-6) in Appendix F. The results of these computations are tabulated

Table 5. Dimensions of on-axis spot diagrams at selected focal plane angles. The spot widths were scaled from plots and have a tolerance of ±5 μm. The spot lengths were taken from computer listings and have tolerances of ±0.5 μm.

Angle (degrees)	Wavelength (μm)	Spot width (μm)	Spot length (μm)
7.0	10.5	103	1794
7.0	11.5	86	3085
7.0	12.5	233	5251
7.5	10.5	59	1726
7.5	11.5	86	3089
7.5	12.5	173	5332
8.0	10.5	59	1651
8.0	11.5	86	3084
8.0	12.5	124	5402
8.25	10.5	74	1616
8.25	11.0	73	2258
8.25	11.5	86	3084
8.25	11.75	93	3576
8.25	12.0	95	4128
8.25	12.25	91	4747
8.25	12.5	87	5440
8.5	10.5	108	1580
8.5	11.5	86	3084
8.5	12.5	64	5478

in Table 6. From Tables 5 and 6 it is found that the depth of focus for a focal plane angle of 8.25 degrees is greater than 1 mm and that the spot width is actually smaller at a location 1 mm closer to the spherical mirror 2 than it is at the conventional meridional focus.

Table 6. Dimensions of spot diagrams for focal planes translated small distances from the meridional focal length. Positive and negative translations signify, respectively, translations away from and toward the spherical mirror 2. Tolerances are ±5 μm for spot width and ±0.5 μm for spot length.

Translation (mm)	Wavelength (μm)	Spot width (μm)	Spot length (μm)
+1	10.5	205	1470
+1	11.5	199	2939
+1	12.5	190	5298
-1	10.5	91	1777
-1	11.5	65	3240
-1	12.5	49	5597
-2	10.5	133	1930
-2	11.5	162	3396
-2	12.5	137	5748

Spot diagrams

The spot diagrams for several wavelengths when the object point is at the center of the entrance slit are plotted in Figure 14. Each spot diagram in this figure has its own scale. As shown in the section on the ray-tracing programs, a value of 76.2 mm must be used for W in the aberration expressions if the results of ray tracing at a wavelength of 11.5 μm are to be compared with the results of the aberration expressions. When W is 76.2 mm, the transverse spherical aberration $\xi_{sph.ab.}$ predicted by Equation (20) is 33 μm and the transverse coma ξ_{coma} predicted by Equation (24) is 8 μm. Thus, by Equation (31) the width of the spot diagram predicted by the aberration expressions is 74 μm. This value for the spot width is 15 percent less than the 86-μm width shown in plot (c) of Figure 14. The maximum spot width in Figure 14 is 95 μm.

Asymmetry in the spot diagram is a manifestation of coma. As shown in plot (c) of Figure 14, the spot diagram for a wavelength of 11.5 μm exhibits a small amount of coma in agreement with the computed transverse coma of 8 μm. The spot diagram for a wavelength of 10.5 μm shows considerable coma, but the width of the spot is less than it is for a wavelength of 11.5 μm.

In order to ascertain whether the image of a point is accurately described by these spot diagrams, the width of these spot diagrams must be compared to the diffraction limit. For a rectangular aperture with width w, the angular



Figure 14. On-axis spot diagrams with the focal plane inclined at an angle of 8.25° to the X-axis for wavelengths (a) 10.5 μm, (b) 11 μm, (c) 11.5 μm, (d) 11.75 μm, (e) 12 μm, (f) 12.25 μm, and (g) 12.5 μm. All dimensions are in microns with each spot diagram having its own scale.

distance between the maximum and the first minimum of the diffraction pattern is given by [*Jenkins* and *White*, 1957]

$$\theta_d = \lambda/w \quad . \tag{72}$$

For the Czerny-Turner optical system,

$$w = W\cos\beta \quad . \tag{73}$$

In the mask plane the linear separation between the maximum and the first minimum is given by

$$\sigma = D\theta_d \quad , \tag{74}$$

where D is the meridional focal length of spherical mirror 2. It follows from Equations (72), (73), (74), and the equation for the meridional focal length given in Appendix F, that

$$\sigma = \frac{\lambda R_2 \cos b}{2W\cos\beta} \quad . \tag{75}$$

For λ equal to 11.5 μm and the parameter values given in Tables 1 and 2, the diffraction limit σ is 110 μm. Thus, the maximum on-axis spot width of 95 μm is less than the diffraction limit.

Since the diameter of the collimated beam used in the ray-trace analysis was 71 mm, the value of L used in Equation (30) must be 71 mm if the results of the ray-tracing analysis and Equation (30) are to be compared. If 71 mm is used in Equation (30), the transverse astigmatism $\eta_{ast.}$ for a wavelength of 11.5 μm is 1570 μm. Thus, by

Equation (32), the length of the spot diagram predicted by the aberration expressions is 3140 μm when the wavelength is 11.5 μm. This length is two percent larger than the 3084-μm length resulting from the ray-tracing analysis and illustrated in plot (c) of Figure 14.

Spectrum line curvature

The spectrum line curvature was computed by tracing quasi-principal rays; that is, rays that are parallel to ray *A* in Figure 4. These rays would be true principal rays if the distance *C* in Figure 4 were the meridional focal length of spherical mirror 1. If this were the case, these rays would strike the center of the grating. The lateral translation for several object heights of this quasi-principal ray is tabulated in Table 7. The object height is the *Y* coordinate of the object point in the entrance slit. For comparison the lateral translation computed from Equation (54) is also tabulated in this table. As shown in Table 7, the ratio of the lateral translations for quasi-principal rays to the analytically-computed principal values are constant to within one percent. Thus, Equation (54) accurately describes the spectrum line curvature of the representative Hadamard spectrometer.

As can be seen from comparing the magnitude of the lateral translations tabulated in Table 7 with the 0.110-mm diffraction limit, spectrum line curvature is a serious aberration. This aberration increases very rapidly with

Table 7. The lateral translation due to spectrum line curvature for several object heights, Y_s, at a 11.5-μm wavelength.

Y_s (mm)	$\Delta X'$ of principal ray from Eq. (54) (mm)	$\Delta X'$ of principal ray from ray tracing (mm)	Ray-trace value / Analytic value
9	0.096	0.103	1.073
14	0.233	0.249	1.069
15	0.268	0.286	1.067
19.05	0.432	0.462	1.069
20	0.476	0.510	1.071
24	0.685	0.734	1.072
29	1.001	1.073	1.072
30	1.071	1.148	1.072

slit height since, as shown by Equation (54), the lateral translation of point image is proportional to the square of the distance above the optical axis.

Selection of the slot width

The slot width must be wider than the resolution limit of the spectrometer optics, and it must allow implementation of a cyclic code. As shown in Figure 14, the width of the spot diagram for an on-axis object point is less than 95 μm for the wavelength interval from 10.5 to 11.5 μm.

This width is less than the 110-μm diffraction limit for a wavelength of 11.5 μm. Ray tracing reveals that the images formed for wavelengths 10.5 and 12.5 μm are located 53 and 59 mm, respectively, from the image formed for the 11.5-μm wavelength. Thus, the aberrations would allow a field stop width of at least 112 mm. However, the optical components of the Minuteman Hadamard spectrometer limit the unobstructed focal plane to 104 mm. Thus a field stop length of 100 mm was selected for the representative Hadamard spectrometer.

As explained in Appendix A, cyclic codes exit when the number of encoded spectral elements N satisfies the following equation:

$$N = 2^n - 1 \quad , \tag{76}$$

where n is an integer greater than unity. Thus, cyclic codes exist for N equal to 127, 255, 511, and 1023. The required slot width to fit these codes within a field stop 100-mm wide are tabulated in Table 8. The 1023 code was rejected for use with the representative Hadamard spectrometer because it requires a slot width less than the 110-μm diffraction limit. A 511 code, which requires a slot width of 196 μm, was selected for the representative Hadamard spectrometer.

Table 8. Required slot width required to fit N spectral elements within a field stop 100-mm wide.

N	Slot width (μm)
127	787
255	392
511	196
1023	98

Theoretical Performance of the Representative Hadamard Spectrometer when Equipped with Straight Slots

Astigmatism and spectrum line curvature combine to severely limit the usable length of straight slots for the representative Hadamard spectrometer. Not only does the curvature of the image of a straight entrance slit increase with the distance above the optical axis, but the width of the image also increases. This width increase can be understood by studying Figure 15. For a straight entrance slit, the locus of principal ray intersection is a parabolic curve according to Equation (53). In Figure 15, the images of object points 1 and 2 are identified by 1' and 2', respectively. As can be seen from this figure, astigmatism causes no significant image broadening at 1' because the long narrow image of point 1 is tangent to the

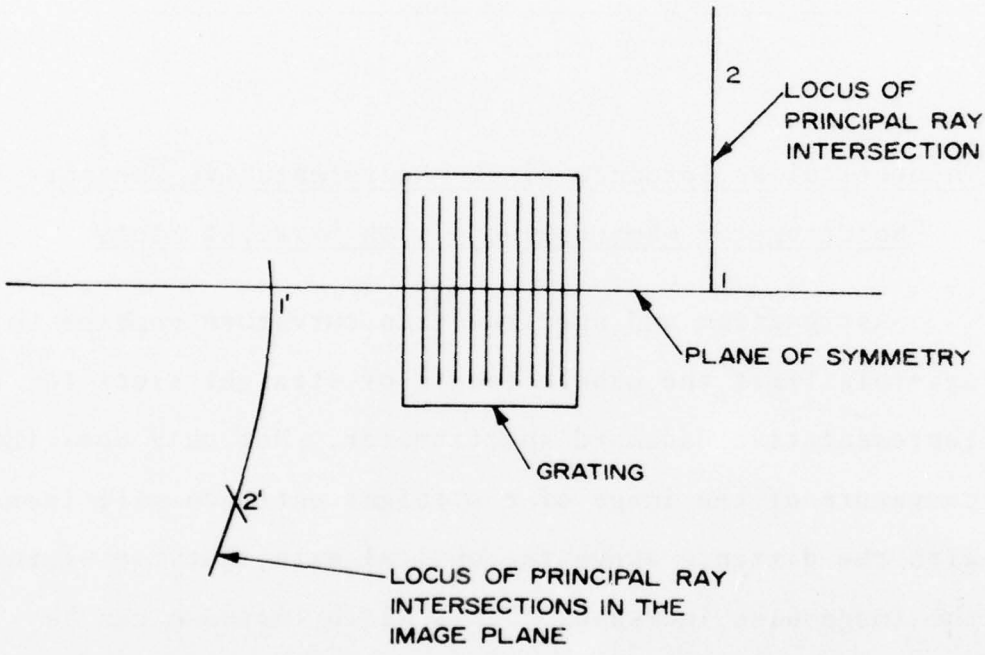


Figure 15. Astigmatism and image curvature combine to broaden the image of a straight entrance slit.

parabolic curve. However, at 2' the image of point 2 crosses the parabolic curve. Hence, astigmatism causes significant image broadening at 2'. As shown in Figure 16, the angle of rotation of the point image increases with the distance of the object point above the optical axis. Spectrum line curvature and astigmatism work against each other; that is, the direction of rotation of the point image is opposite to that which would make the point image tangent to the parabolic curve in Figure 15. Thus, the width of the image increases with the distance from the optical axis.

The Minuteman Hadamard spectrometer cannot image object points closer than 8.2 mm to the optical axis. This limitation is due to obscurations caused by the finite thickness of the two folding mirrors near the Hadamard mask. Therefore, the bottom of the entrance slit is at Y_s equal to 8.2 mm. Since this spectrometer has a large amount of astigmatism and the bottom of the usable entrance slit is a considerable distance above the optical axis, the performance of this spectrometer when equipped with straight slots is severely limited.

If the astigmatism were small, the effects of spectrum line curvature could be partially neutralized by optimizing the alignment of the slots with the spectral images. If the slots are parallel to the entrance slit, spectrum curvature limits the entrance slit length to 7 mm. This value for the entrance slit length follows from Equation (54), a

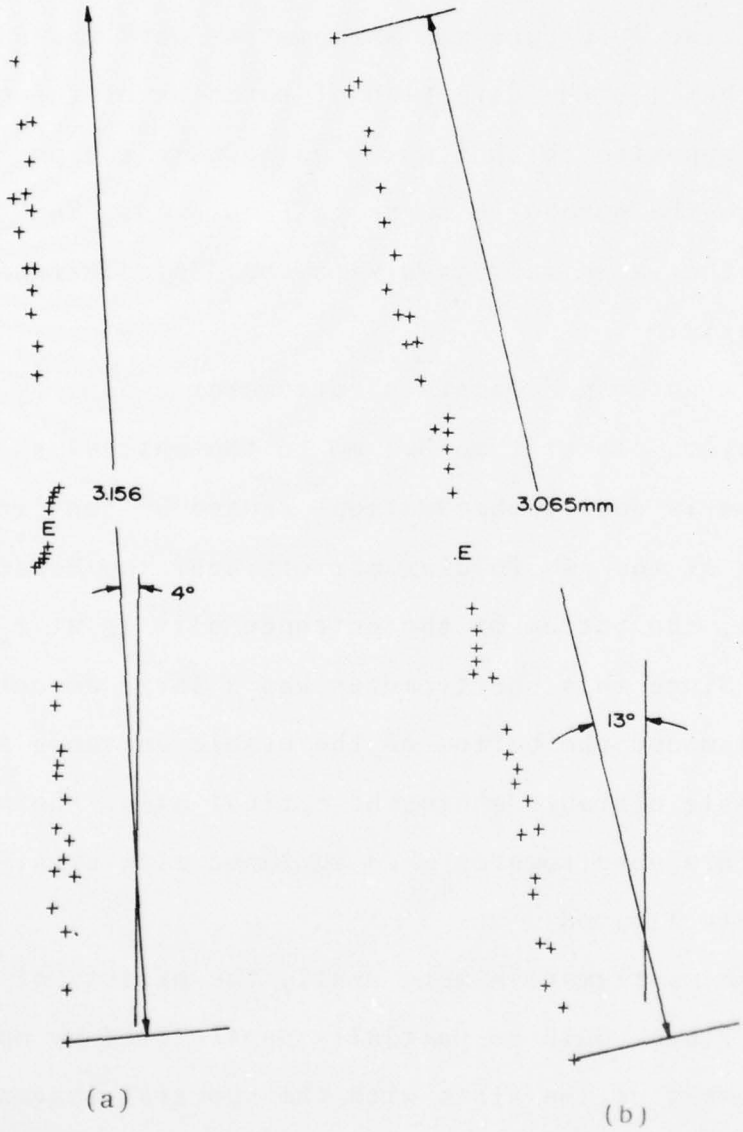
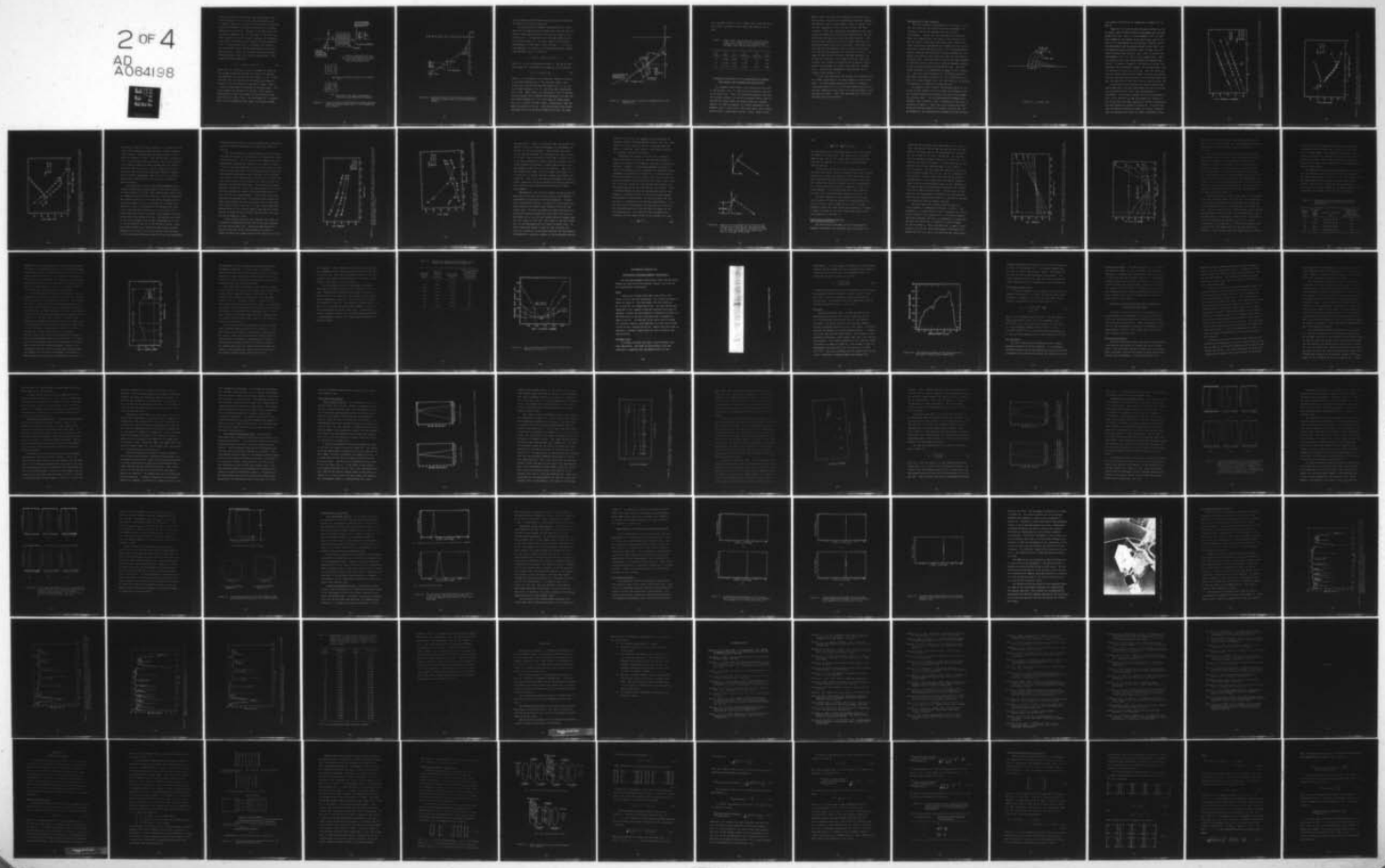


Figure 16. Spot diagrams at a wavelength of 11.5 μm at object heights of (a) 9 mm (b) 29 mm.

AD-A064 198 UTAH STATE UNIV LOGAN ELECTRO-DYNAMICS LAB F/G 20/6
INCREASING THE THROUGHPUT OF HADAMARD SPECTROMETERS BY THE USE --ETC(U)
SEP 78 R W ESPLIN, G A VANASSE, D J BAKER F19628-77-C-0203
UNCLASSIFIED EDL-SRL-78-2 AFGL-TR-78-0232 NL

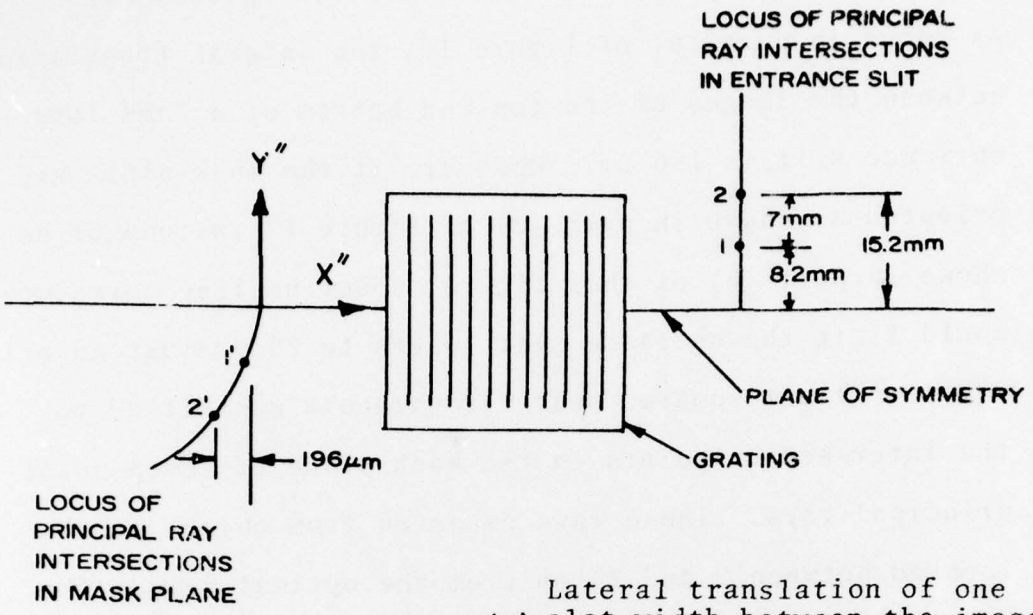
2 OF 4
AD
A064198



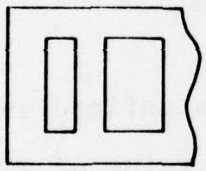
196-μm slot width, and the fact that the bottom of the usable entrance slit is 8.2 mm above the optical axis. As shown in part (a) of Figure 17, the lateral translation between the images of the top and bottom of a 7-mm long entrance slit is 196 μm. However, if the mask slots are oriented as shown in part (c) of Figure 17 instead of as shown in part (b) of this figure, spectrum line curvature would limit the entrance slit length to 20 mm instead of 7 mm. A least-squares best-fit parabola was fitted to the intersection points in the mask plane of seven quasi-principal rays. These rays emanated from object points located between 9 and 29 mm from the optical axis. The equation of this parabola is

$$X'' = -1.498 \times 10^{-3} Y''^2 \quad , \tag{77}$$

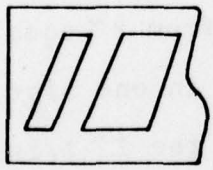
where the $X''Y''$-coordinate system is defined in Figure 18. The maximum difference between the value of X'' computed from Equation (77) and the ray trace data is 1 μm. If the straight slots are parallel to the dashed line shown in Figure 18, all the principal rays from Y'' equal -9 mm to Y'' equal -29 mm would be contained in one slot width. The angle between this dashed line and the Y'' axis appears exaggerated in Figure 18 because of the different scales used for the X'' and Y'' axes. The true angle is 3.2 degrees. Thus, if the astigmatism were small, 20-mm long straight



(a) Lateral translation of one slot width between the images of the top and bottom of a 7 mm long entrance slit.



(b) Mask with slots parallel to entrance slit.



(c) Mask with slot angle optimized to neutralize spectrum line curvature

Figure 17. Image curvature limitation for straight entrance slit and straight mask slots if no astigmatism were present.

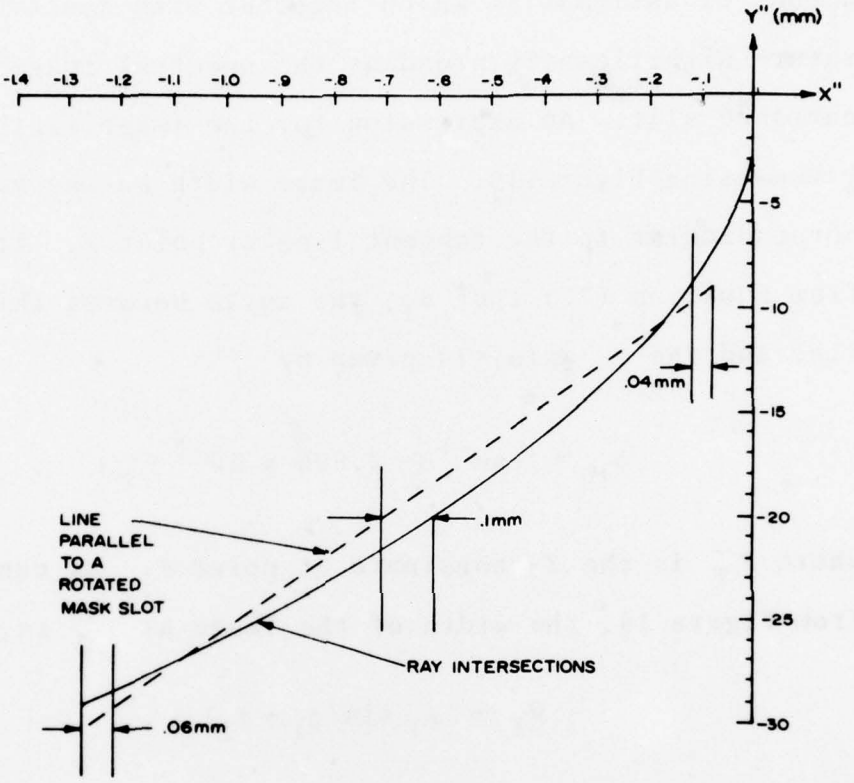


Figure 18. Neutralization of spectrum line curvature by aligning straight slots with the spectral images.

slots could be used provided they were aligned to minimize the effects of spectrum curvature.

The representative Hadamard spectrometer has a large amount of astigmatism which together with spectrum line curvature significantly broadens the spectral images of the entrance slit. An expression for the image width was derived using Figure 19. The image width W_I was measured perpendicular to the tangent line at point T. It follows from Equation (77) that ϕ_1, the angle between this tangent line and the Y'' axis, is given by

$$\phi_1 = \tan^{-1}(-2.996 \times 10^{-3} Y''_T) \quad , \tag{78}$$

where Y''_T is the Y-coordinate at point T. As can be seen from Figure 19, the width of the image at Y''_T is given by

$$W_I = L_I \sin(\phi_1 + \phi_2) \quad , \tag{79}$$

where L_I is the length of the image of a point at T and ϕ_2 is the angle between the Y'' axis and this image. Ray tracing was used to ascertain the values Y''_T, L_I, ϕ_1, and ϕ_2 at object heights of 9, 15, and 29 mm and a wavelength of 11.5 μm. These values are tabulated in Table 9 together with the values of W_I computed from Equations (78) and (79). For object heights of 9, 15, and 29 mm, the image widths are 1.5, 2.2, and 2.7 times larger, respectively, than the mask slot width of 196 μm. Since the bottom of the usable entrance slit is at an object height of 8.2 mm, the image

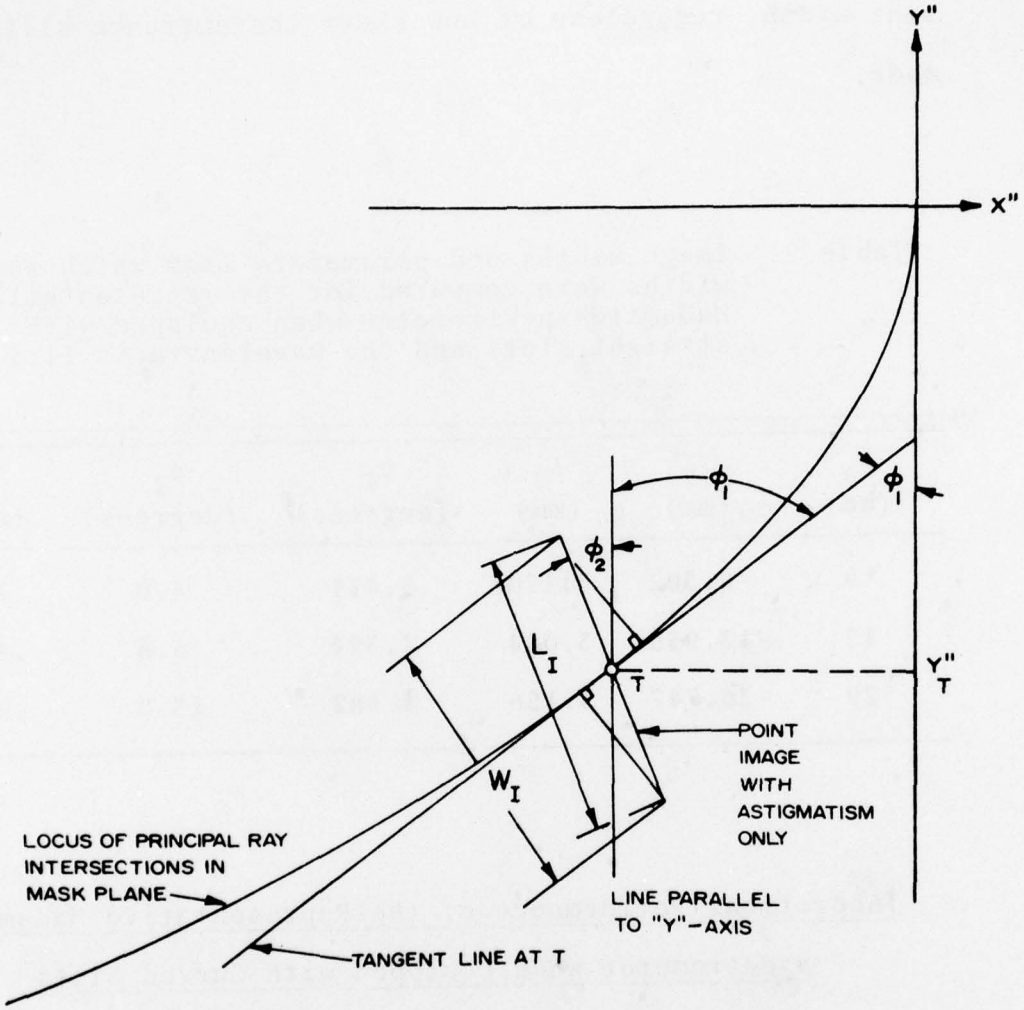


Figure 19. Geometry used to derive an expression for the image width.

of a straight entrance slit is always wider than the 196 μm slot width, regardless of how short the entrance slit is made.

Table 9. Image widths and parameters from which these widths were computed for the representative Hadamard spectrometer when equipped with straight slots and the wavelength is 11.5 μm.

Y_s (mm)	Y_T'' (mm)	L_I (mm)	ϕ_1 (degrees)	ϕ_2 (degrees)	W_I (mm)
9	-8.302	3.170	1.411	4.0	.370
15	-13.955	3.044	2.394	5.6	.422
29	-26.747	3.156	4.582	13.0	.926

Theoretical Performance of the Representative Hadamard Spectrometer when Equipped with Curved Slots

In a Hadamard spectrometer, the curvature of the image of the entrance slit is a function of the image's location in the field stop. Thus, for optimum performance each spectral element requires its own slot curvature which could be achieved by using N masks to encode N spectral elements. However, as shown in Appendix A, a major advantage of the Hadamard code is that cyclic codes exist which can be implemented using a single mask with $2N$-1 slots. When a single

mask is used, the slots are translated across the field stop so that a typical slot encodes many spectral elements. Consequently, when a single mask is used, it appears that the best compromise is for all slots to have the same curvature. Thus, the theoretical performance of the representative Hadamard spectrometer was analyzed with the condition that all mask slots have the same curvature. The slot curvature which maximized the usable entrance slit length was found using ray-tracing data. These data indicate that for the optimized slot curvature the entrance slit can be 20-mm long when the slot width is 196 μm. As shown in the previous section, a straight entrance slit 0.8-mm long requires a slot width of 370 μm. Thus, the entrance slit length can theoretically be made at least a factor of ten longer for curved slots than for straight slots. The optical throughput is proportional to the length of the entrance slit.

It was also shown that the optimum slot curvature does not change significantly for small changes in the grating angle. A grating angle change that causes a change in wavelength from 11.5 to 9.3 μm of the central spectral element was computed to cause only a two percent change in the optimum slot radius. Thus, the same mask can be used for different spectral intervals.

Optimization of slot curvature

The slot curvature was optimized in two steps. First, the slot curvature was optimized with the entrance slit curvature fixed at the optimum value for an Ebert spectrometer. Second, the slot curvature was optimized under the condition that the radius of the entrance slit and the radius of the mask slots were equal. Both these steps required the determination of whether or not a given ray passed through the proper slot. This determination was made by computing the horizontal distance between the slot center line and the point where the given ray intersected the mask plane. This horizontal distance was then compared to half the width of the slot in order to determine whether or not the given ray passed through the slot. This horizontal distance d_s is identified in Figure 20 for a typical ray. The slots were assumed to be constructed using the procedure illustrated in Figure 20. This construction produces a crescent-shaped slot; the slot width W_S, as defined in Figure 20, is constant all along the axis.

As shown by *Fastie* [1952b], the optimum radius of curvature of the entrance slit of an Ebert spectrometer equals the distance between the entrance slit and a line through the grating center. For the representative Hadamard spectrometer, this distance is the X coordinate of the point G_C tabulated in Table 3. Thus, the slot curvature was first optimized with an entrance slit radius of 91.110 mm. The performance of the representative Hadamard with an entrance

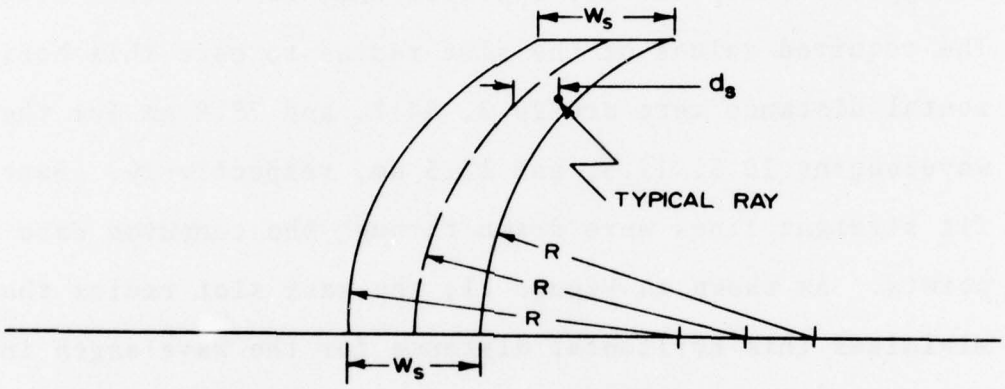


Figure 20. A curved slot.

slit radius of 91.110 mm is summarized in Figures 21, 22 and 23.

Figure 21 is a plot of the horizontal distance d_s for principal rays at three different wavelengths and an object height of 15 mm. The 11.5 μm wavelength is for the spectral element at the center of the field stop, and the 10.5 and 12.5 μm wavelengths are for spectral elements located at approximately the two opposite ends of the field stop. The required values of the slot radius to make this horizontal distance zero are 90.2, 84.7, and 77.8 mm for the wavelengths 10.5, 11.5, and 12.5 μm, respectively. Best-fit straight lines were drawn through the computed data points. As shown in Figure 21, the mask slot radius that minimizes this horizontal distance for the wavelength interval from 10.5 to 12.5 μm is 83.4 mm. With this value for the slot radius and an object height of 15 mm, the maximum value of this horizontal distance is 90 μm which means that the slot width must be 180 μm to collect the principal ray.

Collection of the principal ray does not ensure that sufficient energy for good performance has been collected; the collection of the entire spot diagram must be considered. For an object height of 15 mm, wavelengths of 10.5, 11.5, and 12.5 μm, and an entrance slit radius of 91.110 mm, the slot width required to collect 85 percent of the spot diagram is plotted in Figure 22. If this 85 percent collection criterion is used, this figure indicates that the minimum slot width for proper performance across

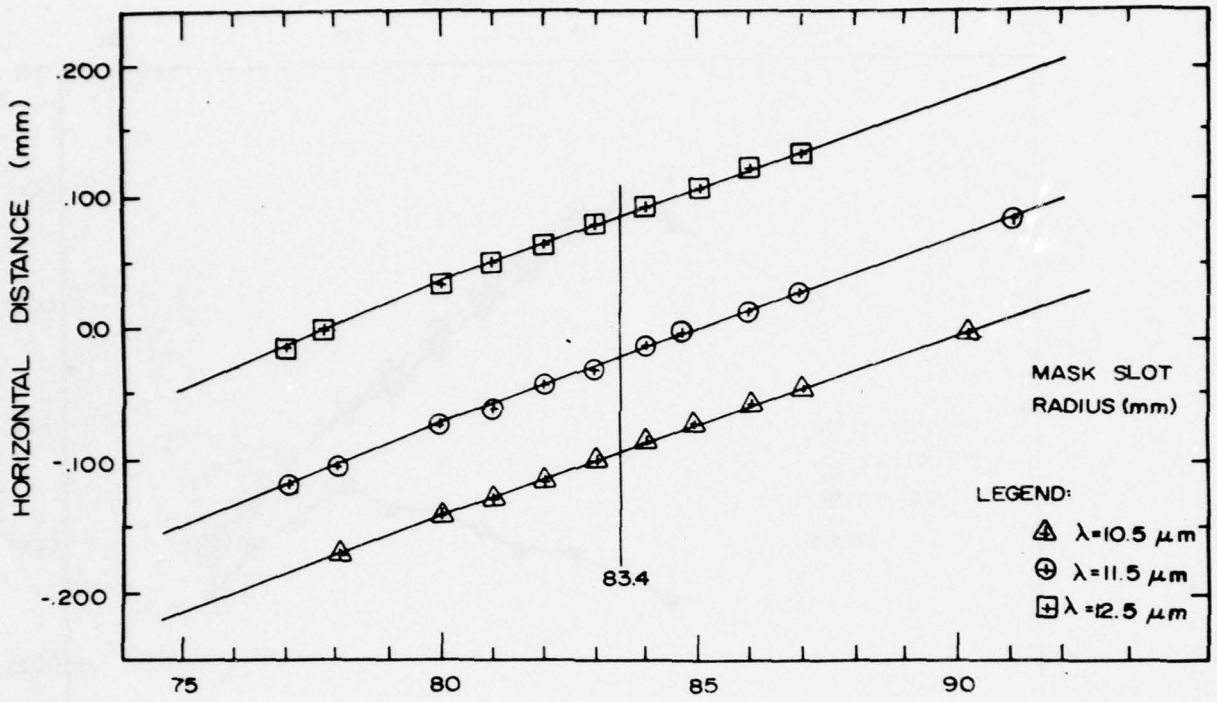


Figure 21. The horizontal distance from the mask slot center line to the principal ray versus the mask slot radius for an entrance slit radius of 91.110 mm and an object height of 15 mm.

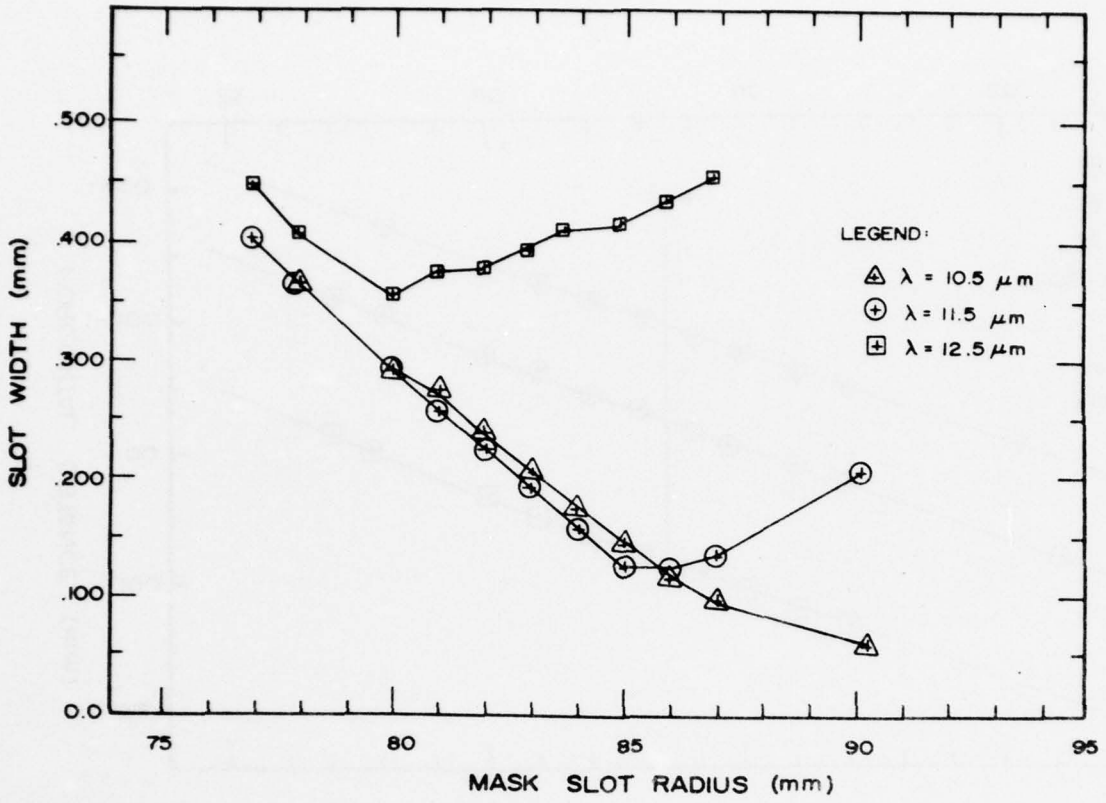


Figure 22. The required mask slot width to collect 85 percent of the spot diagram versus the mask slot radius for an entrance slit radius of 91.110 mm and an object height of 15 mm.

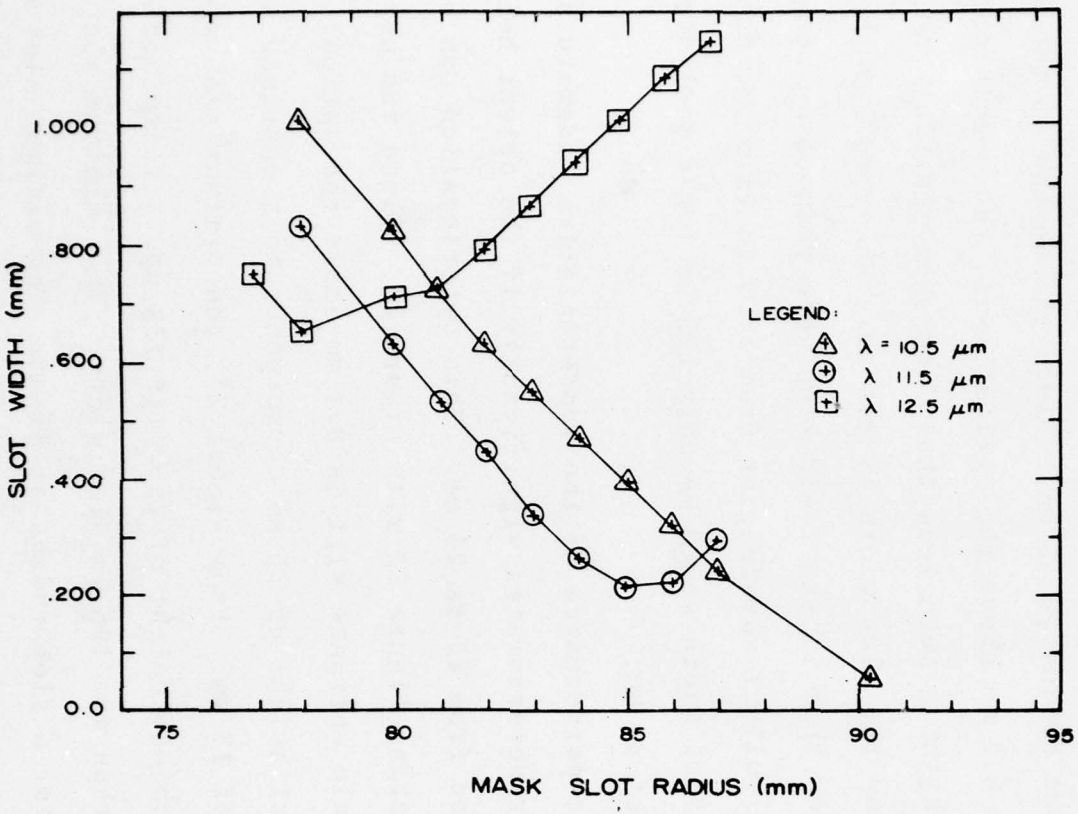


Figure 23. The required mask slot width to collect 85 percent of the spot diagram versus the mask slot radius for an entrance slit radius of 91.110 mm and an object height of 25 mm.

the entire field is 355 μm, a factor of 1.8 larger than the 196-μm slot width which would allow 511 spectral elements to be encoded. This minimum slot width results when the mask slot radius is 80 mm. Since the bottom of the entrance slit is 8.2 mm above the optical axis, the usable entrance slit length is much less than 7 mm when the slot radius is 80 mm and the slot width is 196 μm. However, Figure 22 indicates that if the field stop were reduced by roughly half to collect wavelengths from 10.5 to 11.5 μm, the required slot width would be only 125 μm for a mask slot radius of 86 mm.

The performance of the representative Hadamard spectrometer deteriorates significantly if the object height is increased from 15 to 25 mm. This deterioration can be seen by comparing Figure 22 with Figure 23. Since the bottom of the usable entrance slit is 8.2 mm above the optical axis, an object height of 25 mm corresponds to a entrance slit length of 17 mm. From Figure 23, the minimum slot width for an object height of 25 mm is 725 μm, a factor of 3.7 larger than the 196 μm slot width. This minimum slot width occurs for a slot radius of 81 mm. The minimum slot width for an object height of 25 mm and a wavelength of 11.5 μm is 210 μm, which occurs for a slot radius of 85 mm. Thus, the usable entrance slit length for the central spectral element is less than 17 mm if 196 μm wide slots are used. If the field stop width were reduced to cover the wavelength

interval from 10.5 to 11.5 μm, the minimum slot width would be 265 μm, which would occur for a mask slot radius of 86.6 mm.

The slot curvature was next optimized with the restriction that the radius of the entrance slit equaled the radius of the mask slots. The ray-tracing data computed for this optimization procedure are summarized in Figures 24 and 25. As can be seen from comparing Figure 21 with Figure 24, and Figure 22 with Figure 25, the performance of the representative Hadamard spectrometer can be improved if the entrance slit radius is not required to be 91.110 mm. In Figures 24 and 25 the abscissa is the value of the radius of both the entrance slit and the mask slots. The horizontal distance plotted in Figure 25 is zero for radius values of 95, 118.4, and 145.5 mm when the values of the wavelength are 10.5, 11.5, and 12.5 μm, respectively. A slot radius of 125 mm minimizes the maximum value of the horizontal distance between the principal ray and slot center line for the spectral interval 10.5 to 12.5 μm. For this radius value this maximum value is 55 μm, which implies that the slot width must be at least 110 μm to collect the principal rays when the object height is 15 mm.

A more accurate value for the required slot width can be found by considering all the rays in the spot diagram, not just the principal ray. The slot width required to collect 85 percent of the spot diagram is plotted in Figure 25 versus the common radius of the entrance slit and

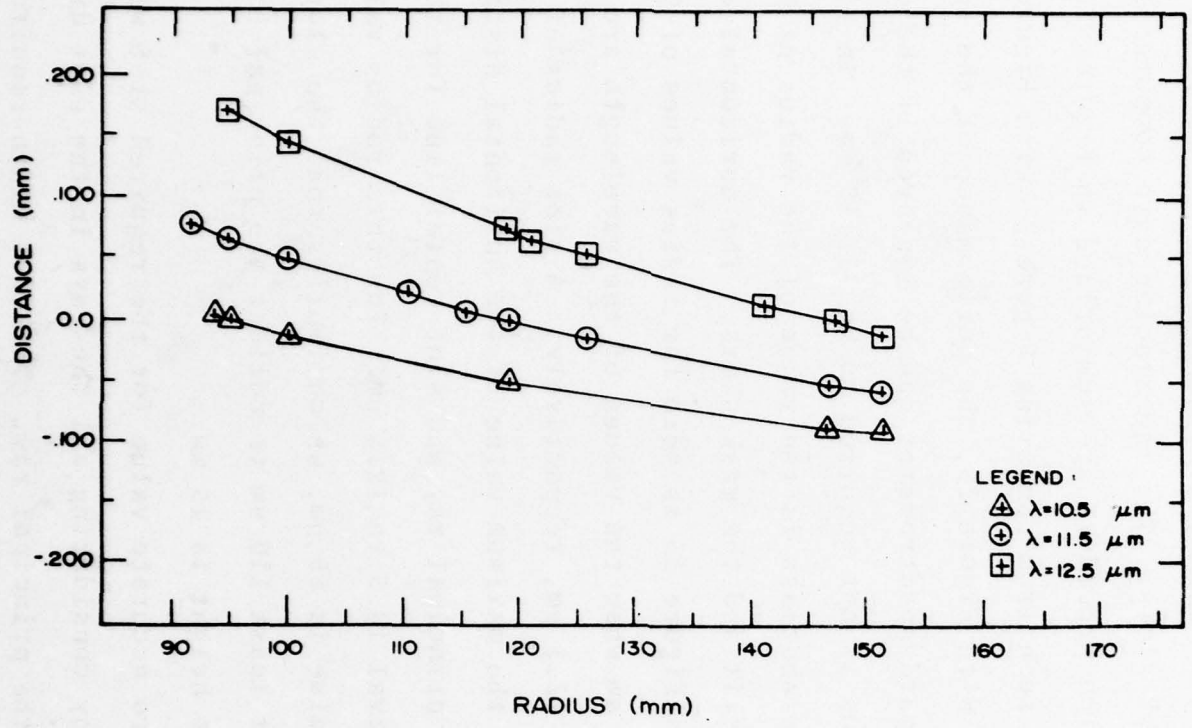


Figure 24. The horizontal distance from the mask slot center line to the principal ray versus the common radius value of the entrance slit and the mask slots for an object height of 15 mm.

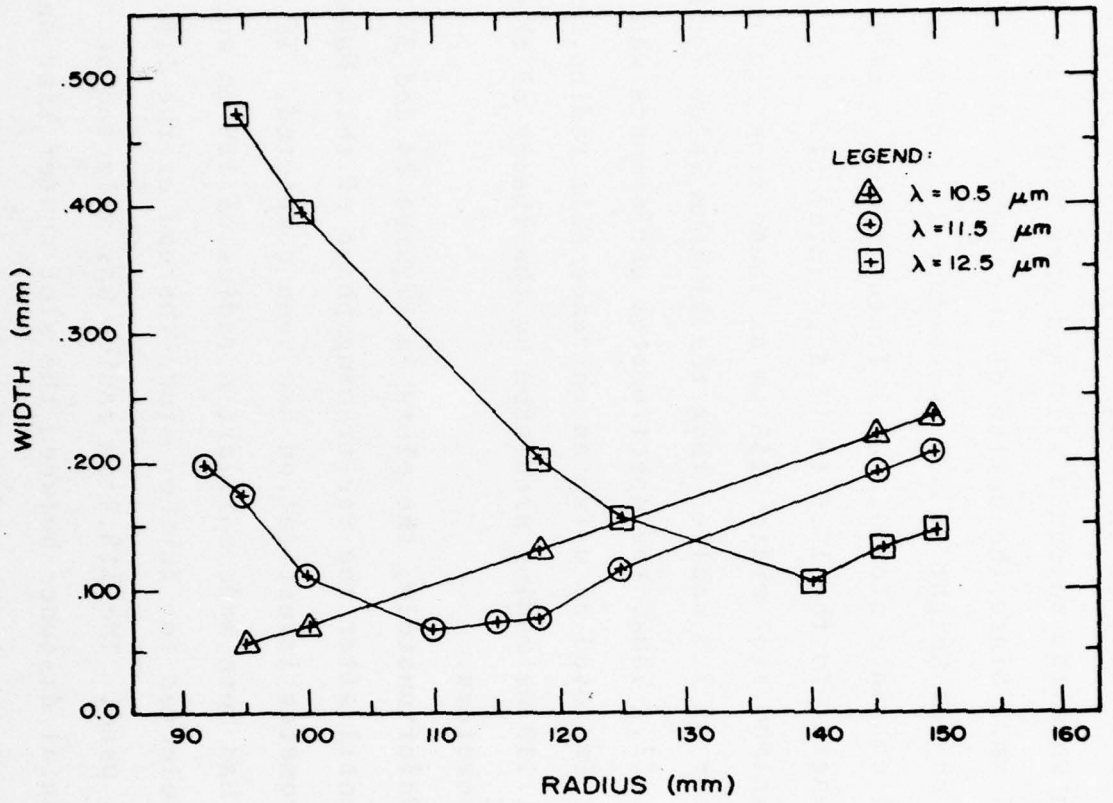


Figure 25. The required mask slot width to collect 85 percent of the spot diagram versus the common radius value of the entrance slit and the mask slots for an object height of 15 mm.

the mask slots. Figure 25 indicates that the minimum slot width is 155 μm for proper performance at wavelengths in the 10.5 to 12.5-μm interval. This minimum slot width occurs when the entrance slit and mask slots have a radius of 125 mm. Since the bottom of the usable entrance slit is at an object height of 8.2 mm, Figure 25 indicates that the usable entrance slot width is longer than 6.8 mm for all wavelengths in the 10.5 to 12.5-μm interval. The value of the minimum slot width, 155 μm as found from Figure 25, is a factor of 2.3 smaller than the minimum value found from Figure 22. Thus, the spectrometer performance was significantly improved by using an entrance slit radius other than the 91.110-mm radius predicted by the theory of Ebert spectrometers.

Unfortunately, the plots in Figures 24 and 25 were not made until after the ray-tracing phase of this Hadamard-spectrometer investigation had been completed. If these plots had been made earlier, a radius of 125 mm would have been selected for further study instead of the 118.4-mm radius used. The 118.4-mm radius was selected because the horizontal distance between the slot center line and the principal ray is zero for the central spectral element when the slot radius is 118.4 mm. This value is the point where the 11.5-μm wavelength plot in Figure 24 equals zero. As can be seen from Figures 24 and 25, the selection of a 118.4 mm instead of 125-mm radius improved the spectrometer performance for spectral elements in the wavelength interval

from 10.5 to 11.5 μm, but degrades this performance for spectral elements with wavelengths close to 12.5 μm. From Figure 25, a slot width of 200 μm is required when the radius is 118.4 mm. This value is sufficiently close to the selected slot width of 196 μm.

Originally the entrance slit was to be located as shown in part (a) of Figure 26, and the data plotted in Figures 21 through 25 was computed using this entrance slit location. However, the Minuteman Hadamard spectrometer could not be adapted to this entrance slit location without revamping its mechanical construction. It was decided to locate the entrance slit as shown in part (b) of Figure 26. For this entrance slit location the slit center line crosses the Y axis at a height of 19.05 mm above the optical axis. This particular height was selected for two reasons. First, it allowed imaging of points 29 mm above the optical axis. Second, a ray parallel with the optic axis which emanates from a point in the entrance slit 19.05 mm above the optical axis is a symmetrical ray for this spectrometer; i.e., this ray strikes the grating 3.414 mm above its center on the dispersion pass and 3.414 mm below its center on the dedispersion pass. The equations used to compute the X coordinate for the object point in the entrance slit were

$$X = \sqrt{R^2 - Y^2} - R \tag{80}$$

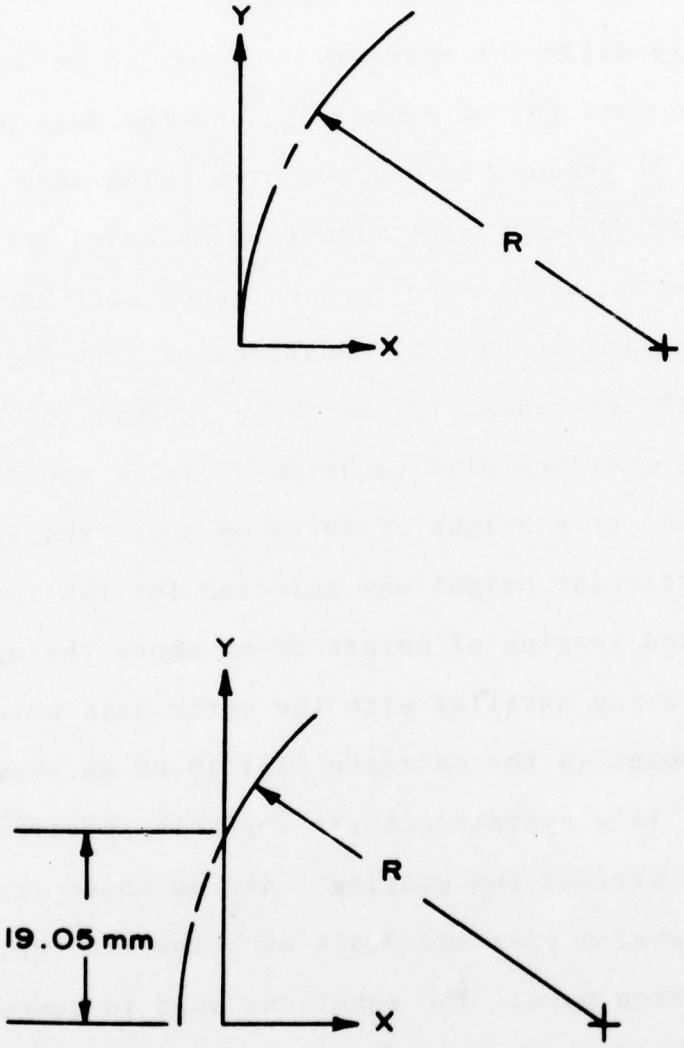


Figure 26. Center line of entrance slit plotted on the coordinate system used for ray tracing when (a) the center line passes through the origin and (b) when the center line crosses the Y axis at a height of 19.05 mm.

and

$$X = \sqrt{R^2 - Y^2} - \sqrt{R^2 - (19.05)^2} \qquad (81)$$

for the entrance slit locations shown in parts (a) and (b) of Figure 26, respectively. The entrance slit location shown in part (b) of this figure and R equal to 118.4 mm were used to compute the rest of the ray-tracing data reported herein.

In the final design the radius of the entrance slit was 118.4 mm, and the radius of the mask slots was 117.6 mm. The mask slot radius was changed to 117.6 mm because this value minimized the root-mean-square distance between the slot center line and the principal ray for a wavelength of 11.5 μm and object points with Y coordinates in the 0 to 29-mm interval. It was shown that for a slot radius of 117.6 mm, this root-mean-square distance is only 4 μm.

The spot diagram for a wavelength of 11.5 μm and a object height of 29 mm was found to be approximately tangent to the slot with a radius of 117.6 mm. For these parameter values the slope of the spot diagram is 13 degrees, as shown in Figure 16, and the slope of the slot at this spot diagram is 13.16 degrees.

Theoretical performance with the slot curvature optimized

The theoretical performance of the representative Hadamard spectrometer was analyzed using a entrance slit

radius of 118.4 mm and a mask slot radius of 117.6 mm. A field stop width of 100.667 mm was used because the slot width of the masks used in the experimental verification was 197 μm and 197 μm x 511 = 100.667 mm. The entrance slit was located as shown in part (b) of Figure 26. This analysis was done in two parts. In the first part of this analysis the grating rotation angle θ_G was fixed at 31.757 degrees. For this angle the wavelength of the central spectral element was 11.5 μm. In the second part of this analysis several values were used for the grating rotation angle. These values were the grating rotation angles used in the experimental phase of this Hadamard investigation when the spectrometer performance was checked using the 0.5461-μm mercury line. In both parts of this analysis, the spectrometer performance was ascertained by computing the required slot width as a function of entrance slit length and spectral element location.

The data taken for a grating rotation angle of 31.757 degrees is summarized in Figures 27 and 28. The parameter Y_s in these plots is the Y coordinate of a point object located in the entrance slit. Since the bottom of the usable entrance slit has a Y coordinate of 8.2 mm, the entrance slit whose top is located at Y_s has a length 8.2 mm less than Y_s. Thus, the plots for Y_s equal to the values 9, 14, 19, 24, and 29 correspond to entrance slit lengths of 0.8, 5.8, 10.8, 15.8, and 20.8 mm, respectively.

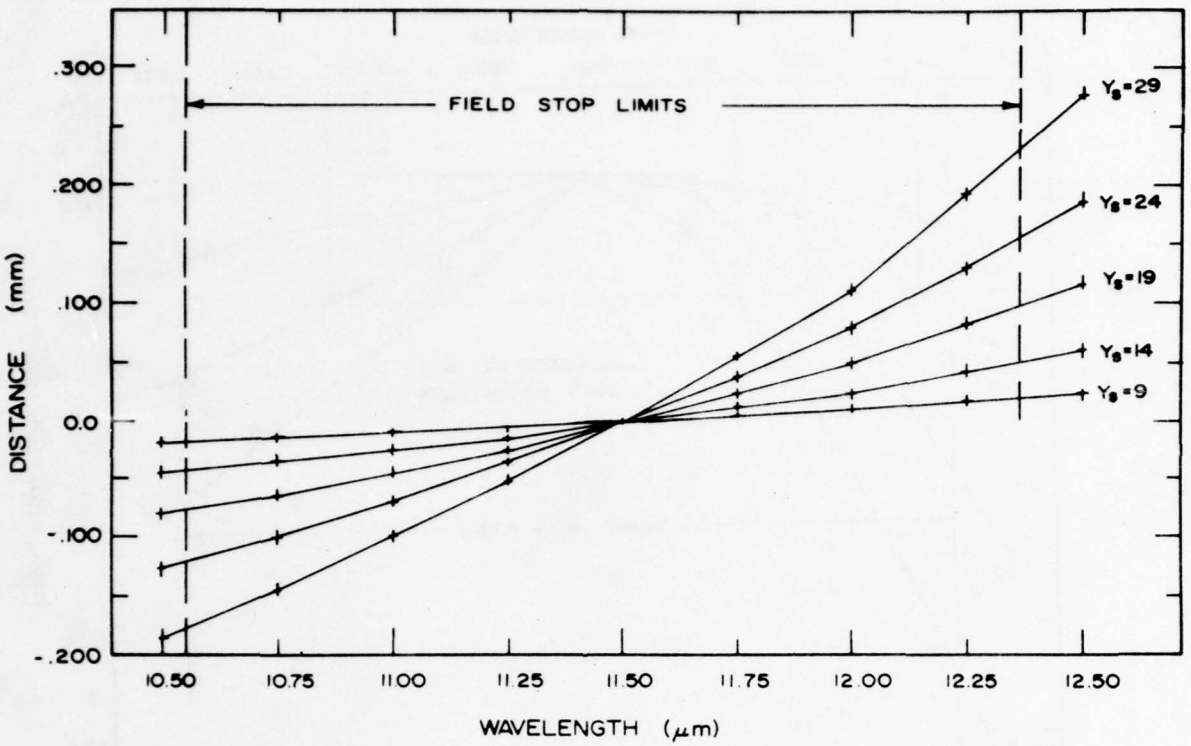


Figure 27. The horizontal distance from the mask slot center line to the principal ray. The parameter Y_s is the height of a point object located in the entrance slit.

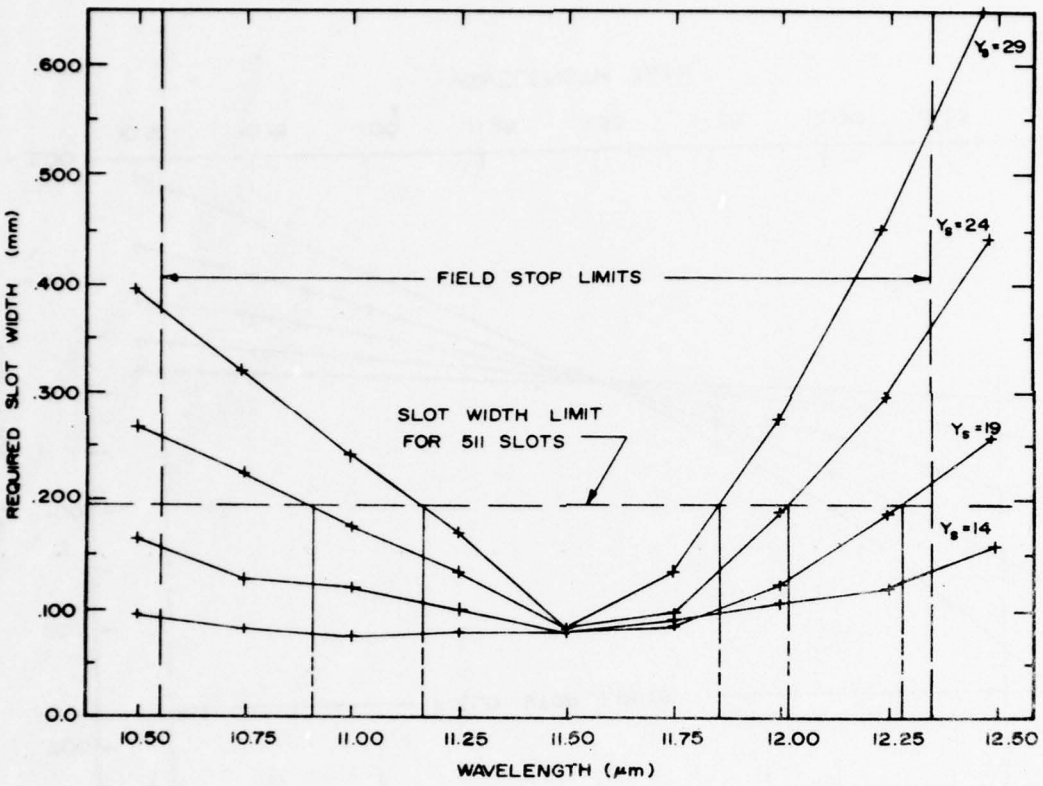


Figure 28. The required mask slot width to collect 85 percent of the spot diagram. The parameter Y_s is the height of a point object located in the entrance slit.

The ends of the field stop are identified by the dashed lines. The field stop limits the spectral passband of the spectrometer to the wavelength interval from 10.55 to 12.36 μm.

The horizontal distance from the slot center line to the principal ray is plotted versus wavelength in Figure 27 for the five object heights specified in the previous paragraph. Figure 27 illustrates the excellent match between the entrance slit image and the mask slot for the 11.5 μm wavelength. It is evident from this figure that this match deteriorates as the wavelength increases or decreases from the 11.5-μm wavelength. This deterioration is slightly worse at the long wavelength end of the field stop than it is at the short wavelength end. The slot width required to collect the chief ray is twice the horizontal distance plotted in Figure 27.

The data plotted in Figures 20 through 27 was computed using the following method to locate the slot center line. A principal ray of the desired wavelength was traced with Y_s, the height of the ray in the entrance slit, equal to zero. The slot center line was then located to pass through the intersection of this point with the mask plane. This method results in conservative values for the slot width because the bottom of the entrance slit is at Y_s equal 8.2 mm, not at Y_s equal zero. A different method was used to locate the slot center line for the data plotted in Figure 28. For this data the slot center line was located

so that it passed through the point where the principal ray from the object point with Y_s equal to 8.2 mm intersects the mask plane. This method of locating the slot center line results in slightly smaller values for the required slot width. Thus, Figure 28 summarizes the most accurate slot width values computed for the representative Hadamard spectrometer.

The spectral intervals over which there is no degradation in resolution with a 197-μm slot width is tabulated for four object heights in Table 10. The data in this table was taken from Figure 28, where the end points of these spectral intervals are identified with fanthom lines. It can be seen from Table 10 that for an object height of 19 mm, a entrance slit length of 10.8 mm, the resolution is

Table 10. The spectral interval over which there is no degradation in resolution for a slot width of 197 μm.

Object height (mm)	Entrance slit length (mm)	Spectral interval (μm)	Percentage of field stop within the spectral interval
14	5.8	10.55 to 12.36	100
19	10.8	10.55 to 12.28	96
24	15.8	10.91 to 12.02	61
29	20.8	11.16 to 11.85	38

degraded over only four percent of the spectral passband. The amount of resolution degradation for spectral elements outside the spectral intervals tabulated in Table 10 can be ascertained from Figure 28. For example, for an object height of 24 mm, an entrance slit length of 15.8 mm, and a wavelength of 12.25 μm, the required slot width is 295 μm. This slot width value is a factor of 1.5 larger than the 197-μm wide slot width of the experimental mask.

The maximum object height for which there is no degradation in resolution is plotted in Figure 29; the data for this plot were extracted from Figure 28. The values of 20.9 and 17.5 mm at the short and long wavelength ends of the field stop, respectively, were determined by linear interpolation. As shown in Figure 29, there is no degradation across the entire field stop when the entrance slit is 9.3-mm (17.5 - 8.2 mm) long. However, terminating the entrance slit length at an object height of 17.5 mm is not a good solution to the resolution degradation at the ends of the field stop. A much better solution is to use a 20.8-mm (29 - 8.2 mm) long entrance slit and mask down the field stop so that the maximum object height at each spectral element complies with Figure 29. Of course, this masking procedure causes the spectrometer's throughput to vary over the spectral passband. However, this throughput variation is not a significant problem because the computer used to invert the Hadamard spectrometer's measurements can also be used to remove the variation in

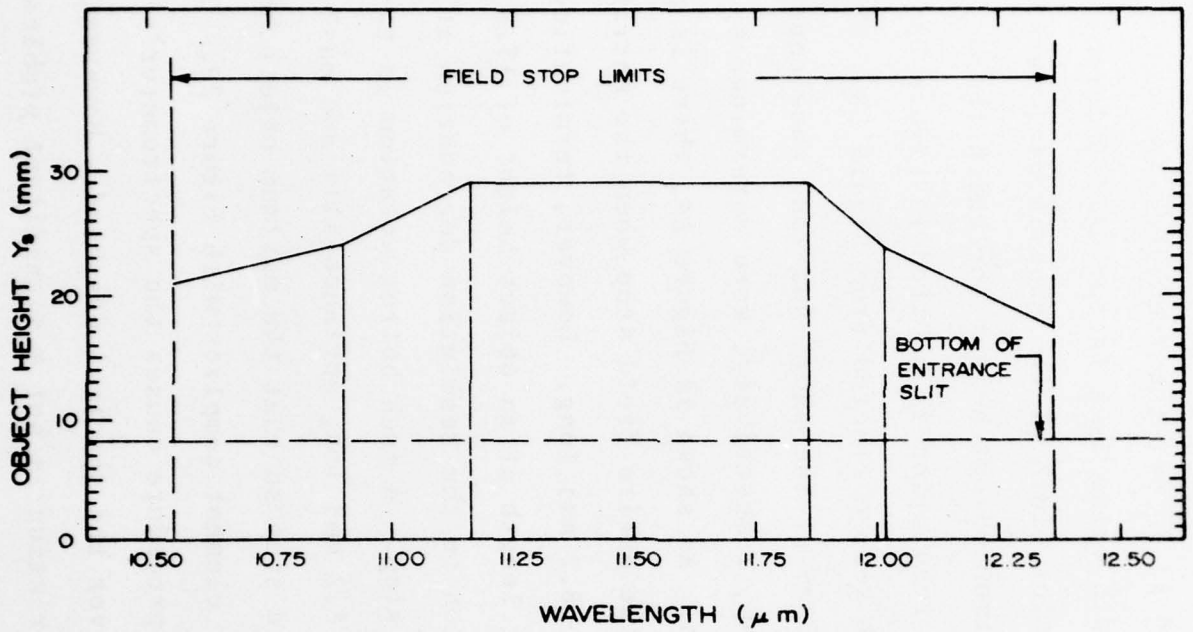


Figure 29. The maximum object height for which there is no significant deterioration in the resolution of the representative Hadamard spectrometer.

the magnitude of the recovered spectrum caused by these throughput variations. In fact, such a procedure is usually necessary in practice, whether or not this masking procedure is used, because the transmittance of the spectrometer as well as the detector response are not usually constant across the spectral passband.

The significant improvement in spectrometer performance resulting from using curved rather than straight slots can be seen by comparing Figure 29 and Table 9. For straight slots and an object height of 9 mm, the image width is 370 μm. Since this width is a factor of 1.9 larger than the 196-μm wide slot used, there is significant degradation in the resolution with straight slots even when the length of the entrance slit approaches zero. At an object height of 29 mm the image width for straight slots is a factor of 10.9 times larger than the slot width required for curved slots.

The first part of the performance analysis was done with a grating rotation angle of 31.757 degrees. In the second part of this analysis the grating rotation angle was varied. This part of the analysis revealed that the spectrometer's performance is approximately constant for grating rotation angles between 24.0 and 31.8 degrees. The optimal radius for the central spectral element was found to vary monotonically from 115.43 to 117.66 mm as the grating rotation angle varies from 25.14 to

31.76 degrees. This variation in the grating angle causes the wavelength of the central spectral element to vary from 9.3 to 11.5 μm. Thus, for a 21 percent change in the wavelength of the central spectral element, the change in the optimal slot radius is only two percent.

It was desired to test the experimental prototype using the 18-th and 19-th orders of the Mercury 0.5461-μm line. Therefore, the required slot width for the object heights 14, 19, 24, and 29 mm were computed at the grating angles tabulated in Table 11. The resulting slot widths are plotted in Figure 30. The spectral element numbers run from 1 to 511, where spectral element number 1 is at the short wavelength end of the field stop. A comparison of Figures 28 and 30 reveals that the spectrometer performance is approximately constant for grating angles between 24.0 and 31.8 degrees.

Table 11. The grating angles and wavelengths used to compute the data plotted in Figure 30.

Spectral element number	Grating rotation angle (degrees)	First-order wavelength (μm)	Order of Mercury 0.5461 line equivalent to first-order wavelength
5	31.2	10.376	19
50	30.7	10.376	19
128	29.8	10.376	19
255	26.8	9.830	18
333	25.9	9.830	18
387	25.3	9.830	18
459	24.5	9.830	18
503	24.0	9.830	18

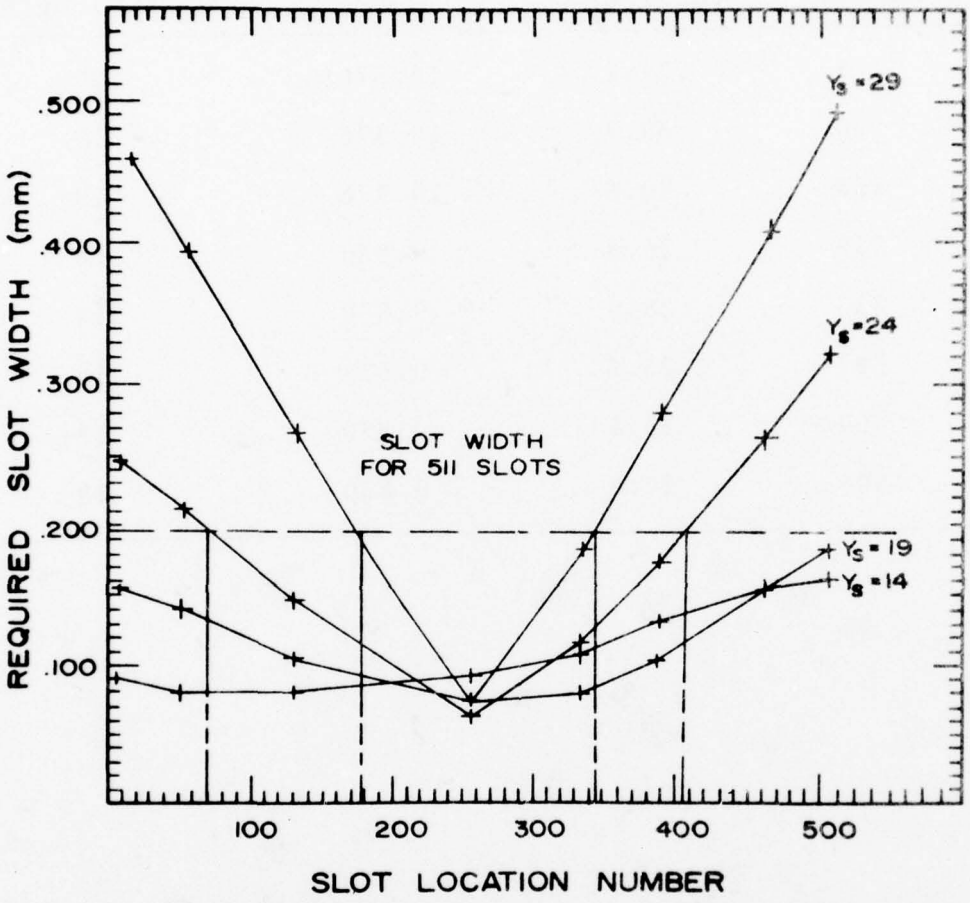


Figure 30. The slot width required for the grating angles tabulated in Table 11.

EXPERIMENTAL VERIFICATION

Experimental Prototype Hadamard Spectrometer

The Minuteman Hadamard spectrometer Model 305-HS, whose design was analyzed in the previous chapter, was used for the experimental verification.

Masks

A mask with straight slots and a mask with a slot radius of 117.6 mm were fabricated. The curved slot mask is shown in Figure 31. For both masks the slot width was 197 μm and the slot length was 20 mm. The mask pattern was generated on the computer using the algorithm described in Appendix C, where the mask pattern is tabulated in Table C-2. The masks were of the $2N$-1 type described in Appendix A, where N was 511. In addition to the slots used to encode the spectral elements, each mask had 511 slots with a width of 100 μm and a spacing of 197 μm. These slots were used to generate a reference signal that was used to monitor the mask position.

Entrance slits

A straight entrance slit and a curved entrance slit were fabricated. The width of the entrance slits was selected to compensate for the magnification of the

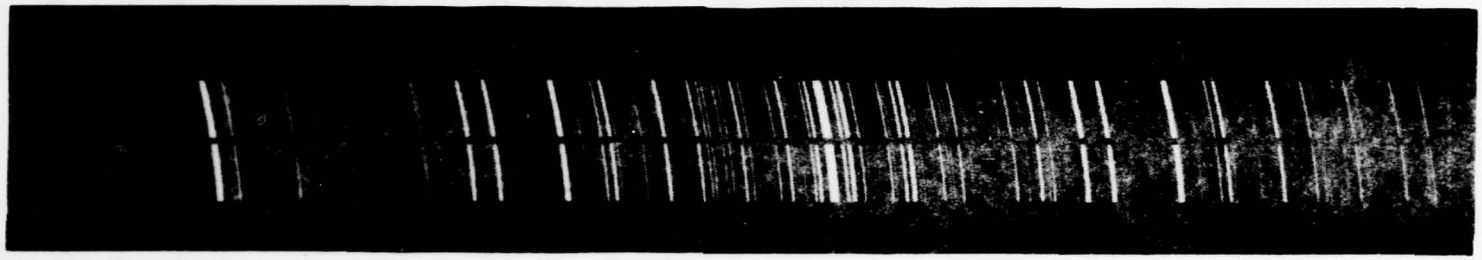


Figure 31. The curved slot Hadamard mask.

spectrometer. It can be shown by making use of the grating equation and the formula for the meridional focal length of a spherical mirror that the lateral magnification of a Czerny-Turner optical system is given by

$$M = \frac{R_2 \cos b \cos \alpha}{R_1 \cos a \cos \beta} \quad . \tag{82}$$

A lateral magnification of 1.15 was computed by substituting the parameter values tabulated in Tables 1 and 2 in Equation (82). This 1.15 value was corroborated with ray-tracing data. The entrance slits were fabricated with an entrance slit width of 197 ÷ 1.15 = 171 μm.

Detectors

Two detectors were used. An EG&G HAV 400 silicon photodiode was used for the visible radiation, and an A.D. Little HgCdTe detector was used for the infrared radiation. The HgCdTe detector was optically immersed giving an apparent detector size of 4 mm square. The HgCdTe detector was mounted in a liquid nitrogen dewar. A bandpass filter was used for the dewar window. This bandpass filter prevented diffraction orders higher than unity from reaching the detector. The relative response of this detector filter combination is shown in Figure 32. The average D^* over the wavelength interval from 8.1 to 13.1 μm was 1.2×10^{10} cm $Hz^{1/2}$ W^{-1}. The corner frequency for the HgCdTe detector was 3 kHz. Therefore, a chopping wheel that chopped the

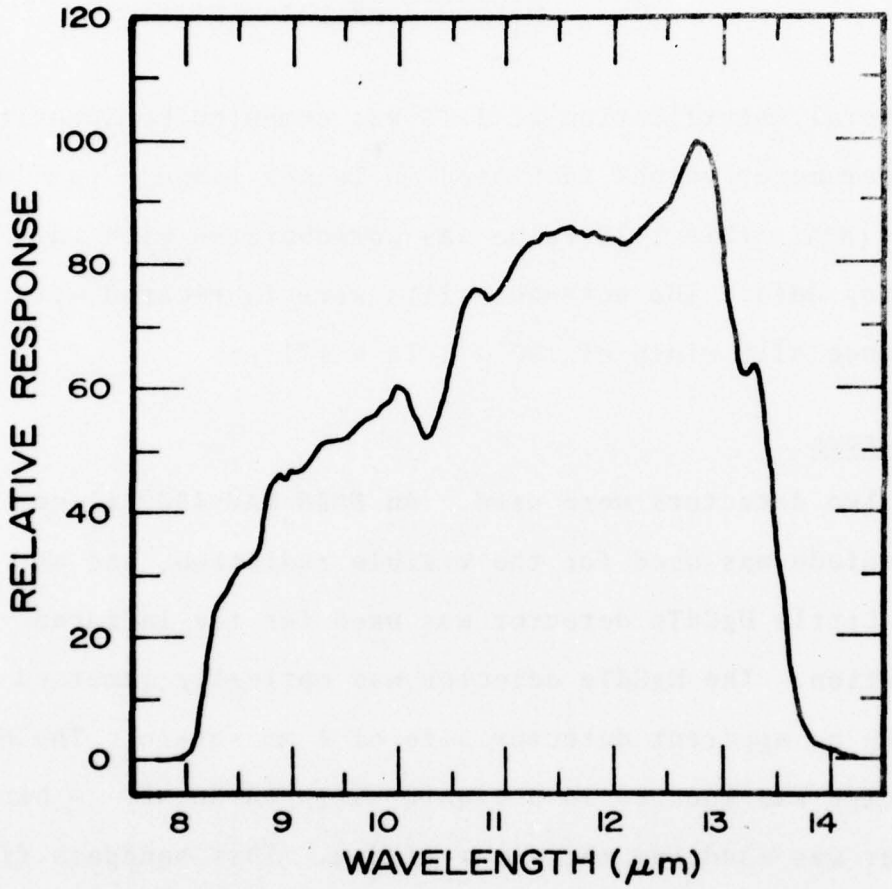


Figure 32. The relative response of the HgCdTe detector and order-sorting filter combination.

incoming radiation at a frequency of 4.8 kHz was installed in front of the entrance slit. Synchronous demodulation was used to recover the detector signal. The chopper was not used for the visible wavelength measurements The 120 Hz modulation of the arc lamp was used to provide the needed modulation for the synchronous detection technique.

The signal-to-noise ratio

As shown in Appendix A, the signal-to-noise ratio of a Hadamard spectrometer is a factor $\sqrt{N}/2$ larger than a monochromator. Therefore, the signal-to-noise ratio of the Hadamard spectrometer with the HgCdTe detector is

$$SNR = \frac{c\,\varepsilon\,A\Omega\,\Delta\lambda\,L_\lambda\,D^*}{(A_d\,\Delta f)^{1/2}} \cdot \frac{\sqrt{511}}{2} \quad , \tag{83}$$

where c is the chopping factor (0.44), ε is the transmittance coefficient (0.58), $A\Omega$ is the throughput (4.8×10^{-4} cm^2 sr), $\Delta\lambda$ is the spectral resolution (3×10^{-3} μm), L_λ is the spectral radiance in W sr^{-1} cm^{-2} μm^{-1}, D^* is 1.2×10^{10} cm Hz$^{1/2}$ W^{-1}, Δf is the electronic bandwidth in Hz, and A_d is the apparent area of the detector (0.16 cm^2).

Data reduction

The data reduction was accomplished with a Digital Equipment Corporation PDP-8/E computer. A Fast Hadamard transform program, which implemented the algorithm described in Appendix D, was written to recover the spectrum from the

encoded measurements. The basic programs used to recover the spectrum, HSPEC, PI, FHT, and PRMPL, are listed in Appendix H. Programs were also written to co-add spectra, to remove the spectral response curve of the spectrometer from the spectrum, and to plot the spectra. A program was written to make the computer-plotter combination function in a manner similar to that of a triggered oscilloscope. This program was used to make the direct-mode measurements which isolated the effects of optical aberrations from effects due to other causes.

Experimental Comparison between the Performance of Curved and Straight Slots

In order to obtain the data for an experimental comparison between the performance of curved and straight slots, the same measurements were made both with curved slots and with straight slots. These measurements indicate that for the experimental prototype the throughput can be approximately a factor of ten larger when curved rather than straight slots are used.

Measurement procedure

Two basic measurement modes were used to experimentally establish the superiority of curved slots over straight slots. The first mode, which is referred to as the direct mode, ascertains directly the extent to which optical aberrations limit performance. For the direct mode, all

departures from the ideal measurement are due to imaging errors. For the second mode, which is referred to as the transform mode, all sources of error cause departures from the ideal measurement. The relative performance between curved and straight slots was ascertained by using both of these measurement modes.

In both the direct and transform measurement modes the emission spectra of line sources were measured, and the resolution obtained using curved slots was compared with that obtained using straight slots. These line sources were mercury and sodium arc lamps. The 18th and 19th orders of the mercury 0.5461-μm line and the 17th order of the sodium doublet at 0.5890 and 0.5896 μm were used. These lines were isolated by inserting suitable optical bandpass filters in the optical train. The 18th and 19th orders of this mercury line provided the equivalent of first-order lines at 9.830 and 10.376 μm, respectively. The 17th order of the sodium line provided the equivalent of a doublet at 10.013 and 10.023 μm. The 10 nm separation of these two lines was useful in demonstrating the resolving power of the prototype.

Inasmuch as the optical surfaces were fabricated for operation with radiation in the 10 μm-range, these surfaces may be rough at the visible wavelengths of the mercury and sodium line sources. Any scattering which resulted from rough optical surfaces could only decrease the measured

resolving power of the prototype. Consequently, the resolution measured with these line sources is a worst-case limit. However, scattering did not appear to significantly affect the resolution for these line sources.

The resolution at a particular spectral element was measured by rotating the grating to locate one of these spectral lines at the desired spectral element. The required grating position was determined by using the following procedure. First, the 550-th mask slot was accurately positioned at the desired spectral element by using the reference signal. Then the grating was rotated until the spectral line passed through slot number 550. The reasons for using slot number 550 are given in the following discussion of the direct measurement mode. The procedure for positioning slot number 550 at a particular spectral element was partially automated by writing a computer program to monitor the reference signal and indicate when the mask was at the required location.

The relationship between the length of the entrance slit and the resolution of the prototype was ascertained by blocking a portion of the entrance slit with black paper so that the effective entrance slit was the desired length. The line spectra were measured with entrance slit lengths of 5, 10, 15, and 20 mm. Because the bottom of the usable entrance slit was 9 mm above the optical axis, these slit lengths were achieved by locating the bottom of the black paper 14, 19, 24 and 29 mm above the optical axis. These

are the same slit length values that were used in the ray-trace analysis of the prototype.

A single element lens was used to image the arc discharge onto the entrance slit. This lens was selected and positioned so that the entire entrance slit was illuminated and the entire area of spherical mirror 1 was filled with light. This imaging arrangement ensured that the optical throughput was determined by the unblocked portion of the entrance slit and the grating.

The direct-measurement mode. In the direct-measurement mode the spectrum was measured directly; that is, no Hadamard transform was required. For this mode all the mask slots except one were covered with black paper. The one open slot was translated across the focal plane as the detector signal was measured. When the prototype was operated in this mode, it had no multiplex advantage. However, this measurement mode allowed a more accurate measurement of slot shape effects than could be made with transform mode measurements.

The mask slot to be left open for the direct measurement mode was selected using two criteria. First, the selected slot had to have two or more opaque slots on either side. This criterion guaranteed that the edges of the open slot were determined by the accurately constructed mask and not by the blocking paper. The two or more opaque slots on either side of the open slot also made it easier to install the blocking paper without damage to the mask. Second, the

selected slot had to be as near to slot number 511 as possible. This criterion maximized the number of spectral elements for which the resolution could be measured. Of the 1021 slot locations, slot number 550 was selected. As can be seen from an examination of Table C-2 of Appendix C, this slot has two opaque slots on one side and five opaque slots on the other side.

Selection of slot number 550 as the open slot limited direct-mode measurements to spectral elements numbered 40 through 511. This limitation is due to the fact that the mask location could be accurately determined from the signal from the reference detector only when slot number 550 is near spectral elements 40 through 511. Due to the mask construction when slot number 550 is located at spectral number 511, the reference slot number 40 is aligned with the reference stop. Conversely, when slot number 550 is at spectral element number 40, the reference slot, slot number 511 is aligned with the reference stop.

After the grating was adjusted to locate a spectral line in the desired spectral element and the entrance slit was masked to the desired length, the spectrum was measured by slowly translating the mask while recording both the signal detector and the reference detector. Only a small portion of the spectrum in the vicinity of the line or doublet was measured. The computer was used to record and plot the spectrum. A computer program was written which enabled the computer to function in a manner similar to that

of a triggered oscilloscope. As the mask was translated at a constant speed by means of a d.c. motor, the voltages from the signal detector and reference detector electronics were sampled at a constant rate. The data were stored so that new data replaced old data until the voltage from the signal electronics exceeded a trigger level. Then samples were saved until the sum of the samples after triggering plus a predetermined number of samples taken before triggering equaled 200. By computing the period of the reference waveform, the program ascertained the number of samples per slot width of mask motion. The spectrum, the data from the signal electronics, was then plotted as a function of mask position.

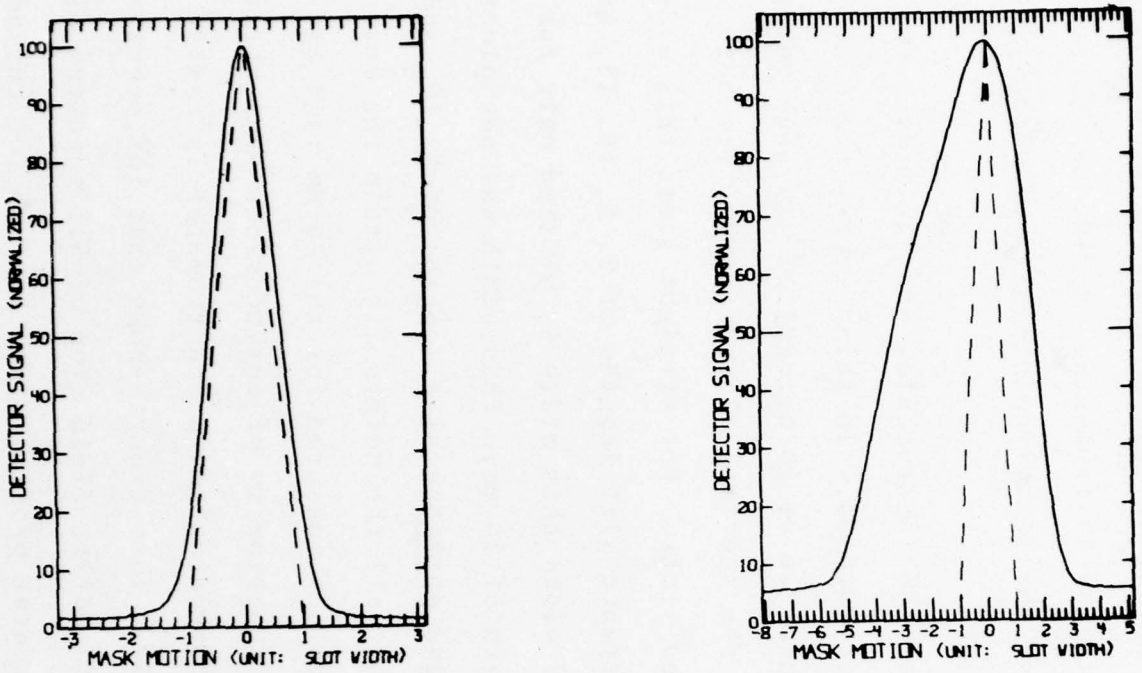
The transform-measurement mode. The transform-measurement mode consisted of operating the prototype as a Hadamard spectrometer. The black paper used in the direct-measurement mode to block all slots but number 550 was removed. This measurement mode had the disadvantage that only one value per spectral element was recovered. This disadvantage was ameliorated by interpolating between these values by using the fast Fourier transform as described by *Gold* and *Rader* [1969]. The spectra of the line sources were measured with both curved and straight slots. The transform-measurement mode eliminated all simulation and removed all need to extrapolate results. A comparison of the spectra measured with the transform-measurement mode demonstrates the improvement that can be made in a state-

of-the-art Hadamard spectrometer by using curved rather than straight slots.

Direct-mode measurements

The instrument profile. The instrumental profile is defined [*James* and *Sternberg*, 1969] as the measured spectrum of a single emission line. The instrumental profile of the prototype when operated in the direct-measurement mode was ascertained by measuring the spectrum of the mercury 0.5461-μm line in the 18th and 19th orders. The instrumental profile was measured at spectral element numbers 50, 128, 255, 383, and 500. At each of these spectral element numbers the instrumental profile for both straight and curved slots was measured with entrance slit lengths of 2, 5, 10, 15, and 20 mm for straight slots and 5, 10, 15, and 20 mm for curved slots.

A typical instrumental profile measurement for each of the two slot shapes is given in Figure 33. This figure gives the measurement instrumental profile at spectral element number 500 with an entrance slit length of 20 mm. It is noted that the two plots in Figure 33 have different abscissa scales. The abscissa is normalized to the width of the exit slot, 197 μm. If the image of the entrance slit perfectly matched the exit slot, the instrumental profile would be the dotted trinagle shown in both plots of Figure 33. As can be seen from this figure, the width of the instrumental profile is approximately five times



(a) curved slots

(b) straight slots

Figure 33. The instrumental profile at spectral element number 500 with an entrance slit length of 20 mm.

greater for straight than it is for curved slots at spectral element number 500 with an entrance slit 20-mm long. Also, the instrumental profile is essentially symmetrical for curved slots, but it is very asymmetrical for straight slots. An asymmetrical instrumental profile can cause errors in measuring the relative intensity of closely spaced spectral lines.

The results of the instrumental profile measurements are summarized in Figure 34. In this figure, the width of the instrumental profile at 50 percent of its peak value is plotted versus the spectral element number for both straight and curved slots. For straight slots this width is plotted for entrance slit lengths of 2, 5, 10, 15, and 20 mm. For curved slots this width is plotted only for an entrance slit length of 20 mm. This width was not plotted for curved slots and entrance slit lengths of 5, 10, and 15 mm because almost all the points lie within the error tolerance of the values measured for the 20-mm tall entrance slit. The superiority of curved slots over straight slots for the prototype Hadamard spectrometer is easily seen from Figure 34. This figure shows that for spectral elements across the entire field stop of 511 spectral elements, the instrumental profile width is less for curved slots with a 20-mm long entrance slit than it is for straight slots with a 2-mm long entrance slit. Thus, the resolution will be approximately the same for curved and straight slots if the entrance slit length is 20-mm long

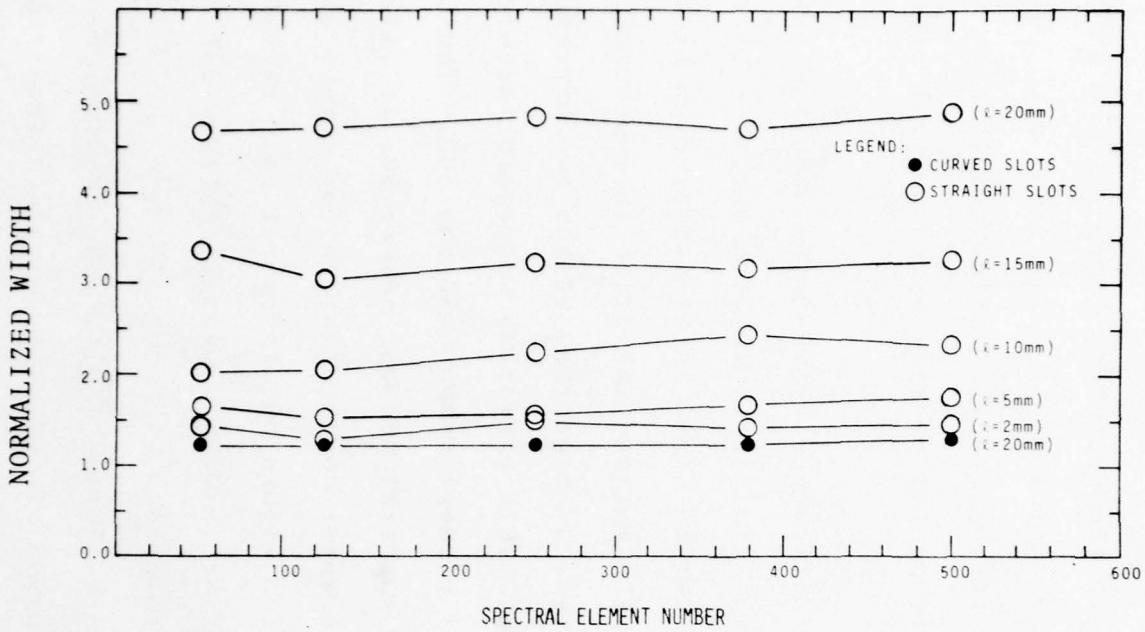


Figure 34. The width of the instrumental profile, normalized to 197 μm, at 50 percent of the peak value. The symbol ℓ represents the entrance slit length.

when curved slots are used and 2-mm long when straight slots are used. Inasmuch as throughput is directly proportional to slit length, the use of curved slots instead of straight slots with the prototype increases the throughput by approximately a factor of 10. Figure 34 also shows that for curved slots there is very little variation in the width of the instrumental profile with spectral element number.

The drastic difference between the amount of variation in the instrumental profile width with entrance slit length for straight and curved slots is illustrated in Figure 35. For curved slots the maximum variation in instrumental profile width occurred, as expected, at the two extreme ends of the field stop. This variation was approximately the same for spectral element numbers 50 and 500. Thus, since Figure 35 is for spectral element number 50, it illustrates approximately the worst-case variation for curved slots. As can be seen from Figure 35, the worst-case variation when curved slots are used was only slightly greater than the measurement tolerance.

A practical resolution limit. The resolution of the prototype with curved slots was ascertained from the instrumental profile measurements. When curved slots were used, there was very little variation in the instrumental profile for changes in the spectral element number. As shown in Figure 34, the width of the instrumental profile with curved slots was essentially constant for all spectral

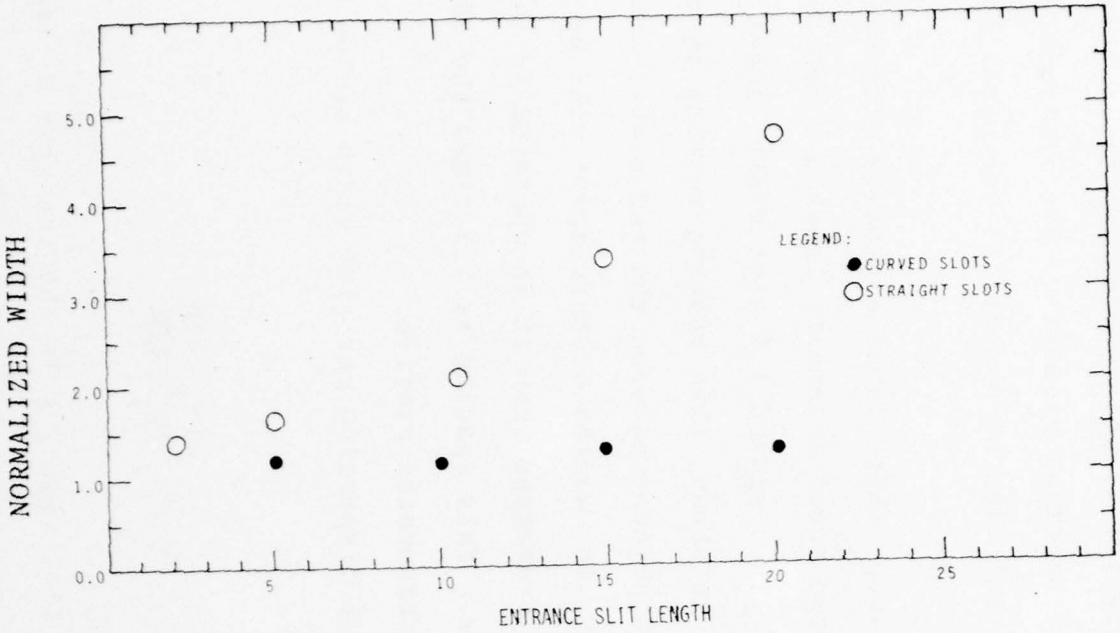


Figure 35. The width of the instrumental profile, normalized to 197 μm, at 50 percent of the peak value for spectral element number 50.

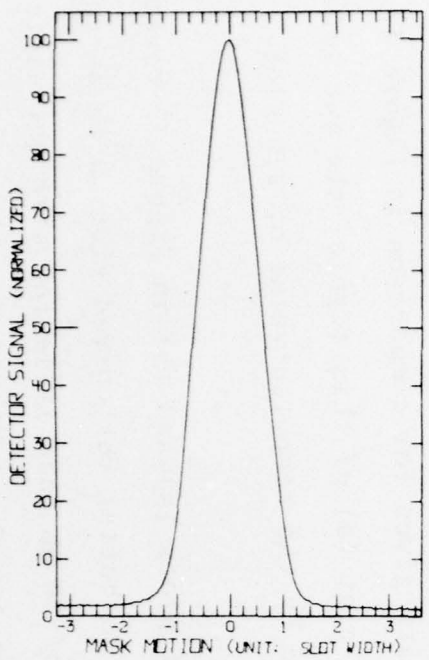
elements. This constant property of the instrumental profile can also be seen by comparing the instrumental profiles for spectral element numbers 500 and 255 shown in Figures 33 and 36, respectively. Thus, the resolution is essentially constant for all spectral elements. The instrumental profile at spectral element number 255 was used to compute the resolution.

In spectroscopy there is no exclusive criterion used to decide when two equal intensity lines are resolved. The spectrum of two lines spaced 1.5 slot widths apart is given in Figure 36. As shown, this spacing results in a dip of approximately 22 percent between the two peaks. Thus, lines spaced 1.5 slot widths or more apart will be clearly resolved by the prototype when it is operated in the direct-measurement mode. This spacing is 1.2 times the 50 percent width of the instrumental profile.

The spectral dispersion per slot width of the prototype is given by

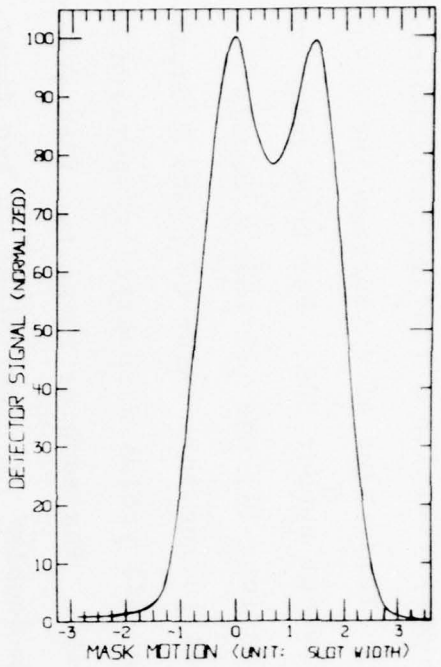
$$\delta\lambda = \frac{2d\, W_s \cos\beta}{k\, R_2 \cos b} \quad , \tag{84}$$

where W_s is the slot width, k is the integral diffraction order, and d, β, R_2, and b are as defined in Figure 4. It follows from this equation that for 197-μm wide mask slots the nominal spectral dispersion of the prototype is 3.5 nm per slot. Thus spectral lines with a wavelength difference



(a)

The curved-slot instrumental profile for spectral element number 255 with an entrance slit length of 20 mm.



(b)

The sum of two plots like the one in (a) with the plots shifted 1.5 slots relative to each other.

Figure 36. The resolution of two equal intensity lines spaced 1.5 slot widths apart.

of 1.5 x 3.5 = 5 nm are clearly resolved when the prototype is operated in the direct-measurement mode.

Resolution of the sodium doublet. The spectrum of the sodium doublet was measured with a grating rotation angle θ_G of 26.8 degrees. This value of θ_G located the 0.5890-μm line in spectral element number 303. For this value of θ_G, it follows from Equations (1) and (2) that β equals 37.3 degrees. Substituting this value of β and k equal to unity into Equation (84) yields a spectral dispersion of 3.8 nm per slot width. Inasmuch as these two 17th order lines of the sodium doublet are equivalent to two first-order lines separated by 10 nm, these two lines are theoretically spaced 2.6 slot widths apart. This spacing is 1.7 times larger than the practical resolution limit of 1.5 slot widths. Measurements of this doublet with both curved and straight slots are given for comparison in Figure 37. As can be seen from plot (a) of this figure, the two lines are indeed separated by the computed value of 2.6 slot widths.

A comparison of plots (a) and (b) in Figure 37 reveals that the resolution is better for curved slots with an entrance slit length of 20 mm than it is for straight slots with an entrance slit length of 2 mm. Thus, these plots confirm that the throughput of the prototype Hadamard spectrometer can be made a factor of ten larger when curved rather than straight slots are used.

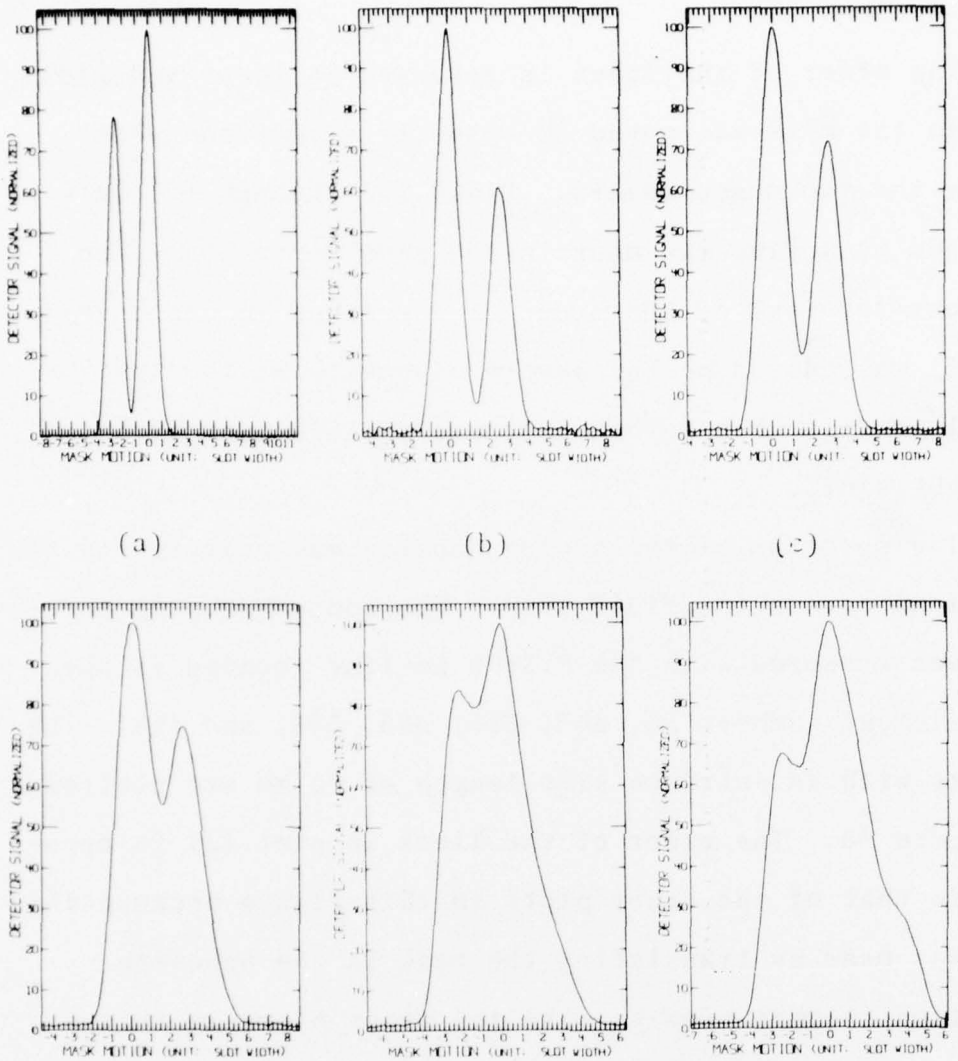


Figure 37. Direct-mode measurements of the sodium doublet with the stronger line at spectral element number 303 with the following conditions: (a) curved slots, ℓ = 20 mm, (b) straight slots, ℓ = 2 mm, (c) straight slots, ℓ = 5 mm, (d) straight slots, ℓ = 10 mm, (e) straight slots, ℓ = 15 mm, (f) straight slots, ℓ = 20 mm. The symbol ℓ is the entrance slit length.

The order of the lines is reversed in these two plots because the mask was moved in opposite directions when making the two measurements. Plots (b) through (f) were all made by moving the mask in the same direction. The apparent reversal of the order of the lines in plots (d) and (f) was caused by the severe asymmetry of the instrumental profile when a long entrance slit is used with straight slots.

The spectrum of the sodium doublet was measured at six locations across the field stop. The sodium doublet spectrum was measured with the 0.5890 μm-line located in spectral element numbers 56, 143, 255, 303, 383, and 496. The results with an entrance slit length of 20 mm are plotted in Figure 38. The order of the lines in plot (d) is opposite to that of the other plots in this figure because this plot was made by translating the mask in the opposite direction to that used to make the other plots in this figure. As can be seen from this figure, the resolution changes only slightly with spectral element number. As predicted by the theoretical computations, the resolution is worst at the two ends of the field stop.

In order to obtain the same resolution at the ends of the field stop as at the field stop center, the entrance slit length must be less than 20 mm. The required slit length for spectral element numbers 56 and 496 was ascertained from measurements of the spectrum of the sodium doublet. The height of the tallest line, h_{max}, and the

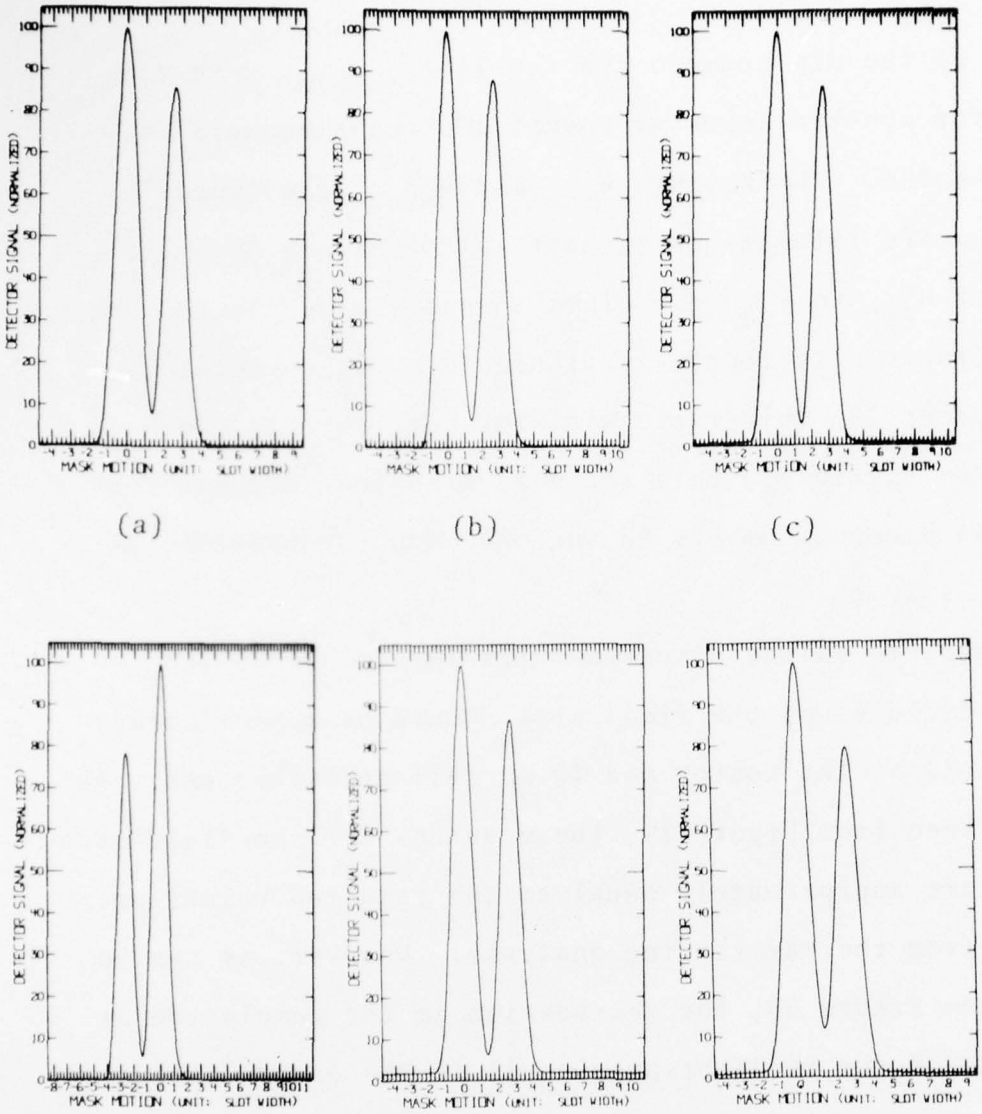
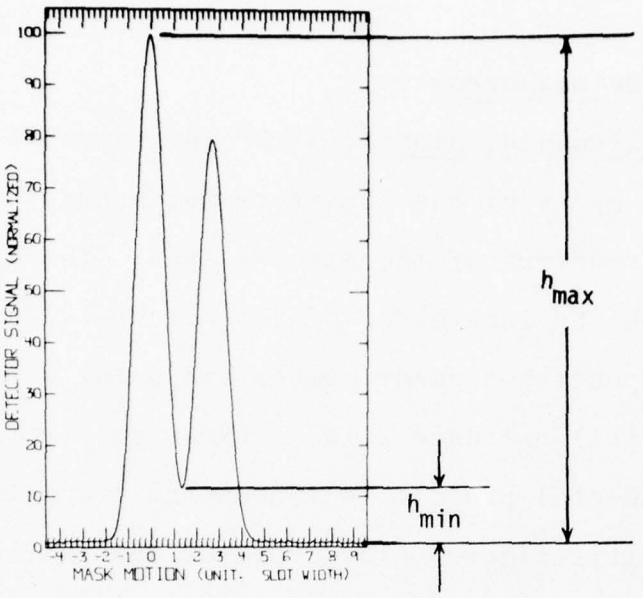


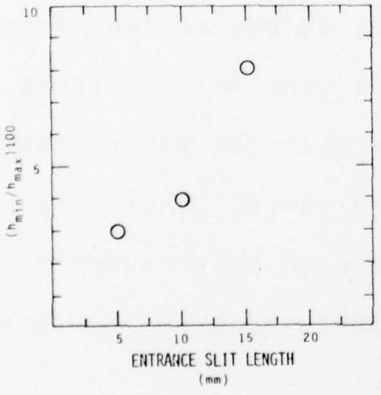
Figure 38. Direct mode measurements of the sodium doublet with an entrance slit length of 20 mm with the stronger line located in the following spectral element numbers: (a) 56, (b) 143, (c) 255, (d) 303, (e) 383, (f) 496.

height of the dip between the two lines, h_{min}, were measured for spectra taken at spectral element numbers 56, 255, and 496. The heights h_{max} and h_{min} for a typical spectrum are illustrated in part (a) of Figure 39. The ratio of h_{min} to h_{max} for slots 56 and 496 is plotted versus entrance slit length in Figure 39. For spectral element number 255 this ratio was four percent. As can be seen from Figure 39, this ratio is also four percent for spectral element numbers 56 and 496 when the entrance slit length is 10 mm.

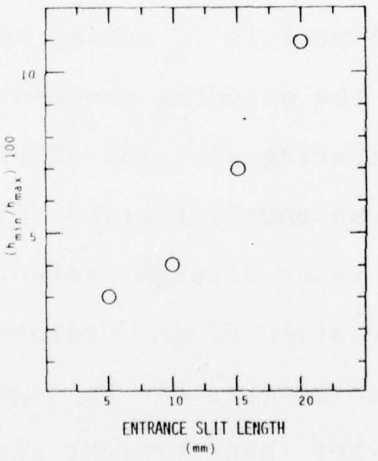
Thus, to maintain constant resolution across the entire field stop, the field stop should be approximately 20-mm tall at the center and 10-mm tall at either end. As can be seen from Figure 29, these values for the field stop height are approximately equal to the required values predicted from the ray-tracing analysis. However, as can be seen from Figure 38, the degradation in the resolution at the ends of the field stop is small if the entire field stop is 20-mm tall. For most measurement requirements, the small degradation in resolution caused by using this field stop instead of one 20-mm tall at the center and 10-mm tall at either end would be an acceptable penalty to gain the factor of two increase in throughput for spectral elements at either end of the field stop.



(a) Definition of h_{min} and h_{max}.



(b) Spectral element number 56.



(c) Spectral element number 496.

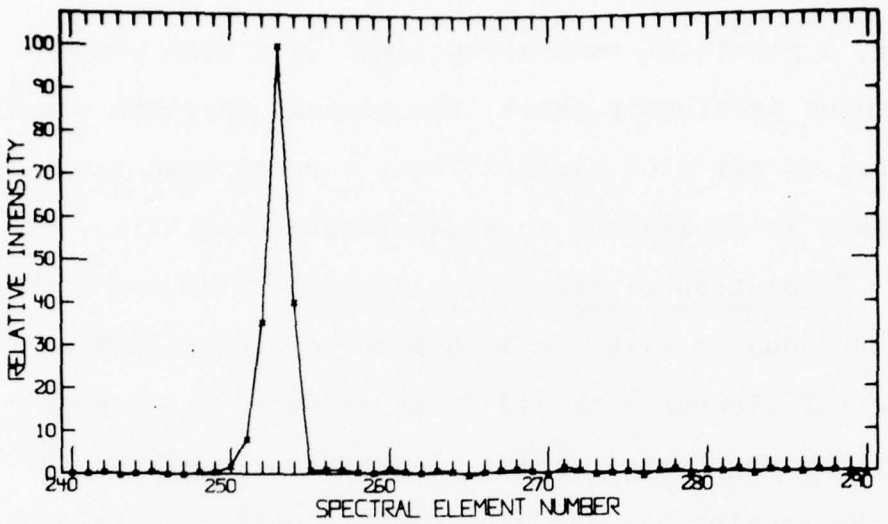
Figure 39. The normalized ratio of the dip height to the maximum spectrum height for the sodium doublet.

Transform-mode measurements

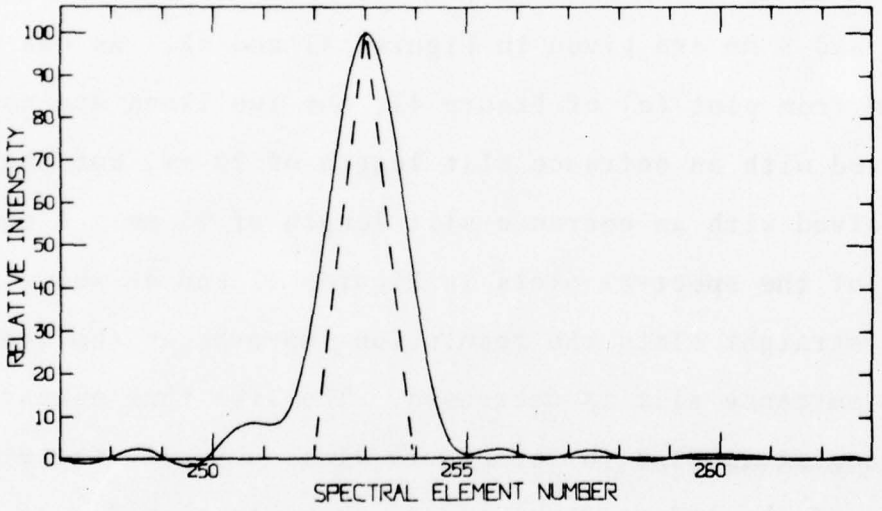
The instrumental profile. The instrumental profile was measured by using the transform-measurement mode to measure the spectrum of the mercury line. The spectrum measured with the 18th order of the mercury 0.5461-μm line located in spectral element number 253 using curved slots and a 20-mm tall entrance slit is shown in Figure 40. The ideal instrumental profile is the dotted triangle in plot (b) of this figure. The width of the instrumental profile at 50 percent of the peak is 1.7 slot widths. This width is 1.36 times larger than the corresponding width measured using the direct measurement mode.

The 36 percent increase in the width of the instrumental profile is caused by errors in practical implementation of the encoding procedure. However, as can be seen from comparing plot (b) of Figure 33 with plot (b) of Figure 40, these encoding errors are much less than the errors caused by using straight rather than curved slots. Therefore, the operation of the prototype when operated as a Hadamard spectrometer can be significantly improved by using curved rather than straight slots.

A practical resolution limit. As previously shown, spectral lines separated by 1.2 times the 50 percent width of the instrumental profile are clearly resolved in the direct-measurement mode. Therefore, a practical resolution limit for the prototype when operated as a Hadamard spectrometer is 1.2 times the 50 percent width of 1.7 slots.



(a) Measured values connected by straight line segments.



(b) Interpolated spectrum.

Figure 40. The spectrum of the 18th order of the mercury 0.5461-μm line measured by operating the prototype Hadamard spectrometer in the transform mode.

Thus, a practical resolution limit is 2 slot widths. As has been previously shown, the nominal spectral dispersion is 3.5 nm per slot width. Thus, a resolution limit of 2 slots is equivalent to a wavelength separation of 7 nm.

Resolution of the sodium doublet. The spectrum of the sodium doublet with the 17th order of the 0.5890-μm line in spectral element number 303 was measured using both straight and curved slots. As previously shown, the lines of the doublet are 2.7 slot widths apart and are equivalent to two first-order lines with a wavelength difference of 10 nm. Measurements of the sodium doublet spectrum taken with straight slots and entrance slit lengths of 20, 15, 10, and 5 mm are given in Figures 41 and 42. As can be seen from plot (a) of Figure 41, the two lines are not resolved with an entrance slit length of 20 mm, but they are resolved with an entrance slit length of 15 mm. A comparison of the spectral plots in Figures 41 and 42 shows that for straight slots the resolution improves as the length of the entrance slit is decreased. The line that appears strongest in plot (b) of Figure 41 is actually the weakest line of the sodium doublet. As shown in plot (e) of Figure 37, this same error was measured in the direct-measurement mode when the entrance slit was 15-mm long. This error is caused by the severe asymmetry of the instrumental profile for long straight slots.

The spectrum of the sodium doublet measured with curved slots and a 20-mm long entrance slit is plotted in

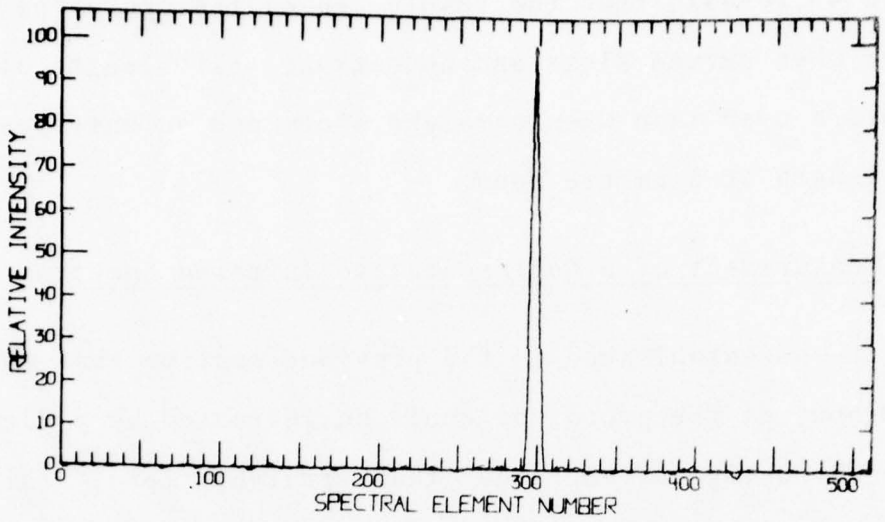
Figure 43. A comparison of plot (b) of Figure 42 with Figure 43 reveals that the resolution of the prototype is better when curved slots and an entrance slit length of 20 mm are used than when straight slots and an entrance slit length of 5 mm are used.

Measurement of a Representative Infrared Spectrum

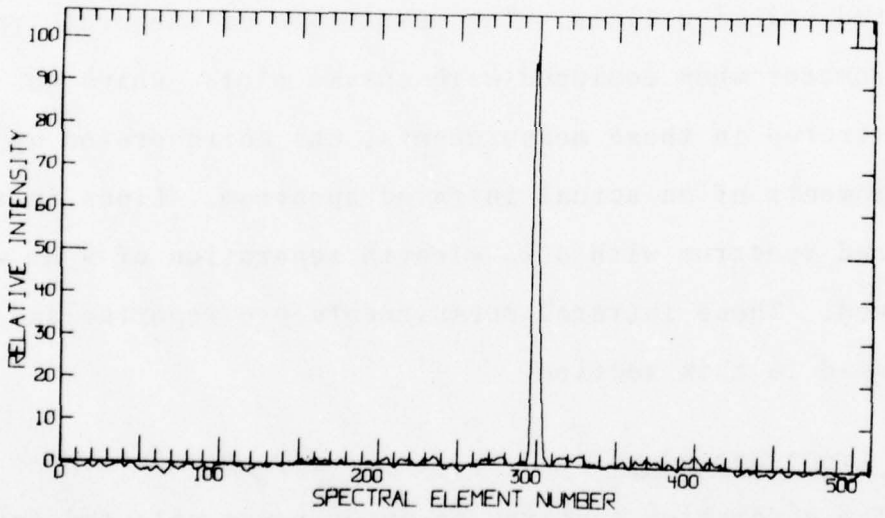
It was established in the previous section that the throughput of the prototype could be increased by a factor of ten by using curved rather than straight slots. This was established from measurements of the 17th, 18th, and 19th orders of visible emission lines, which simulated infrared emission lines. The resolution of the prototype spectrometer when equipped with curved slots, which was demonstrated in these measurements, was corroborated by measurements of an actual infrared spectrum. Lines in this infrared spectrum with a wavelength separation of 9 nm were resolved. These infrared measurements are reported and discussed in this section.

Measurement procedure

The absorption spectrum of ammonia was selected for measurement because it has several absorption lines in the 9 to 13-μm wavelength interval that are sufficiently close together to test the resolution of the prototype. The ammonia spectrum was measured by operating the prototype as a Hadamard spectrometer only; the direct-measurement

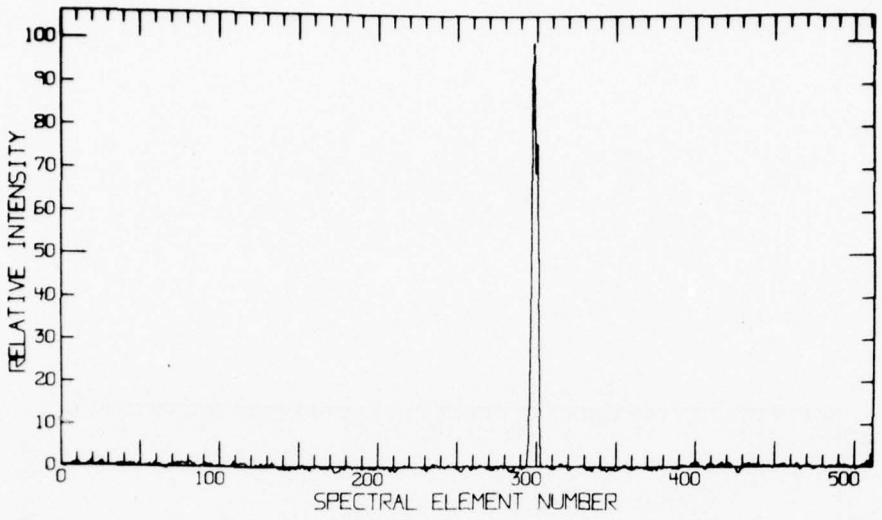


(a)

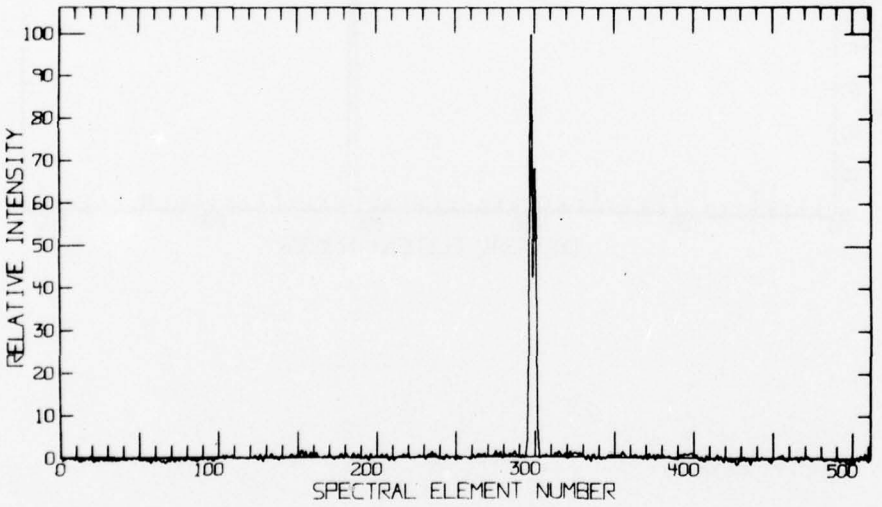


(b)

Figure 41. Transform-mode measurements of the sodium doublet made with straight slots and entrance slit lengths of (a) 20 mm and (b) 15 mm.



(a)



(b)

Figure 42. Transform-mode measurements of the sodium doublet made with straight slots and entrance slit lengths of (a) 10 mm and (b) 5 mm.

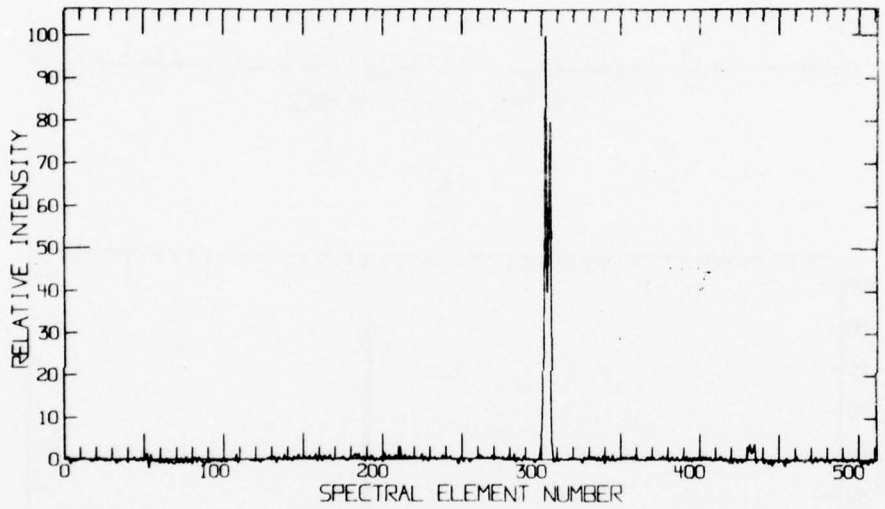


Figure 43. Transform-mode measurements of the sodium doublet with curved slots and a 20-mm long entrance slit.

mode was not used. The equipment configuration is shown in Figure 44. The control console for the prototype Hadamard spectrometer is shown in the foreground of Figure 44. An optical system consisting of two germanium lenses, a 10-cm long absorption cell, and a temperature-regulated blackbody was used to provide the infrared radiation for measurement by the prototype Hadamard spectrometer. The optical throughput of this optical system was greater than that of the prototype Hadamard spectrometer so that the throughput of the combination of this optical system with the prototype was determined by the prototype. The effective length of the entrance slit was 20 mm. The HgCdTe detector system described previously was used.

The ammonia gas was contained in the absorption cell at a pressure of one atmosphere. The concentration of ammonia was controlled by mixing it with argon. The concentration was adjusted by trial and error until the spectrum resembled the ammonia spectrum measured at a pressure of 50 mm of mercury given by the *International Union of Pure and Applied Chemistry* [1961].

The variation with wavelength of the blackbody radiation and of the spectrometer response was removed from the ammonia spectrum. This removal was accomplished by multiplying the measured ammonia spectrum by the reciprocal of the spectrum measured with the absorption cell filled with argon.

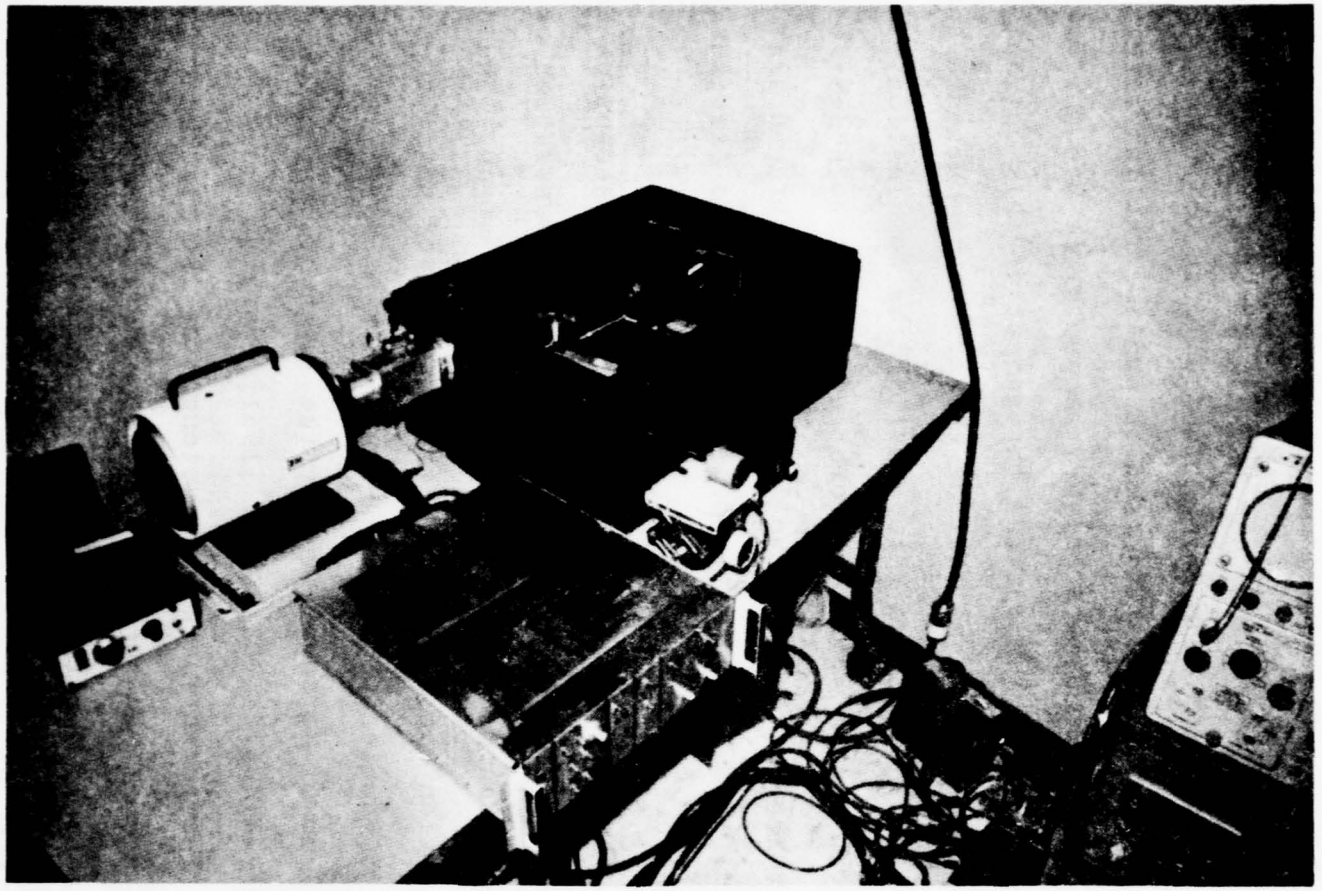


Figure 44. Equipment configuration used to measure absorption spectrum of ammonia.

The measured ammonia spectrum

The 8.8 to 12.3-μm wavelength region of the ammonia absorption spectrum was measured. The 8.8 to 10.7-μm interval was measured using one grating setting, and the 10.6 to 12.3-μm interval was measured using a second grating setting. The spectrum obtained in these two intervals using a 20-second observation time is plotted in Figures 45 and 46, respectively. The wavelengths of the absorption lines that are identified with numbers in these two figures were established by comparing these figures with the ammonia spectrum given by the *International Union of Pure and Applied Chemistry* [1961]. These wavelengths are tabulated in Table 12.

Coadding, the point-by-point addition of repeated measurements of the spectrum, was used to verify that the lines were not noise spikes. The spectrum resulting from nine coadditions of 20-second measurements of the 8.8 to 10.7-μm interval of the ammonia spectrum is given in Figure 47. Similarly, Figure 48 shows the results of ten coadditions for the 10.6 to 12.3-μm interval. As can be seen by comparing Figure 45 with 47, and Figure 46 with Figure 48, coadding does not produce a significant change in the appearance of the numbered lines. Thus, these lines are not random noise spikes.

The practical resolution of the prototype can be ascertained from Figures 45 through 48 and Table 12. Lines Lines 8 and 9, which are separated by 11 nm, are clearly

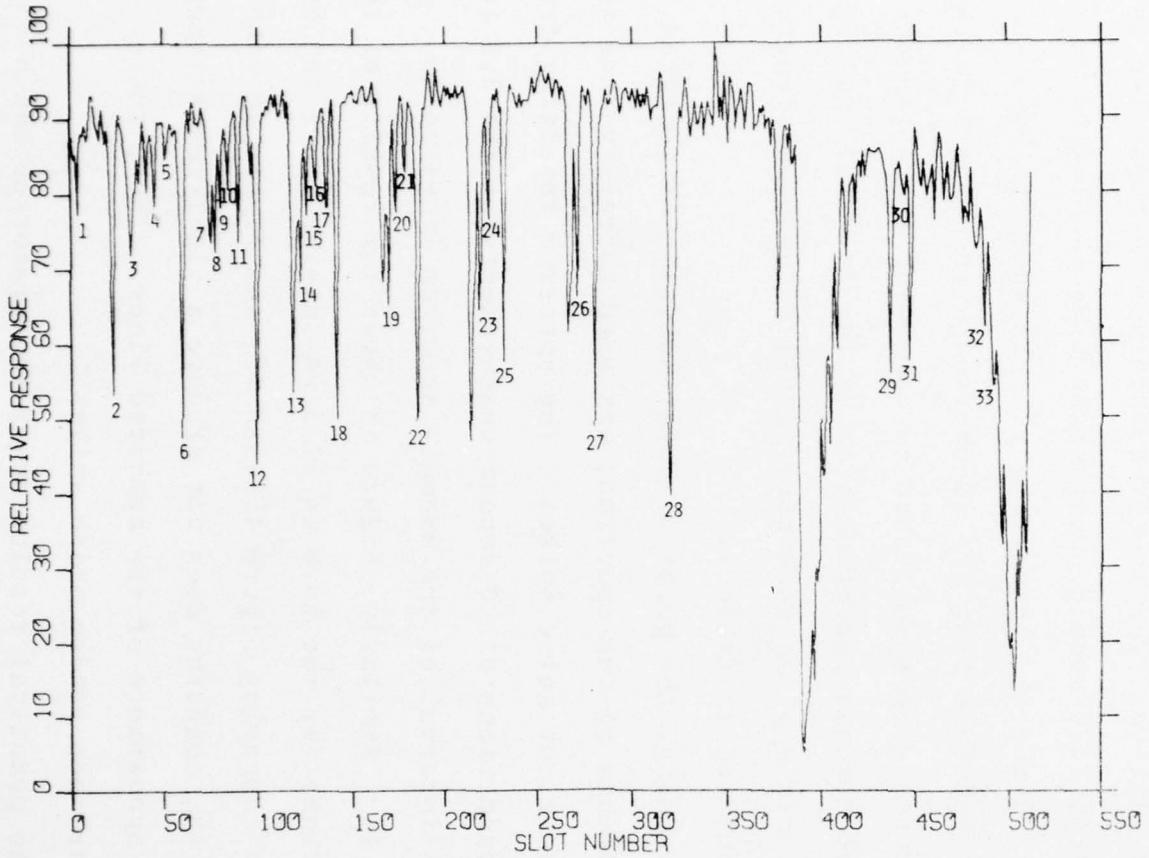


Figure 45. The absorption spectrum of ammonia at a pressure of one atmosphere and a temperature of 25 degrees Celsius measured over the 8.8 to 10.7-μm wavelength interval using the prototype spectrometer in the transform mode with an observation time of 20 seconds.

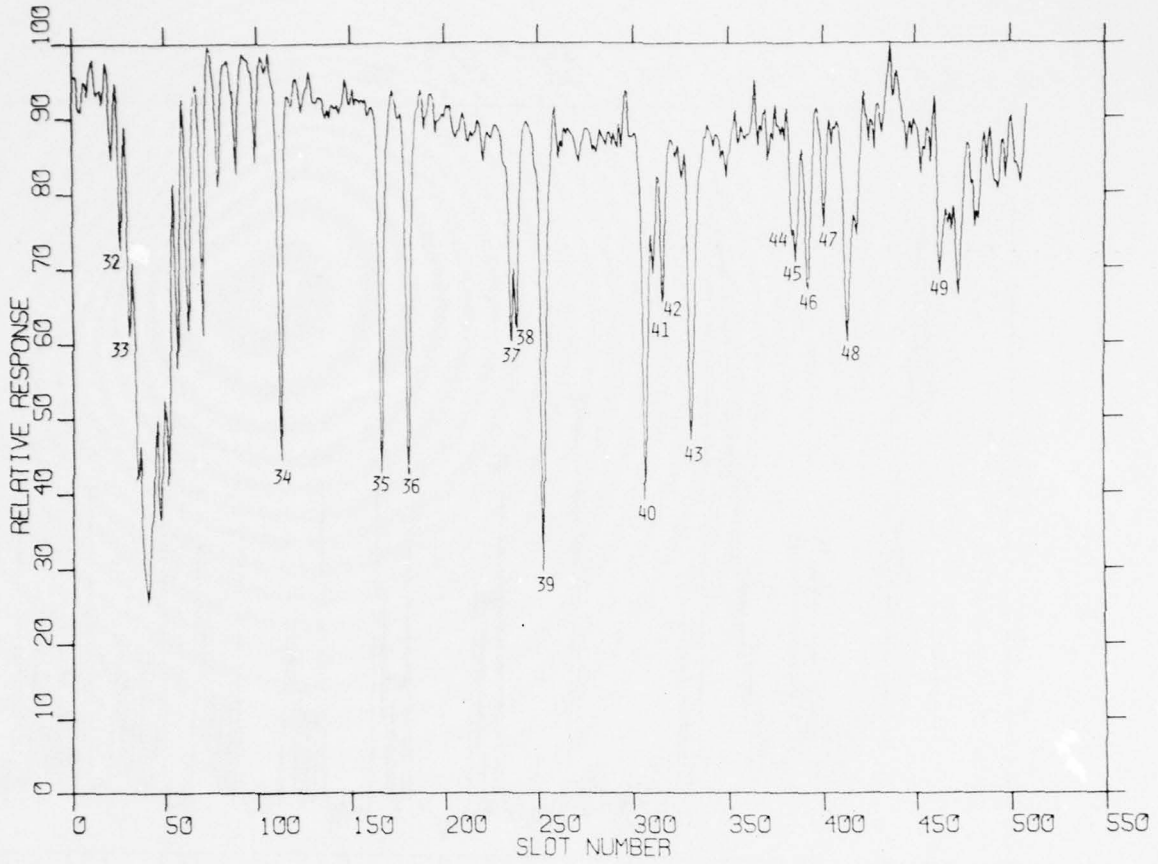


Figure 46. The absorption spectrum of ammonia at a pressure of one atmosphere and a temperature of 25 degrees Celsius measured over the 10.6 to 12.3-μm wavelength interval using the prototype spectrometer in the transform mode with an observation time of 20 seconds.

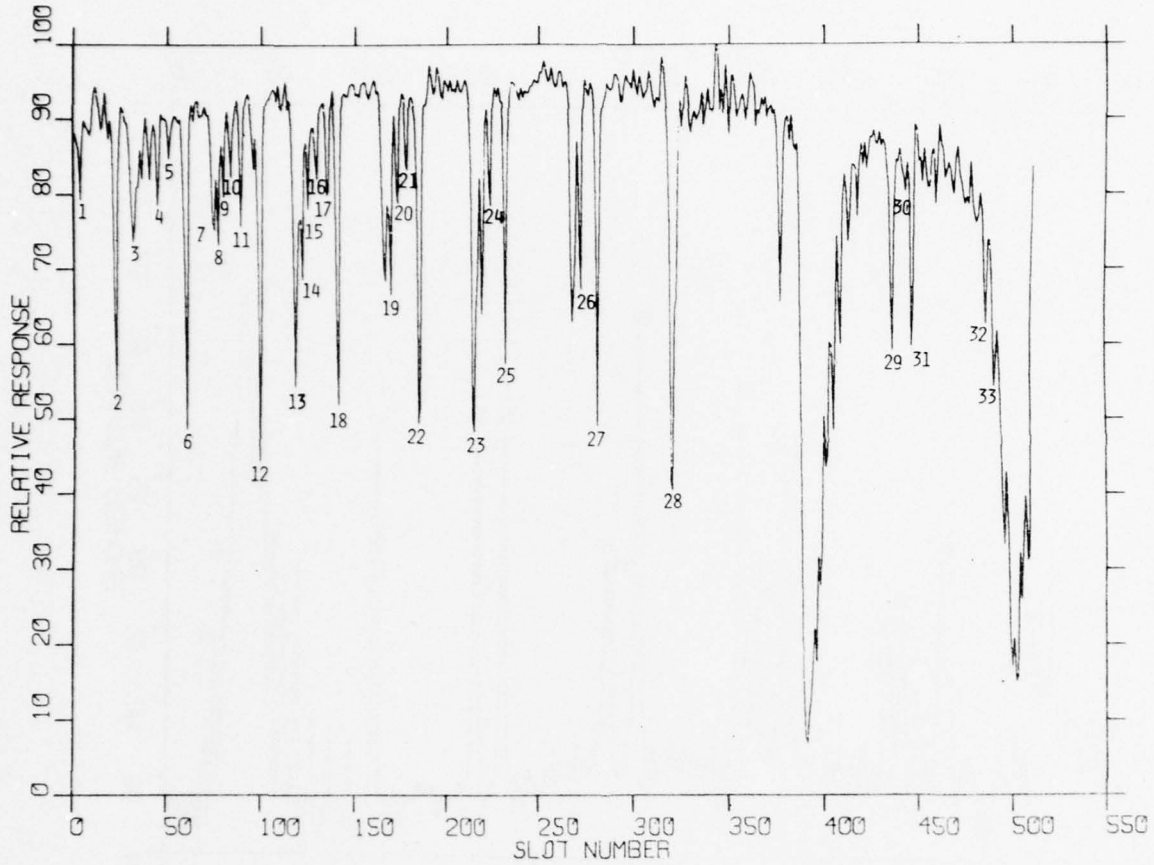


Figure 47. Results of coadding nine measurements of the 8.8 to 10.7-μm wavelength interval of the ammonia absorption spectrum.

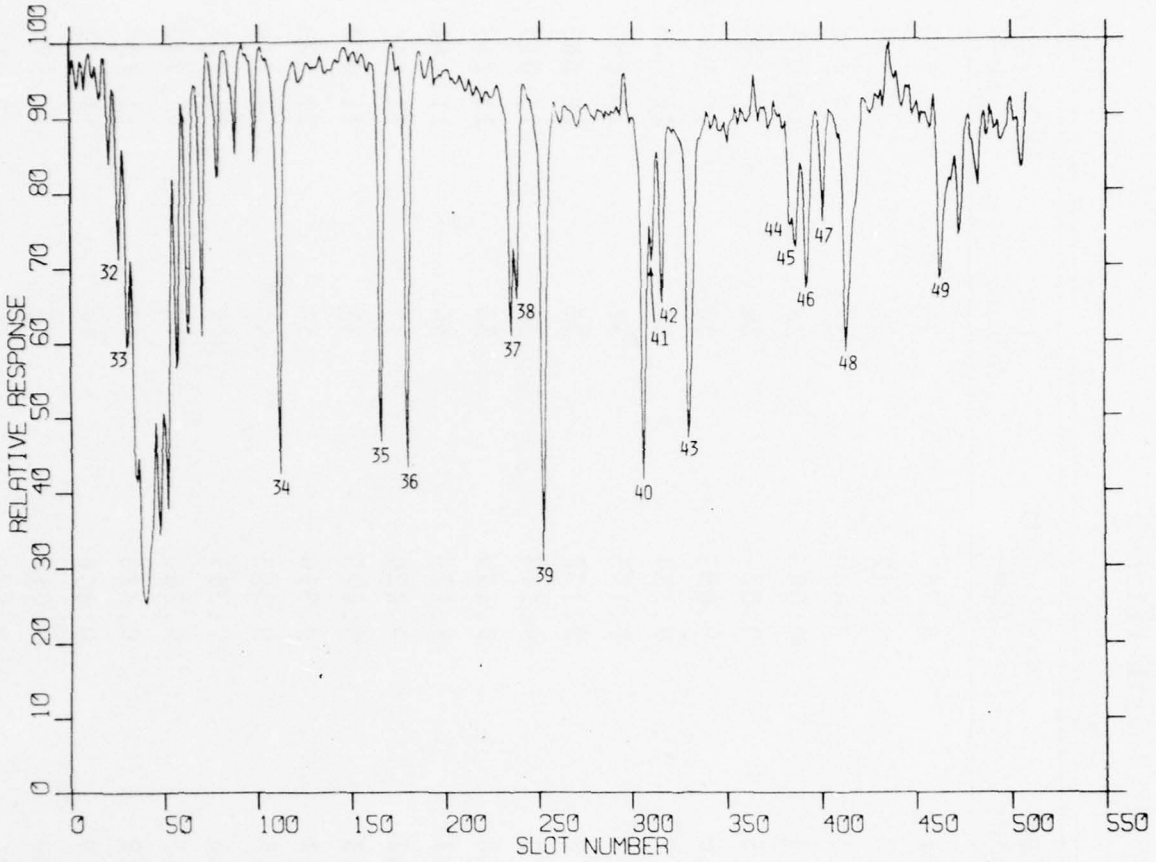


Figure 48. Results of coadding nine measurements of the 10.6 to 12.3-μm wavelength interval of the ammonia absorption spectrum.

Table 12. Wavelengths of absorption lines identified in Figures 45, 46, 47, and 48. These wavelength values were computed by converting the wavenumber values given by the *International Union of Pure and Applied Chemistry* [1961] to wavelength values.

Line number	Wavelength (μm)	Line number	Wavelength (μm)
1	8.767	25	9.737
2	9.912	26	9.889
3	8.949	27	9.926
4	9.003	28	10.075
5	9.027	29	10.506
6	9.063	30	10.534
7*	9.118	31	10.546
7*	9.123	32	10.666
8	9.132	33	10.685
9	9.143	34	11.011
10	9.159	35	11.211
11	9.179	36	11.261
12	9.220	37	11.460
13	9.295	38	11.472
14	9.310	39	11.523
15	9.323	40	11.714
16	9.341	41	11.727
17	9.363	42	11.747
18	9.385	43	11.797
19	9.496	44	11.979
20	9.510	45	11.990
21	9.530	46	12.011
22	9.557	47	12.038
23	9.689	48	12.082
24	9.705	49	12.247

*Line 7 is an unresolved equal intensity doublet.

resolved. Line 7 is an unresolved equal intensity doublet whose lines are separated by 5 nm. The spectral interval between line 8 and the nearest line of this doublet is 9 nm. Thus, the resolution of the prototype Hadamard spectrometer is better than 9 nm but worse than 5 nm. Lines 14 and 15 are separated by 13 nm. The spectral interval between lines 30 and 31 is 12 nm. Lines 40 and 41 have a wavelength separation of 13 nm. Judging from the manner in which the lines discussed in this paragraph are resolved, it can be concluded that the practical resolution of the prototype is better than 10 nm for all spectral elements. This conclusion agrees with the measurements made of the sodium doublet, which had an apparent separation in the 17th order of 10 nm.

CONCLUSIONS

The optical throughput of a Hadamard spectrometer can be significantly larger with optimally curved slots than with straight slots. For the representative Hadamard spectrometer analyzed in this investigation, the improvement was a factor of ten. This improvement results because the effects of astigmatism and spectrum line curvature can be minimized by using curved slots.

Ray-tracing methods are appropriate for optimizing the slot curvature for Hadamard spectrometers. The experimentally measured performance of the representative Hadamard spectrometer with both straight and curved slots was shown to agree with the performance predicted by analytic and ray-tracing procedures.

The resolution degradation caused by straight slots is much greater than the resolution degradation from other causes.

The Hadamard spectrometer can be used to make spectral measurements of practical value. The ammonia absorption spectrum was measured in the 9 to 13-μm wavelength interval using 20-mm tall slots.

When considering whether to use a Hadamard spectrometer to make a spectral measurement, the following

PRECEDING PAGE NOT FILMED
BLANK

characteristics of Hadamard spectrometers are appropriate for consideration:

(1) The Hadamard spectrometer is rugged.

(2) Mechanical tolerances can be on the order of 0.001 inches.

(3) Data-handling requirements do not increase as the resolution increases. The resolution of a Hadamard spectrometer can be increased by using a higher dispersion grating, but the data-handling requirements depend only on the number of spectral elements encoded.

(4) Specific spectral elements can be prevented from reaching the detector by using a suitable field stop. This characteristic can be helpful when it is necessary to measure weak lines located between strong lines.

(5) The dynamic-range requirement on the data electronics is small.

LITERATURE CITED

Ahmed, N., K. R. Rao, and A. L. Abdussattar. 1971. BIFORE or Hadamard Transform. *IEEE Transactions on Audio and Electroacoustics* 19:225-234.

Andrews, H. C. 1970. *Computer Techniques in Image Processing.* Academic Press, New York.

Baumert, L. D. 1964. Codes with Special Correlation. *Digital Communications with Space Applications* (S. W. Golomb, Ed.). Prentice-Hall, Inc., Englewood Cliffs, New Jersey. p. 47-64.

Beutler, H. G. 1945. The Theory of the Concave Grating. *JOSA* 35:311-350.

Born, Max and Emil Wolf. 1965. *Principles of Optics,* Third Edition. Pergamon Press, New York.

Bouchereine, P. and P. Connes. 1963. Interferometer with a Compensated Field for Spectroscopy by the Fourier Transform. *Le Journal de Physique Et Le Radium* 24:134.

Brigham, E. O. 1974. *The Fast Fourier Transform.* Prentice-Hall, Inc., Englewood Cliffs, New Jersey.

Cox, Arthur. 1964. *A System of Optical Design.* Focal Press, New York.

Decker, John A. Jr. 1970. Hadamard-Transform Multiplex Grating Spectrometer. *Aspen International Conference on Fourier Spectroscopy.* AFCRL-71-0019 Special Report 114:429-434.

Decker, J. A. Jr. 1971. Experimental Realization of the Multiplex Advantage with a Hadamard Transform Spectrometer. *Applied Optics* 10:510-514.

Decker, J. A. Jr. 1974. Comments on: Fourier Transform vs. Hadamard Transform Spectrometry. *Applied Optics* 13:1296-1297.

Decker, J. A. Jr. 1977. Hadamard Transform Spectroscopy. *Spectrometric Techniques I* (G. A. Vanasse, Ed.). Academic Press, New York. p. 189-227.

Decker, J. A. Jr. and M. O. Harwit. 1968. Sequential Encoding with Multislit Spectrometers. *Applied Optics* 7:2205-2209.

Despain, A. M. and G. A. Vanasse. 1972. Walsh Functions in Grille Spectroscopy. *Applications of Walsh Functions, 1972 Proceedings*. AD-744-650 p. 30-35.

Esplin, R., R. Shipley and R. Huppi. 1975. *Far Infrared Atmospheric Instrumentation and Measurements*. AFCRL-TR-75-0482.

Fastie, W. G. 1952a. A Small Plane Grating Monochromator. *JOSA* 42:641-647.

Fastie, W. G. 1952b. Image Forming Properties of the Ebert Monochromator. *JOSA* 42:647-651.

Fastie, W. G. 1953. Experimental Performance of Curved Slits. *JOSA* 43:1174-1175.

Fellgett, P. 1951. Ph.D. Thesis, Cambridge University.

Girard, A. 1960. Nouveauz dispositifs de spectroscopie à grande luminosité. *Optica Acta* 7:81-97.

Girard, A. 1963. Spectromètre à Grilles. *Applied Optics* 2:79-87.

Golay, M. 1949. Multi-Slit Spectrometry. *JOSA* 39:437-444.

Golay, M. 1951. Static Multislit Spectrometer and Its Application to the Panoramic Display of Infrared Spectra, *JOSA* 41:468-472.

Gold, Bernard and C. M. Radar. 1969. *Digital Processing of Signals*. McGraw-Hill Publishing Company, New York.

Golomb, S. W. 1967. *Shift Register Sequences*. Holden-Day, Inc., San Francisco, California.

Gottlieb, P. 1968. A Television Scanning Scheme for a Detector-Noise-Limited System. *IEEE Transactions on Information Theory* 14:428-433.

Graauw, Th. de and B. P. Th. Veltman. 1970. Pseudo-Random Binary Sequences for Multiplex Codes. *Applied Optics* 9:2658-2660.

Hadamard, M. J. 1893. Resolution d'une question relative aux determinants. *Bull. Sci. Math.* A17:240-246.

Hansen, P. and J. Strong. 1972. High Resolution Hadamard Transform Spectrometer. *Applied Optics* 11:502-506.

Harmuth, H. 1972. *Transmission of Information by Orthogonal Functions*, Second Edition. Springer-Verlag, New York.

Harwit, M. 1971. Spectrometric Imager. *Applied Optics* 10:1415-1421.

Harwit, M. 1973. Spectrometric Imager, Part 2. *Applied Optics* 12:285-288.

Harwit, M., P. G. Phillips, T. Fine and N. J. A. Sloane. 1970. Doubly Multiplexed Dispersive Spectrometers. *Applied Optics* 9:1149-1154.

Harwit, M., P. Phillips, L. King and D. Briotta, Jr. 1974. Two Asymmetric Hadamard Transform Spectrometers. *Applied Optics* 13:2669-2674.

Hirschfeld, T. and G. Wyntjes. 1973. Fourier Transform vs. Hadamard Transform Spectroscopy. *Applied Optics* 12:2876-2880.

Hirschfeld, T. and G. Wyntjes. 1974. Fourier Transform vs. Hadamard Transform Spectroscopy: Authors' Reply to Comments. *Applied Optics* 13:1740-1741.

Ibbett, R. N., D. Aspinall and J. F. Grainger. 1968. Real-time Multiplexing of Dispersed Spectra in Any Wavelength Region. *Applied Optics* 7:1089-1093.

International Union of Pure and Applied Chemistry. 1961. *Tables of Wavenumbers for the Calibration of Infra-Red Spectrometers*. Butterworths, Washington.

James, J. F. and R. S. Sternberg. 1969. *The Design of Optical Spectrometers*. Chapman & Hall, Ltd., London.

Jenkins, F. A. and H. E. White. 1957. *Fundamentals of Optics*, Third Edition. McGraw-Hill Publishing Company, New York.

Kudo, L. 1960. Plane Grating Monochromators of Ebert, Pfund and Czerny-Turner Types. *Science of Light* 9:1-30.

Larson, L. 1976. An Algorithm to Compute the Sequency Ordered Walsh Transform. *IEEE Transactions on Acoustics, Speech, and Signal Processing*. 24:335-336.

Laws, D. A. 1962. Primary Distortion of an Extended Image by a Plane Grating. *Opt. Acta*. 9:69-71.

Lindblom, P. 1972. Theory of the Two-Mirror Plane-Grating Spectrograph. *JOSA* 62:756-762.

Manz, J. W. 1972. A Sequency Ordered Fast Walsh Transform. *IEEE Transactions on Audio and Electroacoustics* 20:204-205.

Megill, L. R. and L. Droppleman. 1962. Study of the Effect of Large Aperture on the Performance of an Ebert Spectrometer. *JOSA* 52:258-261.

Mertz, L. 1965. *Transformations in Optics*. John Wiley and Sons, Inc. New York.

Mielenz, K. 1964a. Theory of Mirror Spectrographs I. Astigmatic Illumination of Plane Gratings and Prisms. *Journal of Research of the National Bureau of Standards* 68C(4):195-200.

Mielenz, K. 1964b. Theory of Mirror Spectrographs II. General Theory of Focal Surfaces and Slit Curvatures. *Journal of Research of the National Bureau of Standards* 68C(4):201-204.

Mielenz, K. 1964c. Theory of Mirror Spectrographs III. Focal Surfaces and Slit Curvature of Ebert and Ebert-Fastie Spectrographs. *Journal of Research of the National Bureau of Standards* 68C(4):205-213.

Minkowski, R. 1942. Curvature of the Lines in Plane-Grating Spectra. *The Astrophysical Journal* 96:306-308.

Moursund, D. G. and C. S. Duris. 1967. *Elementary Theory and Application of Numerical Analysis*. McGraw-Hill Publishing Company. New York.

Nelson, E. D. and M. L. Fredman. 1970. Hadamard Spectroscopy. *JOSA* 60:1664-1669.

Papoulis. 1965. *Probability, Random Variables, and Stochastic Process*. McGraw-Hill Publishing Company, New York.

Peterson, W. W. and E. J. Weldon, Jr. 1972. Error-Correcting Codes, Second Edition. M.I.T. Press, Cambridge, Massachusetts.

Phillips, P. G. and M. Harwit. 1970. A New Multiplexing Spectrometer with Large Throughput. *Aspen International Conference of Fourier Spectroscopy*. AFCRL-71-0019 Special Report 114:441-444.

Phillips, P. and M. Harwit. 1971. Doubly Multiplexing Dispersive Spectrometer. *Applied Optics* 10:1149-1154.

Phillips, P. and D. Briotta, Jr. 1974. Hadamard-Transform Spectrometry of the Atmospheres of Earth and Jupiter. *Applied Optics* 13:2233-2235.

Protter, M. H. and C. B. Morrey, Jr. 1964. *Modern Mathemational Analysis*. Addison-Wesley Publishing Company, Inc., Reading, Massachusetts.

Randall, H. M. and F. A. Firestone. 1938. A Recording Spectrograph for the Far Infrared. *Rev. Sci. Instr.* 9:404-413.

Reader, J. 1969. Optimizing Czerny-Turner Spectrographs: A Comparison between Analytic Theory and Ray Tracing. *JOSA* 59:1189-1196.

Rupert, C. S. 1952. Slit Curvature in Grating Monochromators Employing Single or Multiple Diffractions. *JOSA* 42:779-781.

Shafer, A., L. R. McGill and L. Droppleman. 1964. Optimization of the Czerny-Turner Spectrometer. *JOSA* 54:879-887.

Sloane, N. J. A. 1970. Reducing the Number of Measurements in Doubly Multiplexed Spectrometers. *Aspen International Conference on Fourier Spectroscopy*. AFCRL-71-0019 Special Report 114:435-440.

Sloane, N. J. A., T. Fine, P. G. Phillips and M. Harwit. 1969. Codes for Multiplex Spectroscopy. *Applied Optics* 8:2130-2106.

Smith, Warren J. 1966. *Modern Optical Engineering*, McGraw-Hill Publishing Company. New York.

Spencer, G. and M. Murty. 1962. General Ray-Tracing Procedure. *JOSA* 52:672-678.

Swift, R., R. Wattson, J. Decker, Jr., R. Paganetti and M. Harwit. 1976. Hadamard Transform Imager and Imaging Spectrometer. *Applied Optics* 15:1595-1609.

Tai, M. H., D. Briotta, Jr., N. Kamath and M. Harwit. 1975a. Practical Multi-Spectrum Hadamard Transform Spectrometer. *Applied Optics* 14:2533-2536.

Tai, M., M. Harwit and Sloane. 1975b. Errors in Hadamard Spectroscopy or Imaging Caused by Imperfect Masks. *Applied Optics* 14:2678-2686.

Tinsley, B. A. 1966. The Circularly Symmetric Grille Spectrometer. *Applied Optics* 5:1139-1145.

Vanasse, G. A. 1972. Multiplex Techniques in Spectroscopy. AFCRL-72-0412.

Vanasse, G. A. and Sakai. 1967. *Fourier Spectroscopy in Progress in Optics VI* (E. Wolf, Ed.) North Holland Publishing Company, Amsterdam. p. 259-330.

Walsh, J. L. 1923. A Closed Set of Orthogonal Functions. *American J. Math.* 55:5-24.

Ware, G. A. 1973. The Effect of a Changing Spectrum on Transform Spectrometry. *Proceedings of the Society of Photo-Optical Instrumental Engineers* 38:125-130.

Watson, E. J. 1962. Primitive Polynomials (Mod 2). *Mathematics of Computation* 16:368-369.

Welford, W. 1962. *Geometrical Optics*. North-Holland Publishing Company, Amsterdam.

Welford, W. 1974. *Aberrations of the Symmetrical Optical System*. Academic Press, New York.

Wyatt, C. L. 1975. Multiplexed Dispersive Spectrometers Using Reduced Background Detectors: Comment 2. *Applied Optics* 14:810.

Wyatt, C. L. and R. W. Esplin. 1974. Multiplexed Dispersive Spectrometers Using Reduced Background Infrared Detectors. *Applied Optics* 13:2651-2653.

Wyatt, C. L., D. Baker and D. Frodsham. 1974. A Direct Coupled Low Noise Preamplifier for Cryogenically Cooled Photoconductive i.r. Detectors. *Infrared Physics* 14:165-176.

APPENDIXES

Appendix A

Hadamard Spectroscopy

The intent of Hadamard spectroscopy is to increase the sensitivity of dispersive spectrometers by using encoding masks based on Hadamard matrices to encode the optical energy. In a singly-encoded Hadamard spectrometer either the entrance or exit slit of a conventional dispersive spectrometer is replaced with a Hadamard encoding mask to produce a spectrometer with the multiplex advantage. In a doubly-encoded Hadamard spectrometer both the entrance and exit slits are replaced with Hadamard encoding masks in order to also provide either spatial resolution or increased throughput.

Hadamard encoding masks

Hadamard encoding masks are based upon Hadamard matrices. Hadamard matrices [*Hadamard*, 1893; *Harmuth*, 1972] are square matrices whose elements are +1's and -1's and which satisfy

$$HH^T = NI \quad , \qquad \text{(A-1)}$$

where H is a Hadamard matrix, H^T is the transpose of H, I is the identity matrix and N is a scalar equal to the rank of the matrix H. It follows from Equation (A-1) that the rows of a Hadamard matrix are orthogonal. As shown by *Sloane et al.* [1969], multiplication of a row vector by a Hadamard matrix can be physically implemented using a mask with transparent and reflecting areas. The reflecting areas correspond to

PRECEDING PAGE NOT FILMED
BLANK

the +1's of the Hadamard matrix, and the transparent areas correspond to the -1's.

For the general Hadamard matrix, N different masks are required to physically implement the multiplication of a row vector by a Hadamard matrix. However, there exists a subset of Hadamard matrices for which this multiplication can be implemented with a single mask. This significant reduction in the number of masks required results because the NxN matrices in this subset of Hadamard matrices contain cyclic $(N-1) \times (N-1)$ submatrices. For the matrices in this subset of Hadamard matrices, the elements in the first row and first column are all +1's. An 8x8 Hadamard matrix which belongs to this subset is shown in part (a) of Figure A-1. The 7x7 submatrix contained within the dotted lines in (a) is cyclic; that is, each row is a cyclic shift left of the row above. Matrices belonging to this subset exit if N is a multiple of 4 and if at least one of the following conditions [*Sloane et al.*, 1969] are satisfied:

(1) $N = p+1$, where p is a prime number,

(2) $N = p(p+2) + 1$, where p and $p+2$ are prime numbers,

(3) $N = 2^p$, where p is an integer.

Since the rows of the $(N-1) \times (N-1)$ cyclic submatrix are independent, this cyclic submatrix can be used to encode $N-1$ components. In this appendix this cyclic submatrix is called the G matrix. Multiplication by either the H matrix or the G matrix can be physically implemented using masks with transparent and reflecting areas.

$$\begin{bmatrix} 1 & 1 & 1 & 1 & 1 & 1 & 1 & 1 \\ 1 & -1 & -1 & -1 & 1 & 1 & -1 & 1 \\ 1 & -1 & -1 & 1 & 1 & -1 & 1 & -1 \\ 1 & -1 & 1 & 1 & -1 & 1 & -1 & -1 \\ 1 & 1 & 1 & -1 & 1 & -1 & -1 & -1 \\ 1 & 1 & -1 & 1 & -1 & -1 & -1 & 1 \\ 1 & -1 & 1 & -1 & -1 & -1 & 1 & 1 \\ 1 & 1 & -1 & -1 & -1 & 1 & 1 & -1 \end{bmatrix}$$

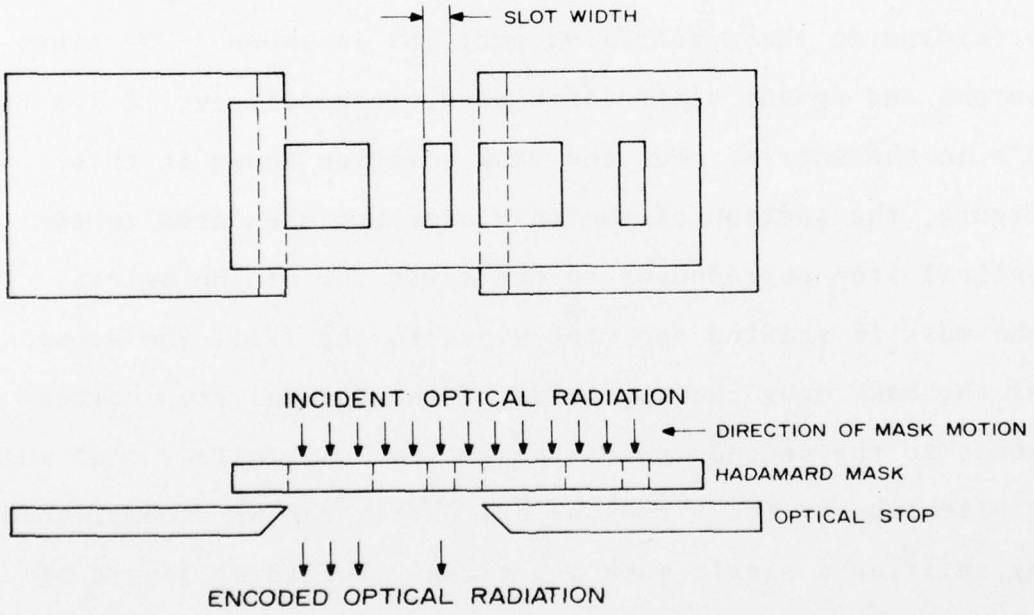
(a)

A 8x8 Hadamard matrix. The submatrix within the dotted lines is a G matrix.

$$\begin{bmatrix} 1 & 1 & 1 & 0 & 0 & 1 & 0 \\ 1 & 1 & 0 & 0 & 1 & 0 & 1 \\ 1 & 0 & 0 & 1 & 0 & 1 & 1 \\ 0 & 0 & 1 & 0 & 1 & 1 & 1 \\ 0 & 1 & 0 & 1 & 1 & 1 & 0 \\ 1 & 0 & 1 & 1 & 1 & 0 & 0 \\ 0 & 1 & 1 & 1 & 0 & 0 & 1 \end{bmatrix}$$

(b)

The corresponding 7x7 cyclic S matrix.



(c)

Implementation of the cyclic matrix in part (b).

Figure A-1. Relationship between Hadamard matrices and Hadamard encoding masks.

Hadamard masks with reflecting and transparent regions have not been used in practice. Instead, the Hadamard masks have been constructed with transparent and opaque areas. These transparent-opaque masks implement the multiplication of a matrix derived from the cyclic G matrix described in the previous paragraph. This matrix is formed from the G matrix by replacing each +1 with a 0 and each -1 with a +1. Obviously, this new matrix is cyclic. In this appendix this matrix of 0's and +1's is called the S matrix. The relationship between the H, G, and S matrices is illustrated in parts (a) and (b) of Figure A-1. In part (c) of this figure, a mask and optical stop suitable for encoding optical energy according to the S matrix of part (b) is shown. The transparent and opaque slots correspond, respectively, to 1's and 0's in the matrix. For the mask position shown in this figure, the section of the mask over the open area in the optical stop corresponds to the first row of the matrix. If the mask is shifted one slot width to the left, the section of the mask over the open area of the optical stop corresponds to the second row of the matrix. It follows that multiplication by the N rows of a S matrix can be accomplished by shifting a single mask N-1 times. The total length of the encoding portion of this single mask is $2N$-1 slot widths wide. If the code were not cyclic, N masks each with an encoding area N slots wide would be required. Thus, the cyclic property of the S matrix is of great practical

significance. For large values of N, this cyclic property makes Hadamard spectroscopy practical.

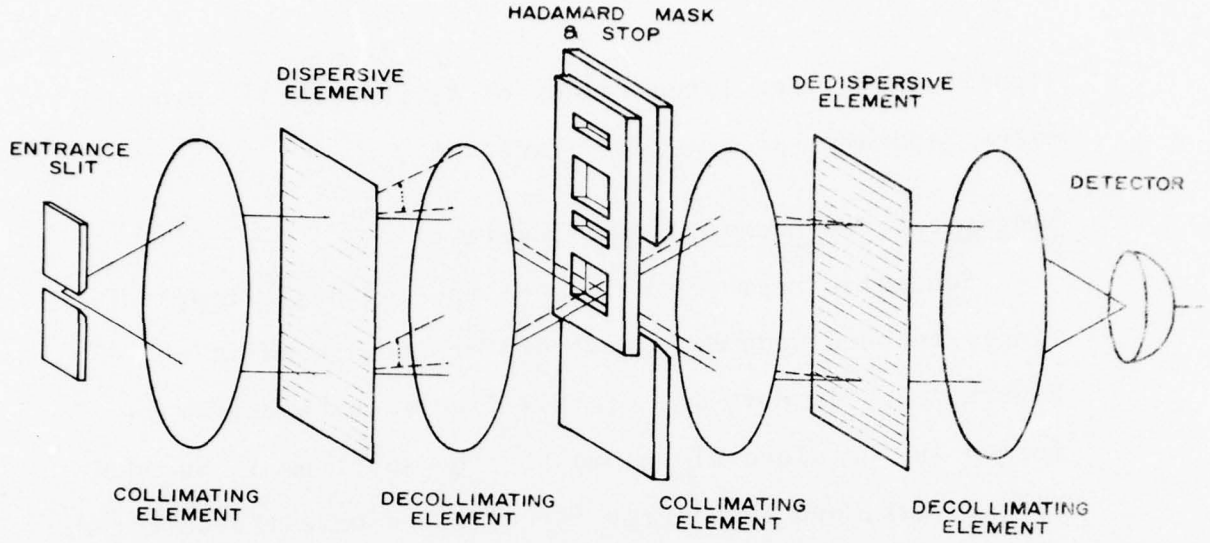
Singly-encoded Hadamard spectrometers

Schematic representations of the two basic types of singly-encoded Hadamard spectrometers are shown in Figure A-2. In part (a) of this figure the spectrum is formed in the plane of the mask; the spectrum is encoded by the mask, and the energy is collected onto the detector. The components following the mask form a white-light image of the entrance slit minimizing the required detector size. The configuration shown in part (b) of Figure A-2 produces the same result without requiring dedispersion, but it can only be used with an extended source.

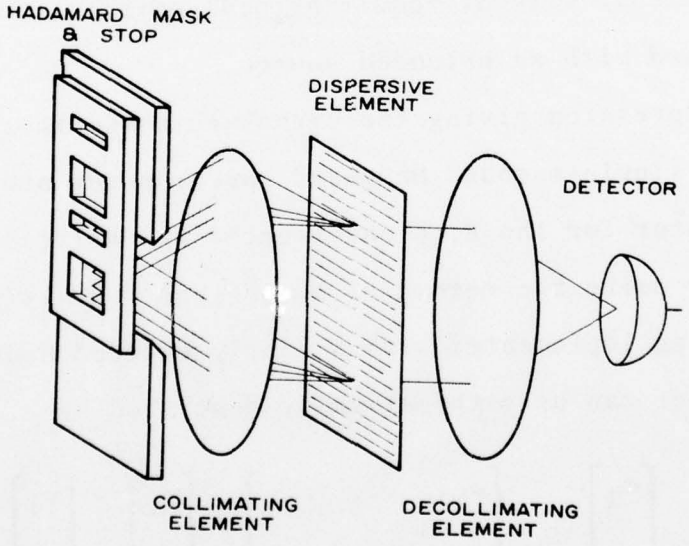
An expression giving the signal-to-noise ratio advantage of a single-encoded Hadamard spectrometer over a monochromator for the H, G and S encoding matrices can be derived by using the method of *Nelson* and *Fredman* [1970]. The encoding implemented with a singly-encoded Hadamard spectrometer can be mathematically described by

$$\begin{bmatrix} m_1 \\ \vdots \\ m_N \end{bmatrix} = \begin{bmatrix} a_{11} & \cdots & a_{1N} \\ \vdots & & \vdots \\ a_{N1} & \cdots & a_{NN} \end{bmatrix} \begin{bmatrix} x_1 \\ \vdots \\ x_N \end{bmatrix} + \begin{bmatrix} n_1 \\ \vdots \\ n_N \end{bmatrix}, \qquad \text{(A-2)}$$

where $m_1, \ldots, m_N$ are the measurements, $\{a_{ij}\}$ is the encoding matrix, $x_1, \ldots, x_N$ are the intensities of the N spectral elements, and $n_1, \ldots, n_N$ represent the noise or uncertainty



(a) The disperse-encode-dedisperse type.



(b) The encode-disperse type

Figure A-2. Basic types of singly-encoded Hadamard spectrometers.

associated with each measurement. If

$$\{b_{ij}\} \triangleq \{a_{ij}\}^{-1} , \tag{A-3}$$

then estimates of the spectral intensities are given by

$$\begin{bmatrix} \hat{x}_1 \\ \vdots \\ \hat{x}_N \end{bmatrix} = \begin{bmatrix} b_{11} & \cdots & b_{1N} \\ \vdots & & \vdots \\ b_{N1} & \cdots & b_{NN} \end{bmatrix} \begin{bmatrix} m_1 \\ \vdots \\ m_N \end{bmatrix} = \begin{bmatrix} x_1 \\ \vdots \\ x_N \end{bmatrix} + \begin{bmatrix} b_{11} & \cdots & b_{1N} \\ \vdots & & \vdots \\ b_{N1} & \cdots & b_{NN} \end{bmatrix} \begin{bmatrix} n_1 \\ \vdots \\ n_N \end{bmatrix} . \tag{A-4}$$

If there is no measurement noise, then the estimated and actual spectral intensities are equal. If there is measurement noise, then the estimate of the intensity of the i-th spectral element is corrupted by the amount

$$b_{i1}\, n_1 + \ldots + b_{iN}\, n_N . \tag{A-5}$$

Since the above expression results from a noise process, it can best be described statistically. If $n_1, \ldots, n_N$ are assumed to be uncorrelated random variables with zero means, the standard deviation of this expression is given by

$$\sqrt{b_{i1}^2 E[n_1^2] + \ldots + b_{iN}^2 E[n_N^2]} \tag{A-6}$$

where the notation $E[\ ]$ denotes the expected value. If $E[n_i^2] = \sigma_N$ for $i = 1, \ldots, N$, the Expression (A-6) can

be written as

$$\sigma_N \sqrt{b_{i1}^2 + \ldots + b_{iN}^2} \quad . \tag{A-7}$$

Thus, the signal-to-noise ratio of a detector-noise-limited singly-encoded Hadamard spectrometer is

$$SNR_{\text{Singly-encoded Hadamard}} = \frac{x_j}{\sigma_N \sqrt{b_{i1}^2 + \ldots + b_{iN}^2}} \quad . \tag{A-8}$$

The signal-to-noise ratio of a detector-noise-limited monochromator is

$$SNR_{\text{Monochromator}} = \frac{x_j}{\sigma_N} \quad . \tag{A-9}$$

It follows from Equations (A-8) and (A-9) that for the i-th spectral element

$$\frac{SNR_{\text{Singly-encoded Hadamard}}}{SNR_{\text{Monochromator}}} = \frac{1}{\sqrt{b_{i1}^2 + \ldots + b_{iN}^2}} \quad . \tag{A-10}$$

Equation (A-10) assumes that the conditions are equal for both the singly-encoded Hadamard and the monochromator; that is, the same detector is used for both spectrometers, the slots in the Hadamard mask are the same length as the exit slit of the monochromator, etc. Equation (A-10) is valid for any singly-encoding matrix; it is only necessary to use the appropriate inverse matrix $\{b_{ij}\}$.

It follows from Equation (A-1) that the inverse of the H matrix is given by

$$H^{-1} = \frac{1}{N} H^T \quad . \tag{A-11}$$

Thus, the absolute value of every element of H^{-1} equals $1/N$. Therefore by Equation (A-10)

$$\frac{SNR_{\text{Singly-encoded Hadamard with the } H\text{-matrix code}}}{SNR_{\text{Monochromator}}} = \frac{1}{\sqrt{\frac{N}{N^2}}} = \sqrt{N} \quad . \tag{A-12}$$

The inverse of the G matrix is given by [*Sloane et al.*, 1969]

$$G^{-1} = \frac{1}{N+1} (G^T - J) \quad , \tag{A-13}$$

where N is a scalar equal to the dimension of G and J is an NxN matrix of +1's. Since the H matrix has an equal number of +1's and -1's in every column except the first and the G matrix is derived from the H matrix by deleting the first row and column, each row of G^T has $(N+1)/2$ elements equal to -1 and $(N+1)/2-1$ elements equal to +1, where N is the dimension of the G matrix. By using this fact in conjunction with Equation (A-13), it follows that each row of G^{-1} contains $(N+1)/2$ elements equal to $-2/(N+1)$ and $(N+1)/2-1$ elements equal to zero. Substituting these values into Equation (A-10) yields

$$\frac{SNR_{\text{Singly-encoded Hadamard with the } G\text{-matrix code}}}{SNR_{\text{Monochromator}}} = \frac{1}{\sqrt{\frac{N+1}{2} \cdot \left(\frac{2}{N+1}\right)^2}} = \sqrt{\frac{N+1}{2}} \approx \sqrt{\frac{N}{2}} \; . \tag{A-14}$$

All the elements in S^{-1} have an absolute value of $2/(N+1)$ [*Sloane et al.*, 1969] where N is the dimension of S. It follows from Equation (A-10) that

$$\frac{SNR_{\text{Singly-encoded Hadamard with } S\text{-matrix code}}}{SNR_{\text{Monochromator}}} = \frac{1}{\sqrt{N\left(\frac{2}{N+1}\right)^2}} = \frac{N+1}{2\sqrt{N}} \approx \frac{\sqrt{N}}{2} \; . \tag{A-15}$$

The values computed using Equation (A-10) for the H, G, and S matrices are tabulated in Table A-1.

Table A-1. A signal-to-noise ratio comparison between singly-encoded Hadamard spectrometers with codes based on H, G, and S matrices and a monochromator.

Encoding matrix	$\frac{SNR_{\text{Singly-encoded Hadamard}}}{SNR_{\text{Monochromator}}}$
H	$\sqrt{N}$
G	$\sqrt{\frac{N+1}{2}} \approx \sqrt{\frac{N}{2}}$
S	$\frac{N+1}{2\sqrt{N}} \approx \frac{\sqrt{N}}{2}$

Doubly-encoded Hadamard spectrometers

Doubly-encoded Hadamard spectroscopy is implemented by replacing both the entrance and exit slits of a dispersive spectrometer with Hadamard encoding masks. If M entrance and N exit slot locations are encoded, there are MN unknowns. These MN unknowns can be represented by an MxN matrix

$$\begin{bmatrix} x_{11} & \cdots & x_{1N} \\ \vdots & & \vdots \\ x_{M1} & \cdots & x_{MN} \end{bmatrix}, \qquad \text{(A-16)}$$

where x_{ij} is the energy passing through the i-th entrance and the j-th exit slot. In order to determine these MN unknowns, MN measurements must be taken. These MN measurements can be taken by placing the entrance and exit masks in M and N positions, respectively. The measurement taken with the entrance and exit masks in positions k and l, respectively, can be represented by

$$m_{kl} = d_{k1}(x_{11}e_{1l} + \cdots + x_{1N}e_{Nl}) + \cdots + d_{kM}(x_{M1}e_{1l} + \cdots + x_{MN}e_{Nl}) + n_{kl}, \qquad \text{(A-17)}$$

where e_{rl} is 1 or 0 depending on whether the r-th exit slot location is open or closed, respectively, with the exit mask in position l, and d_{ks} is 1 or 0 depending on whether the s-th entrance slot location is open or closed,

respectively, with the entrance mask in position k, and n_{kl} is the noise associated with the measurement. The expressions within the parentheses represent the coding at the exit plane while the d_{kj} coefficients represent the encoding at the entrance plane.

By using the notation defined above, the operation of a doubly-encoded Hadamard can be described by the following matrix equation

$$\begin{bmatrix} m_{11} & \cdots & m_{1N} \\ \vdots & & \vdots \\ m_{M1} & \cdots & m_{MN} \end{bmatrix} = \begin{bmatrix} d_{11} & \cdots & d_{1M} \\ \vdots & & \vdots \\ d_{M1} & \cdots & d_{MM} \end{bmatrix} \begin{bmatrix} x_{11} & \cdots & x_{1N} \\ \vdots & & \vdots \\ x_{M1} & \cdots & x_{MN} \end{bmatrix} \begin{bmatrix} e_{11} & \cdots & e_{1N} \\ \vdots & & \vdots \\ e_{N1} & \cdots & e_{NN} \end{bmatrix} + \begin{bmatrix} n_{11} & \cdots & n_{1N} \\ \vdots & & \vdots \\ n_{M1} & \cdots & n_{MN} \end{bmatrix} \tag{A-18}$$

If

$$\{f_{ij}\} \triangleq \{d_{ij}\}^{-1} \tag{A-19}$$

and

$$\{g_{ij}\} \triangleq \{e_{ij}\}^{-1} , \tag{A-20}$$

then estimates of the MN unknowns are given by

$$\begin{bmatrix} \hat{x}_{11} & \cdots & \hat{x}_{1N} \\ \vdots & & \vdots \\ \hat{x}_{M1} & \cdots & \hat{x}_{MN} \end{bmatrix} = \begin{bmatrix} f_{11} & \cdots & f_{1M} \\ \vdots & & \vdots \\ f_{M1} & \cdots & f_{MM} \end{bmatrix} \begin{bmatrix} m_{11} & \cdots & m_{1N} \\ \vdots & & \vdots \\ m_{M1} & \cdots & m_{MN} \end{bmatrix} \begin{bmatrix} g_{11} & \cdots & g_{1N} \\ \vdots & & \vdots \\ g_{N1} & \cdots & g_{NN} \end{bmatrix} =$$

$$\begin{bmatrix} x_{11} & \cdots & x_{1N} \\ \vdots & & \vdots \\ x_{M1} & \cdots & x_{MN} \end{bmatrix} + \begin{bmatrix} f_{11} & \cdots & f_{1M} \\ \vdots & & \vdots \\ f_{M1} & \cdots & f_{MM} \end{bmatrix} \begin{bmatrix} n_{11} & \cdots & n_{1N} \\ \vdots & & \vdots \\ n_{M1} & \cdots & n_{MN} \end{bmatrix} \begin{bmatrix} g_{11} & \cdots & g_{1N} \\ \vdots & & \vdots \\ g_{N1} & \cdots & g_{NN} \end{bmatrix} . \tag{A-21}$$

Thus,

$$\hat{x}_{ij} = x_{ij} + f_{i1}(n_{11}g_{ij} + \ldots + n_{1N}g_{Nj}) + \ldots + f_{iM}(n_{M1}g_{1i} + \ldots + n_{MN}g_{Nj}) \quad \text{(A-22)}$$

The first term on the right is the true signal; all the other terms are noise. Within each parentheses there are N terms and there are M sets of parentheses. Consequently, the noise consists of NM terms of the form

$$f_{rs}\, n_{tu}\, g_{vw} \quad \text{(A-23)}$$

Therefore, if the random variables n_{ij}, $i = 1, \ldots, M$, $j = 1, \ldots, N$, are assumed to be independent, then the standard deviation of the noise equals the square root of the sum of the expected values of the squares of NM terms of the form given in Expression (A-23). For all doubly-encoded Hadamard spectrometers reported in the literature, $\{d_{ij}\}$ and $\{e_{ij}\}$ are S matrices. Consequently, in this appendix it is assumed that $\{d_{ij}\}$ and $\{e_{ij}\}$ are S matrices. Therefore, the absolute value of the elements of $\{f_{ij}\}$ and $\{g_{ij}\}$ are $2/(M+1)$ and $2/(N+1)$, respectively. If $E[n_{ij}] = \sigma_{NM}$ for $i = 1, \ldots, M$ and $j = 1, \ldots, N$, the standard deviation of Equation (A-22) equals

$$\sigma_{NM}\sqrt{MN\left[\frac{4}{(N+1)(M+1)}\right]^2} = \frac{4\sqrt{NM}\,\sigma_{NM}}{(N+1)(M+1)} \approx \frac{4\sigma_{NM}}{\sqrt{NM}} \quad \text{(A-24)}$$

Thus, the signal-to-noise ratio of a doubly-encoded Hadamard spectrometer with a S-matrix code is given by

$$SNR_{\substack{\text{Doubly-encoded Hadamard} \\ \text{with } S\text{-matrix code}}} = \frac{x_{ij}\sqrt{NM}}{4\sigma_{NM}} \quad . \qquad \text{(A-25)}$$

For detector-noise-limited conditions, the signal-to-noise ratio of an instrument that measures each of the NM unknowns in turn is given by

$$SNR_{\text{Sequential}} = \frac{x_{ij}}{\sigma_{NM}} \quad . \qquad \text{(A-26)}$$

Thus, the gain resulting from using a doubly-encoded Hadamard instead of a sequential instrument is given by the ratio of Equation (A-25) to Equation (A-26). This ratio reduces to

$$\frac{SNR_{\text{Doubly-encoded Hadamard}}}{SNR_{\text{Sequential}}} = \frac{\sqrt{NM}}{4} \quad . \qquad \text{(A-27)}$$

If it were possible to use H-matrix encoding, this ratio would be $\sqrt{NM}$. It is obvious that double-encoding is very similar to the singly-encoded case except that NM unknowns are encoded. This doubly-encoded method yields a spectrum for each entrance slot; that is, $x_{i1}, \ldots, x_{iN}$ is the spectrum of the energy falling on the i-th entrance slot location.

AD-A064 198 UTAH STATE UNIV LOGAN ELECTRO-DYNAMICS LAB F/G 20/6
INCREASING THE THROUGHPUT OF HADAMARD SPECTROMETERS BY THE USE --ETC(U)
SEP 78 R W ESPLIN, G A VANASSE, D J BAKER F19628-77-C-0203
UNCLASSIFIED EDL-SRL-78-2 AFGL-TR-78-0232 NL

3 OF 4
AD
A064198



In an ideal dispersive spectrometer the spectrum shifts one location when the entrance slot is shifted one location. Therefore, x_{ij} is the same wavelength as x_{kl} if $(i-j) = (k-l)$. This means that the wavelength along each diagonal of the matrix $\{x_{ij}\}$ is constant. For example, the wavelength along each diagonal line in the following 3x6 matrix is constant:

$$\begin{bmatrix} x_{11} & x_{12} & x_{13} & x_{14} & x_{15} & x_{16} \\ x_{21} & x_{22} & x_{23} & x_{24} & x_{25} & x_{26} \\ x_{31} & x_{32} & x_{33} & x_{34} & x_{35} & x_{36} \end{bmatrix} . \qquad \text{(A-28)}$$

Since an MxN matrix has $M+N-1$ diagonals, $M+N-1$ spectral elements are estimated. The number of estimates of each spectral element is the number of elements in the diagonal. If the energy falling on the entrance mask is homogeneous, a common spectrum with an improved signal-to-noise ratio can be formed by summing the estimates of each spectral element. That is accomplished by summing each diagonal of the estimate matrix $\{x_{ij}\}$. The resulting signal-to-noise ratio improvement of a spectral element is given by the square root of the number of estimates summed. Since a MxN matrix has $N-M+1$ diagonals that have M elements, summing improves the signal-to-noise ratio for the $N-M+1$ spectral elements corresponding to these diagonals by a factor of $\sqrt{M}$. Thus, multiplying Equation (A-25) by $\sqrt{M}$ gives the signal-to-noise ratio of these $N-M+1$ spectral elements

$$SNR_{\substack{\text{for } N\text{-}M\text{+}1 \text{ spectral} \\ \text{elements of a} \\ \text{doubly-encoded Hadamard}}} = \frac{x_{ij} M\sqrt{N}}{4\sigma_{NM}} \quad . \qquad \text{(A-29)}$$

For example, the 3x6 matrix of (A-28) has $M+N-1 = 3+6-1 = 8$ diagonals and $N-M+1 = 6-3+1 = 4$ diagonals with three elements each.

A bound on the signal-to-noise ratio resulting from summing all estimates of each of the N central spectral elements can be established using the following procedure. In an MxN matrix the first diagonal to the right of the central $N-M+1$ diagonals has $M-1$ elements, the second $M-2$, and so on. A similar relationship is true for diagonals to the left of the central $N-M+1$ diagonals. Thus, the k-th diagonals to the right and left of the central $N-M+1$ diagonals have $M-k$ elements. The N most central diagonals consist of $N-M+1$ central diagonals each with M elements plus $(M-1)/2$ diagonals to the immediate right of the central diagonals and $(M-1)/2$ diagonals to the immediate left of the central diagonals. Thus, when measuring the N central spectral elements, the minimum number of estimates of these N spectral elements is $M-(M-1)/2 = (M-1)/2$. The product of Equation (A-25) and $\sqrt{(M-1)/2}$ is a lower bound on the signal-to-noise ratio, namely

$$SNR_{\substack{\text{For the } N \text{ central spectral} \\ \text{elements after summing}}} \leq \frac{x_{ij}\sqrt{NM(M-1)/2}}{4\sigma_{NM}}. \qquad \text{(A-30)}$$

If $M >> 1$, Equation (A-29) is $\sqrt{2}$ larger than Equation (A-30). Thus, the maximum and minimum signal-to-noise ratio differs by only a factor of $\sqrt{2}$ for the N central spectral elements. This $\sqrt{2}$ factor is ignored in the following analysis, and it is assumed that the signal-to-noise ratio for all N spectral elements is given by Equation (A-29).

The signal-to-noise ratio of the N central spectral elements when the estimates of a doubly-encoded Hadamard spectrometer are summed will now be compared with the signal-to-noise ratio of a monochromator that takes the same time as the doubly-encoded Hadamard spectrometer to measure a spectrum. For white noise, the *rms* noise voltage is proportional to the square root of the effective noise bandwidth. Since the effective noise bandwidth is inversely proportional to the time required for one measurement, the *rms* noise voltage is inversely proportional to the square root of the time required for one measurement. If the monochromator and the doubly-encoded Hadamard are to measure the spectrum in the same time T, the times available for each measurement are T/N and T/MN, respectively. Therefore, the ratio of the *rms* measurement noise of the doubly-encoded Hadamard spectrometer to the monochromator is

$$\sqrt{\frac{\frac{MN}{T}}{\frac{N}{T}}} = \sqrt{M} \quad . \tag{A-31}$$

Therefore, the *rms* measurement noise of the monochromator is

$$\sigma_{NM} \Big/ \sqrt{M} \quad , \tag{A-32}$$

and the signal-to-noise ratio of the monochromator is

$$SNR_{\text{Monochromator}} = x_{ij} \sqrt{M} \Big/ \sigma_{MN} \quad . \tag{A-33}$$

The advantage of a doubly-encoded Hadamard over a monochromator for measuring N spectral elements is given by the ratio of Equation (A-29) to Equation (A-33). This ratio reduces to

$$\frac{SNR_{\substack{\text{Doubly-encoded Hadamard} \\ \text{for } N \text{ spectral elements}}}}{SNR_{\text{Monochromator}}} = \frac{\sqrt{MN}}{4} \quad . \tag{A-34}$$

This advantage can be interpreted as the product of a multiplex gain, $\sqrt{N}/2$, and a partial throughput gain, $\sqrt{M}/2$. Since only a partial throughput gain results, this method is not optimum. An optimal encoding method would make the ratio in Equation (A-34) equal to $M\sqrt{N}/4$.

It must not be assumed that simply reducing the number of required measurements automatically improves the signal-to-noise ratio of a doubly-encoded Hadamard spectrometer. This is vividly demonstrated by examining the noise properties of the following encoding scheme proposed by *Sloane* [1970]. Since for N entrance and N exit encoding slots there are $2N$-1 unknowns, a computer can be used to search for $2N$-1 measurements (combinations of entrance and exit mask positions), which yield $2N$-1 linearly independent equations.

Sloane showed that such a search, if done properly, must always be successful. In general there are many such sets of $2N$-1 measurements. The $2N$-1 linearly independent equations can be written in the following matrix form:

$$\begin{bmatrix} m_1 \\ \vdots \\ m_{2N-1} \end{bmatrix} = \begin{bmatrix} a_{11} & \cdots & a_{1(2N-1)} \\ \vdots & & \vdots \\ a_{(2N-1)1} & \cdots & a_{(2N-1)(2N-1)} \end{bmatrix} \begin{bmatrix} x_1 \\ \vdots \\ x_{2N-1} \end{bmatrix} + \begin{bmatrix} n_1 \\ \vdots \\ n_{2N-1} \end{bmatrix}, \quad \text{(A-35)}$$

where m_i, x_i, and n_i, $i = 1, \ldots, 2N-1$, represent the measurements, spectral intensities, and measurement noise, respectively. The form of Equation (A-35) is the same as Equation (A-2) with N replaced by $2N$-1. Consequently, Equation (A-3) through (A-10) can be used to describe the encoding scheme if N in these equations is replaced by $2N$-1. Consequently, Equation (A-10) indicates that for each spectral element x_i,

$$\frac{SNR_{\text{Sloane's } 2N\text{-1 scheme}}}{SNR_{\text{Monochromator}}} = \frac{1}{\sqrt{b^2_{i1} + \ldots + b^2_{i(2N-1)}}}. \quad \text{(A-36)}$$

Sloane published schemes requiring $2N$-1 measurements together with their required inverse matrices for N = 3, 7, 11 and 15. His inverse matrix for N = 7 is given in Figure A-3. Table A-2 tabulates the application of Equation (A-36) to each row of this matrix. As can be seen from Table A-2, the signal-to-noise ratio using Sloane's $2N$-1 encoding scheme does not have the same value for all

COLUMN	1	2	3	4	5	6	7
ROW							
1	-0.3125	-0.2500	-0.1250	-0.0625	-0.0625	0.0625	-0.2500
2	-0.0625	-0.0000	0.3750	-0.0625	-0.0625	-0.1875	0.2500
3	0.1875	-0.2500	-0.1250	0.4375	-0.0625	0.0625	-0.2500
4	-0.3125	-0.0000	0.1250	-0.0625	0.4375	0.0625	0.0000
5	-0.0625	-0.2500	0.1250	-0.0625	-0.0625	0.3125	0.0000
6	-0.0625	0.0000	-0.1250	-0.0625	-0.0625	-0.1875	0.2500
7	0.4375	0.2500	-0.3750	-0.0625	-0.0625	-0.1875	0.0000
8	0.1875	0.5000	-0.3750	-0.0625	-0.0625	0.0625	-0.0000
9	-0.0625	-0.2500	0.6250	-0.0625	-0.0625	0.3125	0.0000
10	-0.3125	-0.5000	0.6250	0.4375	-0.0625	0.0625	-0.0000
11	-0.3125	-0.2500	0.3750	-0.0625	0.4375	-0.4375	-0.2500
12	-0.0625	0.5000	-0.6250	-0.0625	-0.0625	-0.1875	-0.2500
13	-0.0625	-0.2500	0.1250	-0.0625	-0.0625	0.3125	0.0000

COLUMN	8	9	10	11	12	13
ROW						
1	1.1250	-0.1250	0.1875	0.2500	-0.4375	0.0625
2	-0.3750	0.1250	-0.3125	0.0000	0.3125	0.0625
3	0.1250	-0.1250	0.1875	-0.2500	0.0625	0.0625
4	0.1250	-0.1250	-0.0625	0.2500	-0.1875	-0.1875
5	0.1250	0.1250	-0.0625	0.0000	0.0625	-0.1875
6	0.1250	0.1250	0.1875	-0.0000	-0.1875	0.0625
7	-0.3750	0.1250	-0.0625	-0.0000	0.0625	0.3125
8	-0.3750	-0.1250	-0.0625	-0.2500	0.3125	0.3125
9	0.1250	-0.3750	-0.0625	0.0000	0.0625	-0.1875
10	0.6250	-0.1250	-0.0625	0.2500	-0.1875	-0.6875
11	0.6250	0.3750	0.1875	0.2500	-0.4375	-0.4375
12	-0.3750	0.6250	0.1875	-0.0000	-0.1875	0.5625
13	-0.3750	-0.3750	0.4375	0.0000	0.5625	-0.1875

Figure A-3. *Sloane's* [1970] matrix $\{b_{ij}\}$ for $N = 7$.

Table A-2. Comparison between Sloane's doubly-encoded $2N$-1 measurement scheme and a monochromator for $N = 7$. (Both instruments measure $2N$-1 = 13 spectral elements.)

Row number	$\frac{SNR_{\text{Sloane's } 2N\text{-1 scheme}}}{SNR_{\text{Monochromator}}}$
1	.74
2	1.29
3	1.40
4	1.44
5	1.95
6	2.08
7	1.20
8	1.08
9	1.15
10	.72
11	.75
12	.77
13	.99

spectral elements. Table A-2 also shows that the signal-to-noise ratio for five of the 13 spectral elements is actually lower for Sloane's scheme than it is for a monochromator. Equation (A-10) indicates that if a singly-encoded Hadamard spectrometer could be constructed to encode 13 spectral elements, its signal-to-noise ratio advantage over a monochromator would be $\sqrt{13}/2 = 1.8$. Thus, only two of the 13

spectral elements tabulated in Table A-2 have a signal-to-noise advantage larger than that of a singly-encoded Hadamard. The average signal-to-noise advantage over a monochromator for Sloane's $N = 7$ doubly-encoded technique is 1.2; this value is significantly smaller than the advantage of the singly-encoded Hadamard. Thus, it is evident that reducing the required number of measurements is a necessary but not sufficient condition for improving the signal-to-noise ratio of doubly-encoded Hadamard spectrometers.

It is often mistakenly assumed that the signal-to-noise ratio of a doubly-encoded spectrometer is a factor of M instead of $\sqrt{M}$ larger than that of a conventional monochromator. It is apparent from the preceding derivations that the reason why the correct factor is $\sqrt{M}$ is because MN measurements are required to recover N spectral elements. If the proper N measurements could be taken, the signal-to-noise ratio would increase by a factor of M. However, to this date even though doubly-encoding techniques which require only N measurements have been found [*Harwit et al.*, 1974], none increase the value of the ratio given in Equation (A-34).

If $M = N$, then Equation (A-34) reduces to

$$\frac{SNR_{\substack{\text{Doubly-encoded Hadamard} \\ \text{for } N \text{ spectral elements} \\ \text{with } M \text{ equal to } N}}}{SNR_{\text{Monochromator}}} = \frac{N}{4} . \qquad \text{(A-37)}$$

The value given by Equation (A-37) is approximately equal to the advantage of the *Girard* [1960, 1963] grill spectrometer over a monochromator.

Harwit et al., [1974] have proposed a doubly-encoded Hadamard procedure in which each measurement corresponds to the energy of a spectral element. In this case, the spectral elements are not multiplexed, and the gain that is given by Equation (A-37) depends entirely on a throughput gain.

Since it has often been claimed that doubly-encoded Hadamard spectrometers are comparable in performance with a Michelson interferometer, an explicit comparison between the performance of the two instruments is given. The throughputs of a Michelson interferometer and a grating monochromator are [*Vanasse* and *Sakai*, 1967]

$$E_M = 2\pi A_M / R \qquad \text{(A-38)}$$

and

$$E_G = \ell A_G / fR \quad , \qquad \text{(A-39)}$$

respectively, where A_M is the area of the collimator in the Michelson interferometer, R is the resolving power, A_G is the area of the grating, ℓ is the slit length, and f is the focal length of the collimator of the grating spectrometer. Since the Michelson interferometer has the multiplex advantage,

$$\frac{SNR_{\text{Michelson interferometer}}}{SNR_{\text{Monochromator}}} = \frac{E_M}{E_G}\sqrt{N} \quad , \qquad \text{(A-40)}$$

where N is the number of spectral elements. It follows from Equations (A-34), (A-38), (A-39), and (A-40) that

$$\frac{SNR_{\text{Doubly-encoded Hadamard}}}{SNR_{\text{Michelson interferometer}}} = \frac{A_G \ell \sqrt{M}}{8\pi f A_M} \quad , \qquad \text{(A-41)}$$

where M is the number of entrance slots. If an optimal method of doubly-encoding is discovered, the $\sqrt{M}$ in Equation (A-41) should be replaced by M. Since ℓ/f for practical grating spectrometers is less than 1/30,

$$\frac{SNR_{\text{Doubly-encoded Hadamard}}}{SNR_{\text{Michelson interferometer}}} \leq \frac{A_G \sqrt{M}}{240\pi A_M} \quad . \qquad \text{(A-42)}$$

Equation (A-40) implies that if A_G equals A_M, a doubly-encoded Hadamard must have 568 thousand entrance slots (a physical impossibility) in order to have the same signal-to-noise ratio as a Michelson interferometer. This comparison demonstrates that, at the present state-of-the-art, the signal-to-noise ratio of the doubly-encoded Hadamard spectrometer does not approach that of the Michelson interferometer. However, if an optical code is discovered and if it is possible by using holographic gratings to make A_G much larger than A_M, the signal-to-noise ratio of a doubly-encoded Hadamard spectrometer may approach that of a Michelson interferometer.

As shown in the preceding discussion, the *rms* measurement noise for white noise goes up as the square root of the number of measurements. However, in some detection systems the limiting noise is not white. One such case occurs for liquid-helium cooled extrinsic detectors directly coupled in a transimpedance feedback compensation circuit as described by *Wyatt, Baker* and *Frodsham* [1974]. For this situation the *rms* noise is proportional to the number of measurements to the three-halves power [*Wyatt* and *Esplin*, 1974; *Wyatt*, 1975]. Therefore, since a doubly-encoded Hadamard requires a factor of M more measurements than a comparable monochromator measuring N spectral elements, the noise of a doubly-encoded Hadamard spectrometer for this type of noise is a factor of $M^{3/2}$ greater than the noise of a monochromator. Consequently, the noise of the monochromator for this type of noise is given by

$$\frac{\sigma_{NM}}{M^{3/2}} \tag{A-43}$$

and the signal-to-noise ratio of the monochromator is

$$SNR_{\text{Monochromator}} = \frac{x_{ij} M^{3/2}}{\sigma_{NM}} \quad . \tag{A-44}$$

Thus, for this type of noise, the advantage of a doubly-encoded Hadamard spectrometer over a monochromator is given by the ratio of Equation (A-29) to Equation (A-44). This

ratio reduces to

$$\frac{SNR_{\text{Doubly-encoded Hadamard with 3/2 power noise}}}{SNR_{\text{Monochromator}}} = \frac{1}{4}\sqrt{\frac{N}{M}} \cdot \quad \text{(A-45)}$$

Since this ratio decreases as M increases, doubly-encoding schemes which require MN measurements should not be used for detector systems whose noise is proportional to the three-halves power of the number of measurements. However, for the doubly-encoded scheme given by *Harwit et al.* [1974], that requires only N measurements, the advantage of the doubly-encoded Hadamard spectrometer over a monochromator for this type of noise is given by Equation (A-34).

Appendix B

Relationship Between Total-Mean-Square Error and Signal-to-Noise Ratio Descriptions of Hadamard Spectrometers

Several researchers [*Sloane et al.*, 1969; *Harwit et al.*, 1970; *Harwit*, 1971] have described Hadamard performance in terms of total-mean-square error instead of using the signal-to-noise ratio as was done in Appendix A. The total-mean-square error is a measure of the noise in the entire spectrum, while the signal-to-noise ratio describes only one spectral component. The purpose of this appendix is to explain the relationship between these two methods of describing Hadamard spectrometer performance.

The total-mean-square error [*Sloane et al.*, 1969] for N spectral elements is defined by

$$\varepsilon \triangleq E[(x_1-\hat{x}_1)^2 + \ldots + (x_N-\hat{x}_N)^2] \quad , \tag{B-1}$$

where x_i, $i = 1, \ldots, N$ is the true value of the i-th spectral element, $\hat{x}_i$, $i = 1, \ldots, N$ is the estimate of the i-th spectral element, and $E[\ ]$ denotes the expected value of the enclosed random variable. Since the expected value of a sum equals the sum of the expected values [*Papoulis*, 1965], Equation (B-1) can be written as

$$\varepsilon = E[(x_1-\hat{x}_1)^2] + \ldots + E[(x_N-\hat{x}_N)^2] \quad . \tag{B-2}$$

If $E[(x_i-\hat{x}_i)^2] = E[(x_j-\hat{x}_j)^2]$ for all i and j where $i = 1, \ldots, N$, and $j = 1, \ldots, N$, then

$$\varepsilon = N\{E[(x_i-\hat{x}_i)^2]\} \quad . \tag{B-3}$$

Since the standard deviation of the i-th spectral component is given by

$$\sqrt{E[(x_i-\hat{x}_i)^2]} \quad , \tag{B-4}$$

the signal-to-noise ratio of the i-th spectral component is

$$SNR = \frac{x_i}{\sqrt{E[(x_i-\hat{x}_i)^2]}} \quad . \tag{B-5}$$

Therefore, if the assumptions used in deriving Equation (B-3) are satisfied, then

$$SNR = x_i\sqrt{\frac{N}{\varepsilon}} \quad . \tag{B-6}$$

If SNR_1 and SNR_2 are the signal-to-noise ratios for two different codes and ε_1 and ε_2 are their respective total mean-square errors, then it follows from Equation (B-6) that

$$\frac{SNR_1}{SNR_2} = \frac{\varepsilon_2}{\varepsilon_1} \quad . \tag{B-7}$$

As an example of the use of Equation (B-7), this equation is used to compare a monochromator and a singly-encoded Hadamard spectrometer which uses the S-matrix code. The

S-matrix code is explained in Appendix A. It follows from Equation (B-3) that the total-mean-square error of a monochromator is given by

$$\varepsilon_{\text{Monochromator}} = N\sigma^2 \quad , \tag{B-8}$$

where σ^2 is the mean-square error of the noise of a single measurement. *Sloane et al.* [1969] has shown that the total-mean-square error of a singly-encoded Hadamard using the *S*-matrix code is given by

$$\varepsilon_{\substack{\text{Singly-encoded Hadamard} \\ \text{with } S\text{-matrix code}}} = \left(2 - \frac{2}{N+1}\right)^2 \sigma^2 = \left(\frac{2N}{N+1}\right)^2 \sigma^2 . \tag{B-9}$$

It follows from Equations (B-7), (B-8) and (B-9) that

$$\frac{SNR_{\substack{\text{Singly-encoded Hadamard} \\ \text{with } S\text{-matrix code}}}}{SNR_{\text{Monochromator}}} = \sqrt{N\left(\frac{N+1}{2N}\right)^2} = \frac{N+1}{2\sqrt{N}} \approx \frac{\sqrt{N}}{2} . \tag{B-10}$$

Equation (B-10) agrees with Equation (A-15) in Appendix A.

The value of Equation (B-7) and the ratio ε/σ^2 are tabulated in Table B-1 for several Hadamard spectrometer encoding schemes. These encoding schemes are discussed in Appendix A.

Table B-1. The signal-to-noise advantage for several Hadamard spectrometer encoding schemes derived from total-mean-square error expressions in the literature.

Code Scheme	ε/σ^2	$\frac{SNR_{\text{With code}}}{SNR_{\text{Monochromator}}}$
Monochromator	N	1
Singly-encoding schemes:[a]		
H-matrix code	1	$\sqrt{N}$
G-matrix code	$2 - \frac{2}{N+1} = \frac{2N}{N+1}$	$\sqrt{\frac{N+1}{2}} \approx \sqrt{\frac{N}{2}}$
S-matrix code	$\left(2 - \frac{2}{N+1}\right)^2 = \left(\frac{2}{N+1}\right)^2$	$\frac{N+1}{2\sqrt{N}} \approx \frac{\sqrt{N}}{2}$
Doubly-encoding schemes:		
N entrance, N exit slots, N^2 measurements, all estimates of same wavelength summed[b]	$\approx \frac{22.2}{N}$ for N large	$\approx \frac{N}{4.71}$
An asymmetrical encoding scheme with N spectral elements, N entrance slots, N measurements[c]	$\approx \frac{16}{N}$	$\approx \frac{N}{4}$
An asymmetrical encoding scheme with N spectral elements, M entrance slots, N measurements[c]	$\approx \frac{16}{M+1}$	$\approx \frac{\sqrt{N(M+1)}}{4} \approx \frac{\sqrt{MN}}{4}$
An optimal encoding scheme with N spectral elements, M entrance slots, N measurements[d]	$\frac{16}{M^2}$	$\frac{M\sqrt{N}}{4}$

[a] *Sloane et al.*, 1969 refer to the H, G and S matrices as H^T, G^T and S^T matrices, respectively.

[b] *Harwit et al.*, 1970.

[c] *Harwit et al.*, 1974.

[d] As stated in Appendix A, an optical encoding scheme has not yet been found.

Appendix C

Generation of Hadamard Mask Patterns

As explained in Appendix A, for the general case Hadamard encoding of N resolution elements requires N masks each of which is N resolution elements long. However, a subset of Hadamard matrices contains cyclic submatrices which can be used to encode N resolution elements with a single mask $2N$-1 resolution elements long. The use of this single mask instead of N masks is such an important practical advantage that virtually all Hadamard spectrometer codes are based on these cyclic matrices. Therefore, only generation of mask patterns based on these cyclic matrices will be considered in this appendix.

A $(N+1) \times (N+1)$ Hadamard matrix with a cyclic submatrix can be constructed from a pseudo-noise sequence (a PN sequence) of length N by the following procedure. First, a $N \times N$ cyclic matrix is formed using a PN sequence as the first row; each subsequent row is a one-position cyclic shift of the row above it. All shifts must be in the same direction; that is, they must either be all to the left or all to the right. Finally, this $N \times N$ cyclic matrix is converted to an $(N+1) \times (N+1)$ Hadamard matrix by adding a row and column of +1's. To clarify this construction procedure, an example showing the construction of a 8x8 Hadamard matrix is given. The sequence

$$-1 \quad -1 \quad -1 \quad 1 \quad 1 \quad -1 \quad 1 \quad . \qquad \text{(C-1)}$$

is a *PN* sequence of length 7. The 7x7 cyclic matrix constructed from cyclic shifts left of this sequence is

$$\begin{bmatrix} -1 & -1 & -1 & 1 & 1 & -1 & 1 \\ -1 & -1 & 1 & 1 & -1 & 1 & -1 \\ -1 & 1 & 1 & -1 & 1 & -1 & -1 \\ 1 & 1 & -1 & 1 & -1 & -1 & -1 \\ 1 & -1 & 1 & -1 & -1 & -1 & 1 \\ -1 & 1 & -1 & -1 & -1 & 1 & 1 \\ 1 & -1 & -1 & -1 & 1 & 1 & -1 \end{bmatrix} . \qquad \text{(C-2)}$$

Upon addition of a row and column of +1's, this matrix becomes the following 8x8 Hadamard matrix:

$$\begin{bmatrix} 1 & 1 & 1 & 1 & 1 & 1 & 1 & 1 \\ 1 & -1 & -1 & -1 & 1 & 1 & -1 & 1 \\ 1 & -1 & -1 & 1 & 1 & -1 & 1 & -1 \\ 1 & -1 & 1 & 1 & -1 & 1 & -1 & -1 \\ 1 & 1 & 1 & -1 & 1 & -1 & -1 & -1 \\ 1 & 1 & -1 & 1 & -1 & -1 & -1 & 1 \\ 1 & -1 & 1 & -1 & -1 & -1 & 1 & 1 \\ 1 & 1 & -1 & -1 & -1 & 1 & 1 & -1 \end{bmatrix} . \qquad \text{(C-3)}$$

Matrices (C-2) and (C-3) are, respectively, examples of the *G* and *H* matrices defined in Appendix A. As explained in Appendix A, *S* matrices are constructed from *G* matrices by replacing +1's with 0's and -1's with 1's. Therefore, *S* matrices can also be constructed from *PN* sequences. The *S* matrix constructed from the *G* matrix in the above example is given by

$$S = \begin{bmatrix} 1 & 1 & 1 & 0 & 0 & 1 & 0 \\ 1 & 1 & 0 & 0 & 1 & 0 & 1 \\ 1 & 0 & 0 & 1 & 0 & 1 & 1 \\ 0 & 0 & 1 & 0 & 1 & 1 & 1 \\ 0 & 1 & 0 & 1 & 1 & 1 & 0 \\ 1 & 0 & 1 & 1 & 1 & 0 & 0 \\ 0 & 1 & 1 & 1 & 0 & 0 & 1 \end{bmatrix} . \qquad \text{(C-4)}$$

The construction method given above makes construction of cyclic encoding matrices trivial once a *PN* sequence has been constructed. Methods for constructing *PN* sequences are given by *Baumert* [1964]. However, in this appendix a construction method is given for only one type of *PN* sequence; namely, those with $N = 2^n-1$ where n is an integer. An important characteristic of this construction method is that it yields encoding matrices that are compatible with the fast computation algorithm given in Appendix D.

For *PN* sequences of length $N = 2^n-1$, the sequence is most easily generated directly with 0's and 1's rather than with +1's and -1's. If the generalized definition of autocorrelation [*Baumert*, 1964] is used, namely

$$\rho(j) \triangleq \frac{A-D}{A+D} , \qquad \text{(C-5)}$$

then these sequences of 1's and 0's satisfy the requirements of a *PN* sequence. In the above definition A and D are, respectively, the number of agreements and disagreements between the sequence and its cyclic shift of j positions.

If $\rho(0) = 1$ and $\rho(j) = -1/N$ for $j \neq 0$, then the sequence is a *PN* sequence [*Baumert*, 1964]. In order to construct a *PN* sequence of +1's and -1's, the 0's are replaced with +1's and the 1's with -1's. These sequences of 0's and 1's with length 2^n-1 are often called maximal-length sequences (*m*-sequences) [*Peterson* and *Weldon*, 1972]. A method for constructing *m*-sequences from primitive modulo 2 polynomials is described in the following paragraphs.

A sequence of length 2^n-1 can be constructed from a primitive polynomial of degree n. Primitive polynomials are a subset of the set of irreducible polynomials. An irreducible polynomial is a polynomial which cannot be written as the product (modulo 2) of two polynomials of degree greater than 0. An irreducible polynomial is primitive if and only if it is not a factor (modulo 2) of $1-x^p$ for any p less than 2^n-1 (it is a factor when $p = 2^n-1$) [*Peterson* and *Weldon*, 1972]. For example, a primitive polynomial of degree 3 is not a factor of $1-x^p$ for any p less than 7. Since this is an if and only if condition, primitive polynomials of degree n (modulo 2) can be selected from a table of irreducible polynomials like that given by *Golomb* [1967] by selecting those with a period equal to 2^n-1 where n is the degree of the polynomial. A list of irreducible polynomials (modulo 2) with the primitive polynomials identified is given by *Peterson* and *Weldon* [1972]. *Watson* [1962] lists one example of a primitive polynomial for each degree from 1 to 100.

The primitive polynomial tabulated in Table C-1 are taken from his list.

In these lists of polynomials given by Golomb, Peterson and Weldon, octal numbers are used to represent the polynomials. These octal numbers are related to polynomials in the following manner. A modulo 2 polynomial of degree n can be written

$$f(x) = \sum_{i=0}^{n} a_i x^i \quad , \qquad \text{(C-6)}$$

Table C-1. An example primitive polynomial (modulo 2) for each degree from 2 to 15 [*Watson*, 1962].

Degree of polynomial (n)	Period of mask ($N = 2^n-1$)	Primitive polynomial $f(x)$	Octal representation
2	3	x^2+x+1	7
3	7	x^3+x+1	13
4	15	x^4+x+1	23
5	31	x^5+x^2+1	45
6	63	x^6+x+1	103
7	127	x^7+x+1	203
8	255	$x^8+x^4+x^3+x^2+1$	435
9	511	x^9+x^4+1	1021
10	1023	$x^{10}+x^3+1$	2011
11	2047	$x^{11}+x^2+1$	4005
12	4095	$x^{12}+x^6+x^4+x+1$	10123
13	8191	$x^{13}+x^4+x^3+x+1$	20033
14	16383	$x^{14}+x^5+x^3+x+1$	40053
15	32767	$x^{15}+x+1$	100003

where a_i equals either 1 or 0. The octal number used to represent this polynomial is the binary number

$$p = \sum_{i=0}^{n} a_i 2^i \quad , \tag{C-7}$$

converted to base 8. For example, when $f(x) = x^9 + x^4 + 1$, the binary number p is 1,000,010,001, which is 1021 in base 8.

PN sequencies of 0's and 1's with periods given by $N = 2^n - 1$, which are compatible with the fast computation algorithm given in Appendix D, can be generated from primitive polynomials by the following method [*Peterson* and *Weldon*, 1972; *Nelson* and *Fredman*, 1970]. The *PN* sequence can be generated by using the recursion relation

$$e_{m+n} = \sum_{i=0}^{n-1} a_i e_{m+i} \quad , \tag{C-8}$$

where e_k are the elements of the sequence and the summation is done modulo 2; that is, 0 + 0 = 0, 0 + 1 = 1, 1 + 0 = 1, 1 + 1 = 0. To generate the sequence, each of the first n terms, $e_0, \ldots, e_{n-1}$, is set equal to either 0 or 1 with the restriction that they may not all be 0. The remaining $N-n$ elements in the period are generated using Equation (C-8) for each m from 0 to $N-n-1$. Sequences generated from this

recursion relation with different values for $e_0, \ldots, e_{n-1}$ differ only in their starting points.

In order to illustrate this method of generating sequences, a sequence with period 7 is constructed. Since $2^3 - 1 = 7$, a third degree primitive polynomial is required. The third degree primitive polynomial listed in Table C-1 is $f(x) = x^3 + x + 1$, which implies that $a_2 = 0$, $a_1 = 1$ and $a_0 = 1$. Thus, Equation (C-7) becomes

$$e_{m+n} = e_m + e_{m+1} \quad , \tag{C-9}$$

where m goes from 0 to 3 and the addition is modulo 2. Let $e_0 = e_1 = e_2 = 1$. Then, by Equation (C-9),

$$e_3 = e_0 + e_1 = 1 + 1 = 0 \quad , \tag{C-10}$$

$$e_4 = e_1 + e_2 = 1 + 1 = 0 \quad , \tag{C-11}$$

$$e_5 = e_2 + e_3 = 1 + 0 = 1 \quad , \tag{C-12}$$

and

$$e_6 = e_3 + e_4 = 0 + 0 = 0 \quad . \tag{C-13}$$

The generated *PN* sequence is 1110010, which is the same as the first row of the matrix in Equation (C-4). Thus, the 7x7 encoding matrix formed by a cyclic shift left of this *PN* sequence is given in Equation (C-4).

PN sequences can also be generated using an n-stage shift register and modulo 2 adders (these are often called half adders), because the recursion relation of Equation (C-8) describes the operation of the linear sequential switching circuit shown in part (a) of Figure C-1.

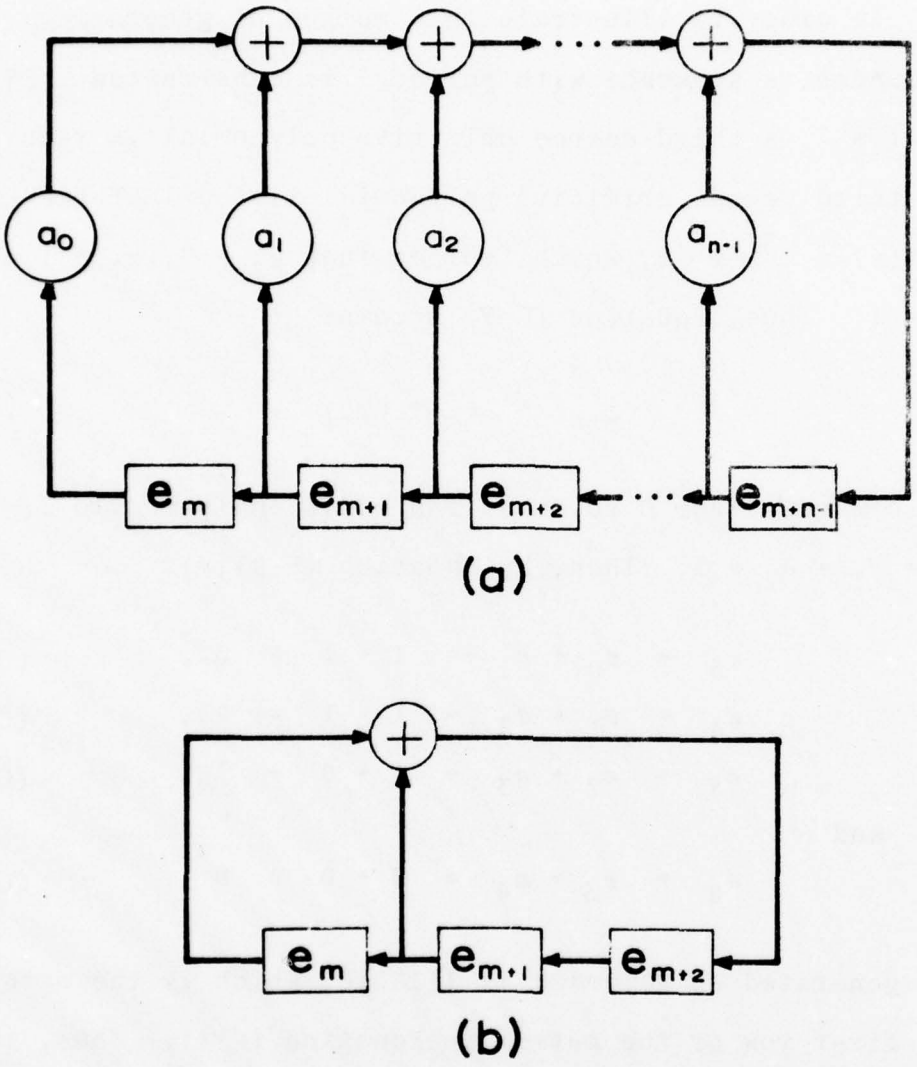


Figure C-1. (a) A general n-stage shift register circuit to generate *PN* sequence with period $N = 2^n - 1$ where the values of (a_i) are determined by a n-th order primitive polynomial. (b) A three-stage shift register circuit based on the primitive polynomial $f(x) = x^3 + x + 1$ which generates the *PN* sequence 1110010.

A three-stage shift-register circuit which generates the *PN* sequence 1110010 is shown in part (b) of Figure C-1.

The cyclic encoding matrices generated from *PN* sequences can be implemented with a mask containing one slot less than two periods of the sequence; that is, $2N-1$ slots. This is accomplished by stepping the mask one slot width at a time past a field stop with an opening the width of N slots. There are N possible successive positions corresponding to the N successive rows of the cyclic encoding matrix. Thus, the $2N-1$ slots for the mask to encode according to Equation (C-4) is specified by the pattern 1110010111001, where a one represents a transparent slot and a zero represents an opaque slot. A computer program was written to generate the pattern for masks with $2N-1$ slots using the recursion relation given in Equation (C-8). This program was used to generate the patterns for the masks constructed in this Hadamard investigation. The computer output from which these masks were constructed constitutes Table C-2.

Table C-2. A $2N$-1 mask pattern for N equal to 511. Codes of 1 and 0 represent transparent and opaque slots, respectively.

Slot	Code	Slot	Code	Slot	Code	Slot	Code	Slot	Code
1	1	51	0	101	0	151	0	201	0
2	1	52	0	102	1	152	0	202	0
3	1	53	1	103	1	153	0	203	0
4	1	54	1	104	0	154	1	204	1
5	1	55	1	105	1	155	0	205	0
6	1	56	0	106	1	156	0	206	1
7	1	57	1	107	0	157	1	207	0
8	1	58	1	108	1	158	1	208	1
9	1	59	0	109	0	159	1	209	1
10	0	60	1	110	1	160	0	210	0
11	0	61	0	111	0	161	0	211	1
12	0	62	0	112	1	162	1	212	0
13	0	63	0	113	1	163	0	213	0
14	0	64	1	114	1	164	1	214	1
15	1	65	1	115	0	165	0	215	1
16	1	66	1	116	0	166	1	216	1
17	1	67	1	117	0	167	0	217	1
18	1	68	0	118	1	168	1	218	1
19	0	69	0	119	0	169	1	219	1
20	1	70	1	120	0	170	0	220	0
21	1	71	1	121	1	171	0	221	1
22	1	72	1	122	1	172	0	222	1
23	1	73	1	123	0	173	0	223	0
24	1	74	1	124	0	174	1	224	0
25	0	75	0	125	0	175	1	225	1
26	0	76	0	126	1	176	0	226	0
27	0	77	1	127	0	177	1	227	0
28	1	78	1	128	0	178	1	228	1
29	0	79	0	129	0	179	1	229	0
30	1	80	1	130	1	180	1	230	0
31	1	81	1	131	0	181	0	231	1
32	1	82	0	132	0	182	1	232	0
33	0	83	0	133	0	183	0	233	1
34	0	84	0	134	0	184	0	234	1
35	1	85	1	135	0	185	1	235	0
36	1	86	0	136	0	186	1	236	1
37	0	87	1	137	0	187	0	237	1
38	0	88	0	138	0	188	1	238	1
39	1	89	1	139	1	189	1	239	1
40	0	90	0	140	0	190	1	240	1
41	0	91	0	141	0	191	0	241	1
42	0	92	1	142	0	192	0	242	0
43	0	93	0	143	0	193	1	243	0
44	0	94	0	144	1	194	0	244	1
45	1	95	0	145	0	195	0	245	0
46	0	96	1	146	0	196	0	246	0
47	0	97	1	147	0	197	1	247	1
48	1	98	1	148	1	198	0	248	1
49	0	99	0	149	1	199	1	249	0
50	1	100	0	150	0	200	0	250	1

251....0	301....0	351....0	401....0	451....1
252....1	302....0	352....1	402....1	452....0
253....0	303....1	353....0	403....0	453....1
254....0	304....0	354....1	404....1	454....0
255....1	305....1	355....1	405....0	455....1
256....1	306....1	356....0	406....1	456....0
257....0	307....0	357....1	407....1	457....0
258....0	308....0	358....1	408....1	458....0
259....1	309....0	359....0	409....1	459....1
260....1	310....1	360....1	410....0	460....0
261....0	311....1	361....1	411....0	461....0
262....0	312....1	362....1	412....1	462....1
263....0	313....0	363....0	413....0	463....0
264....0	314....1	364....1	414....1	464....0
265....0	315....0	365....1	415....1	465....0
266....0	316....1	366....0	416....1	466....0
267....0	317....1	367....0	417....0	467....1
268....1	318....0	368....0	418....1	468....1
269....1	319....0	369....0	419....1	469....0
270....0	320....1	370....0	420....1	470....0
271....0	321....0	371....1	421....0	471....1
272....0	322....1	372....0	422....0	472....1
273....1	323....1	373....1	423....0	473....1
274....1	324....0	374....1	424....0	474....0
275....0	325....0	375....0	425....0	475....0
276....0	326....1	376....1	426....0	476....0
277....1	327....1	377....0	427....1	477....0
278....0	328....1	378....1	428....1	478....1
279....1	329....1	379....1	429....1	479....0
280....0	330....0	380....1	430....0	480....1
281....0	331....0	381....1	431....0	481....1
282....0	332....0	382....1	432....1	482....1
283....1	333....1	383....0	433....1	483....1
284....1	334....1	384....1	434....1	484....0
285....0	335....1	385....0	435....0	485....1
286....1	336....1	386....1	436....1	486....1
287....0	337....1	387....0	437....0	487....0
288....0	338....0	388....1	438....0	488....1
289....1	339....1	389....0	439....1	489....1
290....0	340....1	390....1	440....0	490....0
291....1	341....1	391....0	441....0	491....0
292....1	342....0	392....0	442....1	492....1
293....1	343....1	393....0	443....1	493....1
294....1	344....0	394....0	444....1	494....0
295....1	345....0	395....0	445....1	495....1
296....1	346....0	396....0	446....0	496....0
297....1	347....0	397....1	447....1	497....0
298....0	348....0	398....0	448....0	498....0
299....1	349....1	399....1	449....1	499....0
300....0	350....1	400....0	450....1	500....1

501....1 551....0 601....0 651....0 701....1
502....1 552....0 602....0 652....0 702....0
503....0 553....0 603....1 653....0 703....0
504....1 554....0 604....0 654....0 704....1
505....1 555....0 605....0 655....1 705....0
506....1 556....1 606....0 656....0 706....0
507....1 557....0 607....1 657....0 707....0
508....0 558....0 608....1 658....0 708....1
509....0 559....1 609....1 659....1 709....0
510....0 560....0 610....0 660....1 710....1
511....0 561....1 611....0 661....0 711....0
512....1 562....0 612....0 662....0 712....0
513....1 563....0 613....1 663....0 713....0
514....1 564....1 614....1 664....0 714....0
515....1 565....1 615....0 665....1 715....1
516....1 566....1 616....1 666....0 716....0
517....1 567....0 617....1 667....0 717....1
518....1 568....1 618....0 668....1 718....0
519....1 569....1 619....1 669....1 719....1
520....1 570....0 620....0 670....1 720....1
521....0 571....1 621....1 671....0 721....0
522....0 572....0 622....0 672....0 722....1
523....0 573....0 623....1 673....1 723....0
524....0 574....0 624....1 674....0 724....0
525....0 575....1 625....1 675....1 725....1
526....1 576....1 626....0 676....0 726....1
527....1 577....1 627....0 677....1 727....1
528....1 578....1 628....0 678....0 728....1
529....1 579....0 629....1 679....1 729....1
530....0 580....0 630....0 680....1 730....1
531....1 581....1 631....0 681....0 731....0
532....1 582....1 632....1 682....0 732....1
533....1 583....1 633....1 683....0 733....1
534....1 584....1 634....0 684....0 734....0
535....1 585....1 635....0 685....1 735....0
536....0 586....0 636....0 686....1 736....1
537....0 587....0 637....1 687....0 737....0
538....0 588....1 638....0 688....1 738....0
539....1 589....1 639....0 689....1 739....1
540....0 590....0 640....0 690....1 740....0
541....1 591....1 641....1 691....1 741....0
542....1 592....1 642....0 692....0 742....1
543....1 593....0 643....0 693....1 743....0
544....0 594....0 644....0 694....0 744....1
545....0 595....0 645....0 695....0 745....1
546....1 596....1 646....0 696....1 746....0
547....1 597....0 647....0 697....1 747....1
548....0 598....1 648....0 698....0 748....1
549....0 599....0 649....0 699....1 749....1
550....1 600....1 650....1 700....1 750....1

751....1 801....0 851....1 901....1 951....0
752....1 802....1 852....1 902....0 952....0
753....0 803....1 853....0 903....0 953....1
754....0 804....1 854....1 904....0 954....1
755....1 805....1 855....0 905....0 955....1
756....0 806....1 856....0 906....0 956....1
757....0 807....1 857....0 907....0 957....0
758....1 808....1 858....0 908....1 958....1
759....1 809....0 859....0 909....0 959....0
760....0 810....1 860....1 910....1 960....1
761....1 811....0 861....1 911....0 961....1
762....0 812....0 862....0 912....0 962....1
763....1 813....0 863....1 913....1 963....0
764....0 814....1 864....0 914....0 964....1
765....0 815....0 865....1 915....1 965....0
766....1 816....1 866....1 916....0 966....1
767....1 817....1 867....0 917....1 967....0
768....0 818....0 868....1 918....1 968....0
769....0 819....0 869....1 919....1 969....0
770....1 820....0 870....0 920....1 970....1
771....1 821....1 871....1 921....0 971....0
772....0 822....1 872....1 922....0 972....0
773....0 823....1 873....1 923....1 973....1
774....0 824....0 874....0 924....0 974....0
775....0 825....1 875....1 925....1 975....0
776....0 826....0 876....1 926....1 976....0
777....0 827....1 877....0 927....1 977....0
778....0 828....1 878....0 928....0 978....1
779....1 829....0 879....0 929....1 979....1
780....1 830....0 880....0 930....1 980....0
781....0 831....1 881....0 931....1 981....0
782....0 832....0 882....1 932....0 982....1
783....0 833....1 883....0 933....0 983....1
784....1 834....1 884....1 934....0 984....1
785....1 835....0 885....1 935....0 985....0
786....0 836....0 886....0 936....0 986....0
787....0 837....1 887....1 937....0 987....0
788....1 838....1 888....0 938....1 988....0
789....0 839....1 889....1 939....1 989....1
790....1 840....1 890....1 940....1 990....0
791....0 841....0 891....1 941....0 991....1
792....0 842....0 892....1 942....0 992....1
793....0 843....0 893....1 943....1 993....1
794....1 844....1 894....0 944....1 994....1
795....1 845....1 895....1 945....1 995....0
796....0 846....1 896....0 946....0 996....1
797....1 847....1 897....1 947....1 997....1
798....0 848....1 898....0 948....0 998....0
799....0 849....0 899....1 949....0 999....1
800....1 850....1 900....0 950....1 1000....1

```
1001....0
1002....0
1003....1
1004....1
1005....0
1006....1
1007....0
1008....0
1009....0
1010....0
1011....1
1012....1
1013....1
1014....0
1015....1
1016....1
1017....1
1018....1
1019....0
1020....0
1021....0
```

Appendix D

Multiplication by the Inverse of the S Matrix Using the Fast Hadamard Transform

Since, as shown in Appendix A, Hadamard encoding can be represented by a matrix equation, recovery of the encoded information requires multiplication by the inverse of the encoding matrix. The inverses of the encoding matrices H, G, and S, defined in Appendix A, are given by *Sloane et al.* [1969]. The inverse of the matrix S is

$$S^{-1} = \frac{2}{N+1}\left(2S^T - J\right) \quad , \qquad \text{(D-1)}$$

where N is the dimension of the matrix S and J is an $N \times N$ matrix of +1's. Equation (D-1) indicates that the inverse of S can be formed by transposing the rows and columns of S and replacing each 1 with $2/(N+1)$ and each 0 with $-2/(N+1)$. If each row of S is generated by a cyclic shift left of the row above, S is unchanged by the transpose operation. Thus, for S matrices generated by a shift left, the transpose operation is not required.

However, if the multiplication by S^{-1} is performed using the conventional multiplication algorithm, many operations are redundant. The number of required operations can be significantly reduced by performing redundant operations only once. The elimination of redundant operations is the essential idea on which both the fast Hadamard transform [*Ahmed et al.*, 1971] and the fast Fourier transform

[*Brigham*, 1974] are based. In fact, *Andrews* [1970] has shown that both the fast Hadamard transform (FHT) and the fast Fourier transform (FFT) are specific examples of the same general transform. The algorithm described in this appendix makes use of the FHT to reduce the number of operations required when multiplying a vector by the S^{-1} matrix. This algorithm was published by *Nelson* and *Fredman* [1970] and is valid if the Hadamard mask pattern is generated from a primitive polynomial using the method described in Appendix C.

This algorithm is introduced by using it to recover the spectrum from a singly-encoded Hadamard spectrometer described by the following matrix equation:

$$\begin{bmatrix} m_1 \\ m_2 \\ m_3 \\ m_4 \\ m_5 \\ m_6 \\ m_7 \end{bmatrix} = \begin{bmatrix} 1 & 1 & 1 & 0 & 0 & 1 & 0 \\ 1 & 1 & 0 & 0 & 1 & 0 & 1 \\ 1 & 0 & 0 & 1 & 0 & 1 & 1 \\ 0 & 0 & 1 & 0 & 1 & 1 & 1 \\ 0 & 1 & 0 & 1 & 1 & 1 & 0 \\ 1 & 0 & 1 & 1 & 1 & 0 & 0 \\ 0 & 1 & 1 & 1 & 0 & 0 & 1 \end{bmatrix} \begin{bmatrix} x_1 \\ x_2 \\ x_3 \\ x_4 \\ x_5 \\ x_6 \\ x_7 \end{bmatrix}, \qquad \text{(D-2)}$$

where x_i and m_i (i = 1, ..., 7) are, respectively, the spectral elements and the encoded measurements. As shown in Appendix C, the 7x7 matrix in Equation (D-2) is a S matrix. No information is lost if Equation (D-2) is permuted and a row and column of 0's are added to form the following matrix equation:

$$\begin{bmatrix} 0 \\ m_3 \\ m_5 \\ m_2 \\ m_4 \\ m_6 \\ m_7 \\ m_1 \end{bmatrix} = \begin{bmatrix} 0 & 0 & 0 & 0 & 0 & 0 & 0 & 0 \\ 0 & 1 & 0 & 0 & 1 & 0 & 1 & 1 \\ 0 & 0 & 1 & 0 & 1 & 1 & 1 & 0 \\ 0 & 1 & 1 & 0 & 0 & 1 & 0 & 1 \\ 0 & 0 & 0 & 1 & 0 & 1 & 1 & 1 \\ 0 & 1 & 0 & 1 & 1 & 1 & 0 & 0 \\ 0 & 0 & 1 & 1 & 1 & 0 & 0 & 1 \\ 0 & 1 & 1 & 1 & 0 & 0 & 1 & 0 \end{bmatrix} \begin{bmatrix} 0 \\ x_1 \\ x_2 \\ x_3 \\ x_4 \\ x_5 \\ x_6 \\ x_7 \end{bmatrix} . \qquad \text{(D-3)}$$

Let the vector $\bar{x}$ be defined by the following equation:

$$\begin{bmatrix} \bar{x}_1 \\ \bar{x}_2 \\ \bar{x}_3 \\ \bar{x}_4 \\ \bar{x}_5 \\ \bar{x}_6 \\ \bar{x}_7 \\ \bar{x}_8 \end{bmatrix} \triangleq \begin{bmatrix} 1 & 1 & 1 & 1 & 1 & 1 & 1 & 1 \\ 1 & -1 & 1 & -1 & 1 & -1 & 1 & -1 \\ 1 & 1 & -1 & -1 & 1 & 1 & -1 & -1 \\ 1 & -1 & -1 & 1 & 1 & -1 & -1 & 1 \\ 1 & 1 & 1 & 1 & -1 & -1 & -1 & -1 \\ 1 & -1 & 1 & -1 & -1 & 1 & -1 & 1 \\ 1 & 1 & -1 & -1 & -1 & -1 & 1 & 1 \\ 1 & -1 & -1 & 1 & -1 & 1 & 1 & -1 \end{bmatrix} \begin{bmatrix} 0 \\ m_1 \\ m_2 \\ m_3 \\ m_4 \\ m_5 \\ m_6 \\ m_7 \end{bmatrix} =$$

$$\begin{bmatrix} 0 & 4 & 4 & 4 & 4 & 4 & 4 & 4 \\ 0 & -4 & 0 & 0 & 0 & 0 & 0 & 0 \\ 0 & 0 & -4 & 0 & 0 & 0 & 0 & 0 \\ 0 & 0 & 0 & 0 & -4 & 0 & 0 & 0 \\ 0 & 0 & 0 & -4 & 0 & 0 & 0 & 0 \\ 0 & 0 & 0 & 0 & 0 & 0 & 0 & -4 \\ 0 & 0 & 0 & 0 & 0 & -4 & 0 & 0 \\ 0 & 0 & 0 & 0 & 0 & 0 & -4 & 0 \end{bmatrix} \begin{bmatrix} 0 \\ x_1 \\ x_2 \\ x_3 \\ x_4 \\ x_5 \\ x_6 \\ x_7 \end{bmatrix} . \qquad \text{(D-4)}$$

The matrix of 1's and -1's in Equation (D-4) is a Hadamard matrix. It follows from Equation (D-4) that

$$\begin{bmatrix} x_1 \\ x_2 \\ x_3 \\ x_4 \\ x_5 \\ x_6 \\ x_7 \end{bmatrix} = -\frac{1}{4} \begin{bmatrix} \bar{x}_2 \\ \bar{x}_3 \\ \bar{x}_5 \\ \bar{x}_4 \\ \bar{x}_7 \\ \bar{x}_8 \\ \bar{x}_6 \end{bmatrix} . \qquad \text{(D-5)}$$

In this example, the vector x was recovered from the measurement vector m in three steps. First, the measurement vector was permuted and augmented with a zero element. Second, this permuted and augmented vector was multiplied by a Hadamard matrix. Third, the first element of the resulting vector $\bar{x}$ was deleted, and its remaining elements were permuted and divided by $-1/2(N+1)$. This indirect method of recovering the vector x can be accomplished faster than multiplying the measurement vector by S inverse because the matrix multiplication required in the second step can be performed using the FHT, and the permutations required in the first and third steps can be performed rapidly.

The three steps of the algorithm will now be explained for the general case. The specific example used above will be used to elucidate the algorithm.

Step 1 of the algorithm

In this step a new vector $\bar{m}_\pi$ is formed from the vector m resulting from multiplying the vector x by the S matrix. For a singly-encoded Hadamard spectrometer, the vector m corresponds to the measurements taken with the spectrometer. In order to form this new vector $\bar{m}_\pi$, the vector m is first permuted to form a vector m_π. Then m_π is augmented with a zero to form

$$\bar{m}_\pi = \begin{bmatrix} 0 \\ \hline m_\pi \end{bmatrix} . \qquad \text{(D-6)}$$

The permutation required to convert the vector m to m_π is referred to as the π_1 permutation. When using the algorithm for data reduction, the permutation need only be generated once since it can be easily saved and applied to each set of data. The permutation π_1 can be generated using the following procedure. The transpose of the S matrix is represented by

$$A = \begin{bmatrix} a_{11} & \cdots & a_{1N} \\ \vdots & & \vdots \\ a_{N1} & \cdots & a_{NN} \end{bmatrix} , \qquad \text{(D-7)}$$

where $N = 2^n-1$. The first n rows of this matrix are represented by

$$A_n = \begin{bmatrix} a_{11} & \cdots & a_{1N} \\ \vdots & & \vdots \\ a_{n1} & \cdots & a_{nN} \end{bmatrix} . \qquad \text{(D-8)}$$

For the example,

$$A_3 = \begin{bmatrix} 1 & 1 & 1 & 0 & 0 & 1 & 0 \\ 1 & 1 & 0 & 0 & 1 & 0 & 1 \\ 1 & 0 & 0 & 1 & 0 & 1 & 1 \end{bmatrix} . \qquad \text{(D-9)}$$

The permutation $\pi_1(j) = l$, $j = 1, \ldots, N$, where l is the base 10 equivalent of the binary number represented by the elements in the j-th column of A_n. The most significant binary bit is represented by the bottom row of A_n; that is, l is the base 10 equivalent of the base 2 number $a_{nj}, \ldots, a_{1j}$. The permutation π_1 for the example is tabulated in Table D-1.

Table D-1. The permutation π_1 for the singly-encoded Hadamard spectrometer example described by Equation (D-2).

j	$a_{nj}, \ldots, a_{ij}$	l
1	111	7
2	011	3
3	001	1
4	100	4
5	010	2
6	101	5
7	110	6

The permutation $\pi_1(j) = l$ is implemented by making the j-th element of the measurement vector m the l-th component of the permuted measurement vector m_π. The measurement vector for the example can be represented by

$$m = (m_1, m_2, m_3, m_4, m_5, m_6, m_7)^T \quad . \tag{D-10}$$

It follows from Table D-1 that for the example

$$m_\pi = (m_3, m_5, m_2, m_4, m_6, m_7, m_1)^T \quad . \tag{D-11}$$

By use of Equations (D-6) and (D-11), the augmented vector $\bar{m}_\pi$ for the example can be represented by

$$\bar{m}_\pi = (0, m_3, m_5, m_2, m_4, m_6, m_7, m_1)^T \quad . \tag{D-12}$$

It is noted that the vector to the left of the equal sign in Equation (D-3) is identical to the vector of Equation (D-12).

Step 2 of the algorithm

The second step consists of using the FHT to multiply the vector $\bar{m}_\pi$ by a Hadamard matrix in natural form. In this appendix, a Hadamard matrix which can be generated from

$$H_2 = \begin{bmatrix} 1 & 1 \\ 1 & -1 \end{bmatrix} \tag{D-13}$$

by the recursion relation

$$H_{2k} = \begin{bmatrix} H_k & H_k \\ H_k & -H_k \end{bmatrix} . \qquad \text{(D-14)}$$

is referred to as a Hadamard matrix in natural form. The subscripts in Equation (D-14) indicate the dimension of the matrix; that is, H_k is a kxk matrix.

The number of sign changes along a row in a Hadamard matrix is called the sequency of that row [*Harmuth*, 1972]. It follows from Equations (D-13) and (D-14) that

$$H_4 = \begin{bmatrix} 1 & 1 & 1 & 1 \\ 1 & -1 & 1 & -1 \\ 1 & 1 & -1 & -1 \\ 1 & -1 & -1 & 1 \end{bmatrix} \begin{matrix} \text{Sequency} \\ 0 \\ 3 \\ 1 \\ 2 \end{matrix} \qquad \text{(D-15)}$$

and

$$H_8 = \begin{bmatrix} 1 & 1 & 1 & 1 & 1 & 1 & 1 & 1 \\ 1 & -1 & 1 & -1 & 1 & -1 & 1 & -1 \\ 1 & 1 & -1 & -1 & 1 & 1 & -1 & -1 \\ 1 & -1 & -1 & 1 & 1 & -1 & -1 & 1 \\ 1 & 1 & 1 & 1 & -1 & -1 & -1 & -1 \\ 1 & -1 & 1 & -1 & -1 & 1 & -1 & 1 \\ 1 & 1 & -1 & -1 & -1 & -1 & 1 & 1 \\ 1 & -1 & -1 & 1 & -1 & 1 & 1 & -1 \end{bmatrix} \begin{matrix} \text{Sequency} \\ 0 \\ 7 \\ 3 \\ 4 \\ 1 \\ 6 \\ 2 \\ 5 \end{matrix} , \qquad \text{(D-16)}$$

where the sequency of each row is indicated to the right of these matrices. The Hadamard matrices in Equations (D-16) and (D-4) are identical.

If the rows of a Hadamard matrix in natural form are rearranged in order of increasing sequency, the Hadamard matrix is said to be in ordered form. FHT algorithms exist for both the natural [*Nelson* and *Fredman*, 1970; *Andrews*, 1970; *Ahmed et al.*, 1971] and ordered [*Manz*, 1972; *Larson*, 1976] forms. The FHT for the natural form is used in the algorithm described in this appendix. Inasmuch as the rows of Hadamard matrices in both natural and ordered forms are Walsh functions [*Harmuth*, 1972], the FHT is sometimes called the fast Walsh transform.

Fast transform algorithms can be found if the transform matrix can be factored into matrices with many zero elements [*Andrews*, 1970]. The matrix in Equation (D-16) can be factored as

$$H_8 = W_3 W_2 W_1 \quad , \tag{D-17}$$

where

$$W_1 = \begin{bmatrix} 1 & 1 & 0 & 0 & 0 & 0 & 0 & 0 \\ 1 & -1 & 0 & 0 & 0 & 0 & 0 & 0 \\ 0 & 0 & 1 & 1 & 0 & 0 & 0 & 0 \\ 0 & 0 & 1 & -1 & 0 & 0 & 0 & 0 \\ 0 & 0 & 0 & 0 & 1 & 1 & 0 & 0 \\ 0 & 0 & 0 & 0 & 1 & -1 & 0 & 0 \\ 0 & 0 & 0 & 0 & 0 & 0 & 1 & 1 \\ 0 & 0 & 0 & 0 & 0 & 0 & 1 & -1 \end{bmatrix} , \tag{D-18}$$

$$W_2 = \begin{bmatrix} 1 & 0 & 1 & 0 & 0 & 0 & 0 & 0 \\ 0 & 1 & 0 & 1 & 0 & 0 & 0 & 0 \\ 1 & 0 & -1 & 0 & 0 & 0 & 0 & 0 \\ 0 & 1 & 0 & -1 & 0 & 0 & 0 & 0 \\ 0 & 0 & 0 & 0 & 1 & 0 & 1 & 0 \\ 0 & 0 & 0 & 0 & 0 & 1 & 0 & 1 \\ 0 & 0 & 0 & 0 & 1 & 0 & -1 & 0 \\ 0 & 0 & 0 & 0 & 0 & 1 & 0 & -1 \end{bmatrix} , \qquad \text{(D-19)}$$

and

$$W_3 = \begin{bmatrix} 1 & 0 & 0 & 0 & 1 & 0 & 0 & 0 \\ 0 & 1 & 0 & 0 & 0 & 1 & 0 & 0 \\ 0 & 0 & 1 & 0 & 0 & 0 & 1 & 0 \\ 0 & 0 & 0 & 1 & 0 & 0 & 0 & 1 \\ 1 & 0 & 0 & 0 & -1 & 0 & 0 & 0 \\ 0 & 1 & 0 & 0 & 0 & -1 & 0 & 0 \\ 0 & 0 & 1 & 0 & 0 & 0 & -1 & 0 \\ 0 & 0 & 0 & 1 & 0 & 0 & 0 & -1 \end{bmatrix} . \qquad \text{(D-20)}$$

The matrix in Equation (D-16) can also be factored as

$$H_8 = Q_3 Q_2 Q_1 , \qquad \text{(D-21)}$$

where

$$Q_1 = \begin{bmatrix} 1 & 0 & 0 & 0 & 1 & 0 & 0 & 0 \\ 0 & 1 & 0 & 0 & 0 & 1 & 0 & 0 \\ 0 & 0 & 1 & 0 & 0 & 0 & 1 & 0 \\ 0 & 0 & 0 & 1 & 0 & 0 & 0 & 1 \\ 1 & 0 & 0 & 0 & -1 & 0 & 0 & 0 \\ 0 & 1 & 0 & 0 & 0 & -1 & 0 & 0 \\ 0 & 0 & 1 & 0 & 0 & 0 & -1 & 0 \\ 0 & 0 & 0 & 1 & 0 & 0 & 0 & -1 \end{bmatrix} , \qquad \text{(D-22)}$$

$$Q_2 = \begin{bmatrix} 1 & 0 & 1 & 0 & 0 & 0 & 0 & 0 \\ 0 & 1 & 0 & 1 & 0 & 0 & 0 & 0 \\ 1 & 0 & -1 & 0 & 0 & 0 & 0 & 0 \\ 0 & 1 & 0 & -1 & 0 & 0 & 0 & 0 \\ 0 & 0 & 0 & 0 & 1 & 0 & 1 & 0 \\ 0 & 0 & 0 & 0 & 0 & 1 & 0 & 1 \\ 0 & 0 & 0 & 0 & 1 & 0 & -1 & 0 \\ 0 & 0 & 0 & 0 & 0 & 1 & 0 & -1 \end{bmatrix} , \qquad \text{(D-23)}$$

and

$$Q_3 = \begin{bmatrix} 1 & 1 & 0 & 0 & 0 & 0 & 0 & 0 \\ 1 & -1 & 0 & 0 & 0 & 0 & 0 & 0 \\ 0 & 0 & 1 & 1 & 0 & 0 & 0 & 0 \\ 0 & 0 & 1 & -1 & 0 & 0 & 0 & 0 \\ 0 & 0 & 0 & 0 & 1 & 1 & 0 & 0 \\ 0 & 0 & 0 & 0 & 1 & -1 & 0 & 0 \\ 0 & 0 & 0 & 0 & 0 & 0 & 1 & 1 \\ 0 & 0 & 0 & 0 & 0 & 0 & 1 & -1 \end{bmatrix} . \qquad \text{(D-24)}$$

A third factorization of H_8 is

$$H_8 = P_3 P_2 P_1 , \qquad \text{(D-25)}$$

where

$$P_1 = P_2 = P_3 = \begin{bmatrix} 1 & 1 & 0 & 0 & 0 & 0 & 0 & 0 \\ 0 & 0 & 1 & 1 & 0 & 0 & 0 & 0 \\ 0 & 0 & 0 & 0 & 1 & 1 & 0 & 0 \\ 0 & 0 & 0 & 0 & 0 & 0 & 1 & 1 \\ 1 & -1 & 0 & 0 & 0 & 0 & 0 & 0 \\ 0 & 0 & 1 & -1 & 0 & 0 & 0 & 0 \\ 0 & 0 & 0 & 0 & 1 & -1 & 0 & 0 \\ 0 & 0 & 0 & 0 & 0 & 0 & 1 & -1 \end{bmatrix} . \qquad \text{(D-26)}$$

Equations (D-17), (D-21), and (D-25) correspond, respectively, to the FHT algorithms of *Nelson* and *Fredman*, [1970], *Ahmed et al.*, [1971], and *Andrews*, [1970]. In each case, the matrix H_8 is factored into three matrices each with only two nonzero elements per row. Thus, to multiply a vector by one of the rows requires only one addition or subtraction. Therefore, since H_8 can be factored into three matrices each with eight such rows, multiplication of a vector by H_8 requires only $3 \times 8 = 24$ additions or subtractions.

In general, multiplication of a vector by H_N requires $N \log_2 N$ additions or subtractions. Signal-flow graphs are helpful in identifying the pattern of the operations required. Signal-flow graphs for

$$t = H_8 y \qquad \text{(D-27)}$$

with the factorizations given in Equation (D-17), (D-21) and (D-25) are given in Figure D-1, where $y = (y_1, \ldots, y_8)$ and $t = (t_1, \ldots, t_8)^T$. The columns of nodes numbered 1, 2, and 3 in Figure D-1 correspond to multiplication by the matrices which have subscriptions of 1, 2, and 3 in Equations (D-17), (D-21) and (D-25).

Any FHT algorithm for Hadamard matrices in natural form can be used to perform step 2. However, only the algorithm given by *Nelson* and *Fredman* [1972] is described in further detail. A signal-flow for their FHT algorithm is given in Figure D-2. The form of the signal-flow graphs in Figure D-2

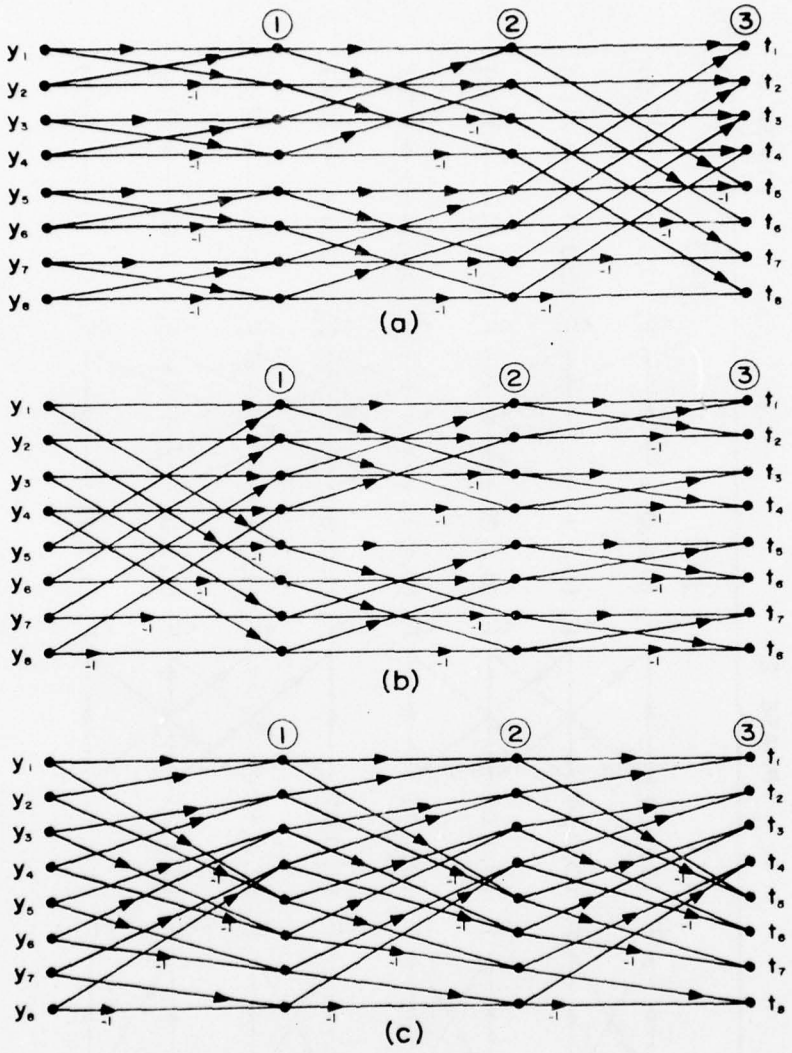


Figure D-1. FHT signal flow graphs. (a), (b), and (c) correspond, respectively, to Equations (D-17), (D-21), and (D-25).

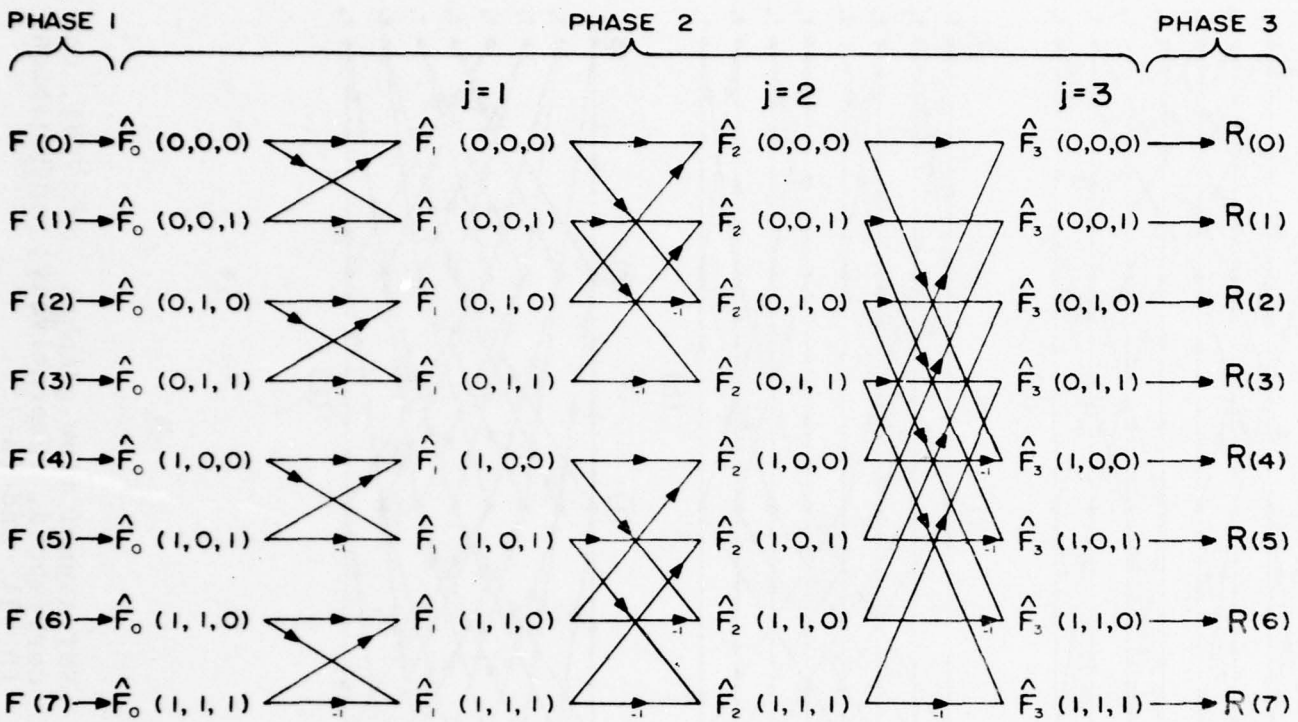


Figure D-2. The signal flow graph for the FHT algorithm of *Nelson* and *Fredman* [1972] with $N = 7$.

and part (a) of Figure D-1 are identical; only the notation is different. Their FHT algorithm consists of three phases.

Phase 1 of the FHT algorithm. Let the vector to be transformed be represented by $[F(0), \ldots, F(2^n-1)]$, where n is an integer. For the binary n tuples $(\mu_{n-1}, \mu_{n-2}, \ldots, \mu_0)$, set

$$\hat{F}_0(\mu_{n-1}, \mu_{n-2}, \ldots, \mu_0) = F\left(\sum_{j=0}^{n-1} 2^j \mu_j\right) . \quad \text{(D-28)}$$

Equation (D-28) simply means that $\hat{F}_0(\mu_{n-1}, \ldots, \mu_0)$ is set equal to $F(k)$, where $\mu_{n-1}, \mu_{n-2}, \ldots, \mu_0$ is the base 2 number corresponding to the base 10 number k. Thus, as shown in Figure D-2, $\hat{F}_0(1,1,0) = F(6)$ since n equals 3 for a vector with eight elements.

Phase 2 of the FHT algorithm. The required additions and subtractions are identified using the recursion relation

$$\hat{F}_j(\mu_{n-1},\ldots,\mu_j,\mu_{j-1},\ldots,\mu_0) = \hat{F}_{j-1}(\mu_{n-1},\ldots,\mu_j,0,\mu_{j-2},\ldots,\mu_0)$$

$$+ (-1)^{\mu_{j-1}} \hat{F}_{j-1}(\mu_{n-1},\ldots,\mu_j,1,\mu_{j-2},\ldots,\mu_0) , \quad \text{(D-29)}$$

for $1 \leq j \leq n$. For example, $\hat{F}_2(0,1,1) = \hat{F}_1(0,0,1) - \hat{F}_1(0,1,1)$ in Figure D-2.

Phase 3 of the FHT algorithm. The third phase is similar to the first phase. Set

$$R\left(\sum_{j=0}^{n-1} 2^j \mu_j\right) = \hat{F}_n(\mu_{n-1}, \ldots, \mu_0) \quad , \qquad \text{(D-30)}$$

for the 2^n binary n tuples $(\mu_{n-1}, \ldots, \mu_0)$. The vector $[R(0), \ldots, R(2^n-1)]$ is the Hadamard transform of the vector $[F(0), \ldots, F(2^n-1)]$.

In summary, step 2 of the algorithm consists of transforming the vector $\bar{m}_\pi$ into the vector $\bar{x}$ by means of the FHT.

Step 3 of the algorithm

In this step the vector x is recovered from the vector $\bar{x}$. This recovery is accomplished by deleting the first element of the vector $\bar{x}$ to form the vector $\hat{x}$. Then $\hat{x}$ is permuted to form the vector x_π. Finally, each component of x_π is multiplied by $-2/(N+1)$ to recover the vector x.

The permutation required to convert the vector $\hat{x}$ to the vector x_π is referred to as the π_2 permutation. Just as for the π_1 permutation, the π_2 permutation need only be generated once when doing data reduction because it can be easily saved and applied to each set of data. The permutation π_2 can be generated using the following procedure. The columns of the matrix A given in Equation (D-7) are permuted to form a matrix B whose l-th column is the j-th column of A, where $\pi_1(j) = l$. Thus, for the singly-encoded Hadamard example described by Equation (D-2), the matrix B is given by

$$(j = \quad 3,\ 5,\ 2,\ 4,\ 6,\ 7,\ 1)$$

$$B = \begin{bmatrix} 1 & 0 & 1 & 0 & 1 & 0 & 1 \\ 0 & 1 & 1 & 0 & 0 & 1 & 1 \\ 0 & 0 & 0 & 1 & 1 & 1 & 1 \\ 1 & 1 & 0 & 0 & 1 & 1 & 0 \\ 0 & 1 & 1 & 1 & 1 & 0 & 0 \\ 1 & 1 & 0 & 1 & 0 & 0 & 1 \\ 1 & 0 & 1 & 1 & 0 & 1 & 0 \end{bmatrix} , \qquad \text{(D-31)}$$

$$(l = \quad 1,\ 2,\ 3,\ 4,\ 5,\ 6,\ 7)$$

where the values of j and l above and below the columns of B identify the column number of each column in the matrices A and B, respectively. For example, the second column of this B matrix is the fifth column of the corresponding A matrix. The π_1 permutation used to form this B matrix is tabulated in Table D-1.

In order to compute the permutation π_2, a matrix C is formed by extracting n columns of the matrix B. This matrix is given by

$$C = \begin{bmatrix} c_{11} & \cdots & c_{1n} \\ \vdots & & \vdots \\ c_{N1} & & c_{Nn} \end{bmatrix} , \qquad \text{(D-32)}$$

where the j-th column of C is the 2^{j-1} column of B. For the example, $n = 3$. Therefore, since $2^{1-1} = 1$, $2^{2-1} = 2$, and $2^{3-1} = 4$, the C matrix for the example is formed from the first, second and fourth columns of the B matrix in Equation (D-31). Consequently, for the example

$$C = \begin{bmatrix} 1 & 0 & 0 \\ 0 & 1 & 0 \\ 0 & 0 & 1 \\ 1 & 1 & 0 \\ 0 & 1 & 1 \\ 1 & 1 & 1 \\ 1 & 0 & 1 \end{bmatrix} . \qquad \text{(D-33)}$$

The permutation π_2 is computed from the matrix C. The permutation $\pi_2(k) = l$, $l = 1, \ldots, N$, where k is the base 10 equivalent of the l-th row of the C matrix. The most significant binary bit is represented by the entry in the right-hand column of matrix C. Thus, k is the base 10 equivalent of the binary number $c_{ln} \ldots c_{l1}$. The permutation π_2 for the example is tabulated in Table D-2.

Table D-2. The permutation π_2 for the singly-encoded Hadamard spectrometer described by Equation (D-2).

l	$c_{ln} \ldots c_{l1}$	k
1	001	1
2	010	2
3	100	4
4	011	3
5	110	6
6	111	7
7	101	5

Step 3 of the algorithm can be summarized as follows. The vector $\bar{x}$ is converted to the vector $\hat{x}$ by deleting the first element. Then permutation $\pi_2(k) = l$ is used to convert $\hat{x}$ to the vector x_π. The l-th component of x_π is the k-th component of $\hat{x}$. The vector x is recovered by multiplying each element of x_π by $-2/(N+1)$. Thus, for the example, if the vector $\bar{x}$ resulting from step 2 of the algorithm is represented by

$$\bar{x} = (\bar{x}_1, \bar{x}_2, \bar{x}_3, \bar{x}_4, \bar{x}_5, \bar{x}_6, \bar{x}_7, \bar{x}_8)^T \quad , \tag{D-34}$$

then

$$\hat{x} = (\bar{x}_2, \bar{x}_3, \bar{x}_4, \bar{x}_5, \bar{x}_6, \bar{x}_7, \bar{x}_8)^T \quad . \tag{D-35}$$

It follows from Table D-2 and Equation (D-35) that for the example

$$x_\pi = (\bar{x}_2, \bar{x}_3, \bar{x}_5, \bar{x}_4, \bar{x}_7, \bar{x}_8, \bar{x}_6)^T \quad . \tag{D-36}$$

Multiplying each element of the vector in Equation (D-36) by $-2/(N+1)$, where $N = 7$, yields

$$x = -\frac{1}{4}(\bar{x}_2, \bar{x}_3, \bar{x}_5, \bar{x}_4, \bar{x}_7, \bar{x}_8, \bar{x}_6)^T \quad . \tag{D-37}$$

Equation (D-37) is identical to Equation (D-5).

Evaluation of the algorithm

The algorithm described in this appendix is evaluated using the following criteria: first, the number of operations required, and second, the number of computer storage

locations required. The algorithm is compared, using these two criteria, to conventional multiplication by S^{-1} as well as to a method which exploits some of the properties of the S^{-1} matrix. In the following evaluation, N is the number of elements in the vector x. Throughout this appendix, the vector x is the vector recovered by multiplying the data vector by S^{-1}.

If conventional multiplication is used to recover the N elements of x, then N^2 multiplications, $N(N-1)$ addition-subtraction operations, and N^2 storage locations are required. However, the number of multiplications as well as the number of storage locations can be reduced by exploiting the properties of S^{-1}. As can be seen from Equation (D-1), the matrix S^{-1} can be represented by the scalar $2/(N+1)$ times a NxN matrix of +1's and -1's. By exploiting this representation of S^{-1}, multiplication by S^{-1} can be accomplished with $N(N-1)$ addition-subtraction operations and N multiplications. If the S matrix is constructed using the method described in Appendix C, the matrix S^{-1} is cyclic. Therefore it is only necessary to store one row of S^{-1} which requires N storage locations. It is also necessary to have N storage locations to store the N elements of x. Thus, multiplication by S^{-1} can be accomplished using $2N$ storage locations if the cyclic property of S^{-1} inverse is exploited. In this appendix, the algorithm which exploits the two properties of S^{-1} in the manner described above is called the exploited algorithm.

The algorithm described in this appendix required $(N+1)\log(N+1)$ addition-subtraction operations, N multiplications, and two permutations of N-dimensional vectors. In the remainder of this appendix this algorithm is referred to as the fast algorithm, because it requires significantly fewer operations than the conventional multiplication algorithm or the exploited algorithm. The permutations required by the fast algorithm can be accomplished by exchanging the contents of $2N$ storage locations.

The fast algorithm requires storage locations to perform the FHT and also to store the permutations π_1 and π_2. The storage requirements of the FHT can be deduced from the signal-flow graph in Figure D-1. The minimum storage requirement for the FHT is $N+2$. However, in order to achieve this minimum, $[(N+1)/2]\log_2(N+1)$ exchanges of storage locations are required. The number of exchanges of storage locations can be reduced to zero if $2(N+1)$ storage locations are allocated to perform the FHT. Storage of the π_1 and π_2 permutations requires $2N$ storage locations. Thus, the fast algorithm requires $2(N+1) + 2N = 4N + 2$ storage locations.

The required number of operations and storage locations for the conventional multiplication algorithm, the exploited algorithm, and the fast algorithm are summarized in Table D-3.

Table D-3. The required number of computer storage locations and operations for three algorithms which implement multiplication by S^{-1}.

Algorithm	Storage locations	Operations		
		Addition-subtraction	Multiplication	Exchange contents of storage locations
Conventional multiplication	N^2	$N(N-1)$	N^2	0
Exploited	$2N$	$N(N-1)$	N	0
Fast	$4N+2$	$(N+1)\log_2(N+1)$	N	$2N$

The speed of computation advantage of the fast algorithm over the exploited algorithm results because the fast algorithm requires fewer addition-subtraction operations than the exploited algorithm. The number of multiplications required by both of these algorithms is the same. A comparison of the number of addition-subtraction and exchange operations required for these two algorithms is given in Table D-4. As can be seen from this table, the ratio of the addition-subtraction operations for these two algorithms increases rapidly as N increases. For N = 511, the value of N for the Hadamard masks used in the spectrometer constructed for this Hadamard study, the fast algorithm requires a factor of 57 fewer addition-subtraction operations than the exploited algorithm. For N = 511, the number of addition-subtraction and exchange operations is a factor of 46 less for the fast algorithm than for the exploited algorithm. Since the time required for the computer to exchange the contents of two storage locations is on the order of the time required to perform an addition-subtraction operation, multiplication by S^{-1} for N = 511 can be accomplished 46 times faster using the fast algorithm than by using the exploited algorithm.

Computer programs to implement the algorithm

A basic set of computer programs to implement this algorithm using a Digital Equipment Corporation PDP-8/E are listed in Appendix H. Multiplication by S^{-1} is accomplished

Table D-4. A numerical comparison of the computer operations required for the fast algorithm and the exploited algorithm.

n	Number of elements in the vector $N=2^n-1$	Number of addition-subtraction operations: Exploited algorithm $N(N-1)$	Number of addition-subtraction operations: Fast algorithm $(N+1)\log_2(N+1)$	Number of exchange operations for the fast algorithm $2N$	Ratio of exploited algorithm operations to fast algorithm operations: Addition-subtraction operations $\frac{N(N-1)}{(N+1)\log_2(N+1)}$	Ratio of exploited algorithm operations to fast algorithm operations: Addition-subtraction and exchange operations $\frac{N(N-1)}{(N+1)\log_2(N+1)+2N}$
3	7	42	24	14	1.75	1.11
4	15	210	64	30	3.28	2.23
5	31	930	160	62	5.81	4.19
6	63	3,906	384	126	10.71	7.66
7	127	16,002	896	254	17.86	13.91
8	255	64,770	2,048	510	31.63	25.32
9	511	260,610	4,608	1,022	56.56	46.29
10	1,023	1,045,506	10,240	2,046	102.10	85.10

by calling the subroutine HSPEC. This subroutine calls the subroutine FHT which uses the fast Hadamard transform algorithm described by Equation (D-28) through (D-30). However, before the subroutine HSPEC is called, the main programs PI and PRMPL must be run to generate permutations equivalent to π_1 and π_2.

Appendix E

A General Ray-Tracing Procedure

This appendix describes how to use the ray-tracing procedure of *Spencer* and *Murty* [1962]. This ray-tracing procedure is well suited to digital computer implementation; it is an algebraic rather than a trigonometric procedure. It is also general enough to be used with almost any practical optical system. The general applicability of this ray-tracing procedure is accomplished by describing each optical surface in terms of a local coordinate system, whose position and orientation relative to a reference coordinate system is specified. In this ray-tracing procedure, a ray is specified by its direction cosines and the Cartesian coordinates of a point on the ray. A ray is traced through an optical surface by using the following four steps. First, the coordinates of a point on the ray as well as the direction cosines of the ray are transformed from the reference coordinate system to the local coordinate system of the optical surface. Second, the coordinates, in the local coordinate system, of the point where the ray intersects the optical surface are computed. Third, the direction cosines, in the local coordinate system, of the ray after its direction is altered by the surface are computed. This change in direction is due to either reflection, refraction, or diffraction. Fourth, the coordinates computed in the second step, as well as the direction cosines computed in the third

PRECEDING PAGE NOT FILMED
BLANK

step, are transformed from the local coordinate system to the reference coordinate system. In some cases, it is possible to omit the first and the fourth steps and perform the second and third steps using the reference coordinate system. This appendix described how to perform these four steps.

Transformation to the local coordinate system

The reference and the local coordinate systems are shown in Figure E-1. The $\bar{x}\bar{y}\bar{z}$-coordinate system is the reference coordinate system, and the xyz-coordinate system is the local coordinate system of the optical surface. The points $\bar{O}$ and O are the origins of the reference and local coordinate systems, respectively. The point P is an arbitrary point on the ray. The coordinates of the point O are $\bar{x}_O$, $\bar{y}_O$, and $\bar{z}_O$ in the reference coordinate system. The coordinates of the point P are x_P, y_P, and z_P in the local coordinate system and $\bar{x}_P$, $\bar{y}_P$, and $\bar{z}_P$ in the reference coordinate system. The direction cosines of the ray are k, l, and m in the local coordinate system and $\bar{k}$, $\bar{l}$, and $\bar{m}$ in the reference coordinate system. As given by *Spencer* and *Murty* [1962], the transformation equations from the reference coordinate system to the local coordinate system are

$$\begin{bmatrix} x_P \\ y_P \\ z_P \end{bmatrix} = R \begin{bmatrix} \bar{x}_P - \bar{x}_O \\ \bar{y}_P - \bar{y}_O \\ \bar{z}_P - \bar{z}_O \end{bmatrix} \qquad \text{(E-1)}$$

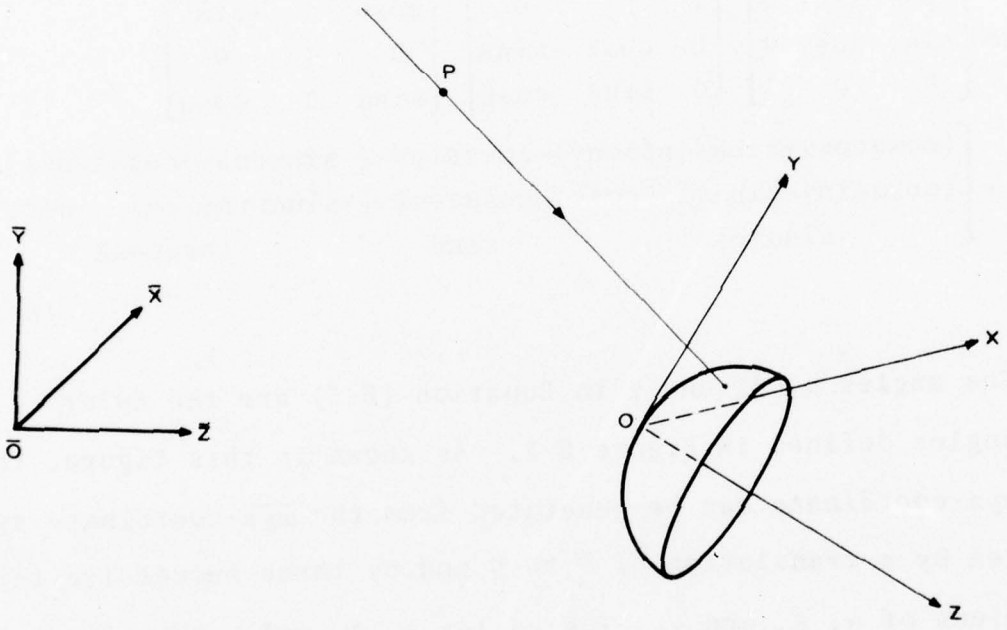


Figure E-1. The reference coordinate system $(\bar{X},\bar{Y},\bar{Z})$ and the local coordinate system (X,Y,Z) of the optical surface. The point P is a point on the ray.

and

$$\begin{bmatrix} k \\ l \\ m \end{bmatrix} = R \begin{bmatrix} \bar{k} \\ \bar{l} \\ \bar{m} \end{bmatrix} , \qquad \text{(E-2)}$$

where

$$R = \begin{bmatrix} \cos\gamma & -\sin\gamma & 0 \\ \sin\gamma & \cos\gamma & 0 \\ 0 & 0 & 1 \end{bmatrix} \begin{bmatrix} 1 & 0 & 0 \\ 0 & \cos\beta & -\sin\beta \\ 0 & \sin\beta & \cos\beta \end{bmatrix} \begin{bmatrix} \cos\alpha & 0 & -\sin\alpha \\ 0 & 1 & 0 \\ \sin\alpha & 0 & \cos\alpha \end{bmatrix}$$

$$= \begin{bmatrix} (\cos\alpha\cos\gamma+\sin\alpha\sin\beta\sin\gamma) & -\cos\beta\sin\gamma & (-\sin\alpha\cos\gamma+\cos\alpha\sin\beta\sin\gamma) \\ (\cos\alpha\sin\gamma-\sin\alpha\sin\beta\cos\gamma) & \cos\beta\cos\gamma & (-\sin\alpha\sin\gamma-\cos\alpha\sin\beta\cos\gamma) \\ \sin\alpha\cos\beta & \sin\beta & \cos\alpha\cos\beta \end{bmatrix} . \qquad \text{(E-3)}$$

The angles α, β, *and* γ *in Equation* (E-3) are the Euler angles defined in Figure E-2. As shown in this figure, the xyz-coordinate can be generated from the $\bar{x}\bar{y}\bar{z}$-coordinate system by a translation of $\bar{O}$ to O and by three successive rotations of α, β, and γ. The angles α, β, and γ are all positive when the rotations are in the directions shown in Figure E-2.

Computer subroutines to implement the transformation from the reference coordinate system to the local coordinate system are listed in Appendix H. The rotation matrix R of Equation (E-3) is computed by the subroutine RMAT. The transformations of Equations (E-1) and (E-2) are performed by the subroutines TRNS1 and TRNS2, respectively.

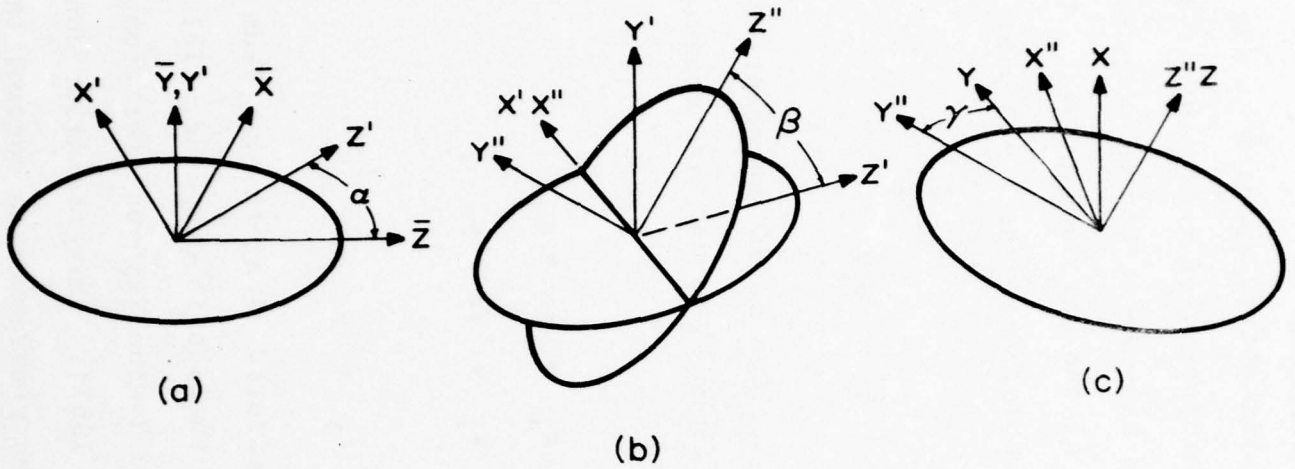


Figure E-2. Transformation of the coordinate system $(\bar{X},\bar{Y},\bar{Z})$ into the local coordinate system (X,Y,Z) after translating $\bar{O}$ to O. (a) The angular rotation α transforms $(\bar{X},\bar{Y},\bar{Z})$ into (X',Y',Z'). (b) The angular rotation β transforms (X',Y',Z') into (X'',Y'',Z''). (c) The angular rotation γ transforms (X'',Y'',Z'') into (X,Y,Z).

Computation of the coordinates of the point of intersection of the ray with the optical surface

The number of arithmetic operations can be minimized by computing the coordinates of the point of intersection in steps. This step-by-step method of computation prevents repeated evaluation of the same quantities. The length h of the ray from the point P to the $z = 0$ plane is computed first using

$$h = z_P/m \quad . \tag{E-4}$$

The coordinates x_1, y_1, and z_1 of the point, where the ray strikes the plane defined by $z = 0$, are computed next using the equations

$$x_1 = kh + x_P \quad , \tag{E-5}$$

$$y_1 = lh + y_P \quad , \tag{E-6}$$

and

$$z_1 = 0 \quad . \tag{E-7}$$

Next, the distance measured along the ray from the $z = 0$ plane to the optical surface is computed. This distance is computed using the Newton-Raphson iteration technique [*Moursund* and *Duris*, 1967]. This technique converges rapidly and allows the programmer to control the accuracy of the solution. The value of s is found using the iteration equation

$$s_{j+1} = s_j - \frac{f(x_j, y_j, z_j)}{\frac{df}{ds}(x_j, y_j, z_j)} \quad , \tag{E-8}$$

where

$$f(x, y, z) = 0 \tag{E-9}$$

is the equation of the optical surface,

$$x_j = k s_j + x_1 \quad , \tag{E-10}$$

$$y_j = l s_j + y_1 \quad , \tag{E-11}$$

and

$$z_j = m s_j \quad . \tag{E-12}$$

The derivative in Equation (E-8) can be computed from the equation

$$\frac{df}{ds}(x_j, y_j, z_j) = k \left.\frac{\partial f}{\partial x}\right|_{(x_j, y_j, z_j)} + l \left.\frac{\partial f}{\partial y}\right|_{(x_j, y_j, z_j)} + m \left.\frac{\partial f}{\partial z}\right|_{(x_j, y_j, z_j)} \quad , \tag{E-13}$$

where the notation

$$\left.\frac{\partial f}{\partial x}\right|_{(x_j, y_j, z_j)} \tag{E-14}$$

represents $\partial f / \partial x$ evaluated at $x = x_j$, $y = y_j$, and $z = z_j$. The iteration is begun with

$$s_1 = 0 \tag{E-15}$$

and continued until

$$|s_{j+1} - s_j| < \varepsilon \quad , \tag{E-16}$$

where ε is the allowable error in computing s. After this iteration procedure is terminated, the coordinates x_f, y_f, and z_f of the point where the ray intersects the surface are computed from the equations

$$x_f = ks_f + x_1 \quad , \tag{E-17}$$

$$y_f = ls_f + y_1 \quad , \tag{E-18}$$

and

$$z_f = ms_f \quad , \tag{E-19}$$

where s_f is the final value of s_{j+1}.

A set of direction numbers for the surface normal at the point where the ray strikes the surface are required to compute the change in the direction of the ray caused by either reflection, refraction or diffraction. A set of direction numbers K, L, and M for this normal can be computed using

$$K = \left.\frac{\partial f}{\partial x}\right|_{(x_f, y_f, z_f)} \quad , \tag{E-20}$$

$$L = \left.\frac{\partial f}{\partial y}\right|_{(x_f, y_f, z_f)} \quad , \tag{E-21}$$

and

$$M = \left.\frac{\partial f}{\partial z}\right|_{(x_f, y_f, z_f)} \quad . \tag{E-22}$$

In order to use Equations (E-8), (E-20), (E-21), and (E-22) to trace a ray through a particular optical surface, the function f for that surface must be used. For example,

$$f(x,y,z) = x^2 + y^2 + z^2 - 2Rz = 0 \qquad \text{(E-23)}$$

represents a spherical surface whose center is at $x = 0$, $y = 0$, and $z = R$. This surface passes through the origin and is symmetrical about the z axis. If the optical surface shown in Figure E-1 is spherical, the sign of R is positive for the surface in this figure. When f is represented by Equation (E-23),

$$\frac{\partial f}{\partial x} = 2x \quad , \qquad \text{(E-24)}$$

$$\frac{\partial f}{\partial y} = 2y \quad , \qquad \text{(E-25)}$$

and

$$\frac{\partial f}{\partial z} = 2(z-R) \quad . \qquad \text{(E-26)}$$

Substituting Equations (E-24), (E-25), and (E-26) in Equation (E-13) yields

$$\frac{df}{ds}(x_j,y_j,z_j) = 2[k x_j + l y_j + m(z_j-R)] \quad . \qquad \text{(E-27)}$$

Therefore, it follows from Equations (E-8), (E-23), and (E-27) that for a spherical surface which can be represented by Equation (E-23)

$$s_{j+1} = s_j - \frac{x_j^2 + y_j^2 + z_j^2 - 2Rz}{2[k x_j + l y_j + m(z_j - R)]} \quad . \qquad \text{(E-28)}$$

It follows from Equations (E-20), (E-21), (E-22), (E-24), (E-25), and (E-26) that for this surface

$$K = 2x_f \quad , \qquad \text{(E-29)}$$

$$L = 2y_f \quad , \qquad \text{(E-30)}$$

and

$$M = 2(z_f - R) \quad . \qquad \text{(E-31)}$$

However, the required number of arithmetic operations can be reduced by deleting the factor of 2 in Equations (E-29), (E-30) and (E-31). This deletion is possible because a new set of direction numbers can be generated from an existing set of direction numbers by multiplying each of the existing direction numbers by the same constant [*Protter* and *Morrey*, 1964]. A computer subroutine named ITSP which computes x_f, y_f, z_f, K, L, and M for a spherical surface is listed in Appendix H.

Another common optical surface, besides the sphere, is the paraboloid of revolution. A paraboloid of revolution which passes through the origin and is symmetrical about the z axis can be represented by

$$f(x,y,z) = x^2 + y^2 - 2Tz \quad , \qquad \text{(E-32)}$$

where T is a constant. The sign of the z coordinates of points on this surface is the same as the sign of T. If the optical surface in Figure E-1 is a paraboloid of revolution, the sign of T is positive for the surface in this figure. It follows from Equations (E-8), (E-13), and (E-32) that for a paraboloid of revolution represented by Equation (E-32),

$$s_{j+1} = s_j - \frac{x_j^2 + y_j^2 - 2T z_j}{2(k x_j + l y_j - T m)} \quad . \tag{E-33}$$

For this surface, it follows from Equations (E-20), (E-21), (E-22), and (E-32) that

$$K = 2x_f \quad , \tag{E-34}$$

$$L = 2y_f \quad , \tag{E-35}$$

and

$$M = -2T \quad . \tag{E-36}$$

In order to minimize the required number of arithmetic operations, the factor of 2 in Equations (E-34), (E-35), and (E-36) should be dropped; that is, x_f, y_f, and $-T$ should be used for the direction numbers of the normal at the point where the ray intersects the paraboloid of revolution specified by Equation (E-32). A computer subroutine named ITPR which computes x_f, y_f, z_f, K, L, and M for a paraboloid of revolution is listed in Appendix H.

The coordinates of the point where a ray strikes a plane can be computed from Equations (E-5), (E-6), and (E-7)

if the local coordinate system is located so that the plane is defined by the equation

$$z = 0 \quad . \tag{E-37}$$

A suitable set of direction numbers for the surface normal at all points on this plane is given by

$$K = 0 \quad , \tag{E-38}$$

$$L = 0 \quad , \tag{E-39}$$

and

$$M = 1 \quad . \tag{E-40}$$

The point where a ray intersects a plane can also be computed in the reference coordinate system. A plane can be specified in the reference coordinate system by the equation

$$A(\bar{x} - \bar{x}_2) + B(\bar{y} - \bar{y}_2) + C(\bar{z} - \bar{z}_2) = 0 \quad , \tag{E-41}$$

where x_2, y_2, and z_2 are coordinates of an arbitrary point on the plane and A, B, and C are a set of direction numbers of a line normal to the plane. The ray can be specified by the equations

$$\bar{x} = \bar{x}_p + g\bar{k} \quad , \tag{E-42}$$

$$\bar{y} = \bar{y}_p + g\bar{l} \quad , \tag{E-43}$$

and

$$\bar{z} = \bar{z}_p + g\bar{m} \quad , \tag{E-44}$$

where g is the distance along the ray from the point P to the point on the ray with coordinates $\bar{x}$, $\bar{y}$, and $\bar{z}$. The value of g which corresponds to the point where the ray strikes the plane can be found by simultaneously solving Equations (E-41) through (E-44) for g. The solution is given by

$$g = \frac{A(\bar{x}_2 - \bar{x}_P) + B(\bar{y}_2 - \bar{y}_P) + C(\bar{z}_2 - \bar{z}_P)}{A\bar{k} + B\bar{l} + C\bar{m}} \quad . \qquad \text{(E-45)}$$

The $\bar{x}$, $\bar{y}$, and $\bar{z}$ coordinates of the point where a ray strikes a plane can be computed by first computing the required value of g from Equation (E-45) and then substituting this value in Equations (E-42), (E-43), and (E-44). A computer subroutine named ITPL which computes the coordinates of the point where a ray intersects a plane by using Equations (E-42) through (E-45) is listed in Appendix H.

Computation of the direction cosines of the ray after its direction is altered by the optical surface

Three processes which change the direction of a ray are considered: 1) refraction, 2) reflection, and 3) diffraction by a diffraction grating.

Refraction. As proven by *Spencer* and *Murty* [1962], the direction cosines of the ray after refraction are given by

$$k' = \mu k + \Gamma K \quad , \qquad \text{(E-46)}$$

$$l' = \mu l + \Gamma L \quad , \qquad \text{(E-47)}$$

and

$$m' = \mu m + \Gamma M \quad . \tag{E-48}$$

The value of μ is computed from the equation

$$\mu = \frac{N}{N'} \quad , \tag{E-49}$$

where N is the index of refraction of the medium in which the ray travels before it strikes the optical surface and N' is the index of refraction at the medium into which the ray is refracted. The value of Γ is found by solving the equation

$$\Gamma^2 + 2a\Gamma + b \quad , \tag{E-50}$$

where

$$a = \frac{\mu(kK + lL + mM)}{K^2 + L^2 + M^2} \tag{E-51}$$

and

$$b = \frac{\mu^2 - 1}{K^2 + L^2 + M^2} \quad . \tag{E-52}$$

Equation (E-50) can be solved by using the quadratic equation or the Newton-Raphson iteration method. The iteration equation for the Newton-Raphson method is

$$\Gamma_{j+1} = \Gamma_j - \frac{\Gamma_j^2 + 2a\Gamma_j + b}{2(\Gamma_j + a)} \quad . \tag{E-53}$$

This equation simplifies to

$$\Gamma_{j+1} = \frac{\Gamma_j^2 - b}{2(\Gamma_j + a)} \quad . \tag{E-54}$$

Equation (E-54) will converge to the correct root if the iteration is started with

$$\Gamma_1 = \frac{-b}{2a} \quad . \tag{E-55}$$

The procedure to compute the direction cosines of the refracted ray is to first compute Γ to the desired accuracy using Equation (E-54), and then substitute this value of Γ into Equations (E-46), (E-47), and (E-48). A computer subroutine named RFR which implements this procedure is listed in Appendix H.

Reflection. Reflection can be described by using the law of refraction with $N = N'$. Thus, by Equation (E-49) μ equals unity for reflection. If unity is substituted for μ in Equation (E-52), b equals zero. Therefore, Equation (E-50) simplies to

$$\Gamma(\Gamma + 2a) = 0 \tag{E-56}$$

for reflection. The physically correct root is

$$\Gamma = -2a \quad . \tag{E-57}$$

Thus, no iteration is required to compute Γ for reflection. Substituting the value of Γ given by Equation (E-57) and μ

equal to unity in Equations (E-46), (E-47), and (E-48) yields

$$k' = k - 2a K \quad , \tag{E-58}$$

$$l' = l - 2a L \quad , \tag{E-59}$$

and

$$m' = m - 2a M \quad . \tag{E-60}$$

Thus, the procedure for computing the direction cosines of the reflected ray is to first compute a from Equation (E-51), with μ equal to unity, and then substitute this value of a into Equations (E-58), (E-59), and (E-60). A computer subroutine named RFL which implements this procedure is listed in Appendix H.

Diffraction by a diffraction grating. As proven by *Spencer* and *Murty* [1962], the direction cosines of the ray after diffraction by a diffraction grating are given by

$$k' = k - \Lambda u + \Gamma K \quad , \tag{E-61}$$

$$l' = l - \Lambda v + \Gamma L \quad , \tag{E-62}$$

and

$$m' = m - \Lambda w + \Gamma M \quad . \tag{E-63}$$

The rulings of most practical grating can be specified by the intersection of a family of parallel planes with the grating surface as illustrated in Figure E-3. For gratings whose rulings can be specified in this way, the values of

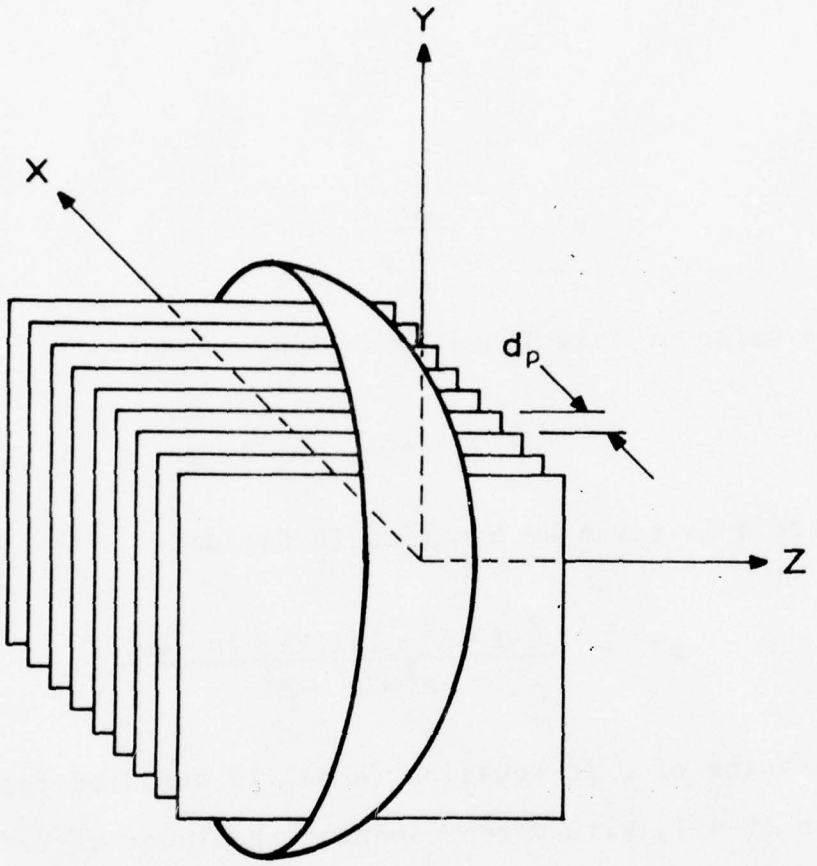


Figure E-3. Specification of the rulings of a conventional grating by means of the intersection of a family of parallel planes with the grating surface.

u, v, and w are computed from the following equations:

$$u = \frac{1}{\sqrt{1 + K/(K^2 + L^2)}} , \tag{E-64}$$

$$v = \frac{-KL\mu}{L^2 + K^2} , \tag{E-65}$$

and

$$w = \frac{-KM\mu}{L^2 + M^2} . \tag{E-66}$$

The value of Γ is found by solving

$$\Gamma^2 + 2a\Gamma + b' = 0 , \tag{E-67}$$

where a is given by Equation (E-51) and

$$b' = \frac{\mu^2 - 1 + \Lambda^2 - 2\mu\Lambda(ku + lv + mw)}{K^2 + L^2 + M^2} . \tag{E-68}$$

The value of μ in Equation (E-68) is computed from Equation (E-49), with N representing the index of refraction of the medium in which the ray travels before striking the grating, and N' representing the index of refraction of the medium in which the diffracted ray travels. Since the form of Equations (E-50) and (E-67) are identical, it follows from Equation (E-54) that the value of Γ which satisfies Equation (E-67) can be found by using the iteration equation

$$\Gamma_{j+1} = \frac{\Gamma_j^2 - b'}{2(\Gamma_j + a)} \quad . \tag{E-69}$$

For a reflection grating, the iteration indicated by Equation (E-69) should be started with

$$\Gamma_1 = \frac{b'}{2a} - 2a \quad . \tag{E-70}$$

The value of Λ is computed from the equation

$$\Lambda = \frac{n\lambda}{N'd} \quad , \tag{E-71}$$

where n is the integral diffraction order, λ is the wavelength and d is the grating spacing in the region where the ray intersects the grating. If in the region where the ray strikes the grating the spacing between the planes which specify the rulings is d_p as shown in Figure E-3, then

$$d = \frac{d_p}{u} \quad . \tag{E-72}$$

The following three steps are used to compute the direction cosines of the diffracted ray. First, the values of u, v, w, a, b' and Λ are computed. Second, the value of Γ is computed to the desired accuracy. Third, the direction cosines are computed using Equations (E-61), (E-62), and (E-63). A computer subroutine named DFR which uses this procedure to compute the direction cosines of a ray diffracted by a plane grating is listed in Appendix H. However,

this subroutine performs all computations in the reference coordinate system; coordinate system transformations immediately before and immediately after this subroutine is called are not required. This subroutine and the subroutine ITPL can be used together to trace the path of rays interacting with a plane diffraction grating.

Transformation to the reference coordinate system

The coordinates x_f, y_f, and z_f where the ray intersects the surface and the direction cosines k', l', and m' of the ray leaving the surface are transformed to the reference coordinate system using the equations

$$\begin{bmatrix} \bar{x}_f \\ \bar{y}_f \\ \bar{z}_f \end{bmatrix} = R^{-1} \begin{bmatrix} x_f \\ y_f \\ z_f \end{bmatrix} + \begin{bmatrix} \bar{x}_O \\ \bar{y}_O \\ \bar{z}_O \end{bmatrix} \tag{E-73}$$

and

$$\begin{bmatrix} \bar{k}' \\ \bar{l}' \\ \bar{m}' \end{bmatrix} = R^{-1} \begin{bmatrix} k' \\ l' \\ m' \end{bmatrix} . \tag{E-74}$$

The inverse of R is the transpose of R; that is,

$$R^{-1} = R^T . \tag{E-75}$$

The computer subroutine RMAT, which is listed in Appendix H, computes R^{-1} as well as R. The computer subroutines TRNS3

and TRNS4, which are also listed in Appendix H, evaluate Equations (E-73) and (E-74), respectively.

Summary

This ray-tracing procedure consists of repeated applications, at each optical surface, of the following four steps: 1) transform to the local coordinate system, 2) find where the ray strikes the surface, 3) find the direction of the ray after it interacts with the surface, and 4) transform back to the reference coordinate system. In some cases it is advantageous to omit the first and fourth steps. The computer subroutines RMAT, TRNS1, TRNS2, TRNS3, TRNS4, ITSP, ITPL, ITPR, RFR, RFL, and DFR perform these four steps. These subroutines can be used to trace rays through a particular optical system by writing a computer program which calls these subroutines in the order required for that particular optical system. For example, the programs CT1, CT2, CT3, CT4, CT5, and CT6, which are listed in Appendix H, illustrate how these subroutines can be used to trace rays through a Czerny-Turner spectrometer.

Appendix F

Derivation of Expression for Meridional Focal Length of a Spherical Mirror

Meridional rays are those rays which lie in a plane containing the optical axis of the system. The location of the meridional image point, the point where meridional rays are focused, is found by first tracing a principal ray from the object point and then solving the following equation for t' [*Smith*, 1966]

$$\frac{N' \cos^2 I'}{t'} = \frac{N \cos I}{t} + \phi \quad . \tag{F-1}$$

The variables t and t' are, respectively, the distances measured along the principal ray from the optical surface to the object and image points. The variables N and N' are, respectively, the indices of refraction before and after the optical surface. The variables I and I' are, respectively, the angles between the principal ray and the surface normal before and after this ray strikes the optical surface. The symbol ϕ, the oblique power of the surface, is defined by

$$\phi \triangleq (N' \cos I' - N \cos I)/R \quad , \tag{F-2}$$

where R is the radius of the optical surface.

For reflection

$$I' = -I \quad , \tag{F-3}$$

PRECEDING PAGE NOT FILMED
BLANK

and in air

$$N' = -N \quad . \tag{F-4}$$

For a spherical mirror, Equations (F-2), (F-3), and (F-4) indicate that the oblique power is

$$\phi = -\frac{2 \cos I}{R} \quad . \tag{F-5}$$

If the incident rays are collimated, t is infinite. If Equation (F-5) is substituted into Equation (F-1) and the resulting equation is solved for t' with t infinite, then

$$t' = -\frac{R}{2} \cos I \quad . \tag{F-6}$$

Equation (F-6) gives the distance, measured along a principal ray, from the spherical mirror to its meridional focus. The meridional focus of a spherical mirror is illustrated in Figure F-1.

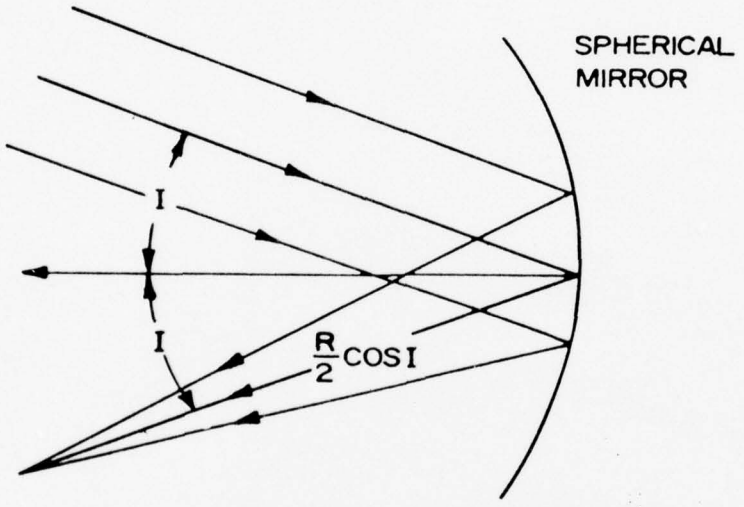


Figure F-1. The meridional focal length of a spherical mirror.

Appendix G

Derivation of an Expression for the Grating Rotation Angle of a Czerny-Turner Spectrograph

A closed-form equation which can be used to compute the required angular setting of the grating for a Czerny-Turner spectrograph so that radiation of the desired wavelength is at the center of the focal plane is derived in this appendix.

The angles used in this derivation are illustrated in Figure G-1. The diffracted ray shown in this figure ultimately strikes the center of the focal plane. The reference line in this figure bisects the angle formed by the incident ray and this diffracted ray. The angle θ_1 which is one half of the angle between these two rays is a constant. The angles α and β are, respectively, the angles of incidence and diffraction. These angles satisfy the grating equation [*Born* and *Wolf*, 1965]

$$\sin\alpha + \sin\beta = k\lambda/d \quad , \tag{G-1}$$

where k is the integral order of the diffraction, d is the distance between grating rulings, and λ is the wavelength of the radiation that is directed to the center of the spectrograph's focal plane. It can be seen from Figure G-1 that

$$\theta_G = \alpha + \theta_1 \tag{G-2}$$

PRECEDING PAGE NOT FILMED
BLANK

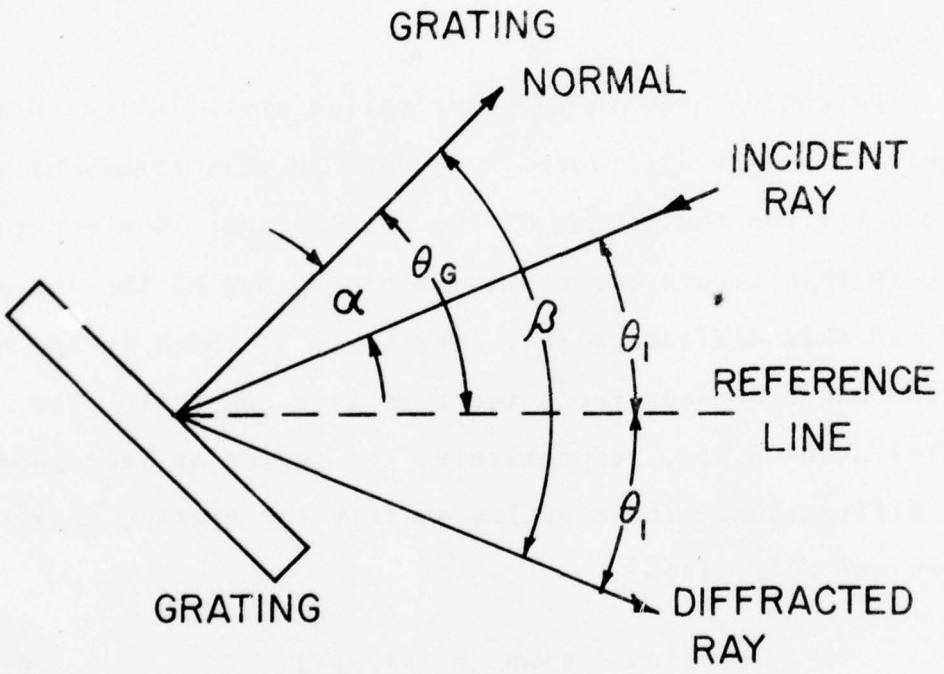


Figure G-1. The optical path, in the region of the grating, of a ray that passes through the center of the focal plane in a Czerny-Turner spectrograph.

and

$$\beta = \alpha + 2\theta_1 \quad . \tag{G-3}$$

If Equation (G-3) is substituted in Equation (G-1) and the trigonometric identity for the sine of the sum of two angles is applied, the resulting equation is

$$\sin\alpha + \sin\alpha \cos 2\theta_1 + \cos\alpha \sin 2\theta_1 = k\lambda/d \quad . \tag{G-4}$$

By the use of the trigonometric identities for the sine and cosine of twice an angle, it can be shown that Equation (G-4) is equivalent to

$$\sin\alpha + \sin\alpha(2\cos^2\theta_1 - 1) + 2\cos\alpha \sin\theta_1 \cos\theta_1 = k\lambda/d \quad . \tag{G-5}$$

If Equation (G-5) is expanded and if the trigonometric identify for the sine of the sum of two angles is again used, this equation reduces to

$$2\cos\theta_1 \sin(\alpha + \theta_1) = k\lambda/d \quad . \tag{G-6}$$

If Equation (G-2) is substituted in Equation (G-6), the resulting equation can be written as

$$\sin\theta_G = \frac{k\lambda}{2d \cos\theta_1} \quad . \tag{G-7}$$

As can be seen from this equation, the sine of θ_G is linearly proportional to the wavelength of the radiation at the focal plane center.

THIS PAGE IS BEST QUALITY PRACTICABLE
FROM COPY FURNISHED TO DDC

APPENDIX H

Computer Program Listings

General purpose ray-tracing subroutines

```
C       SUBROUTINE TRNS1
```

```
 1  C       SUBROUTINE TRNS1
 2  C
 3  C
 4          SUBROUTINE TRNS1(RM,X,Y,Z,XZERO,YZERO,ZZERO)
 5  C
 6  C       THIS SUBROUTINE CONVERTS THE CARTESIAN COORDINATES FROM
 7  C       THE ORIGINAL COORDINATE SYSTEM TO THE NEW COORDINATE SYSTEM.
 8  C
 9  C  INPUT
10  C       RM IS THE ROTATION MATRIX
11  C       ON INPUT X,Y,Z ARE THE COORDINATES IN THE ORIGINAL COORDINATE
12  C       SYSTEM.
13  C       XZERO,YZERO,ZZERO ARE THE COORDINATES OF THE ORIGIN OF THE
14  C       NEW COORDINATE SYSTEM IN THE ORIGINAL COORDAINATE SYSTEM.
15  C
16  C  OUTPUT
17  C       ON OUTPUT X,Y,Z ARE THE COORDINATES IN THE NEW
18  C       COORDINATE SYSTEM.
19  C
20  C       THIS IS A RAY TRACING PROGRAM ADAPTED FROM THE METHODS OF
21  C       SPENCER AND MURTY JOSA VOL.52, P.672, 1961.
22  C
23          DIMENSION RM(3,3),C(3),D(3)
24          D(1)=X-XZERO
25          D(2)=Y-YZERO
26          D(3)=Z-ZZERO
27          DO 3 I=1,3
28          TOTAL=0.
29          DO 4 J=1,3
30  4       TOTAL=RM(I,J)*D(J)+TOTAL
31  3       C(I)=TOTAL
32          X=C(1)
33          Y=C(2)
34          Z=C(3)
35          RETURN
36          END
```

PRECEDING PAGE NOT FILMED
BLANK

THIS PAGE IS BEST QUALITY PRACTICABLE
FROM COPY FURNISHED TO DDC

```
C       SUBROUTINE TRNS2
```

```
      C       SUBROUTINE TRNS2
      C
      C
              SUBROUTINE TRNS2(RM,DK,DL,DM)
      C
      C       THIS SUBROUTINE CONVERTS THE DIRECTION COSINES FROM THE
      C       ORIGINAL COORDINATE SYSTEM TO THE NEW COORDINATE SYSTEM.
      C
      C   INPUT
      C       RM IS THE ROTATION MATRIX
      C       ON INPUT DK,DL,DM ARE THE DIRECTION COSINES IN THE ORIGINAL
      C       COORDINATE SYSTEM
      C
      C   OUTPUT
      C       ON OUTPUT DK,DL,DM ARE THE DIRECTION COSINES IN THE NEW
      C       COORDINATE SYSTEM.
      C
      C       THIS IS A RAY TRACING PROGRAM ADAPTED FROM THE METHODS
      C       OF SPENCER AND MURTY JOSA VOL. 52, P. 672, 1961.
      C
      C
              DIMENSION RM(3,3),C(3),D(3)
              D(1)=DK
              D(2)=DL
              D(3)=DM
              DO 3 I=1,3
              TOTAL=0.
              DO 4 J=1,3
          4   TOTAL=RM(I,J)*D(J)+TOTAL
          3   C(I)=TOTAL
              DK=C(1)
              DL=C(2)
              DM=C(3)
              RETURN
              END
```

```
C       SUBROUTINE TRNS3
```

```
      C       SUBROUTINE TRNS3
      C
      C
              SUBROUTINE TRNS3(RMI,X,Y,Z,XZERO,YZERO,ZZERO)
      C
      C       THIS SUBROUTINE CONVERTS THE CARTESIAN COORDINATES FROM
      C       THE NEW COORDINATE SYSTEM BACK TO THE ORIGINAL COORDINATE
      C       SYSTEM.
      C
      C   INPUT
      C       RMI IS THE ROTATION MATRIX INVERSE.
      C       ON INPUT X,Y,Z ARE THE COORDINATES IN THE NEW COORDINATE
      C       SYSTEM.
      C       XZERO,YZERO,ZZERO ARE THE COORDINATES OF THE ORIGIN OF THE NEW
      C       COORDINATE SYSTEM IN THE ORIGINAL COORDINATE SYSTEM.
      C
      C   OUTPUT
      C       ON OUTPUT X,Y,Z ARE THE COORDINATES IN THE ORIGINAL COORDINATE
      C       SYSTEM.
      C
      C       THIS IS A RAY TRACING PROGRAM ADAPTED FROM THE METHODS OF
      C       SPENCER AND MURTY JOSA VOL. 52, P. 672, 1961.
      C
              DIMENSION RMI(3,3),C(3),D(3)
              D(1)=X
              D(2)=Y
              D(3)=Z
              DO 3 I=1,3
              TOTAL=0.
              DO 4 J=1,3
          4   TOTAL=RMI(I,J)*D(J)+TOTAL
          3   C(I)=TOTAL
              X=C(1)+XZERO
              Y=C(2)+YZERO
              Z=C(3)+ZZERO
              RETURN
              END
```

THIS PAGE IS BEST QUALITY PRACTICABLE
FROM COPY FURNISHED TO DDC

```
C       SUBROUTINE TRNS4
```

```
      C       SUBROUTINE TRNS4
      C
      C
              SUBROUTINE TRNS4(RMI,DK,DL,DM)
      C
      C       THIS SUBROUTINE CONVERTS THE DIRECTION COSINES FROM THE NEW
      C       COORDINATE SYSTEM BACK TO THE ORIGINAL COORDINATE SYSTEM.
      C
      C   INPUT
      C       RMI IS THE ROTATION MATRIX INVERSE.
      C       ON INPUT DK,DL,DM ARE THE DIRECTION COSINES IN THE NEW
      C       COORDINATE SYSTEM.
      C
      C   OUTPUT
      C       ON OUTPUT DK,DL,DM ARE THE DIRECTION COSINES IN THE ORIGINAL
      C       COORDINATE SYSTEM.
      C
      C       THIS IS A RAY TRACING PROGRAM ADAPTED FROM THE METHODS OF
      C       SPENCER AND MURTY JOSA VOL.52,P.672,1961.
      C
              DIMENSION RMI(3,3),C(3),D(3)
              D(1)=DK
              D(2)=DL
              D(3)=DM
              DO 3 I=1,3
              TOTAL=0.
              DO 4 J=1,3
          4   TOTAL=RMI(I,J)*D(J)+TOTAL
          3   C(I)=TOTAL
              DK=C(1)
              DL=C(2)
              DM=C(3)
              RETURN
              END
```

```
C       SUBROUTINE RMAT
```

```
      C       SUBROUTINE RMAT
      C
      C
              SUBROUTINE RMAT(ALPHA,BETA,GAMMA,RM,RMI)
      C
      C       THIS SUBROUTINE CALCULATES THE ROTATION MATRIX AND ITS INVERSE
      C       FOR THE TRANSFORMATION FROM THE OLD TO A NEW COORDINATE
      C       SYSTEM.
      C
      C       ALPHA,BETA,GAMMA ARE THE EULER ANGLES IN RADIANS.
      C
      C       RM IS THE ROTATION MATRIX.
      C
      C       RMI IS THE ROTATION MATRIX INVERSE.
      C
      C       THIS IS A RAY TRACING PROGRAM ADAPTED FROM THE METHOS OF
      C       SPENCER AND MURTY JOSA VOL.52, P.672, 1961.
      C
      C
              DIMENSION RM(3,3),RMI(3,3)
              RM(1,1)=COS(ALPHA)*COS(GAMMA)+SIN(ALPHA)*SIN(BETA)*SIN(GAMMA)
              RM(1,2)=-COS(BETA)*SIN(GAMMA)
              RM(1,3)=-SIN(ALPHA)*COS(GAMMA)+COS(ALPHA)*SIN(BETA)*SIN(GAMMA)
              RM(2,1)=COS(ALPHA)*SIN(GAMMA)-SIN(ALPHA)*SIN(BETA)*COS(GAMMA)
              RM(2,2)=COS(BETA)*COS(GAMMA)
              RM(2,3)=-SIN(ALPHA)*SIN(GAMMA)-COS(ALPHA)*SIN(BETA)*COS(GAMMA)
              RM(3,1)=SIN(ALPHA)*COS(BETA)
              RM(3,2)=SIN(BETA)
              RM(3,3)=COS(ALPHA)*COS(BETA)
              DO 1 I=1,3
              DO 1 J=1,3
          1   RMI(I,J)=RM(J,I)
              RETURN
              END
```

THIS PAGE IS BEST QUALITY PRACTICABLE
FROM COPY FURNISHED TO DDC

C SUBROUTINE ITPL

```
C       SUBROUTINE ITPL
C
        SUBROUTINE ITPL(DK,DL,DM,XZERO,YZERO,ZZERO,X1,Y1,Z1,
        1A,B,C)
C
C       THIS SUBROUTINE COMPUTES THE POINT OF INTERSECTION
C       OF A RAY WITH A PLANE.
C
C       DK,DL,DM ARE DIRECTION NUMBERS OF THE LINE.
C
C       XZERO,YZERO,ZZERO ON INPUT ARE THE COORDINATES OF A POINT ON
C       THE RAY.
C
C       XZERO,YZERO,ZZERO ON OUTPUT ARE THE COORDINATES OF THE
C       POINT OF INTERSECTION.
C
C       X1,Y1,Z1 ARE THE COORDINATES OF A POINT ON THE PLANE.
C
C       A,B,C ARE DIRECTION NUMBERS OF THE PLANE NORMAL.
C
C
        S=A*(X1-XZERO)+B*(Y1-YZERO)+C*(Z1-ZZERO)
        T=S/(A*DK+B*DL+C*DM)
        XZERO=XZERO+DK*T
        YZERO=YZERO+DL*T
        ZZERO=ZZERO+DM*T
        RETURN
        END
```

THIS PAGE IS BEST QUALITY PRACTICABLE
FROM COPY FURNISHED TO DDC

```
C       ITSP SUBROUTINE
```

```
C       ITSP SUBROUTINE
C
        SUBROUTINE ITSP(DK,DL,DM,X,Y,Z,R,E,ERR,S,P,I,SK,SL,SM)
C
C
C       THIS SUBROUTINE COMPUTES THE POINT OF INTERSECTION OF A
C       RAY WITH A SPHERICAL SUFACE WHICH HAS ITS VERTEX AT THE
C       POINT X=0,Y=0,Z=0.
C
C       THIS PROGRAM ALSO COMPUTES DIRECTION NUMBERS OF THE SURFACE
C       NORMAL AT THE INTERSECTION POINT.
C
C       DK,DL,DM ARE THE DIRECTION COSINES OF THE INCIDENT RAY.
C
C       X,Y,Z ON INPUT ARE THE COORDINATES OF THE POINT FROM
C       WHICH THE INCIDENT RAY EMANATES.
C
C       X,Y,Z ON OUTPUT ARE THE COORDINATES OF THE POINT OF
C       INTERSECTION WITH THE SPHERICAL SURFACE.
C
C       R IS THE RADIUS OF THE SPHERE.
C       R IS POSITIVE IF THE SURFACE IS CONVEX TO THE INCIDENT
C       RAY.
C       R IS NEGATIVE IF THE SURFACE IS CONCAVE TO THE INCIDENT RAY.
C
C       E IS THE CONVERGENCE PARAMETER.  THE NEWTON-RAPHSON
C       ITERATION CONTINUES UNTIL EITHER THE ABSOLUTE VALUE OF
C       THE DIFFERENCE BETWEEN SUCCESSIVE ITERATIONS IS LESS THAN
C       E OR 50 ITERATIONS HAVE BEEN PERFORMED.
C
C       ERR IS THE ABSOLUTE VALUE OF THE DIFFERENCE BETWEEN THE
C       LAST TWO ITERATIONS.
C
C       S IS THE DISTANCE ALONG THE RAY FROM THE Z=0 PLANE TO THE
C       POINT OF INTERSECTION OF THE RAY WITH THE SPHERE.
C       S IS NEGATIVE IF THE POINT OF INTERSECTION IS ON THE
C       NEGATIVE Z SIDE OF THE X-Y PLANE.
C       S IS POSITIVE IF THE CONVERSE IS TRUE.
C
C       P IS THE TOTAL PATH ALONG THE RAY FROM THE EMANATING
C       POINT TO THE POINT OF INTERSECTION.
C       P IS POSITIVE FOR A TRUE RAY.  A NEGATIVE VALUE OF P INDICATES
C       A VIRTUAL PATH, AN EXTENSION OF THE RAY IN THE DIRECTION
C       OPPOSITE TO THE DIRECTION OF PROPAGATION, CONVERGENCE TO
C       THE WRONG INTERSECTION POINT HAS OCCURRED.
C
C       A NEWTON-RAPHSON ITERATION OF THE TYPE X=G(X) IS USED.
C       CONVERGENCE IS GOOD IF G(X) DOES NOT GO TO INFINITY CLOSE
C       TO X=0, THE STARTING POINT OF THE ITERATION.
C
C
C       I IS THE NUMBER OF ITERATIONS PERFORMED.  IF I=50
C       CONVERGENCE HAS NOT OCCURRED.
C
C
C       SK,SL,SM ARE THE DIRECTION NUMBERS OF THE SURFACE NORMAL
C       AT THE INTERSECTION POINT.
C
C       THIS IS A RAY TRACING PROGRAM ADAPTED FROM THE METHODS
C       OF SPENCER AND MURTY JOSA VOL.52.,P. 672, 1961.
C
C
        I=1
        SZERO=-Z/DM
        X1=X+DK*SZERO
        Y1=Y+DL*SZERO
        S=0.
1       X=X1+DK*S
        Y=Y1+DL*S
        Z=DM*S
        TEMP=S-(X*X+Y*Y+Z*Z-2.*R*Z)/(2.*(X*DK+Y*DL+Z*DM-R*DM))
        ERR=ABS(S-TEMP)
        I=I+1
        S=TEMP
        IF(ERR-E)2,2,3
```

```
 76  3       CONTINUE
 77          IF(I-50)1,2,2
 78  2       X=X1+DK*S
 79          Y=Y1+DL*S
 80          Z=DM*S
 81          SK=X
 82          SL=Y
 83          SM=Z-R
 84          P=SZERO+S
 85          RETURN
 86          END
```

THIS PAGE IS BEST QUALITY PRACTICABLE
FROM COPY FURNISHED TO DDC

```
C       SUBROUTINE ITPR

  1 C       SUBROUTINE ITPR
  2 C
  3 C
  4         SUBROUTINE ITPR(DK,DL,DM,X,Y,Z,P,E,ERR,S,Q,I,SK,SL,SM)
  5 C
  6 C
  7 C       THIS SUBROUTINE CALCULATES THE POINT OF INTERSECTION
  8 C       OF A RAY WITH A PARABOLOID OF REVOLUTION.  THE EQUATION
  9 C       IS X**2+Y**2=2*P*Z.
 10 C
 11 C       THE VERTEX OF THE PARABOLOID IS AT X=0,Y=0,Z=0
 12 C
 13 C       A NEWTON-RAPHSON ITERATION OF THE TYPE S=G(S),
 14 C       G(S)=F(S)/F'(S), IS USED.
 15 C
 16 C       THE PROGRAM ALSO COMPUTES THE DIRECTION NUMBERS OF THE
 17 C       SURFACE NORMAL AT THE POINT OF INTERSECTION.
 18 C
 19 C       DK,DL,DM ARE THE DIRECTION COSINES OF THE INCIDENT RAY.
 20 C
 21 C       X,Y,Z ON INPUT ARE THE COORDINATES OF THE POINT FROM
 22 C       WHICH THE RAY EMANATES.
 23 C
 24 C       X,Y,Z ON OUTPUT ARE THE COORDINATES OF THE POINT OF
 25 C       INTERSECTION OF THE RAY WITH THE PARABOLOID SURFACE.
 26 C
 27 C       P/2 IS THE DISTANCE FROM THE VERTEX TO THE FOCUS.
 28 C
 29 C       P IS POSITIVE IF THE PARABOLOID OPENS ALONG THE POSITIVE
 30 C       Z AXIS.  P IS NEGATIVE IF THE PARABOLOID OPENS ALONG THE
 31 C       NEGATIVE Z AXIS.
 32 C
 33 C       E IS THE CONVERGENCE PARAMETER.  THE NEWTON-RAPHSON ITERATION
 34 C       CONTINUES UNTIL EITHER THE ABSOLUTE VALUE OF THE DIFFERENCE
 35 C       BETWEEN SUCCESSIVE ITERATIONS IS LESS THAN E OR 50 ITERATIONS
 36 C       HAVE BEEN PERFORMED.
 37 C
 38 C       ERR IS THE ABSOLUTE VALUE OF THE DIFFERENCE BETWEEN
 39 C       THE LAST TWO ITERATIONS PERFORMED.
 40 C
 41 C       S IS THE DISTANCE FROM THE Z=0 PLANE TO THE POINT OF
 42 C       INTERSECTION ON THE PARABOLOID.
 43 C       S IS POSITIVE IF THE INTERSECTION POINT HAS A POSITIVE Z
 44 C       COORDINATE AND NEGATIVE IF THE CONVERSE IS TRUE.
 45 C
 46 C       Q IS THE TOTAL PATH ALONG THE RAY FROM THE EMANATING POINT
 47 C       TO THE POINT OF INTERSECTION.
 48 C       Q IS POSITIVE FOR A TRUE RAY.  A NEGATIVE VALUE OF Q
 49 C       INDICATES A VIRTUAL PATH, AN EXTENTION OF THE RAY IN THE
 50 C       DIRECTION OPPOSITE TO THE DIRECTION OF PROPAGATION.
 51 C       THAT IS, CONVERGENCE TO THE WRONG POINT HAS OCCURRED.
 52 C
 53 C       I IS THE NUMBER OF ITERATIONS PERFORMED.  IF I=50 CONVERGENCE
 54 C       TO THE DESIRED ACCURACY DID NOT OCCUR.
 55 C
 56 C       SK,SL,SM ARE DIRECTION NUMBERS OF THE SURFACE NORMAL AT THE
 57 C       POINT OF INTERSECTION.
 58 C
 59 C       THIS IS A RAY TRACING PROGRAM ADAPTED FROM THE METHODS OF
 60 C       SPENCER AND MURTY JOSA VOL. 52, P. 672, 1961.
 61 C
 62 C
 63         I=1
```

THIS PAGE IS BEST QUALITY PRACTICABLE
FROM COPY FURNISHED TO DDC

```
      SZERO=-Z/DM
      X1=X+DK*SZERO
      Y1=Y+DL*SZERO
      S=0.
1     X=X1+DK*S
      Y=Y1+DL*S
      Z=DM*S
      TEMP=S-(X**X+Y**Y-2.*P*Z)/(2.*X*DK+2.*Y*DL-2.*P*DM)
      ERR=ABS(S-TEMP)
      I=I+1
      S=TEMP
      IF(ERR-E)2,2,3
3     CONTINUE
      IF(I-50)1,2,2
2     X=X1+DK*S
      Y=Y1+DL*S
      Z=DM*S
      SK=X
      SL=Y
      SM=-P
      Q=SZERO+S
      RETURN
      END
```

C RFL SUBROUTINE

```
C     RFL SUBROUTINE
C
      SUBROUTINE RFL(DK,DL,DM,SK,SL,SM)
C
C
C     THIS SUBROUTINE COMPUTES THE DIRECTION OF A REFLECTED
C     RAY.
C
C     DK,DL,DM ON INPUT ARE THE COMPONENTS OF A UNIT VECTOR
C     IN THE DIRECTION OF THE INCIDENT RAY.
C
C     DK,DL,DM ON OUTPUT ARE THE COMPONENTS OF A UNIT VECTOR
C     IN THE DIRECTION OF THE REFLECTED RAY.
C
C     SK,SL,SM ARE DIRECTION NUMBERS OF A LINE NORMAL TO THE
C     SURFACE AT THE POINT OF REFLECTION.
C
C     THIS IS A RAY TRACING PROGRAM ADAPTED FROM THE METHODS
C     OF SPENCER AND MURTY JOSA VOL.52, P. 672, 1961.
C
C
      A=(DK*SK+DL*SL+DM*SM)/(SK*SK+SL*SL+SM*SM)
      DK=DK-2.*A*SK
      DL=DL-2.*A*SL
      DM=DM-2.*A*SM
      RETURN
      END
```

C SUBROUTINE RFR

```
C     SUBROUTINE RFR
C
C
      SUBROUTINE RFR(DK,DL,DM,SK,SL,SM,XN1,XN2,E,ERR,I)
C
C
C     THIS SUBROUTINE COMPUTES THE DIRECTION OF A RAY REFRACTED
C     AT AN INTERFACE BETWEEN TWO MEDIUMS OF DIFFERING INDICES
C     OF REFRACTION.
C
C     DK,DL,DM ON INPUT ARE THE COMPONENTS OF A UNIT VECTOR
C     IN THE DIRECTION OF THE INCIDENT RAY.
C
C     DK,DL,DM ON OUTPUT ARE THE COMPONENTS OF A UNIT VECTOR
C     IN THE DIRECTION OF THE REFRACTED RAY.
C
C     SK,SL,SM ARE DIRECTION NUMBERS OF A LINE NORMAL TO THE
C     SURFACE OF REFRACTION AT THE POINT WHERE THE INCIDENT RAY
C     STRIKES THE REFRACTING SURFACE.
C
```

THIS PAGE IS BEST QUALITY PRACTICABLE
FROM COPY FURNISHED TO DDC

```
      C       XN1 IS THE INDEX OF REFRACTION FOR THE INCIDENT MEDIUM.
      C
      C       XN2 IS THE INDEX OF REFRACTION FOR THE REFRACTING MEDIUM.
      C
      C       E IS THE CONVERGENCE PARAMETER.  THE NEWTON-RAPHSON
      C       ITERATION CONTINUES UNTIL EITHER THE ABSOLUTE VALUE OF
      C       THE DIFFERENCE BETWEEN SUCCESSIVE ITERATIONS IS LESS
      C       THAN E OR 50 ITERATIONS HAVE BEEN PERFORMED.
      C
      C       ERR IS THE ABSOLUTE VALUE OF THE DIFFERENCE BETWEEN
      C       THE LAST TWO ITERATIONS PERFORMED.
      C
      C       I IS THE NUMBER OF ITERATIONS PERFORMED.  IF I=50
      C       CONVERGENCE TO THE DESIRED ACCURACY HAS NOT OCCURRED.
      C
      C       THIS IS A RAY TRACING PROGRAM ADAPTED FROM THE METHODS
      C       OF SPENCER AND MURTY JOSA VOL.52, P 672, 1961.
      C
      C
              I=1
              XMU=XN1/XN2
              TIDE=SK*SK+SL*SL+SM*SM
              A=XMU*(DK*SK+DL*SL+DM*SM)/TIDE
              B=(XMU*XMU-1.)/TIDE
              GAMMA=(-B)/(2.*A)
    1         T=(GAMMA*GAMMA-B)/(2.*(GAMMA+A))
              ERR=ABS(T-GAMMA)
              I=I+1
              GAMMA=T
              IF(ERR-E)2,2,3
    3         CONTINUE
              IF(I-50)1,2,2
    2         DK=XMU*DK+GAMMA*SK
              DL=XMU*DL+GAMMA*SL
              DM=XMU*DM+GAMMA*SM
              RETURN
              END

C       SUBROUTINE DFR

      C       SUBROUTINE DFR
      C
              SUBROUTINE DFR(DK,DL,DM,SK,SL,SM,XLMB,D,XN1,BK,E,ERR,I)
      C
      C
      C       THIS SUBROUTINE COMPUTES THE DIRECTION OF A RAY DIFFRACTED
      C       BY A REFLECTION PLANE GRATING.
      C
      C       DK,DL,DM ON INPUT ARE COMPONENTS OF A UNIT VECTOR IN THE
      C       DIRECTION OF THE INCIDENT RAY.
      C
      C       DK,DL,DM ON OUTPUT ARE THE COMPONENTS OF A UNIT VECTOR
      C       IN THE DIRECTION OF THE DIFFRACTED RAY.
      C
      C       SK,SL,SM ARE DIRECTION NUMBERS OF A LINE NORMAL TO THE
      C       GRATING SURFACE. EITHER THE INWARD OR OUTWARD NORMAL MAY
      C       BE USED.
      C
      C       XLMB IS THE WAVELENGTH OF THE INCIDENT AND DIFFRACTED
      C       RADIATION IN AIR.
      C
      C       D IS THE GRATING SPACING.
      C
      C       THIS PROGRAM ASSUMES THAT THE INCIDENT AND DIFFRACTED
      C       RAYS ARE IN THE SAME MEDIUM.
      C
      C       XN1 IS THE INDEX OF REFRACTION OF THE MEDIUM IN WHICH THE
      C       INCIDENT AND DIFFRACTED RAYS PROPAGATE.
      C
      C       BK IS THE ORDER OF INTERFERENCE.
      C
      C       E IS THE CONVERGENCE PARAMETER.  THE NEWTON-RAPHSON ITERATION
      C       CONTINUES UNTIL EITHER THE ABSOLUTE VALUE OF THE DIFFERENCE
      C       BETWEEN SUCCESSIVE ITERATIONS IS LESS THAN E OR 50 ITERATIONS
      C       HAVE BEEN PERFORMED.
      C
      C       ERR IS THE ABSOLUTE VALUE OF THE DIFFERENCE BETWEEN THE
```

THIS PAGE IS BEST QUALITY PRACTICABLE
FROM COPY FURNISHED TO DDC

```
      C       LAST TWO ITERATIONS PERFORMED.
      C
      C       I IS THE NUMBER OF ITERATIONS WHICH WERE PERFORMED. IF
      C       I=50 CONVERGENCE TO THE REQUIRED ACCURACY DID NOT OCCUR.
      C
      C       GAMMA IS THE ROOT OF THE QUADRATIC EQUATION GENERATED BY
      C       THE PROGRAM.
      C
      C       THIS PROGRAM ASSUMES THE GRATING RULINGS ARE PRODUCED BY
      C       A FAMILY OF PARALLEL PLANES WHICH ARE ALL PARALLEL TO THE
      C       Y-Z PLANE.  THE SEPERATION BETWEEN ADJACENT PLANES IS D.
      C
      C       U,V,W (WHICH ARE GENERATED IN THE PROGRAM) ARE THE DIRECTION
      C       COSINES OF A LINE OF UNIT LENGTH ALONG THE GRATING SURFACE
      C       NORMAL TO THE RULINGS.
      C
      C       THIS IS A RAY TRACING PROGRAM ADAPTED FROM THE METHODS OF
      C       SPENCER AND MURTY JOSA VOL.52, P.672, 1961.
      C
      C
            TEA=SL*SL+SM*SM
            U=1./SQRT(1.+SK*SK/TEA)
            V=-SK*SL*U/TEA
            W=-SK*SM*U/TEA
            I=1
            DELTA=(RK*XLMB)/(XN1*D)
            T=SK*SK+SL*SL+SM*SM
            A=(DK*SK+DL*SL+DM*SM)/T
            B=(DELTA*DELTA-2.*DELTA*(DK*U+DL*V+DM*W))/T
            GAMMA=B/(2.*A)-2.*A
    1       TEMP=(GAMMA*GAMMA-B)/(2.*(GAMMA+A))
            ERR=ABS(TEMP-GAMMA)
            I=I+1
            GAMMA=TEMP
            IF(ERR-E)2,2,3
    3       CONTINUE
            IF(I-50)1,2,2
    2       DK=DK-DELTA*U+GAMMA*SK
            DL=DL-DELTA*V+GAMMA*SL
            DM=DM-DELTA*W+GAMMA*SM
            RETURN
            END
```

THIS PAGE IS BEST QUALITY PRACTICABLE
FROM COPY FURNISHED TO DDC

Programs representative of those used in the ray-tracing analysis of the Czerny-Turner optical system

```
C       PROGRAM SEGMENT CT1

 1  C       PROGRAM SEGMENT CT1
 2  C
 3  C       THIS IS THE FIRST SEGMENT OF A CHAINED PROGRAM TO TRACE
 4  C       41 RAYS THROUGH A CZERNY-TURNER SPECTROMETER.
 5  C
 6  C       THIS SEGMENT, CALLED CT1, COMPUTES THE DIRECTION COSINES OF
 7  C       THE CHIEF RAY.
 8  C
 9  C  INPUT
10  C       THE CZERNY-TURNER SPECTROMETER PARAMETERS ARE READ FROM THE
11  C       RKBO:CZPR.DA FILE.
12  C       THE X AND Y COORDINATES OF A POINT IN THE INPUT SLIT FROM
13  C       WHICH THE CHIEF RAY EMANATES IS REQUESTED BY THE TELETYPE.
14  C
15  C  OUTPUT
16  C       THE DIRECTION COSINES OF THE CHIEF RAY ARE LOADED INTO THE
17  C       FIRST 3 LOCATION OF RKBO:CRAY.DA.
18  C       THE X,Y,Z COORDINATES OF THE OBJECT POINT (IN THE INPUT SLIT)
19  C       ARE LOADED INTO LOCATIONS 4 AND 5 OF THE SAME FILE.
20  C
21  C  SUBPROGRAMS CALLED
22  C       CRAY
23  C       RMAT
24  C       TRNS1
25  C       TRNS2
26  C       TRNS3
27  C       TRNS4
28  C       ITSP
29  C       ITPL
30  C       RFL
31  C
32  C
33          DIMENSION AP(25)
34          ZS=0.
35          WRITE(1,99)
36          READ(1,100)XS,YS
37          CALL IOPEN('RKBO','CZPR')
38          READ(4,101)(AP(I),I=1,25)
39          R1=AP(1)
40          XM1=AP(2)
41          YM1=AP(3)
42          ZM1=AP(4)
43          EA=AP(5)
44          XG=AP(11)
45          YG=AP(12)
46          ZG=AP(13)
47          GK=AP(14)
48          GL=AP(15)
49          GM=AP(16)
50          CALL CRAY(XS,YS,XM1,YM1,ZM1,R1,EA,XG,YG,ZG,GK,GL,GM,DK,DL,DM)
51          CALL OOPEN('RKBO','CRAY')
52          WRITE(4,101)DK,DL,DM,XS,YS,ZS
53          CALL OCLOSE
54          CALL CHAIN('CT2')
55  99      FORMAT('COORDINATES OF OBJECT POINT IN INPUT SLIT'///)
56  100     FORMAT('X=',E20.9/'Y=',E20.9)
57  101     FORMAT(25A6)
58          END
```

THIS PAGE IS BEST QUALITY PRACTICABLE
FROM COPY FURNISHED TO DDC

C PROGRAM SEGMENT CT2

```
C       PROGRAM SEGMENT CT2
C
C       THIS IS THE SECOND SEGMENT OF A CHAINED PROGRAM TO TRACE
C       41 RAYS THROUGH A CZERNY TURNER SPECTROMETER.
C
C       THIS SEGMENT CALLED CT2 COMPUTES THE DIRECTION COSINES
C       OF THE 41 RAYS FROM THE OBJECT POINT (XS,YS,ZS) IN THE
C       INPUT SLIT.
C       THESE 41 RAYS FORM CONES ABOUT THE CHIEF RAY, THE OUTER
C       CONE BEING THE F/NUMBER CONE.
C
C
C  INPUT
C       THE CZERNY-TURNER SPECTROMETER PARAMETERS ARE READ FROM THE
C       RKB0:CZPR.DA FILE.
C
C  OUTPUT
C       THE DIRECTION COSINES ARE LOADED INTO THE AK,AL,AM ARRAYS.
C       AK CONTAINS THE DIRECTION COSINES WITH RESPECT TO THE X AXIS.
C       AL CONTAINS THE DIRECTION COSINES WITH RESPECT TO THE Y AXIS.
C       AM CONTAINS THE DIRECTION COSINES WITH RESPECT TO THE Z AXIS.
C
C  SUBPROGRAMS CALLED
C       DCOS
C       AREA
C       RMAT
C       TRNS4
C
C
      COMMON XP,YP,ZP,AK,AL,AM
      COMMON R1,XM1,YM1,ZM1,EA1,R2,XM2,YM2,ZM2,EA2,XG,YG,ZG
      COMMON GK,GL,GM,D,XPLT,YPLT,ZPLT,PLTK,PLTL,PLTM,WAVEL
      COMMON BETA,GAMMA,E,XS,YS,ZS
      DIMENSION XP(41),YP(41),ZP(41),AK(41),AL(41),AM(41),WM(25)
      BETA=0.
      GAMMA=0.
      E=.0001
      CALL IOPEN('RKB0','CZPR')
      READ(4,100)(WM(I),I=1,25)
      R1=WM(1)
      XM1=WM(2)
      YM1=WM(3)
      ZM1=WM(4)
      EA1=WM(5)
      R2=WM(6)
      XM2=WM(7)
      YM2=WM(8)
      ZM2=WM(9)
      EA2=WM(10)
      XG=WM(11)
      YG=WM(12)
      ZG=WM(13)
      GK=WM(14)
      GL=WM(15)
      GM=WM(16)
      D=WM(17)
      XPLT=WM(18)
      YPLT=WM(19)
      ZPLT=WM(20)
      PLTK=WM(21)
      PLTL=WM(22)
      PLTM=WM(23)
      WAVEL=WM(24)
      FNO=WM(25)
      CALL IOPEN('RKB0','CRAY')
      READ(4,100)DK,DL,DM,XS,YS,ZS
C     LOAD DIRECTION COSINES OF RAYS INTO THE AK,AL,AM ARRAYS.
      CALL DCOS(DK,DL,DM,FNO)
      CALL CHAIN('CT3')
100   FORMAT(25A6)
      END
```

THIS PAGE IS BEST QUALITY PRACTICABLE
FROM COPY FURNISHED TO DDC

C PROGRAM SEGMENT CT3

```
C       PROGRAM SEGMENT CT3
C
C       THIS IS THE THIRD SEGMENT OF A CHAINED PROGRAM TO TRACE
C       41 RAYS THROUGH A CZERNY-TURNER SPECTROMETER.
C
C       THIS SEGMENT CALLED CT3 TRACES THE 41 RAYS FROM THE OBJECT
C       POINT IN THE INPUT SLIT THROUGH REFLECTION FROM THE
C       COLLIMATOR MIRROR.
C
C  INPUT
C       ALL INPUT TRANSFERED IN COMMON BY CHAINING OPERATION.
C
C  OUTPUT
C       OUTPUT IS TRANSFERED TO CT4 THROUGH COMMON BY THE
C       CHAINING OPERATION.
C       THE ARRAYS XP,YP,ZP CONTAIN THE X,Y,Z COORDINATES
C       RESPECTIVELY OF THE 41 RAY INTERSECTIONS WITH THE
C       COLLIMATOR MIRROR.
C       THE ARRAYS AK,AL,AM CONTAIN THE DIRECTION COSINES OF
C       THE 41 RAYS AFTER REFLECTION FROM THE COLLIMATOR MIRROR.
C       AK CONTAINS THE DIRECTION COSINES WITH RESPECT TO THE X AXIS.
C       AL CONTAINS THE DIRECTION COSINES WITH RESPECT TO THE Y AXIS.
C       AM CONTAINS THE DIRECTION COSINES WITH RESPECT TO THE Z AXIS.
C       THE CZERNY-TURNER SPECTROMETER PARAMETERS ARE ALSO TRANSFERED
C       TO CT4 THOUGH COMMON BY THE CHAINING OPERATION.
C
C  SUBPROGRAMS CALLED
C       RMAT
C       TRNS1
C       TRNS2
C       TRNS3
C       TRNS4
C       RFL
C       ITSP
C
C
        COMMON XP,YP,ZP,AK,AL,AM
        COMMON R1,XM1,YM1,ZM1,EA1,R2,XM2,YM2,ZM2,EA2,XG,YG,ZG
        COMMON GK,GL,GM,D,XPLT,YPLT,ZPLT,PLTK,PLTL,PLTM,WAVEL
        COMMON BETA,GAMMA,E,XS,YS,ZS
        DIMENSION XP(41),YP(41),ZP(41),AK(41),AL(41),AM(41)
        DIMENSION RM(3,3),RMI(3,3)
        CALL RMAT(EA1,BETA,GAMMA,RM,RMI)
C       TRANSFORM OBJECT POINT TO COORDINATE SYSTEM OF COLLIMATOR.
        CALL TRNS1(RM,XS,YS,ZS,XM1,YM1,ZM1)
        DO 10 I=1,41
        DK=AK(I)
        DL=AL(I)
        DM=AM(I)
        X=XS
        Y=YS
        Z=ZS
        CALL TRNS2(RM,DK,DL,DM)
        CALL ITSP(DK,DL,DM,X,Y,Z,R1,E,ERR,S,P,IQ,SK,SL,SM)
        CALL RFL(DK,DL,DM,SK,SL,SM)
        CALL TRNS3(RMI,X,Y,Z,XM1,YM1,ZM1)
        CALL TRNS4(RMI,DK,DL,DM)
        AK(I)=DK
        AL(I)=DL
        AM(I)=DM
        XP(I)=X
        YP(I)=Y
10      ZP(I)=Z
        CALL CHAIN('CT4')
        END
```

THIS PAGE IS BEST QUALITY PRACTICABLE
FROM COPY FURNISHED TO DDC

C PROGRAM SEGMENT CT4

```
C       PROGRAM SEGMENT CT4
C
C       THIS IS THE FOURTH SEGMENT OF A CHAINED PROGRAM TO TRACE
C       41 RAYS THROUGH A CZERNY-TURNER SPECTROMETER.
C
C       THIS SEGMENT, CALLED CT4, TRACES THE 41 RAYS FROM THE
C       COLLIMATOR MIRROR THROUGH DIFFRACTION FROM THE GRATING.
C
C  INPUT
C       ALL INPUT TRANSFERED IN COMMON BY CHAINING OPERATION.
C
C  OUTPUT
C       OUTPUT IS TRANSFERED TO CT5 THROUGH COMMON BY THE
C       CHAINING OPERATION.
C       THE ARRAYS AK,AL,AM CONTAIN THE DIRECTION COSINES OF
C       THE 41 RAYS AFTER DIFFRACTION FROM THE GRATING.
C       AK CONTAINS THE DIRECTION COSINES WITH RESPECT TO THE X AXIS.
C       AL CONTAINS THE DIRECTION COSINES WITH RESPECT TO THE Y AXIS.
C       AM CONTAINS THE DIRECTION COSINES WITH RESPECT TO THE Z AXIS.
C       THE ARRAYS XP,YP,ZP CONTAIN THE X,Y,Z COORDINATES RESPECTIVELY
C       OF THE 41 RAY INTERSECTIONS WITH THE GRATING.
C       THE CZERNY-TURNER SPECTROMETER PARAMETERS ARE ALSO TRANSFERED
C       TO CT5 THROUGH COMMON BY THE CHAINING OPERATION.
C
C  SUBPROGRAMS CALLED
C       ITPL
C       DFR
C
C
      COMMON XP,YP,ZP,AK,AL,AM
      COMMON R1,XM1,YM1,ZM1,EA1,R2,XM2,YM2,ZM2,EA2,XG,YG,ZG
      COMMON GK,GL,GM,D,XPLT,YPLT,ZPLT,PLTK,PLTL,PLTM,WAVEL
      COMMON BETA,GAMMA,E,X,Y,Z
      DIMENSION XP(41),YP(41),ZP(41),AK(41),AL(41),AM(41)
      BK=1.
      XN1=1.
      DO 10 I=1,41
      X=XP(I)
      Y=YP(I)
      Z=ZP(I)
      DK=AK(I)
      DL=AL(I)
      DM=AM(I)
      CALL ITPL(DK,DL,DM,X,Y,Z,XG,YG,ZG,GK,GL,GM)
      CALL DFR(DK,DL,DM,GK,GL,GM,WAVEL,D,XN1,BK,E,ERR,IQ)
      XP(I)=X
      YP(I)=Y
      ZP(I)=Z
      AK(I)=DK
      AL(I)=DL
10    AM(I)=DM
      CALL CHAIN('CT5')
      END
```

THIS PAGE IS BEST QUALITY PRACTICABLE
FROM COPY FURNISHED TO DDC

```
C       PROGRAM SEGMENT CT5

 1  C       PROGRAM SEGMENT CT5
 2  C
 3  C       THIS IS THE FIFTH SEGMENT OF A CHAINED PROGRAM TO TRACE
 4  C       41 RAYS THROUGH A CZERNY-TURNER SPECTROMETER.
 5  C
 6  C       THIS SEGMENT, CALLED CT5, TRACES THE 41 RAYS FROM THE
 7  C       GRATING THROUGH REFLECTION WITH THE CAMERA MIRROR
 8  C       TO THE IMAGE PLANE.
 9  C
10  C  INPUT
11  C       ALL INPUT TRANSFERED IN COMMON BY CHAINING OPERATION.
12  C
13  C  OUTPUT
14  C       OUTPUT IS TRANSFERED TO CT6 THROUGH COMMON BY THE CHAINING
15  C       OPERATION.
16  C       THE ARRAYS XP,YP,ZP CONTAIN THE X,Y,Z COORDINATES RECPECTIVELY
17  C       OF THE 41 RAY INTERSECTIONS WITH THE IMAGE PLANE.
18  C       THE ARRAYS AK,AL,AM CONTAIN THE DIRECTION COSINES OF THE
19  C       41 RAYS AFTER REFLECTION FROM THE CAMERA MIRROR.
20  C       AK CONTAINS THE DIRECTION COSINES WITH RESPECT TO THE X AXIS.
21  C       AL CONTAINS THE DIRECTION COSINES WITH RESPECT TO THE Y AXIS.
22  C       AM CONTAINS THE DIRECTION COSINES WITH RESPECT TO THE Z AXIS.
23  C       THE CZERNY-TURNER SPECTROMETER PARAMETERS ARE ALSO TRANSFERED
24  C       TO CT6 THROUGH COMMON BY THE CHAINING OPERATION.
25  C
26  C  SUBPROGRAMS CALLED
27  C       RMAT
28  C       TRNS1
29  C       TRNS2
30  C       TRNS3
31  C       TRNS4
32  C       ITSP
33  C       RFL
34  C       ITPL
35  C
36  C
37          COMMON XP,YP,ZP,AK,AL,AM
38          COMMON R1,XM1,YM1,ZM1,EA1,R2,XM2,YM2,ZM2,EA2,XG,YG,ZG
39          COMMON GK,GL,GM,D,XPLT,YPLT,ZPLT,PLTK,PLTL,PLTM,WAVEL
40          COMMON BETA,GAMMA,E
41          DIMENSION XP(41),YP(41),ZP(41),AK(41),AL(41),AM(41)
42          DIMENSION RM(3,3),RMI(3,3)
43          CALL RMAT(EA2,BETA,GAMMA,RM,RMI)
44          DO 10 I=1,41
45          X=XP(I)
46          Y=YP(I)
47          Z=ZP(I)
48          DK=AK(I)
49          DL=AL(I)
50          DM=AM(I)
51          CALL TRNS1(RM,X,Y,Z,XM2,YM2,ZM2)
52          CALL TRNS2(RM,DK,DL,DM)
53          CALL ITSP(DK,DL,DM,X,Y,Z,R2,E,ERR,S,P,IQ,SK,SL,SM)
54          CALL RFL(DK,DL,DM,SK,SL,SM)
55          CALL TRNS3(RMI,X,Y,Z,XM2,YM2,ZM2)
56          CALL TRNS4(RMI,DK,DL,DM)
57          AK(I)=DK
58          AL(I)=DL
59          AM(I)=DM
60          CALL ITPL(DK,DL,DM,X,Y,Z,XPLT,YPLT,ZPLT,PLTK,PLTL,PLTM)
61          XP(I)=X
62          YP(I)=Y
63  10      ZP(I)=Z
64          READ(1,100)M1
65          IF(M1-1632)16,12,16
66  12      CALL CHAIN('CTS')
67  16      CALL CHAIN('CT6')
68  100     FORMAT('CHAIN TO CURVED SLIT ROUTINE (Y OR N)-?',A1)
69          END
```

AD-A064 198 UTAH STATE UNIV LOGAN ELECTRO-DYNAMICS LAB F/G 20/6
INCREASING THE THROUGHPUT OF HADAMARD SPECTROMETERS BY THE USE --ETC(U)
SEP 78 R W ESPLIN, G A VANASSE, D J BAKER F19628-77-C-0203
UNCLASSIFIED EDL-SRL-78-2 AFGL-TR-78-0232 NL

4 OF 4
AD
A064198



END
DATE
FILMED
4 -79
DDC

THIS PAGE IS BEST QUALITY PRACTICABLE
FROM COPY FURNISHED TO DDC

C PROGRAM SEGMENT CT6

```
C       PROGRAM SEGMENT CT6
C
C       THIS SEGMENT PRINTS OUT THE COORDINATES OF THE RAYS
C
        COMMON XP,YP,ZP,AK,AL,AM
        COMMON R1,XM1,YM1,ZM1,EA1,R2,XM2,YM2,ZM2,EA2,XG,YG,ZG
        COMMON GK,GL,GM,D,XPLT,YPLT,ZPLT,PLTK,PLTL,PLTM,WAVEL
        COMMON BETA,GAMMA,E
        DIMENSION XP(41),YP(41),ZP(41),AK(41),AL(41),AM(41)
        WRITE(1,100)
        READ(1,102)MM
        IF(1632-MM)12,5,12
5       CONTINUE
        DO 10 I=1,41
10      WRITE(1,101)XP(I),YP(I),ZP(I)
12      READ(1,103)M2
        IF(1632-M2)14,13,14
13      CALL CHAIN('PLTMM')
14      READ(1,104)M3
        IF(1632-M3)16,15,16
15      READ(1,105)SEG
        CALL CHAIN(SEG)
16      STOP
100     FORMAT(10X,'X',20X,'Y',20X,'Z'//)
101     FORMAT(2(E16.9,4X),E16.9)
102     FORMAT('PRINT X,Y,Z COORDINATES (Y OR N)?-',A1)
103     FORMAT('PLT POINTS IN X-Y PLANE (Y OR N)?-',A1)
104     FORMAT('CHAIN TO ANOTHER SEGMENT (Y OR N)?-',A1)
105     FORMAT('CHAIN TO ',A6)
        END
```

THIS PAGE IS BEST QUALITY PRACTICABLE
FROM COPY FURNISHED TO DDC

C PROGRAM SEGMENT CTS

```
C       PROGRAM SEGMENT CTS
C
C
C       THIS SEGMENT,CALLED CTS, COMPUTES THE PERPENDICULAR DISTANCE
C       FROM THE CENTER LINE OF A CURVED SLIT TO THE 41 RAYS IN
C       THE CZERNY-TURNER SPOT DIAGRAM.
C
C       THIS PROGRAM IS CHAINED TO FROM CTS.
C
C       ALL DISTANCES ARE IN MILLIMETERS.
C
C
        COMMON XP,YP,ZP,AK,AL,AM
        COMMON R1,XM1,YM1,ZM1,EA1,R2,XM2,YM2,ZM2,EA2,XG,YG,ZG
        COMMON GK,GL,GM,D,XPLT,YPLT,ZPLT,PLTK,PLTL,PLTM,WAVEL
        DIMENSION XP(41),YP(41),ZP(41),AK(41),AL(41),AM(41)
C       CONVERT X COORDINATES TO A COORDINATE SYSTEM WTIH AN X AXIS
C       PARALLEL TO THE IMAGE PLANE.
C       THE Y AXIS IS UNCHANGED.
        DO 5 I=1,41
5       XP(I)=XP(I)/PLTM
        READ(1,102)R
        WRITE(1,104)
        READ(1,105)XC
        XC=XC/PLTM
        READ(1,103)M1
        WRITE(1,108)
        WRITE(1,109)
        IF(M1-1632)14,20,14
C       SLIT CURVED AWAY FROM GRATING
14      CONTINUE
        DO 18 I=1,41
        XI=XP(I)
        YI=YP(I)
        PHO=SQRT((XC-R-XI)**2+YI**2)-R
18      WRITE(1,110)I,PHO
        GO TO 25
C       SLIT CURVED TOWARD THE GRATING
20      CONTINUE
        DO 22 I=1,41
        XI=XP(I)
        YI=YP(I)
        PHO=R-SQRT((XI-XC-R)**2+YI**2)
22      WRITE(1,110)I,PHO
25      READ(1,111)M2
        IF(1632-M2)28,26,28
26      CALL CHAIN('PLTMM')
28      STOP
102     FORMAT('RADIUS OF SLIT CURVE (ALWAYS POSITIVE)=',E20.9)
104     FORMAT('CHIEF RAY FROM ON AXIS POINT')
105     FORMAT('STRIKES THE IMAGE PLANE AT X=',E20.9)
103     FORMAT('IS THE SLIT CURVED TOWARD THE GRATING (Y OR N)-?',A1
108     FORMAT(///'RAY NUMBER AND PERPENDICULAR DISTANCE FROM SLIT'/
        1'CENTER LINE TO RAY INTERCEPT'//
        2'A PLUS DISTANCE MEANS THE RAY IS ON THE GRATING SIDE OF TH-'/
        3'SLIT CENTER LINE AND VICE VERSA')
109     FORMAT(///'RAY',' DISTANCE')
110     FORMAT(I3,F8.3)
111     FORMAT('PLOT SPOT DIAGRAM ON IMAGE PLANE (Y OR N)-?',A1)
        END
```

THIS PAGE IS BEST QUALITY PRACTICABLE
FROM COPY FURNISHED TO DDC

C SUBROUTINE AREA

```
C       SUBROUTINE AREA
C
C
        SUBROUTINE AREA(R,N1,N2,PHO)
C
C       THIS SUBROUTINE DETERMINES THE COORDINATES OF RAY
C       CIRCLES SO THAT THE AREAS OF EACH ANNULUS FORMED BY
C       SUCCESSIVE CIRCLES ARE EQUAL.
C
C  INPUT
C       R IS THE RADIUS OF THE RAY CIRCLE WITH THE LARGEST
C       DIAMETER.
C       N1 IS THE NUMBER OF RAY CIRCLES DESIRED.
C       N2 IS THE NUMBER OF RAYS IN EACH CIRCLE
C
C  OUTPUT
C       XP,YP ARE ARRAYS WHICH CONTAIN THE X AND Y COORDINATES
C       RESPECTIVELY OF THE (N1*N2+1) RAYS.
C       PHO CONTAINS THE RADII OF THE N1 RAY CIRCLES
C
C  NO SUBPROGRAMS CALLED
C
        COMMON XP,YP,ZP,AK,AL,AM
        DIMENSION XP(41),YP(41),ZP(41),AK(41),AL(41),AM(41)
        DIMENSION PHO(5)
        PHO(N1)=R
        XN1=FLOAT(N1)
        XN2=FLOAT(N2)
        LIME=N1-1
        DO 10 I=1,LIME
        XI=FLOAT(I)
        NUT=N1-I
10      PHO(NUT)=SQRT((XN1-XI)/XN1)*PHO(N1)
        ANGLE=2.*3.14159265/XN2
        IDLE=0
        DO 20 IND1=1,N1
        THETA=0.
        DO 15 IX=1,N2
        IDLE=IDLE+1
        XP(IDLE)=COS(THETA)*PHO(IND1)
        YP(IDLE)=SIN(THETA)*PHO(IND1)
        THETA=THETA+ANGLE
15      CONTINUE
20      CONTINUE
        NOT=N1*N2+1
        XP(NOT)=0.
        YP(NOT)=0.
        RETURN
        END
```

THIS PAGE IS BEST QUALITY PRACTICABLE
FROM COPY FURNISHED TO DDC

```
C       SUBROUTINE DCOS

  1  C        SUBROUTINE DCOS
  2  C
  3           SUBROUTINE DCOS(DK,DL,DM,FNO)
  4  C
  5  C        THIS SUBROUTINE COMPUTES THE DIRECTION COSINES OF 41 RAYS
  6  C        WHICH FORM CONES EMANATING FROM THE OBJECT POINT AROUND
  7  C        THE CHIEF RAY WITH THE DIRECTION COSINES DK,DL,DM.
  8  C
  9  C   INPUT
 10  C        DK,DL,DM ARE THE DIRECTION COSINES OF THE CHIEF RAY.
 11  C        FNO IS THE F/NUMBER OF THE RADIATION CONE OF MAXIMUM SOLID
 12  C        ANGLE.
 13  C
 14  C   OUTPUT
 15  C        AK,AL,AM ARE ARRAYS WHICH CONTAIN THE DIRECTION COSINES OF
 16  C        THE 41 RAYS WITH RESPECT TO THE X,Y, AND Z AXES RESPECTIVELY.
 17  C
 18  C   SUBROUTINES CALLED
 19  C        AREA
 20  C        RMAT
 21  C        TRNS4
 22  C
 23           COMMON XP,YP,ZP,AK,AL,AM
 24           DIMENSION XP(41),YP(41),ZP(41),AK(41),AL(41),AM(41)
 25           DIMENSION RM(3,3),RMI(3,3),PHO(5)
 26           F=500.
 27           RR=F/(FNO*2.)
 28           N1=5
 29           N2=8
 30           CALL AREA(RR,N1,N2,PHO)
 31  C        COMPUTE DIRECTION COSINES ABOUT THE CHIEF RAY WITH DIRECTION
 32  C        COSINES (0,0,1)
 33           AK(41)=0.
 34           AL(41)=0.
 35           AM(41)=1.
 36           I=1
 37           DO 4 J=1,5
 38           A=PHO(J)
 39           DD=SQRT(A*A+F*F)
 40           DO 4 I2=1,8
 41           AK(I)=-XP(I)/DD
 42           AL(I)=-YP(I)/DD
 43           AM(I)=F/DD
 44           I=I+1
 45  4        CONTINUE
 46           IF(ABS(DK)+ABS(DL)-1.E-14)42,42,6
 47  C        CONVERT DIRECTION COSINES TO FORM CONES ABOUT THE DESIRED
 48  C        CHIEF RAY.
 49  6        DD=SQRT(DM**2+DK**2)
 50           ALPHA=ATAN(DK/DM)
 51           BETA=ATAN(DL/DD)
 52           GAMMA=0.
 53           CALL RMAT(ALPHA,BETA,GAMMA,RM,RMI)
 54           DO 10 I=1,41
 55           DK=AK(I)
 56           DL=AL(I)
 57           DM=AM(I)
 58           CALL TRNS4(RMI,DK,DL,DM)
 59           AK(I)=DK
 60           AL(I)=DL
 61  10       AM(I)=DM
 62  42       RETURN
 63           END
```

THIS PAGE IS BEST QUALITY PRACTICABLE
FROM COPY FURNISHED TO DDC

```
C       SUBROUTINE CRAY
```

```
      C       SUBROUTINE CRAY
      C
      C
              SUBROUTINE CRAY(X,Y,XM1,YM1,ZM1,R1,EA,XG,YG,ZG,GK,GL,GM,
              1CK,CL,CM)
      C
      C       THIS SUBROUTINE COMPUTES THE DIRECTION COSINES OF THE
      C       CHIEF RAY OF A POINT IN THE INPUT PLANE OF THE
      C       CZERNY TURNER SPECTROGRAPH.
      C       THE CHIEF RAY IS THE RAY WHICH STRIKES THE GRATING AT ITS
      C       CENTER.
      C       THE ORIGIN OF THE CARTESIAN COORDINATE SYSTEM IS LOCATED AT
      C       THE CENTER OF THE INPUT SLIT IN THE CORRECTED LOCATION.
      C
      C  INPUT
      C       X,Y ARE THE COORDINATES OF THE POINT IN THE INPUT PLANE.
      C       X AND Y MUST BE EQUAL TO OR GREATER THAN ZERO.
      C       XM1,YM1,ZM1 ARE THE COORDINATES OF THE CENTER OF THE
      C       COLLIMATOR MIRROR.
      C       R1 IS THE RADIUS OF CURVATURE OF THE COLLIMATOR MIRROR.
      C       EA IS THE EULER ALPHA OFF-AXIS ANGLE OF THE COLLIMATOR
      C       MIRROR EXPRESSED IN RADIANS.
      C       XG,YG,ZG ARE THE COORDINATES OF THE GRATING CENTER.
      C       GK,GL,GM ARE THE DIRECTION COSINES OF THE GRATING NORMAL
      C
      C  OUTPUT
      C       CK,CL,CM ARE THE DIRECTION COSINES OF THE CHEIF RAY FROM
      C       THE POINT (X,Y,0).
      C
      C  SUBPROGRAMS CALLED
      C       RMAT
      C       TRNS1
      C       TRNS2
      C       TRNS3
      C       TRNS4
      C       ITSP
      C       ITPL
      C       RFL
      C
              DIMENSION RM(3,3),RMI(3,3)
              CK=0.
              CL=0.
              CM=1.
              BETA=0.
              GAMMA=0.
              Z=0.
      C       FIRST ESTIMATE OF THE REQUIRED DIRECTION COSINES
              DK=0.
              DL=0.
              DM=1.
              E=.0001
              XX=X
              YY=Y
              ZZ=Z
      C       TRANSFORM TO COORDINATE SYSTEM OF COLLIMATOR.
              CALL RMAT(EA,BETA,GAMMA,RM,RMI)
      C       ITERATE THE DIRECTION COSINES
              DO 50 I=1,50
              CALL TRNS1(RM,XX,YY,ZZ,XM1,YM1,ZM1)
              CALL TRNS2(RM,DK,DL,DM)
              CALL ITSP(DK,DL,DM,XX,YY,ZZ,R1,E,ERR,S,P,IQ,SK,SL,SM)
              CALL RFL(DK,DL,DM,SK,SL,SM)
      C       TRANSFORM BACK TO ORIGINAL COORDINATE SYSTEM.
              CALL TRNS3(RMI,XX,YY,ZZ,XM1,YM1,ZM1)
              CALL TRNS4(RMI,DK,DL,DM)
              XXX=XX
              YYY=YY
              ZZZ=ZZ
              CALL ITPL(DK,DL,DM,XX,YY,ZZ,XG,YG,ZG,GK,GL,GM)
              IF(XX-XG+YY-YG-1.E-3)60,60,40
              IF(XX-XG-1.E-3)41,41,40
      40      XX=XXX-(XX-XG)/2.
      41      YY=YYY-(YY-YG)/2.
              ZZ=ZZZ
              DIS=SQRT((X-XX)**2+(Y-YY)**2+(Z-ZZ)**2)
              DK=(XX-X)/DIS
```

THIS PAGE IS BEST QUALITY PRACTICABLE
FROM COPY FURNISHED TO DDC

```
77              DL=(YY-Y)/DIS
78              DM=(ZZ-Z)/DIS
79              CK=DK
80              CL=DL
81              CM=DM
82    50        CONTINUE
83    60        WRITE(1,208)
84              WRITE(1,210)XX,YY,ZZ
85              WRITE(1,204)
86    62        WRITE(1,205)CK,CL,CM
87              RETURN
88    204       FORMAT('DIRECTION COSINES OF CHIEF RAY'//)
89    205       FORMAT('CK=',E20.9,'CL=',E20.9,'CM=',E20.9)
90    208       FORMAT('RAY COORDINATES AT GRATING')
91    210       FORMAT('X=',E20.9,'Y=',E20.9,'Z=',E20.9)
92              END
```

THIS PAGE IS BEST QUALITY PRACTICABLE
FROM COPY FURNISHED TO DDC

```
C       MAIN PROGRAM CZPR
```

```
C       MAIN PROGRAM CZPR
C
C       PROGRAM TO CREATE A DATA FILE, RKBO:CZPR.DA, CONTAINING THE
C       CZERNY TURNER PARAMETERS.
C  INPUT
C       ALL INPUT WILL BE REQUESTED BY THE TELETYPE.
C  OUTPUT
C       DATA FILE RKBO:CZPR.DA
C
C-------CONTENTS OF CZPR.DA----------------
C
C  PARAMETERS OF COLLIMATOR MIRROR
C       LOCATION 1=RADIUS OF CURVATURE.
C       LOCATION 2=X COORDINATE OF MIRROR CENTER.
C       LOCATION 3=Y COORDINATE OF MIRROR CENTER.
C       LOCATION 4=Z COORDINATE OF MIRROR CENTER.
C       LOCATION 5=OFF-AXIS ANGLE IN RADIANS (EULER ALPHA ANGLE).
C  PARAMETERS OF CAMERA MIRROR
C       LOCATION 6=RADIUS OF CURVATURE.
C       LOCATION 7=X COORDINATE OF MIRROR CENTER.
C       LOCATION 8=Y COORDINATE OF MIRROR CENTER.
C       LOCATION 9=Z COORDINATE OF MIRROR CENTER.
C       LOCATION 10=OFF-AXIS ANGLE IN RADIANS (EULER ALPHA ANGLE)
C  PARAMETERS OF GRATING
C       LOCATION 11=X COORDINATE OF GRATING CENTER.
C       LOCATION 12=Y COORDINATE OF GRATING CENTER.
C       LOCATION 13=Z COORDINATE OF GRATING CENTER.
C       LOCATION 14=DIRECTION COSINE WITH RESPECT TO X AXIS OF
C       GRATING NORMAL.
C       LOCATION 15=DIRECTION COSINE WITH RESPECT TO Y AXIS OF
C       GRATING NORMAL.
C       LOCATION 16=DIRECTION COSINE WITH RESPECT TO Z AXIS OF
C       GRATING NORMAL.
C       LOCATION 17=GRATING SPACING.
C  PARAMETERS OF IMAGE PLANE
C       LOCATION 18=X COORDINATE OF A POINT ON THE IMAGE PLANE.
C       LOCATION 19=Y COORDINATE OF A POINT ON THE IMAGE PLANE.
C       LOCATION 20=Z COORDINATE OF A POINT ON THE IMAGE PLANE.
C       LOCATION 21=DIRECTION COSINE WITH RESPECT TO X AXIS OF THE
C       IMAGE PLANE NORMAL.
C       LOCATION 22=DIRECTL,SM)
        WRITE(1,214)
        WRITE(1,206)X,Y,Z,ERR,IQ
        CALL RFL(DK,DL,DM,SK,SL,SM)
        CALL TRNS3(RMI,X,Y,Z,XM2,YM2,ZM2)
        CALL TRNS4(RMI,DK,DL,DM)
        WRITE(1,207)
        WRITE(1,210)X,Y,Z
        CALL ITPL(DK,DL,DM,X,Y,Z,XPLT,YPLT,ZPLT,PLTK,PLTL,PLTM)
        WRITE(1,215)
        WRITE(1,210)X,Y,Z
        STOP
100     FORMAT('THE VALUE OF ZM1=',E20.7)
204     FORMAT('COORDINATES OF OBJECT POINT IN THE COLLIMATOR LENS
        1 SYSTEM')
205     FORMAT('DK=',E20.9,'DL=',E20.9,'DM=',E20.9)
206     FORMAT('X=',E20.9,'Y=',E20.9,'Z=',E20.9/'ERR=',E20.9,
        1'IQ=',I3)
207     FORMAT('RAY COORDINATES IN ORIGINAL SYSTEM')
208     FORMAT('RAY COORDINATES AT GRATING')
209     FORMAT('DIFFRACTION')
210     FORMAT('X=',E20.9,'Y=',E20.9,'Z=',E20.9)
211     FORMAT('DIRECTION COSINES IN THE COLLIMATOR LENS SYSTEM')
212     FORMAT('RAY COORDINATES IN COLLIMATOR SYSTEM')
213     FORMAT('DK=',E20.9,'DL=',E20.9,'DM=',E20.9/
        1'ERR=',E20.9,'IQ=',I3)
214     FORMAT('RAY COORDINATES IN CAMERA SYSTEM')
215     FORMAT('RAY COORDINATES AT MASK PLANE')
        END
```

THIS PAGE IS BEST QUALITY PRACTICABLE
FROM COPY FURNISHED TO DDC

Basic programs to recover the spectrum from the measurements of a Hadamard spectrometer

```
C
      SUBROUTINE HSPEC(NP,XM,S)
C
C
C     SUBROUTINE TO COMPUTE THE SPECTRUM FROM THE MEASUREMENTS
C     OF A HADAMARD SPECTROMETER WITH A SHIFT LEFT CODE.
C     THE SUBROUTINE USES A FAST HADAMARD TECHNIQUE.
C
C
C  INPUT
C     NP IS THE NUMBER OF MEASUREMENTS AND SPECTRAL COMPONENTS.
C     NP MAY BE 7,15,31,63,127,255,511
C     XM IS A VECTOR CONTAINING THE NP MEASUREMENTS.
C
C
C  OUTPUT
C     S IS A VECTOR CONTAINING THE NP SPECTRAL COMPONENTS.
C
C
C  LOAD
C     FHT
C     /I OPTION
C
C
C  DATA ARRAYS
C     RKB0:L1.DA AND RKB0:L2.DA MUST BE CREATED PREVIOUSLY BY
C     RUNNING PROGRAM PI FOR THE VALUE OF NP USED IN THIS
C     SUBROUTINE.
C
C
      DIMENSION XM(512),S(512),L(512)
C     PERMUTE THE MEASUREMENT VECTOR
      CALL IOPEN('RKB0','L1')
      READ(4,110)(L(I),I=1,512)
110   FORMAT(512A2)
      S(1)=0.
      N=NP+1
      DO 20 I=2,N
      IND=L(I)
20    S(I)=XM(IND)
      CALL FHT(N,S,XM)
C     PERMUTE THE FHT OUTPUT VECTOR TO GET THE SPECTRUM
      CALL IOPEN('RKB0','L2')
      READ(4,110)(L(I),I=1,512)
      DI=-FLOAT(N)/2.
      DO 30 I=1,NP
      IND=L(I)
30    S(I)=XM(IND)/DI
      RETURN
      END
```

THIS PAGE IS BEST QUALITY PRACTICABLE
FROM COPY FURNISHED TO DDC

```
C       SUBROUTINE FHT
```

```
      C       SUBROUTINE FHT
      C
              SUBROUTINE FHT(N,F,FP)
      C
      C
              SUBROUTINE TO TAKE FAST HADAMARD TRANSFORM
      C
      C   INPUT
      C       N IS THE SIZE OF THE INPUT DATA ARRAY.
      C       VALID ARRAY SIZES ARE 8,16,32,64,128,256,512.
      C       F IS THE DATA ARRAY TO BE TRANSFORMED.
      C
      C   OUTPUT
      C       N IS UNCHANGED
      C       FP CONTAINS THE HADAMARD TRANSFORM ARRAY.
      C
      C
              DIMENSION F(512),FP(512)
      S       CLA CLL
      S       DCA K /PUT ZERO IN K
      S       TAD I \N
      S  L11, CLL  /DETERMINE K SUCH THAN N=2**K
      S       RAR
      S       INC K /K IS THE EXPONENT OF 2
      S       SZA
      S       JMP L11
      S       CLA CLL
      S       IAC /SUBTRACT ONE TO GET PROPER VALUE OF K
      S       CIA
      S       TAD K
      S       DCA K
      S       TAD K
      S       CIA
      S       DCA C5  /SET C5 TO MINUS K
      S       TAD C5
      S       DCA C6 /SET C6 TO MINUS K
      S  L8,  INC IND /INCREASE LEVEL IN FHT TREE
      S       CLA CLL
      S       TAD I \N
      S       CIA
      S       DCA C1 /SET C1 TO MINUS 2**K.
      S       TAD IND /SET A1 TO MINUS THE TREE LEVEL
      S       CIA
      S       DCA A1
      S  L7,  INC INDEX /SET BINARY INDEX
      S       CLA CLL
      S       TAD INDEX
      S       DCA \II /SET FORTRAN INDEX
      S       TAD A1
      S       DCA C3 /SET C3&C4 TO MINUS THE TREE LEVEL
      S       TAD A1
      S       DCA C4
      S       IAC /SUBTRACT ONE FROM INDEX TO GET PROPER INDEX
      S       CIA /FOR FHT MANIPULATIONS
      S       TAD INDEX
      S       DCA INFHT /INFHT IS FHT INDEX
      S       TAD INFHT /INFHT IS THE FAST HADAMARD TRANSFORM INDEX
      S  L1,  RAR /SET PROPER INDEX BIT TO ZERO
      S       ISZ C3
      S       JMP L1
      S       CLL
      S  L2,  RAL
      S       ISZ C4
      S       JMP L2
      S       IAC /ADD ONE TO FHT INDEX TO GET FORTRAN INDEX
      S       DCA \I1
      S       TAD A1
      S       DCA C3
      S       TAD A1
      S       DCA C4
      S       TAD INFHT /LOAD FHT INDEX
      S  L3,  RAR /SET PROPER INDEX BIT TO ONE
      S       ISZ C3
      S       JMP L3
      S       CLL
      S       CML
```

THIS PAGE IS BEST QUALITY PRACTICABLE
FROM COPY FURNISHED TO DDC

```
77  S L4,    RAL
78  S        ISZ C4
79  S        JMP L4
80  S        IAC /ADD ONE TO INDEX
81  S        DCA \I2 /TO GET FORTRAN INDEX
82  S        TAD A1
83  S        DCA C3
84  S        TAD A1
85  S        DCA C4
86  S        TAD INFHT /LOAD FHT INDEX
87  S L5,    RAR /DETERMINE WHETHER TO ADD OR SUBTRACT
88  S        ISZ C3
89  S        JMP L5
90  S        CLA
91  S L6,    RAL
92  S        ISZ C4
93  S        JMP L6
94  S        SZA
95  S        JMP BB
96  S        CLA CLL /CLEAR AC BEFORE ENTERING FORTRAN STATEMENT
97           FP(II)=F(I1)+F(I2)
98  S        JMP BBB
99  S BB,    CLA CLL /MUST CLEAR THE AC BEFORE FORTRAN STATEMENTS
100          FP(II)=F(I1)-F(I2)
101 S BBB,   ISZ C1
102 S        JMP L7
103 S        CLA CLL
104 S        TAD I \N
105 S        CIA
106 S        DCA C3 /SET C3 TO MINUS N=2**K
107 S        DCA INDEX /SET INDEX TO ZERO
108 S        ISZ C6 /SKIP ON TOP FHT TREE LEVEL TO SAVE TIME
109 S        JMP L9
110 S        JMP E1
111 SL9,     INC INDEX
112 S        TAD INDEX
113 S        DCA \II /SET ARRAY F EQUAL TO ARRAY FP
114          F(II)=FP(II)
115 S        ISZ C3
116 S        JMP L9
117 S E1,    CLA CLL
118 S        DCA INDEX  /SET INDEX TO ZERO
119 S        ISZ C5
120 S        JMP L8
121 S        CLA CLL /SET IND TO ZERO SO THAT FHT CAN BE CALLED
122 S        DCA IND /AGAIN WITHOUT RELOADING
123          RETURN
124 S INDEX,0
125 S INFHT,0
126 S A1,    0
127 S IND,   0
128 S C1,    0
129 S C2,    0
130 S C3,    0
131 S C4,    0
132 S C5,    0
133 S C6,    0
134 S K,     0
135          END


C       MAIN PROGRAM PI


  1  C       MAIN PROGRAM PI
  2  C
  3  C       THIS PROGRAM COMPUTES THE REQUIRED PERMUTATIONS OF THE
  4  C       MEASUREMENT VECTOR AND THE OUTPUT VECTOR OF THE
  5  C       FAST HADAMARD PROGRAM SO THAT THE FHT CAN BE USED
  6  C       TO COMPUTE THE SPECTRUM OF DATA ENCODED WITH A SHIFT
  7  C       LEFT MASK GENERATED ACCORDING TO THE ALGORITHM  IN
  8  C       HADAMARD SPECTROSCOPY BY E.D NELSON & M.L. FREDMAN
  9  C       JOSA VOL 60,1664 (1970).
 10  C
 11  C
 12  C  INPUT
 13  C       THE COEFFICIENTS OF THE PRIMITIVE POLYNOMIAL ARE READ
 14  C       FROM RKBO:PRMPL.DA.
 15  C       RKBO:PRMPL.DA MUST BE GENERATED BY RUNNING THE PROGRAM
```

THIS PAGE IS BEST QUALITY PRACTICABLE
FROM COPY FURNISHED TO DDC

```
16  C       PRMPL BEFORE THIS PROGRAM IS USED.
17  C
18  C  OUTPUT
19  C       THE PERMUTATION OF THE MEASUREMENT VECTOR IS STORED IN
20  C       RKB0:L1.DA AND THE PERMUTATION OF THE FHT OUTPUT VECTOR
21  C       IS STORED IN RKB0:L2.DA FOR THE VALUE OF NP INPUT.
22  C
23  C       NP IS THE NUMBER OF SPECTRAL ELEMENTS.
24  C       NP MAY BE 7,15,31,63,127,255,511.
25  C
26  C
27  C
28  C  LOAD
29  C       MOD2
30  C       /I/O OPTIONS
31  C
32  C
33          COMMON MASK
34          DIMENSION MASK(1021),L1(512),L2(512),IA(20),IE(20),LP(56)
35          READ(1,100)NP
36  100     FORMAT('NUMBER OF SPECTRAL ELEMENTS='I5)
37  S       CLA CLL
38  S       DCA \NS  /SET NS EQUAL TO 0
39  S       TAD \NP
40  S       IAC  /LOAD NP+1 INTO AC
41  S L11,  CLL
42  S       RAR  /DETERMINE NS SUCH THAT NP=2**NS-1
43  S       INC \NS
44  S       SZA
45  S        JMP L11
46  S       CLA CLL
47  S       IAC /SUBTRACT 1 TO GET PROPER NS
48  S       CIA
49  S       TAD \NS
50  S       DCA \NS
51  S       CLA CLL
52          L=NS+1
53          LZ=NS-1
54  C       LOAD COEFFICIENTS OF PRIMITIVE POLYNOMIAL
55          CALL IOPEN('RKB0','PRMPL')
56          READ(4,120)(LP(I),I=1,56)
57          J=0
58  1       J=J+1
59          IT=LP(J)
60          IF(IT-NS)1,2,1
61  2       DO 3 I=1,L
62          J=J+1
63  3       IA(I)=LP(J)
64  C       CREATE CODES 1 TO NP
65          DO 5 I=1,NS
66          L1(I)=1
67          MASK(I)=1
68  5       IE(I)=1
69          DO 12 II=L,NP
70          ISUM=0
71          DO 10 I=1,NS
72          I1=IA(I)*IE(I)
73  10      ISUM=MOD2(I1,ISUM)
74          DO 11 I=1,LZ
75  11      IE(I)=IE(I+1)
76          IE(NS)=ISUM
77          MASK(II)=ISUM
78  12      L1(II)=ISUM
79  C       CREATE CODES (NP+1) TO (2*NP-1)
80  C       BY SHIFTING LEFT
81          NL=NP+1
82          NH=2*NP-1
83          J=0
84          DO 30 I=NL,NH
85          J=J+1
86  30      MASK(I)=L1(J)
87          NT=NS
88          NL=NS-1
89          DO 60 J=1,NP
90          NC=NT
91  S       CLA CLL
92  S       DCA \I
93          DO 55 I=1,NL
94          IT=MASK(NC)
```

THIS PAGE IS BEST QUALITY PRACTICABLE
FROM COPY FURNISHED TO DDC

```
 95  S        CLA CLL  /LOAD BINARY NUMBER INTO L.
 96  S        TAD \L
 97  S        TAD \II
 98  S        RAL
 99  S        DCA \L
100  55       NC=NC-1


C        MAIN PROGRAM FT


101           II=MASK(NC)
102  S        CLA CLL
103  S        TAD \L
104  S        TAD \II
105  S        DCA \L
106           NT=NT+1
107  C        L1(L+1) CONTAINS THE INDEX OF THE MEASUREMENT VECTOR
108  C        COMPONENT WHICH IS TO BECOME THE L+1 COMPONENT OF THE
109  C        VECTOR WHICH IS OPERATED ON BY THE FHT.
110  60       L1(L+1)=I
111           CALL OOPEN('REBO',L1)
112           WRITE(4,120)(L1(I),I=1,512)
113  120      FORMAT(512R2)
114           CALL OCLOSE
115           J5=0
116           DO 80 I=1,NP
117  S        CLA CLL
118  S        DCA \K
119           LZ=NL
120           DO 70 II=1,NL
121           L=2**LZ+1
122  C        IF IS COLUMN OF  MATRIX A REQUIRED
123           IF=L1(J)
124           NT=MASK(IF+1,5)
125  S        CLA CLL
126  S        TAD \K
127  S        TAD \NT
128  S        RAL
129  S        DCA \K
130  70       LZ=LZ-1
131           IP=L1(J)
132           NT=MASK(IP+1,5)
133  S        CLA CLL
134  S        TAD \K
135  S        TAD \NT
136  S        DCA \K
137  C        L2(I) CONTAINS THE INDEX OF THE FHT OUTPUT VECTOR WHICH IS
138  C        TO BECOME COMPONENT  I OF THE SPECTRUM VECTOR.
139           L2(I)=L1I
140  80       J5=J5+1
141           CALL OOPEN('REBO',L2)
142           WRITE(4,120)(L2(I),I=1,512)
143           CALL OCLOSE
144           STOP
145           END


C        FUNCTION MOD2


  1  C        FUNCTION MOD2
  2  C
  3           FUNCTION MOD2(I1,I2)
  4  C        FUNCTION TO ADD MODULO 2. (0+0=0,0+1=1,1+0=1,1+1=0)
  5           IT=I1+I2
  6           IF(IT-2)1,2,1
  7  1        MOD2=IT
  8           GO TO 3
  9  2        MOD2=0
 10  3        RETURN
 11           END
```

THIS PAGE IS BEST QUALITY PRACTICABLE
FROM COPY FURNISHED TO DDC

C MAIN PROGRAM PRMPL

```
C       MAIN PROGRAM PRMPL
C
C       PROGRAM TO STORE PRIMITIVE POLYNOMIALS FROM DEGREE 3 TO
C       DEGREE 9.
C
C
C       LOAD WITH /O OPTIONS
C
        DIMENSION LP(56)
        J=0
        NS=3
        DO 80 JX=1,7
        J=J+1
        LP(J)=NS
        NH=NS+1
        WRITE(1,100)NS
100     FORMAT(///'DEGREE=',I3)
        DO 40 I=1,NH
        J=J+1
40      READ(1,130)LP(J)
130     FORMAT(I2)
80      NS=NS+1
        CALL OOPEN('RKB0','PRMPL')
        WRITE(4,140)(LP(I),I=1,56)
140     FORMAT(56A2)
        CALL OCLOSE
        STOP
        END
```

DISTRIBUTION LIST

Director
Defense Advanced Rsch Proj Agency
Architect Building
1400 Wilson Blvd.
Arlington, VA 22209
Attn: Lt Col W.A. Whitaker

Director
Defense Advanced Rsch Proj Agency
Architect Building
1400 Wilson Blvd.
Arlington, VA 22209
Attn: Lt. Col. W. Cuneo

Defense Documentation Center
Cameron Station
Alexandria, VA 22314
Attn: TC

Defense Documentation Center
Cameron Station
Alexandria, VA 22314
Attn: TC

Director
Defense Nuclear Agency
Washington, DC 20305
Attn: RAAE Charles A. Blank

Director
Defense Nuclear Agency
Washington, DC 20305
Attn: TITL Tech Library

Director
Defense Nuclear Agency
Washington, DC 20303
Attn: TITL Tech Library

Director
Defense Nuclear Agency
Washington, DC 20305
Attn: RAEV Harold C. Fitz, Jr.

Director
Defense Nuclear Agency
Washington, D.C. 20305
Attn: TISI Archives

Director
Defense Nuclear Agency
Washington, DC 20305
Attn: DDST

Director
Defense Nuclear Agency
Washington, DC 20305
Attn: Major R. Bigoni/RAAE

Director of Defense Research
and Engineering
Department of Defense
Washington, DC 20301
Attn: DD/S&SS (OS)
Daniel Brockway

Director of Defense Research
& Engineering
Department of Defense
Washington, DC 20301
Attn: DD/S&SS
Daniel Brockway

Commander
Field Command
Defense Nuclear Agency
Kirtland AFB, NM 87115
Attn: FCPR

Chief Livermore Division
Field Command DNA
Lawrence Livermore Lab.
P.O. Box 808
Livermore, CA 94550
Attn: FCPRL

Commander/Director
Atmospheric Sciences Laboratory
US Army Electronics Command
White Sands Missile Range,
New Mexico 88002
Attn: H. Ballard (3 copies)

Commander/Director
Atmospheric Sciences Laboratory
US Army Electronics Command
White Sands Missile Range,
New Mexico 88002
Attn: DRSEL-BL-SY-A F. Niles
(3 copies)

Commander
Harry Diamond Laboratories
2800 Powder Mill Road
Adelphi, MD 20783
Attn: DRXDO-NP, F.H. Wiminetz

Commander
US Army Nuclear Agency
Fort Bliss, TX 79916
Attn: MONA-WE

Director
BMD Advanced Tech Center
Huntsville, AL 35808
Attn: ATC-T, M. Capps

Director
BMD Advanced Tech Center
Huntsville, AL 35807
Attn: ATCOO, W. Davies

Dep.Chief of Staff for Rsch,
DEV & ACO
Department of the Army
Washington, DC 20310
Attn: MBC Division

Dep.Chief of Staff for Rsch,
DEV & ACO
Department of the Army
Washington, DC 20310
Attn: DAMA-CSZ-O

Dep.Chief of Staff for Rsch
DEV & ACO
Department of the Army
Washington, DC 20310
Attn: DAMA-WSZC

Director
US Army Ballistic Research Lab
Aberdeen Proving Grounds
Maryland 21005
Attn: DRXBR-AM G. Keller

Director
US Army Ballistic Research Lab
Aberdeen Proving Grounds
Maryland 21005
Attn: DRXRD-BSP J. Heimerl

Director
US Army Ballistic Research Lab
Aberdeen Proving Grounds
Maryland, 21005
Attn: John Mester

Director
US Army Ballistic Research Lab
Aberdeen Proving Grounds
Maryland, 21005
Attn: Tech Library

Commander
US Army Electronics Command
Fort Monmouth, NJ 37703
Attn: Inst for Expl Research

Commander
US Army Electronics Command
Fort Monmouth, NJ 37703
Attn: DRSEL (5 copies)

Commander
US Army Electronics Command
Fort Monmouth, NJ 37703
Attn: Stanley Kronenberger

Commander
US Army Electronics Command
Fort Monmouth, NJ 37703
Attn: Weapons Effects Sec.

Commander
US Army Foreign Sci & Tech Ctr
220 7th Street, NE
Charlottesville, VA 22901
Attn: Robert Jones

Chief
US Army Research Office
P.O. Box 12211
Triangle Park, NC 27709
Attn: Robert Mace

Commander
Naval Oceans Systems Center
San Diego, CA 92152
Attn: Code 2200 I. Rothmuller

Commander
Naval Oceans Systems Center
San Diego, CA 92152
Attn: Code 2200 W. Moler

Commander
Naval Oceans Systems Center
San Diego, CA 92152
Attn: Code 2200 H. Hughes

Commander
Naval Oceans Systems Center
San Diego, CA 92152
Attn: Code 2200 R. Pappert

Commander
Naval Oceans Systems Center
San Diego, CA 92152
Attn: Code 2200 J.R. Richter

Director
Naval Research Laboratory
Washington, DC 20375
Attn: Code 7712 D.P. McNutt

Director
Naval Research Laboratory
Washington, DC 20375
Attn: Code 7701 Jack D. Brown

Director
Naval Research Laboratory
Washington, DC 20375
Attn: Code 2600 Tech Lib.

Director
Naval Research Laboratory
Washington, DC 20375
Attn: Code 7127 C.Y.Johnson

Director
Naval Research Laboratory
Washington, DC 20375
Attn: Code 7700 T.P.Coffey

Director
Naval Research Laboratory
Washington, DC 20375
Attn: Code 7709 Wahab Ali

Director
Naval Research Laboratory
Washington, DC 20375
Attn: Code 7750 D.F.Strobel

Director
Naval Research Laboratory
Washington, DC 20375
Attn: Code 7750 P. Juluenne

Director
Naval Research Laboratory
Washington, DC 20375
Attn: Code 7750 J. Fedder

Director
Naval Research Laboratory
Washington, DC 20375
Attn: Code 7750 S. Ossakow

Director
Naval Research Laboratory
Washington, DC 20375
Attn: Code 7750 J. Davis

Superintendent
Naval Post Graduate School
Monterey, CA 93940
Attn: Tech Reports Librarian

Commander
Naval Surface Weapons Center
White Oak, Silver Spring, MD 20910
Attn: Code WA501 Navy Nuc Prgms

Commander
Naval Surface Weapons Center
White Oaks, Silver Spring MD 20910
Attn: Technical Library

Commander
Naval Intelligence Support Center
4301 Suitland Rd. Bldg 5
Washington, DC 20390
Attn: Document Control

AF Geophysics Laboratory, AFSC
Hanscom AFB, MA 01731
Attn: LKB Kenneth S W Champion

AF Geophysics Laboratory, AFSC
Hanscom AFB, MA 01731
Attn: OPR Alva T. Stair
(5 copies)

AF Geophysics Laboratory, AFSC
Hanscom AFB, MA 01731
Attn: Opr J. Ulwick

AF Geophysics Laboratory, AFSC
Hanscom AFB, MA 01731
Attn: OPR R. Murphy

AF Geophysics Laboratory, AFSC
Hanscom AFB, MA 01731
Attn: OPR J. Kennealy

AF Geophysics Laboratory, AFSC
Hanscom AFB, MA 01731
Attn: PHG J.C. McClay

AF Geophysics Laboratory, AFSC
Hanscom AFB, MA 01731
Attn: LKD Rosco Narcisi

AF Geophysics Laboratory, AFSC
Hanscom AFB, MA 01731
Attn: LKO R. Huffman

AF Weapons Laboratory, AFSC
Kirtland AFB, NM 87117
Attn: Maj G. Ganong, DYM

Commander
ASD
WPAFB, OH 45433
Attn: ASD-YH-EX
Lt Col Robert Leverette

SAMSO/AW
P.O. Box 92960
Worldway Postal Center
Los Angeles, CA 90009
Attn: SZJ Major L. Doan

SAMSO/SW
P.O. Box 92960
Worldway Postal Center
Los Angeles, CA 90009
Attn: AW

AFTAC
Patric AFB, FL 32925
Attn: Tech Library

AFTAC
Patric AFB, FL 32925
Attn: TD

HQ Air Force Systems Command
Andrews AFB
Washington, DC 20331
Attn: DLS

HQ Air Force Systems Command
Andrews AFB
Washington, DC 20331
Attn: Tech Library

HQ Air Force Systems Command
Andrews AFB
Washington, DC 20331
Attn: OLCAE

HQ Air Force Systems Command
Andrews AFB
Washington, DC 20331
Attn: DLTW

HQ Air Force Systems Command
Andrews AFB
Washington, DC 20331
Attn: DLXP

HQ Air Force Systems Command
Andrews AFB
Washington, DC 20331
Attn: SDR

HQ USAF/RD
Washington, DC 20330
Attn: RDQ

Commander
Rome Air Development Center
Griffiss AFB, NY 13440
Attn: J.J. Simons OCSC

Div. of Military Application
US Energy Rsch & Dev Admin
Washington, DC 20545
Attn: DOC CON

Los Alamos Scientific Lab
P.O. Box 1663
Los Alamos, NM 87545
Attn: DOC CON R.A. Jeffries

Los Alamos Scientific Lab
P.O. Box 1663
Los Alamos, NM 87545
Attn: DOC CON CR Mehl ORG 5230

Los Alamos Scientific Lab
P.O. Box 1663
Los Alamos, NM 87545
Attn: DOC CON H.V. Argo

Los Alamos Scientific Lab
P.O. Box 1663
Los Alamos, NM 87545
Attn: DOC CON M. Tierney J-10

Los Alamos Scientific Lab
P.O. Box 1663
Los Alamos, NM 87545
Attn: DOC CON Robert Brownlee

Los Alamos Scientific Lab
P.O. Box 1663
Los Alamos, NM 87545
Attn: DOC CON Wm Maier

Los Alamos Scientific Lab
P.O. Box 1663
Los Alamos, NM 87545
Attn: DOC CON John Zinn

Los Alamos Scientific Lab
P.O. Box 1663
Los Alamos, NM 87545
Attn: DOC CON Reference Lib.
Ann Beyer

Sandia Laboratories
Livermore Laboratory
P.O. Box 965
Livermore, CA 94556
Attn: DOC CON T. Cook ORG
8007

Sandia Laboratories
P.O. Box 5800
Alburquerque, NM 87115
Attn: DOC CON
W.D. Brown ORG 1353

Sandia Laboratories
P.O. Box 5800
Albuquerque, NM 87115
Attn: DOC CON
L. Anderson ORG 1247

Sandia Laboratories
P.O. Box 5800
Albuquerque, NM 87115
Attn: DOC CON
Morgan Kramma ORG 5720

Sandia Laboratories
P.O. Box 5800
Albuquerque, NM 87115
Attn: DOC CON
Frank Hudson ORG 1722

Sandia Laboratories
P.O. Box 5800
Albuquerque, NM 87115
Attn: DOC CON ORG 3422
Sandia Repts Coll.

Argonne National Laboratory
Records Control
9700 South Cass Avenue
Argonne, IL 60439
Attn: DOC CON D. W. Green

Argonne National Laboratory
Records Control
9700 South Cass Avenue
Argonne, IL 60439
Attn: DOC CON
LIR SVCS RPTS SEC

Argonne National Laboratory
Records Control
9700 South Cass Avenue
Argonne, IL 60439
Attn: DOC CON S. Garelnick

Argonne National Laboratory
Records Control
9700 South Cass Avenue
Argonne, IL 60439
Attn: DOC CON G.T. Reedy

University of California
Lawrence Livermore Laboratory
P.O. Box 808
Livermore, CA 94550
Attn: W.H. Duewer Gen L-404

University of California
Lawrence Livermore Laboratory
P.O. Box 808
Livermore, CA 94550
Attn: Julius Chang L-71

University of California
Lawrence Livermore Laboratory
P.O. Box 808
Livermore, CA 94550
Attn: G.P. Haugen L-404

University of California
Lawrence Livermore Laboratory
P.O. Box 808
Livermore, CA 94550
Attn: D.J. Wuerales L-142

California, State of
Air Resource Board
9528 Telsia Avenue
Al Monte, CA 91731
Attn: Leo Zafonte

Calif. Institute of Technology
Jet Propulsion Laboratory
4800 Oak Grove Drive
Pasadena, CA 91103
Attn: Joseph A. Jello

US Energy Rsch & Dev Admin
Div. of Headquarters Services
Library Branch G-043
Washington, DC 20545
Attn: DOC CON Class Tech Lib

Department of Transportation
Office of the Secretary
TAD-44. 1, Room 10402-B
400 7th Street S.W.
Washington, DC 20590
Attn: Samuel C. Coroniti

NASA
Goddard Space Flight Center
Greenbelt, MD 20771
Attn: A. C. Aiken

NASA
Goddard Space Flight Center
Greenbelt, MD 20771
Attn: A. Tempkin

NASA
Goddard Space Flight Center
Greenbelt, MD 20771
Attn: A. J. Bauer

NASA
Goddard Space Flight Center
Greenbelt, MD 20771
Attn: Technical Library

NASA
Goddard Space Flight Center
Greenbelt, MD 20771
Attn: J. Siry

NASA
600 Independence Avenue S.W.
Washington, DC 20545
Attn: A. Gessow

NASA
600 Independence Avenue S.W.
Washington, DC 20546
Attn: D.P. Cauffman

NASA
600 Independence Avenue S.W.
Washington, DC 20546
Attn: Lt Col D.R. Hallenbeck
Code SG

NASA
600 Independence Avenue S.W.
Washington, DC 20545
Attn: R. Fellows

NASA
600 Independence Avenue S.W.
Washington, DC 20546
Attn: A. Schardt

NASA
600 Independence Avenue S.W.
Washington, DC 20546
Attn: M. Tepper

NASA
Langley Research Center
Langley Station
Hampton, VA 23365
Attn: C. Schexnayder MS-168

NASA
Ames Research Center
Moffett Field, CA 90435
Attn: N-25404 W. L. Starr

NASA
Ames Research Center
Moffett Field, CA 94035
Attn: N-254-4 R. Whitten

NASA
Ames Research Center
Moffett Field, CA 94035
Attn: N-254-4 I.G. Poppoff

NASA
Ames Research Center
Moffett Field, CA 94035
Attn: N-254-3 N.H. Farlow

NASA
George C. Marshall Space Flt.
Center
Huntsville, AL 35812
Attn: C. R. Balcher

NASA
George C. Marshall Space Flt.
Center
Huntsville, AL 35812
Attn: N. H. Stone

NASA
George C. Marshall Space Flt.
Center
Huntsville, AL 35812
Attn: W. A. Oran

NASA
George C. Marshall Space Flt.
Center
Huntsville, AL 35812
Attn: Code ES22 John Watts

NASA
George C. Marshall Space Flt.
Center
Huntsville, AL 35812
Attn: W. T. Roberts

NASA
George C. Marshall Space Flt.
Center
Huntsville, AL 35812
Attn: R. D. Hudson

NASA
George C. Marshall Space Flt.
Center
Huntsville, AL 35812
Attn: R. Chappell

Albany Metallurgy Research Ctr.
US Bureau of Mines
P.O. Box 70
Albany, OR 97321
Attn: Eleanor Abshire

Central Intelligence Agency
RD/SI RM 5G48 HQ Building
Washington, DC 20505
Attn: NED/OSI-2G48 HQS

Department of Commerce
National Bureau of Standards
Washington, DC 20234
Attn: Sec Officer James Devoe

Department of Commerce
National Bureau of Standards
Washington, DC 20234
Attn: Sec Officer S. Abramowitz

Department of Commerce
National Bureau of Standards
Washington, DC 20234
Attn: Sec Officer J Cooper

Department of Commerce
National Bureau of Standards
Washington, DC 20234
Attn: Sec Officer G.A. Sinnatt

Department of Commerce
National Bureau of Standards
Washington, DC 20234
Attn: Sec Officer K Kessler

Department of Commerce
National Bureau of Standards
Washington, DC 20234
Attn: Sec Officer M. Krauss

Department of Commerce
National Bureau of Standards
Washington, DC 20234
Attn: Sec Officer L. Gevantman

Nat'l Oceanic & Atmospheric
Administration
Environmental Research Lab
Department of Commerce
Boulder, CO 80302
Attn: George C. Reid
Aeronomy Lab

Nat'l Oceanic & Atmospheric
Administration
Environmental Research Lab
Department of Commerce
Boulder, CO 80302
Attn: Eldon Ferguson

Nat'l Oceanic & Atmospheric
Administration
Environmental Research Lab
Department of Commerce
Boulder, CO 80302
Attn: Fred Fehsenfeld

Aero-Chem Resch Lab, Inc.
P.O. Box 12
Princeton, NJ 08540
Attn: A. Fontijn

Aero-Chem Resch Lab, Inc.
P.O. Box 12
Princeton, NJ 08540
Attn: H. Pergament

Aerodyne Research, Inc.
Bedford Research Park
Crosby Drive
Bedford, MA 01730
Attn: F. Bien

Aerodyne Research, Inc.
Bedford Research Park
Crosby Drive
Bedford, MA 01730
Attn: M. Camac

Aeronomy Corporation
217 S. Neil Street
Champaign, IL 61828
Attn: A. Bowhill

Aerospace Corporation
P.O. Box 92957
Los Angeles, CA 90009
Attn: N. Cohen

Aerospace Corporation
P.O. Box 92957
Los Angeles, CA 90009
Attn: Harris Mayer

Aerospace Corporation
P.O. Box 92957
Los Angeles, CA 90009
Attn: Sidney W. Kash

Aerospace Corporation
P.O. Box 92957
Los Angeles, CA 90009
Attn: T. Widhoph

Aerospace Corporation
P.O. Box 92957
Los Angeles, CA 90009
Attn: R. J. McNeal

Aerospace Corporation
P.O. Box 92957
Los Angeles, CA 90009
Attn: R. Grove

Aerospace Corporation
P.O. Box 92957
Los Angeles, CA 90009
Attn: Irving M. Garfunkel

Aerospace Corporation
P.O. Box 92957
Los Angeles, CA 90009
Attn: Thomas D. Taylor

Aerospace Corporation
P.O. Box 92957
Los Angeles, CA 90009
Attn: V. Josephson

Aerospace Corporation
P.O. Box 92957
Los Angeles, CA 90009
Attn: Julian Reinheimer

Aerospace Corporation
P.O. Box 92957
Los Angeles, CA 90009
Attn: R. D. Rawcliffe

Avco-Everett Research Lab, Inc.
2385 Revere Beach Parkway
Everett, MA 02149
Attn: Technical Library

Avco-Everett Research Lab, Inc.
2385 Revere Beach Parkway
Everett, MA 02149
Attn: George Sutton

Battelle Memorial Institute
505 King Avenue
Columbus, OH 43201
Attn: Donald J. Hamman

Battelle Memorial Institute
505 King Avenue
Columbus, OH 43201
Attn: Donald J. Ham

Battelle Memorial Institute
505 King Avenue
Columbus, OH 43201
Attn: STOIAC

Battelle Memorial Institute
505 King Avenue
Columbus, OH 43201
Attn: Richard K. Thatcher

Brown Engineering Co., Inc.
Cummings Research Park
Huntsville, AL 35807
Attn: N. Passino

The Trustees of Boston College
Chestnut Hill Campus
Chestnut Hill, MA 02167
Attn: Chairman Dept. of Chem.

Brown Engineering Co., Inc.
Cummings Research Park
Huntsville, AL 35807
Attn: Ronald Patrick

California at Riverside, Univ. of
Riverside, CA 92502
Attn: Alan C. Lloyd

California at Riverside, Univ. of
Riverside, CA 92502
Attn: James N. Pitts, Jr.

California at San Diego, Univ. of
3175 Miramar Road
La Jolla, CA 92037
Attn: S. C. Lin

California University of
Berkeley Campus Room 318
Sproul Hall
Berkeley, CA 94720
Attn: Sec Officer for
Harold Johnston

California University of
Berkeley Campus Room 318
Sproul Hall
Berkeley, CA 94720
Attn: Sec Officer for F. Mozer

California University of
Berkeley Campus Room 318
Sproul Hall
Berkeley, CA 94720
Attn: Sec Officer for Dept of
Chem. W. H. Miller

California, State of
Air Resources Board
9528 Telstar Avenue
El Monte, CA 91731
Attn: Leo Zafonte

Calspan Corporation
P.O. Box 235
Buffalo, NY 14221
Attn: C. E. Treanor

Calspan Corporation
P.O. Box 235
Buffalo, NY 14221
Attn: G. C. Valley

Calspan Corporation
P.O. Box 235
Buffalo, NY 14221
Attn: M. G. Dunn

Calspan Corporation
P.O. Box 235
Buffalo, NY 14221
Attn: W. Wurster

Colorado, University of
Office of Contracts & Grants
380 Administrative Annex
Boulder, CO 80302
Attn: A. Phelps JILA

Colorado, University of
Office of Contracts & Grants
380 Administrative Annex
Boulder, CO 80302
Attn: Jeffrey B. Pearce LASP

Colorado, University of
Office of Contracts & Grants
380 Administrative Annex
Boulder, CO 803032
Attn: C. Beaty JILA

Colorado, University of
Office of Contracts & Grants
380 Administrative Annex
Boulder, CO 80302
Attn: C. Lineberger JILA

Colorado, University of
Office of Contracts & Grants
380 Administrative Annex
Boulder, CO 80302
Attn: C. A. Barth LASP

Columbia University, Trustees
City of New York
La Mont Doherty Geological
Observatory-Torrey Cliff
Palisades, NY 19064
Attn: B. Phelan

Columbia University, Trustees
City of New York
116th Street & Broadway
New York, NY 10027
Attn: Richard N. Zare

Columbia University, Trustees
City of New York
116th & Broadway
New York, NY 10027
Attn: Sec Officer H.M. Foley

Concord Sciences
P.O. Box 113
Concord, MA 01742
Attn: Emmett A. Sutton

Denver, University of
Colorado Seminary
Denver Research Institute
P.O. Box 10127
Denver, CO 80210
Attn: Sec. Officer for Van Zyl

Denver, University of
Colorado Seminary
Denver Research Institute
P.O. Box 10127
Denver, CO 80210
Attn: Sec Officer for D. Murcray

General Electric Company
Tempo-Center for Advanced Studies
816 State Street (P.O. Drawer QO)
Santa Barbara, CA 93102
Attn: DASAIC

General Electric Company
Tempo-Center for Advanced Studies
816 State Street (PO Drawer QO)
Santa Barbara, CA 93102
Attn: Warren S. Knapp

General Electric Company
Tempo-Center for Advanced Studies
816 State Street (PO Drawer QO)
Santa Barbara, CA 93102
Attn: Tim Stephens

General Electric Company
Tempo-Center for Advanced St.
816 State St. (PO Drawer QO)
Santa Barbara, CA 93102
Attn: Don Chandler

General Electric Company
Tempo-Center for Advanced St.
816 State St. (PO Drawer QO)
Santa Barbara, CA 93102
Attn: B. Cambill

General Elec. Co. Space Div.
Valley Forge Space Center
Goddard Blvd.
King of Prussia
P.O. Box 8555
Philadelphia, PA 19101
Attn: M. H. Bortner
Space Science Lab

General Elec. Co. Space Div.
Valley Forge Space Center
Goddard Blvd.King of Prussia
P.O. Box 8555
Philadelphia, PA 19101
Attn: J. Burns

General Elec. Co. Space Div.
Valley Forge Space Center
Goddard Blvd.King of Prussia
P.O. Box 8555
Philadelphia, PA 19101
Attn: F. Alyea

General Elec. Co. Space Div.
Valley Forge Space Center
Goddard Blvd.King of Prussia
P.O. Box 8555
Philadelphia, PA 19101
Attn: P. Z. Sands

General Elec. Co. Space Div.
Valley Forge Space Center
Goddard Blvd.King of Prussia
P.O. Box 8555
Philadelphia, PA 19101
Attn: R. H. Edsall

General Elec. Co. Space Div.
Valley Forge Space Center
Goddard Blvd.King of Prussia
P.O. Box 8555
Philadelphia, PA 19101
Attn: T. Baurer

General Research Corporation
P.O. Box 3587
Santa Barbara, CA 93105
Attn: John Ise, Jr.

Geophysical Institute
University of Alaska
Fairbanks, AK 99701
Attn: D. Henderson

Geophysical Institute
University of Alaska
Fairbanks, AK 99701
Attn: J. S. Wagner Physics Dept.

Geophysical Institute
University of Alaska
Fairbanks, AK 99701
Attn: B. J. Watkins

Geophysical Institute
University of Alaska
Fairbanks, AK 99701
Attn: T. N. Davis

Geophysical Institute
University of Alaska
Fairbanks, AK 99701
Attn: R. Parthasarathy

Geophysical Institute
University of Alaska
Fairbanks, AK 99701
Attn: Neal Brown

Lowell, University of
Center for Atmospheric Research
450 Aiken Street
Lowell, MA 01854
Attn: G. T. Best

Lockheed Missiles & Space Co.
3251 Hanover Street
Palo Alto, CA 94304
Attn: John Kumer Dept 52-54

Lockheed Missiles & Space Co.
3251 Hanover Street
Palo Alto, CA 94304
Attn: John Cladis Dept 52-12

Lockheed Missiles & Space Co.
3251 Hanover Street
Palo Alto, CA 94304
Attn: B. McCormac Dept 52-54

Lockheed Missiles & Space Co.
3251 Hanover Street
Palo Alto, CA 94304
Attn: T. James Dept 52-54

Lockheed Missiles & Space Co.
3251 Hanover Street
Palo Alto, CA 94304
Attn: B. Reagan Dept 52-12

Lockheed Missiles & Space Co.
3251 Hanover Street
Palo Alto, CA 94304
Attn: M. Walt Dept 52-10

Lockheed Missiles & Space Co.
3251 Hanover Street
Palo Alto, CA 94304
Attn: R. Johnson Dept 52-12

Lockheed Missiles & Space Co.
3251 Hanover Street
Palo Alto, CA 94304
Attn: R. Sears Dept 52-14

Lockheed Missiles & Space Co.
3251 Hanover Street
Palo Alto, CA 94304
Attn: J. R. Winkler

Institute for Defense Analyse
400 Army-Navy Drive
Arlington, VA 22202
Attn: Ernest Bauer

Institute for Defense Analyse
400 Army-Navy Drive
Arlington, VA 22202
Attn: Hans Wolfhard

Mission Research Corporation
735 State Street
Santa Barbara, CA 93101
Attn: D. Archer

Mission Research Corporation
735 State Street
Santa Barbara, CA 93101
Attn: D. Fischer

Mission Research Corporation
735 State Street
Santa Barbara, CA 93101
Attn: M. Scheibe

Mission Research Corporation
735 State Street
Santa Barbara, CA 93101
Attn: D. Sappenfield

Mission Research Corporation
735 State Street
Santa Barbara, CA 93101
Attn: D. Sowle

Photometrics, Inc.
442 Marrett Road
Lexington, MA 02173
Attn: Irving L. Kofsky

Physical Dynamics, Inc.
P.O. Box 1069
Berkeley, CA 94701
Attn: J. B. Workman

Physical Dynamics, Inc.
P.O. Box 1069
Berkeley, CA 94701
Attn: A. Thompson

Physical Sciences, Inc.
30 Commerce Way
Woburn, MA 01801
Attn: Kurt Wray

Physical Sciences, Inc.
30 Commerce Way
Woburn, MA 01801
Attn: R. L. Taylor

Physical Sciences, Inc.
30 Commerce Way
Woburn, MA 01801
Attn: G. Caledonia

Physics International Co.
2700 Merced Street
San Leandro, CA 94577
Attn: Doc Con for Tech Lib

Pittsburgh, University of
Commonwealth Sys of Higher Ed.
Cathedral of Learning
Pittsburgh, PA 15213
Attn: Wade L. Fite

Pittsburgh, University of
Commonwealth Sys of Higher Ed.
Cathedral of Learning
Pittsburgh, PA 15213
Attn: Manfred A. Biondi

Pittsburgh, University of
Commonwealth Sys of Higher Ed.
Cathedral of Learning
Pittsburgh, PA 15213
Attn: Frederick Kaufman

Pittsburgh, University of
Commonwealth Sys of Higher Ed.
Cathedral of Learning
Pittsburgh, PA 15213
Attn: Edward Gerjuoy

Princeton Univ. Trustees of
Forrestal Campus Library
Box 710
Princeton University
Princeton, NJ 08540

R & D Associates
P.O. Box 9695
Marina Del Rey, CA 90291
Attn: Richard Latter

R & D Associates
P.O. Box 9695
Marina Del Rey, CA 90291
Attn: R. G. Lindgren

R & D Associates
P.O. Box 9695
Marina Del Rey, CA 90291
Attn: Bryan Gabbard

R & D Associates
P.O. Box 9695
Marina Del Rey, CA 90291
Attn: H. A. Oru

R & D Associates
P.O. Box 9695
Marina Del Rey, CA 90291
Attn: Robert E. Lelevier

R & D Associates
P.O. Box 9695
Marina Del Rey, CA 90291
Attn: R. P. Turco

R & D Associates
P.O. Box 9695
Marina Del Rey, CA 90291
Attn: Forrest Gilmore

R & D Associates
P.O. Box 9695
Marina Del Rey, CA 90291
Attn: D. Dee

R & D Associates
1815 N. Ft. Myer Drive 11th fl.
Arlington, VA 22209
Attn: Herbert J. Mitchell

R & D Associates
1815 N. Ft. Myer Drive 11th fl.
Arlington, VA 22209
Attn: J. W. Rosengren

Rand Corporation
1700 Main Street
Santa Monica, CA 90406
Attn: Cullen Crain

Science Applications, Inc.
P.O. Box 2351
La Jolla, CA 92038
Attn: Daniel A. Hamlin

Science Applications, Inc.
P.O. Box 2351
La Jolla, CA 92038
Attn: David Sachs

Space Data Corporation
1333 W. 21st St.
Tempe, AZ 85282
Attn: Edward F. Allen

SRI International
333 Ravenswood Avenue
Menlo Park, CA 94025
Attn: M. Baron

SRI International
333 Ravenswood Avenue
Menlo Park, CA 94025
Attn: L. Leadabrand

SRI International
333 Ravenswood Avenue
Menlo Park, CA 94025
Attn: Walter G. Chestnut

SRI International
1611 North Kent Street
Arlington, VA 22209
Attn: Warren W. Berning

SRI International
1611 North Kent Street
Arlington, VA 22209
Attn: Charles Hulbert

Stewart Radiance Laboratory
1 DeAngelo Drive
Bedford, MA 01730
Attn: R. J. Huppi
(25 copies)

Technology International Corp.
75 Wiggins Avenue
Bedford, MA 01730
Attn: W. P. Roquist

United Technologies Corp.
755 Main Street
Hartford, CT 06103
Attn: H. Michels

United Technologies Corp.
755 Main Street
Hartford, CT 06103
Attn: Robert Bullis

Utah State University
Logan, UT 84322
Attn: Doran Baker

Utah State University
Logan, UT 84322
Attn: Kay Baker

Utah State University
Logan, UT 84322
Attn: C. Wyatt

Utah State University
Logan, UT 84322
Attn: D. Burt

Visidyne, Inc.
19 Third Avenue
Northwest Industrial Park
Burlington, MA 01803
Attn: Henry J. Smith

Visidyne, Inc.
19 Third Avenue
Northwest Industrial Park
Burlington, MA 01803
Attn: J. W. Carpenter

Visidyne, Inc.
19 Third Avenue
Northwest Industrial Park
Burlington, MA 01803
Attn: William Reidy

Visidyne, Inc.
19 Third Avenue
Northwest Industrial Park
Burlington, MA 01803
Attn: T. C. Degges

Visidyne, Inc.
19 Third Avenue
Northwest Industrial Park
Burlington, MA 01803
Attn: Charles Humphrey

Visidyne, Inc.
19 Third Avenue
Northwest Industrial Park
Burlington, MA 01803
Attn: J. Reed

Wayne State University
1064 MacKenzie Hall
Detroit, MI 48202
Attn: Pieter K. Rol
Chem Engrg & Mat Sci

Wayne State University
1064 MacKenzie Hall
Detroit, MI 48202
Attn: R. H. Kummler

Wayne State University
Dept. of Physics
Detroit, MI 48202
Attn: Walter E. Kauppila

Yale University
New Haven, CT 06520
Attn: Engineering Dept.

AF Geophysics Laboratory, AFSC
Hanscom AFB, MA 01731
Attn: OPR B. Sandford
(10 copies)

Director
Defense Advanced Rsch Proj Agcy
Architect Building
1400 Wilson Blvd.
Arlington, VA 22209
Attn: S. Zakanycz /STO

Director
Defense Advanced Rsch Proj Agcy
Architect Building
1400 Wilson Blvd.
Arlington, VA 22209
Attn: P. Clark /STO

Director
Defense Advanced Rsch Proj Agcy
Architect Building
1400 Wilson Blvd.
Arlington, VA 22209
Attn: E. Kopf /STO

Director
Defense Advanced Rsch Proj Agcy
Architect Building
1400 Wilson Blvd.
Arlington, VA 22209
Attn: Program Management
(MIS Division)
(2 copies)

Director
Defense Advanced Rsch Proj Agcy
Architect Building
1400 Wilson Blvd.
Arlington, VA 22209
Attn: J. Jenney /STO

Commander
Naval Electronics Systems Command
Naval Electronics Systems Command Hq.
Washington, DC 20360
Attn: PME 117

OSD-ASDI the Pentagon
Washington, DC 20301
Attn: Mr. W. Henderson

OSD-ASDI the Pentagon
Washington, DC 20301
Attn: Mr. A. Albrecht

US Arms Control & Disarmament Agency
Department of State
Washington, DC 20451
Attn: Dr. F. Elmer

Commander, US Army Missile Command
Redstone Arsenal, AL 35809
Attn: DRDMI-NS Mr. Drake

Commander, US Army Missile Command
Redstone Arsenal, AL 35809
Attn: DRDMI/REI Mr. Jackson

Missile Intelligence Agency
Redstone Arsenal
Huntsville, AL 35809
Attn: DRSMI-YDL

Hq USAF
Washington, DC 20330
Attn: Col L. Deliso, RDSD

Hq USAF
Washington, DC 20330
Attn: Lt Col C. Heimach, RDSD

Hq USAF
Washington DC 20330
Attn: Lt Col G. Watts, RDSD

Air Force Systems Command
Andrews Air Force Base
Washington, DC 20334
Attn: Capt D. Beadner, DLCEA

Air Force Systems Command
Andrews Air Force Base
Washington, DC 20334
Attn: Maj W. Kurowski, XRID

SAMSO, P.O. Box 92960
Worldwide Postal Center
Los Angeles, CA 90009
Attn: Col J. McCormick, SZ

SAMSO, P.O. Box 92960
Worldwide Postal Center
Los Angeles, CA 90009
Attn: Col R. W. Johnson, DY

SAMSO, P.O. Box 92960
Worldwide Postal Center
Los Angeles, CA 90009
Attn: Lt Col R. Shields, SZD

SAMSO, P.O. Box 92960
Worldwide Postal Center
Los Angeles, CA 90009
Attn: Lt Col E. Gee, DYA

Rome Air Develop. Center, AFSO
Griffiss Air Force Base
Rome, NY 13440
Attn: Mr. D. D. Dylis, IRAD

Air Force Propulsion Lab
Edwards Air Force Base, CA 93523
Attn: Dr. J. D. Stewart

Air Force Armament Lab
Eglin Air Force Base, FL 32542
Attn: Capt W. Rothschild, DLMQ

Foreign Technology Division
Wright-Patterson AFB OH 45433
Attn: Mr. T. Larson

Foreigh Technology Division
Wright-Patterson AFB OH 45433
Attn: Mr. R. C. Frick

Air Force Avionics Lab
Air Force Systems Command
Wright-Patterson AFB, OH 45433
Attn: Mr. W. Edwards

Arnold Engineering Development
Center, TN 37389
Attn: Dr. H. E. Scott

Arnold Engineering Development
Center, TN 37389
Attn: Dr. W. K. McGregor

Arnold Engineering Development
Center, TN 37389
Attn: Dr. C. Peters

Naval Weapons Center
China Lake, CA 93555
Attn: Mr. W. L. Capps

Naval Weapons Center
China Lake, CA 93555
Attn: Dr. M. Benton

Naval Weapons Center
China Lake, CA 93555
Attn: Dr. L. Wilkins

Central Intelligence Agency
Washington, DC 20505
Attn: Mr. Berguist

Aerospace Corporation
El Segundo Operations
P.O. Box 95085
Los Angeles, CA 90045
Attn: Dr. F. Simmons

Aerospace Corporation
El Segundo Operations
P.O. Box 95085
Los Angeles, CA 90045
Attn: Dr. R. Lee

Aerospace Corporation
El Segundo Operations
P.O. Box 95085
Los Angeles, CA 90045
Attn: Dr. C. Randall

Aerospace Corporation
El Segundo Operations
P.O. Box 95085
Los Angeles, CA 90045
Attn: Dr. H. Graff

Aerospace Corporation
El Segundo Operations
P.O. Box 95085
Los Angeles, CA 90045
Attn: Dr. J. Ator

Institute for Defense Analysis
400 Army-Navy Drive
Arlington, VA 22202
Attn: Dr. H. G. Wolfhard

Institute for Defense Analysis
400 Army-Navy Drive
Arlington, VA 22202
Attn: Dr. L. Biberman

Aerodyne Research, Inc.
Bedford Research Park
Crosby Drive
Bedford, MA 01730
Attn: Dr. J. Draper

Aerodyne Research Inc.
Bedford Research Park
Crosby Drive
Bedford, MA 01730
Attn: Dr. H. Camac

Block Engineering
19 Blackstone Street
Cambridge, MA 02139
Attn: Dr. M. Weinberg

Carson System, Inc.
4630 Campus Drive
Newport Beach, CA 92660
Attn: Dr. John Carson

CALSPAN
4455 Genesee St.
Buffalo, NY 14221
Attn: Dr. C. Treanor

CALSPAN
4455 Genesee St.
Buffalo, NY 14221
Attn: Dr. W. Wurster

Environmental Research Inst of Michigan
P.O. Box 618
Ann Arbor, MI 48107
Attn: Mr. G. Lindquist

Environmental Research Inst of Michigan
P.O. Box 618
Ann Arbor, MI 48107
Attn: Mr. R. Legault

GASL
Merrick & Stewart Avenues
Westbury, NY 11590
Attn: R. R. Vaglio-Laurin

Grumman Aerospace Corp.
Research Dept - Plant 35
Bethpage, Long Island, NY 11714
Attn: Dr. M. Slack

Grumman Aerospace Corp.
Research Dept - Plant 35
Bethpage, Long Island, NY 11714
Attn: Dr. D. Moyer

Hughes Aircraft Company
Culver City, CA 90230
Attn: Mr. I. Sandback

Lockheed Missiles & Space Co.
3251 Hanover Street
Palo Alto, CA 94304
Attn: Dr. D. Pecka

Lockheed Misiles & Space Co.
3251 Hanover Street
Palo Alto, CA 94304
Attn: Dr. E. Smith

Riverside Research Institute
1701 Fort Myer Drive
Arlington, VA 22209
Attn: R. C. Passut

Rockwell International Corp.
Space Division/SF12
12214 S. Lakewood Blvd.
Downey, CA 90241
Attn: Richard T. Pohlman

Science Applications, Inc.
P.O. Box 2531
La Jolla, CA 92037
Attn: Dr. Jim Myer

Defense Intelligence Agency
Washington, DC 20301
Attn: Mr. S. Berler DT-1A

R&D Associates
4640 Admiralty Way
P.O. Box 9695
Marina Del Ray, CA 90291
Attn: Mr. Bryan Gabbard

General Electric Company
Aircraft Engine Group
Evandale Plant
Cincinnati, OH 45215
Attn: B. Wilton, Mail Code E198

Boeing Aerospace Co.
P.O. Box 3707
Seattle, WA 98124
Attn: D.M. Owens M/S 8H27

Northrup Aircraft Division
3901 W. Broadway
Hawthorne, CA 90250
Attn: Dr. J. Cashen

Air Force Avionics Lab
Wright-Patterson AFB, OH 45433
Attn: Dr. R. B. Sanderson/WRP

Air Force Avionics Lab
Wright-Patterson AFB, OH 45433
Attn: B. J. Sabo/WRA-1/Library

Aeronautical Systems Division
Wright-Patterson AFB, OH 45433
Attn: D.J. Wallick/ENFTV

Aeronautical Systems Division
Wright-Patterson AFB, OH 45433
Attn: Major L. Basten/AEWA

Air Force Flight Systems Lab/FXB
Wright-Patterson AFB, OH 45433
Attn: Dan Fragga

Hq Strategic Air Command/XPES
Offutt AFB, NE 68113
Attn: Major B. Stephen
(2 copies)

Air Force Technical Applications
Center/TAS
Patrick AFB, FL 32925
Attn: Capt R. Zwirnbaum